THE UNIVERSITY
of ADELAIDE

Application of Multilateral Jet for Partial Pre-Mixing

Chia Xiong Thong

A THESIS SUBMITTED IN FULFILLMENT OF THE REQUIREMENTS FOR THE DEGREE OF PHD IN MECHANICAL ENGINEERING

FEBRUARY 2017

Abstract

The feasibility of multilateral jet mixing to produce partially premixed flames is studied in this thesis. Partially premixed flames are ubiquitous in many practical combustion systems, whilst controlled partially premixed flames are more stable and resilient towards extinction. It is hypothesized that, better control of flames is possible through multilateral jet mixing, in particular when reactants' composition is variable. The technique of using multilateral jet for mixing has not been tested thoroughly and the fundamental fluid mechanics associated with the resulting flows is still unclear. The overall aim of this study is to understand the fundamental flow characteristics of multilateral jet in a confined cross-flow and to explore the feasibility and limitations of this technique to better control the stability of turbulent jet flames. Hence, this thesis aims to explore: the flow structures and characteristics inside and outside the nozzle; the side-jets mixing modes and parameters; mixing efficacy; and the flame structures in the near-field of the nozzle exit.

The study was conducted in two parts: isothermal water-based flow studies; and turbulent reacting flows studies. Experimental campaigns under isothermal conditions were used to investigate the flow structures and regimes that can be produced by varying the side-jets to primary flow momentum ratio (MR). The experiments were conducted with nozzles consisting of four side-jets (4SJ), equi-spaced and located one primary diameter upstream of the nozzle exit, with the nozzle placed in a closed-loop water tunnel. This study employed Planar Laser Induced Fluorescence (PLIF)

and Particle Image Velocimetry (PIV), two non-intrusive laser diagnostic techniques, to study the mixing and flow fields, respectively. The flow Reynolds number, based on the primary jet diameter, ranged from 1300 to 6500. Different mixing regimes were identified to correspond to different momentum ratios. These regimes are: streaming flow; impinging flow; and backflow regime. The PIV results show that the side-jets in the streaming flow regime does not alter the primary flow field significantly. The impinging side-jets form a stagnation point upstream, which diverts primary flow over the stagnation region. Increasing the momentum ratio further leads to the backflow regime, which shows flapping characteristics upstream.

The effects of the side-jets momentum ratio on the near-field flow, downstream of the primary jet nozzle exit were also investigated. This study shows that with the increase in momentum ratio, the coherent large-scale vortices roll-ups in the near-field become less apparent and more random multi-scale vortices are observed. Furthermore, increasing the momentum ratio further increases the centreline turbulence intensity and velocity decay of the jet in near-field. The existence of the side-jets alters the velocity and secondary flow distribution (dye) profile at the nozzle exit. These profile modification and increase in centreline turbulence and velocity decay persist to approximately two primary diameters downstream before morphing to a Gaussian profile, consistent with that of a round jet.

Similar experiments were also conducted using the same primary flow with three side-jets (3SJ) mounted one primary diameter upstream of the exit plane, and with momentum ratios varied. This study shows that for both the 3SJ and 4SJ configurations and at low flow momentum ratio, Counter-rotating Vortex Pairs (CVPs) appear. When the side-jets penetrate the primary flow centreline, axis-switching of the CVPs are observed. Commercially available Computational Fluid Dynamics

(CFD) package ANSYS CFX was used to further interrogate the vortices after axis-switching and determined that the vortices are rotational, which advect flow in the nozzle, both towards and away from the flow centreline. This study also shows that classical Jets in Cross-Flow (JICF) scaling methods are not suitable for scaling the trajectory of the side-jet in a confined flow. The trajectory of the individual JICF are affected by: existence of adjacent jets; confinement geometries; and restrictions posed by the primary flow centreline. The backflow length for both the 3SJ and 4SJ can be scaled to the MR and the number of side-jets. A constant for the scaling, k is identified as 0.18, for the dye mixture fraction scaling method and 0.16 for the velocity scaling method. It is also found that the 4SJ configurations generally show higher turbulence and vorticity than the 3SJ due to the increase in primary flow blockage ratio.

Experiments were also conducted on partially premixed flames of natural gas and air. The primary nozzle was constructed of a stainless steel long-pipe with 25.4 mm inner diameter. Both 3SJ and 4SJ nozzle configurations were examined under the influence of different flow MR. The PIV on the centreplane, downstream from the nozzle exit for 4SJ shows that the velocity profiles are symmetrical and similar for the planes in the side-jets' axis and 45° offset. This similarity seem to happen despite the obvious differences in the mixing profile generated at the nozzle exit shown in earlier studies. Flame photography was conducted with a standard DSLR at different exposure time. The physical flame length for the lifted flames, with momentum-ratio matching the impinging flow regime is markedly shorter than that in the backflow regime. Transitioning from lifted flames to attached flames shows a reduction in OH* emission, usually associated with reduction in temperature, at the flame front. Furthermore, the study also shows that flow cases with higher momentum-ratio are more stable than the lower momentum-ratio case despite similar air-to-fuel ratio.

The various studies conducted in this thesis have shown that multi-lateral jet mixing is a feasible, simple and effective technique to partial premix reactants. The momentum ratio is able to provide additional control to stabilize the turbulent flame independent of equivalence ratio. More work is needed to better optimize this technique. In particular, a further understanding of the reactive scalars distribution in the generated flames; the development of high fidelity predictive models of these flames and the adaptability of the nozzle to different fuels' compositions, are all needed if this technique is to be developed further.

Contents

Declaration

I certify that this work contains no material which has been accepted for the award of any other degree or diploma in my name, in any university or other tertiary institution, and to the best of my knowledge and belief, contains no material previously published or written by another person, except where due reference has been made in the text. In addition, I certify that no part of this work will, in the future, be used in submission in my name, for any other degree or diploma in any university or other tertiary institution without the prior approval of the University of Adelaide and where applicable, any partner institution responsible for the joint-award of this degree.

I give consent to this copy of my thesis, when deposited in the University Library, being made available for loan and photocopying, subject to the provisions of the Copyright Act 1968.

The author acknowledges that copyright of published work contained within this thesis resides with the copyright holder(s) of those works.

I also give permission for the digital version of my thesis to be made available on the web, via the University's digital research repository, the Library Search and also through the world wide web search engines, unless permission has been granted by the University to restrict access for a period of time.

I acknowledge the support I have received for my research through the provision of an Australian Government Research Training Program Scholarship.

Chia Xiong Thong

(a1186303)

Acknowledgement

I would like to express my deepest gratitude and appreciation to my supervisors Prof Bassam Dally, Dr Cristian Birzer and Dr Peter Kalt, for being great mentors to me over the past few years. Your valuable advice on both life and academic matters is much appreciated.

I would also like to thank both my parents and my partner Lenna for keeping up with my selfishness while studying for my Ph.D., over the past four years, and also for putting my responsibilities on hold. Thank you for being supportive and understanding.

I would like to acknowledge my office-mates: soon-to-be Drs JingJing Ye and Chen Xiao, Dr Manabendra Saha and Dr Dahe Gu, for making my time in the office enjoyable.

A special mention goes to my lunch-mates soon-to-be Drs JinHan Lim and Kimberley Kueh for walking with me through this treacherous road-less-taken. Also Kristin Hah and Eelin Tek whom walk the same path.

I would also like to acknowledge the support received from Marc Simpson, Stephen Kloeden, and the rest of the workshop and administration staffs. Also, a shout out to others whom I've met in this journey, and I've failed to mention.

Chapter 1

Introduction

1.1 Energy and Combustion

Combustion plays a vital role in today's society and provides cornerstones for societal developments, such as: electricity generation, industrial processes, transport, and heating and illumination. The roles of combustion have evolved through time, from simple human activities to complicated processes, spurred by the technology advances and catalysed by the Industrial Revolution. This evolution of combustion is also reflected by the displacement of traditional biomass based fuels (charcoal, firewood, and dried crops) by fossil fuels (coal, petroleum and natural gas) due to the higher energy and power density, and the lower costs of productions [1]. Combustion processes are important and critical to many aspects of our lives in the present and are expected to remain relevant in the foreseeable future. This dependency on combustion is not only anchored upon our individual needs, but the high demand for the natural resources coupled with their uneven distribution influences the economy of various industrialized nations [2]. With limited natural and financial resources, it is evident that combustion processes still need to be improved where possible.

Combustion of fossil fuels, whilst playing an important role in boosting local economies

and indirectly providing job security, has adverse effects on environment and population health. The combustion of fossil fuels results in the emission of carbon captured over the millennia back into the atmosphere at a rate that exceeds the natural rate of carbon evolution into the litosphere [3]. The addition of anthropogenic carbon traps additional heat in the atmosphere and further contributed to Greenhouse Effect, which has devastating effect globally, be it to the environment or global population [4]. Although there is a general shift away from fossil fuel combustion, they are still present and widely utilized in industry, hence improvements in combustion processes are essential to reduce fossil fuel combustion impact on the environment.

The reduction in the production of anthropogenic carbon has been a major motivation for research to improve efficiency from current systems and the introduction of renewable energy technology. The steady expansion of knowledge in this field has allowed for harvesting of energy from different sources in nature, i.e. sun, wind, and tidal. Based on a realistic growth of 2.5% annually, renewables are projected to contribute around 120 Quadrillion Btu (35 Billion MWh) (Figure 1.1) towards the world's energy consumption. This is an encouraging growth however, the demand of energy is projected to surge towards the 800 Quadrillion Btu [5]. Therefore, the combustion of fossil fuels (liquid, coal and natural gas) is still vital to cope with this demand.

The transition from fossil fuel to renewables depends on five unique factors: scale of shift; energy density; power density; intermittency; and geographic distribution [1]. These affect the reliance of most industrial activities on combustion. Current developments in wind and solar harnessing activities put realistic power densities of wind and solar to around $3W/m^2$ and $20W/m^2$, respectively. This produces significantly lower power density than fossil fuels which average around $100W/m^2$ [6]. The

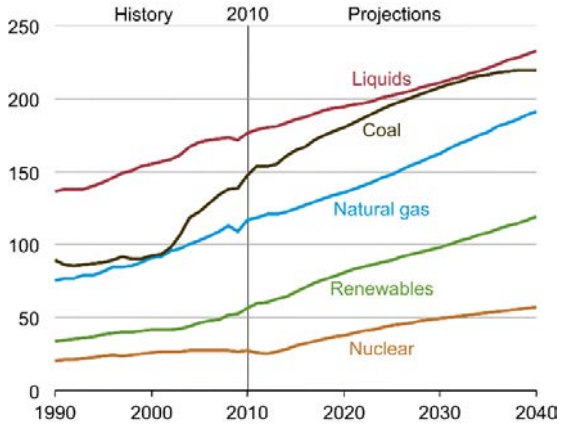

Figure 1.1: World energy consumption by fuel type, 1990-2040 (Quadrillion Btu)[5]

uneven distribution of natural resources required (some places may not be as windy or sunny as the others) and the dependence on the forces of nature are outstanding issues that still affect the effective application of renewable energies. In addition, difficulties tapping into renewables for industrial high temperature applications, for example in kilns, smelting furnaces and gas turbines, contribute to the continuous application of fuel combustion. Therefore, the need to increase the efficiency and controllability of combustion devices to mitigate their influence on the environment and operate the most optimal way is still high.

1.2 Flame stability and control

For combustion, mixing of fuel and air has first order effects on flame characteristics [7]. For practical combustion applications, it is vital to be able to control and maintain generated flames' stability. Flame characteristics can be influenced by burner aerodynamics [8], which indirectly affect the fuel-air mixing. This is further complicated by the various blends of fuel currently used in the industry. Therefore, different burner aerodynamics and infrastructures may be required to accommodate the combustion of these different fuels.

Fuel blends differ physically (density and viscosity) and chemically (such as volatility). These differences may lead to different characteristics time scales for chemical reactions which impacts combustion operability. Furthermore, corresponding to these differences, the performance and thermal efficiencies of the fuels vary for different fuel-air mixing intensities [9, 10], equivalence ratio, and heating limits [11]. While fuel properties and purity can make a large difference in the flames stability and pollutant emission, mixing of the fuel and air still plays an ever important role in ensuring the complete combustion and the conditions that reduce emission, and enhance energy transfer. In addition, different fuel-air mixing intensity to achieve stability and required soot propensity also differs by fuel blends [11]. It is a challenge to effectively mix the different blends of fuel to meet the optimum performance required of the system.

Control and stability of flames are highly important for it to be practical in the industry. The required flame characteristics differ depending on the application. Flame instability (unsteady flow oscillations in a combustion system) can be catastrophic for high temperature systems [7]. Current methods for flame stabilization can be categorized as passive and active methods. Both methods have advantages and disadvantages in mixing and stabilizing flames. Passive control methods commonly involve physical alterations or additions to the fuel nozzle. Laboratory scales passive control methods have been proven to be effective in stabilizing flames [12] and its characteristics will be further discussed in Chapter 2. These passive control methods do not allow much control options of the mixing process. Hence, in the absence of any mixing control mechanism, the fuel injectors are used to modulate the flow field and combustion process [7].

Active mixing mechanisms such as movable tabs and acoustic forcing allow certain

degrees of control of fuel-air mixing intensity. However, the price to actively control mixing and stabilization is high and comes in the forms of: higher energy input; more complex set up; and higher/regular maintenance to ensure uninterrupted operations. Therefore, there is a need to explore alternative mixing control strategies that are simple, but allows better control of the fuel and air.

1.3 Multilateral jet for gas reactants mixing

The current study is focussed on the concept of multilateral jet for reactants mixing. The combustion nozzle used for this study incorporates lateral side-jets that inject into the primary nozzle at a certain distance upstream of the exit plane. Side-jets are well studied and are known to produce large-scale complex vortices, which may impact the combustion processes by modulating reactants mixing. However, the fundamentals of side-jets for this application are not well understood.

These jets can carry either fuel or air, which when injected into the primary jet, can create a partially premixed mixture that exits the primary jet. The flame is stabilized outside the primary long-pipe nozzle and the partial premixing is expected to improve flame stability and provide better control of the mixing. While a variety of nozzle cross-sections can be used, the simple round nozzle geometry will be used for the current study due to its use in the industry.

Partial premixing of fuel and air is not new and is used extensively in gas turbines. Partial premixing is defined as “situations where the fluid parcel is compositionally inhomogeneous covering a wide range of mixture fractions including flammable as well as non-flammable fluid" [13]. It is desirable as a method to control the flame temperature (to reduce Thermal NOx formation). Below flammability limits, it also provides the safety features of non-premixed combustion and has been shown to

stabilize flames by producing higher strain resistant [14] and shorter flame length [15], hence more stable than non-premixed flames. Partial premixing has been attempted through jet in a co-flow [16], jets in counter-flow [14], and recent attempts to control partial premixing include recessing concentric jet [13].

The general aim of this thesis is to explore the feasibility of using multiple lateral jet to establish stable turbulent jet combustion by partially premixing reactants upstream of the nozzle exit, before being expelled into the combustion zone. To do so, it is vital to identify the mechanisms which side-jets influence the mixing in jet flows. Additionally, this study quantifies the effect of side-jets on non-premixed turbulent flame characteristics and flow-chemistry interaction in the reaction zone.

1.4 Thesis layout

This thesis is in the format of a thesis by publication, in accordance with the rules and regulations of The University of Adelaide. Chapter 1 introduces the big picture view of the research field, motivation and the thesis layout. Chapter 2 provides a literature review to highlight gaps in the research field, thus leading to specific aims, objectives and hypothesis of the current work, and how they will be addressed in the following chapters. Chapter 3-6 contain copies of journal articles/manuscripts where the author is the main contributor. These represent the results and discussion chapters from this work. Chapter 7 provides a summary of the results, suggestions for future work and conclusion arising from this study. Conference publications which result from this work can be seen in the appendices.

Chapter 2

Background Literature

Combustion is a complex chemical reaction process that converts dormant chemical energy stored within fuels to practical forms such as heat and light. The complexity of the combustion processes spans general fields of fluid mechanics, heat transfer and thermodynamics, and reaction kinetics.

Recent advancements of renewable energy technologies have made it possible to reduce the dependence on combustion for energy generation. This reduces the production of pollutants such as greenhouse gases, soot, NOx, sulphur oxides, and other trace elements commonly associated with fossil-fuel combustion. Despite the advent of renewables technologies to produce energy from solar, wind or the ocean currents, combustion is still needed for mineral processing, metals production, smelting, rotary kilns for cement production, or transport. Therefore, combustion is still relevant both for today's society and in the foreseeable future, and studies are required to optimize combustion processes, to maximize heat output and reduce pollutants emissions. These provide the main motivations of the current study of multilateral jet burners, for this thesis.

2.1 Overview of turbulent jet flames

In industry, the requirements for the different burners vary greatly depending on applications and this makes it difficult to tailor the performances of flames to its intended applications [8]. For example a gas turbine requires high intensity combustion with reactants residence time in the order of milliseconds, while a radiant and 'lazy' flame is desirable in furnaces and kilns where the residence time spans are typically in order of a few seconds [8]. This is further complicated by the desire to control reactants mixing intensity to optimize the performances for burners. However, most industrial flames are generated from a form of turbulent jet issuing from round orifice burners [17] with variations in aerodynamic addition to cater to the different flame types. Therefore, it is obvious that there is a niche for burners with flexibility to allow for the manipulation of mixing, and subsequently flames.

Despite the many burner designs in industry, almost all practical combustions are turbulent [18, 19], and so, is of interest for the current investigation. These induce flow interactions in a wide variety of length and time scales within the flow [20]. The flames generated are constrained (flame spread and length) to the geometry of the combustion chamber itself and hence, direct impingement of flames on the chambers' surfaces are normally avoided to prevent damage [21]. To achieve this, various parameters including: air/fuel mixture; fluid dynamics (aerodynamics) and thermodynamics conditions; mixing intensity; local temperature; and flow strain rates, are usually manipulated [19]. Of these, aerodynamics play a major role to control the flame characteristics, and in particular to control mixing intensity [22]. The resulting burner's performance is generally reflected by it's respective combustion dynamics, i.e. flame stability, radiation, and emissions (such as NOx, SOx, CO and soot) [8, 22]. Therefore, the current study presented in this thesis aims to capitalize on the aerodynamics features generated by the applications of multilateral jet mixing.

Flame radiation is the dominant mode of heat transfer in most practical high temperature applications with open flames, which is attributed to the fourth power dependence of radiant heat transfer on the temperature differential [23]. The features of turbulent jet flames are coupled to the flow dynamics (such as turbulence), thermodynamics and heat transfer, and the reactants composition variable in the system [20, 23–25]. Most studies to enhance combustion and improve flame stability focus on the interactions of turbulence and chemistry as they play a direct role in influencing the structures and stability of the flame, reaction rate, and relationship between species concentration [20, 23]. The current study strives to systematically decipher the flow and turbulence field in order to enhance flame stability and mixing.

Despite the overall burning rate in the flames being heavily influenced by turbulent mixing, the heat release from combustion also reduces the entrainment rate of ambient flow into the jet flow-field [26]. The influence of flow turbulence on the flame flow-field can be characterized to some extent, by the turbulence field in the 'cold' reactants ahead of the flames [25, 27]. Therefore, by altering the flow dynamics upstream of the combustion zone, it is possible that the flame's characteristics can be manipulated.

To generate turbulent flames, sufficiently large flow Reynolds Number (Re) is required [28]. The large Re renders the influence of Kelvin-Helmholtz (KH) instability, which governs the evolution of large-scale structures, more significant [27]. Three-dimensional instabilities are induced near the nozzle exit that cascade to smaller vortices in the mixing layer, which initiate the transition of flame into turbulent flame. This is further illustrated in Figure 2.1. The coupling of both 3-dimensional large-scale and small-scale mixing generally initiate the vortex-braid region in the

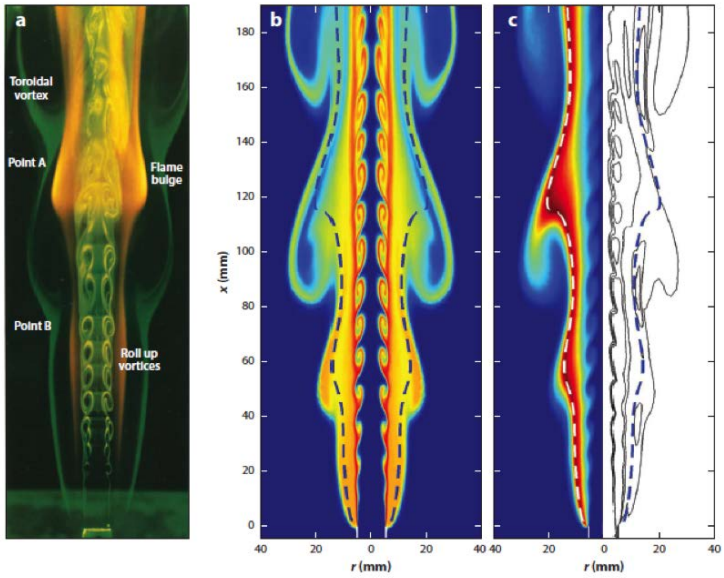

Figure 2.1: (a) Visualization of a methane jet diffusion flame at Re = 2390, which shows the smaller vortical roll-ups in the flow, (b) large-scale roll-ups at the shear layer, and (c) temperature and vorticity contours in the flow-field. Flames generated are marked in (b) and (c) by the dashed lines. Adapted from Linan et al. [28].

shear layer, and this affects the local flame extinction and the formation of random flamelets [25, 27].

In turbulent jet flames, two-dimensional instabilities lead to different vortical patterns despite equally affecting the reaction intensity and combustion stability [25, 27, 28]. The buoyant flow induced by the reaction heat release produce shear layer instabilities in the form of large-scale structures, toroidal vortices, and subsequently smaller eddies, which are responsible for the “flickering” often observed with a diffusion flame [25, 27]. This flickering phenomenon and self-sustained oscillations are dominated by the flow instabilities. The unsteady nature of flames are difficult to predict owing to the continuous distortion, expansion, production and dissipation of flame surfaces [27, 28].

The vortical roll-ups in the flow play an important role in transporting fresh reactants into the combustion regions [27]. The flame-vortex interactions increase the local temperature of an undriven flame above the steady state, and therefore determines the rate of reaction in the flow and amplitude of the pressure pulse, which is generally associated with vortex burnout [27]. Therefore, it is not exaggerating to say that these structures influence the shape of the flames, besides other parameters such as laminar flame speed, fuel concentration, local velocity gradient, and flow Lewis Number [29].

The initial conditions upstream are generally taken as a reference condition, and as previously mentioned, can be manipulated, to a certain extent, to alter the flow dynamics in a turbulent flame, in addition to other flow conditions such as frequency, interaction and energy distribution among the various length scales [27]. Hence, modification of the flow instabilities in flames by generating 3-dimensional structures (for example through Jets in Cross-Flow (JICF)) could potentially enhance the decay of large-scale structures to small-scale structures, which may lead to enhanced reactants mixing and increase global combustion reaction rate [27]. However, the large-scale instabilities surrounding the flame may not be affected by the flow perturbations [28]. The impact of JICF on mixing in turbulent jet flames, however, remained untested.

Diluting the reactants with air or inert gases has been proven to decrease flame length, and this potentially moves the reaction zones into regions of high shear stress [15]. Such change reduces both the global and local fuel residence time, which if sufficiently short, allows flame chemistry to be far from equilibrium and altering the characteristics of the flame [15]. This will be attempted by partial premixing the reactants via multilateral jet mixing.

2.1.1 Premixed, non-premixed, and partially premixed flames

For academic purposes, flames are traditionally classified as premixed and non-premixed, depending on the fuel conditions. The actual combustion process, however, is much more complex with the inclusion of various mixed mode combustors and other practical devices, where partial premixing of reactants are ubiquitous [13, 30]. Mixed mode devices are tailored for their intended applications and may involve: charge stratification; direct injection; and exhaust gas circulation methods [30].

In reality, premixing both fuel and air required for combustion pose an explosion hazard [31]. Premixed flames, aside from being influenced by flow turbulence and mixing rate [27, 31], also propagate into regions of diffusion-controlled regions of the flame [32].

The premixed flame propagates in a self-supporting regime, which features are strongly coupled to the dependence of the reaction rate on temperature, expressed in the Arrhenius law for reaction rate $\propto exp(E/T)$, where E is the activation energy measured in temperature units and T the flame temperature. This implies that, in regions where strongly exothermic reaction is involved, a slight increase in temperature locally will ignite and cause reactions, which will eventually propagate over the whole gas mixture. The relationship between the flow and reactions remains complex due to their interdependency [33].

To introduce premixed flames briefly, they are often depicted with a thin flame sheet which separates the reactants from the products of reactions. The surface of this flame sheet is connected but is highly wrinkly (as it is convected, bent and strained by flow turbulence). The laminar flame speed of premixed flames is dependent on local conditions [33], such as the thermochemical state of the reactants [31].

The flame stretch affects the strain rate and flame curvature and increases the flame front surface area whilst regions with large positive tangential strain rates greatly decrease flame thickness. Furthermore, flow induced wrinkling and stretching significantly affect the reaction layer, which could lead to large variation in the local reaction rates. However, these distortions may not necessarily increase the global consumption of reactants [27].

Fuel and air are initially separated in many practical combustion systems due to the risks of flashback in a premixed system [28]. With such approach, termed turbulent non-premixed flames, the flames become mixing controlled and that allows the control of the flame length, volume, emission characteristics, and stability.

The fuel and oxidizer in turbulent non-premixed flames (TNF), initially separated, mix and burn at the reaction zone [32]. The reaction zones for non-premixed flames are often associated with zones based on reactants inter-diffusion [32]. Here, reactants coexist in small concentrations as most reactants, after “diffusing” from opposite sides, are consumed by the reactions. The reaction time is very short and produces high temperature regions [28]. Some studies also attribute the TNF to having two reaction zones (double flame), i.e. a rich premixed zone on the fuel-rich side, and a lean zone on the oxidizer’s side, respectively.

As mentioned, fuel and air mixtures do not exist in a homogeneous state in practical combustion systems, but mostly occur in a partially premixed mode [13, 34]. These are based on observation that the mixture upstream of the lifted-flame’s statistically stable position are partially premixed reactants mixture. This compositional inhomogeneity induced at the flame base can vary in time due to the flow instabilities

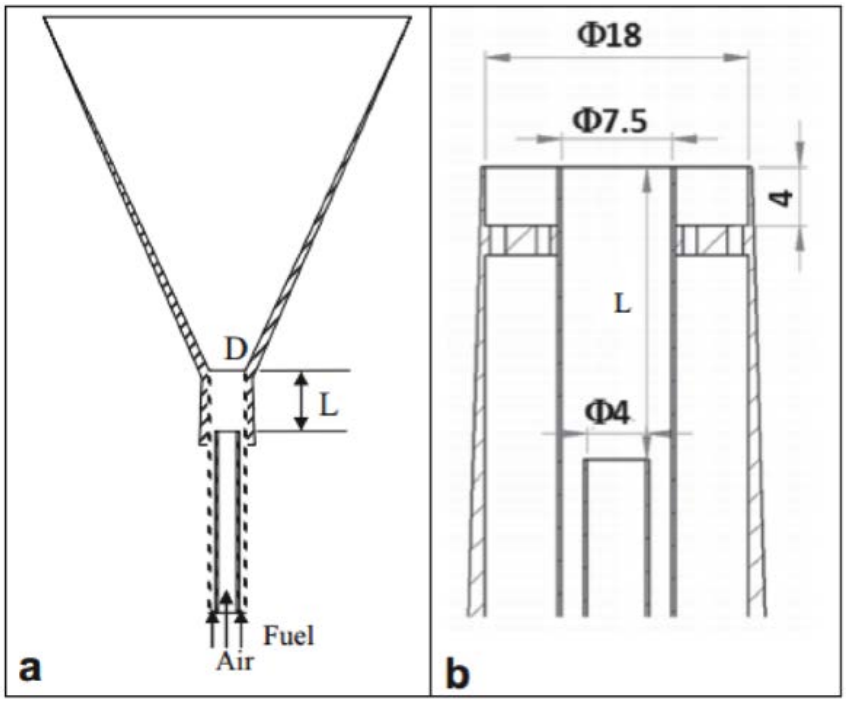

Figure 2.2: Schematic diagrams of two different concentric burners capable of providing inhomogeneous inlets [13].

that characterize turbulent jet flow [13].

Partial premixing describes the situations where fluid parcels are compositionally inhomogeneous and covers a wide range of mixture fractions [13]. Mixing continues to occur in these fluid parcels as they are transported into the reaction zones [13, 35]. A feature of partial premixing is that both diffusion like reaction zones and premixed propagating layers exist within close proximity, and thus it is described as a hybrid flame possessing both characteristics of the premixed and non-premixed flame [35]. These non-homogeneous mixtures are found to contribute to flame stability at high Reynolds Number and also suggest the formation of triple flame structures. This indirectly highlights the potential that a controlled partially premixed flame has over conventional premixed and non-premixed flames.

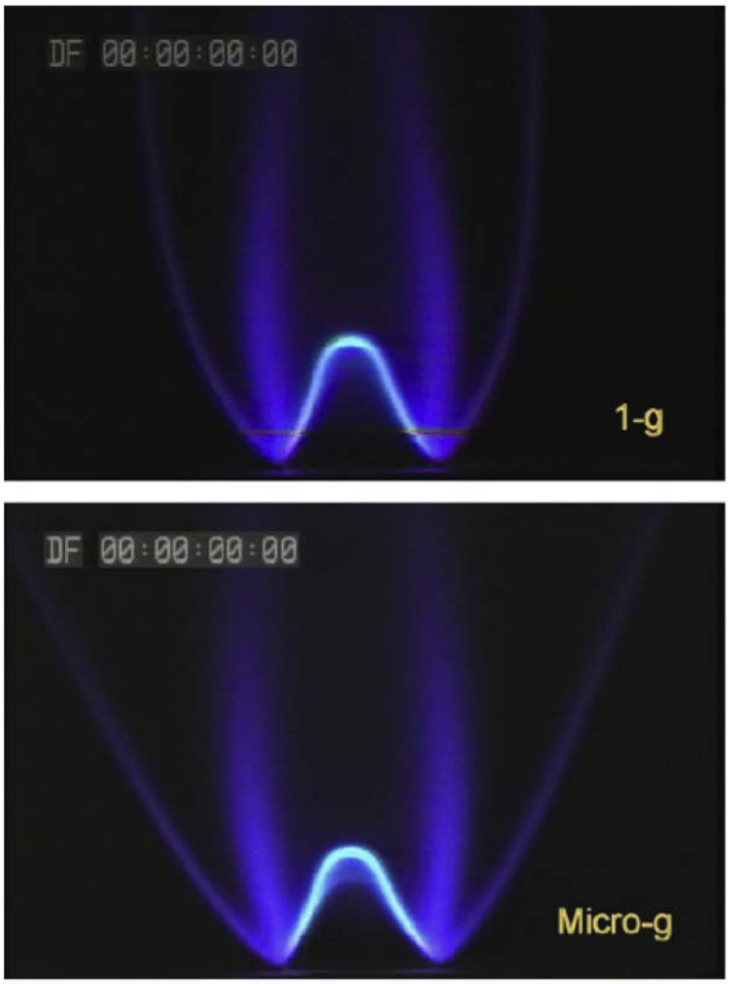

Figure 2.3: Triple flames established on a Wolfhard-Parker slot burner at normal gravity (top) and in micro-gravity (bottom). Adapted from Aggarwal(2009)

Partial premixing can be intentionally induced at the inlets (similar to premixing) or generated within the combustor, between the injector plane and the base of a lifted flame [13]. Partial premixing has been generated using concentric tube burners, as shown in Figure 2.2, with an adjustable inner pipe to provide the degree of partial premixing required [13]. It was also argued that partially premixed flames show greater stability than conventional non-premixed flames [36]. The rationale behind generating partial premixing is to increase the resistance of the flame to extinction caused by straining. However, both burners in Figure 2.2(a) and Figure 2.2(b) require

external stabilization mechanisms, i.e. a conical section [37] and a pilot co-flow [13]. Therefore, despite intentionally generating and controlling the partial premixing, the flames generated still require external stabilization mechanisms for additional stability.

Triple flame

As suggested by the term "triple flame", the flame burns on three modes simultaneously in different zones namely: a fuel-rich zone; a fuel-lean zone; and a non-premixed reaction zone, which anchors both the fuel-rich and -lean zone. This is in contrast to non-premixed flames, which has only one reaction zone. The reaction zones are spatially separated but "synergistically" coupled through thermochemical and fluid mechanics interaction between them, which influences the global flame structure [35].

Figure 2.3 shows a typical triple-flame or tribrachial flame that is generated over a slot burner. As presented in the figure, two premixed reaction zones form the "wings" of the flame and a non-premixed reaction zone is established in between (thick and bright region). These three reaction zones merge at a "triple point" upstream. A better representation of the triple-flames can be observed in the schematic diagram in Figure 2.4. The coexistence between these three burning zones indicates that the edge of the flame is located along the stoichiometric contour [29].

2.1.2 Reactants mixing mechanism

Mixing of the fuel and oxidant in turbulent jet flames is typically the rate-limiting step, and to a first order, controls the primary combustion processes in industrial scale non-premixed flames [21]. Mixing influences various characteristics typical of flames, and this include: combustion instabilities; emissions such as NOx, CO, CO_2,

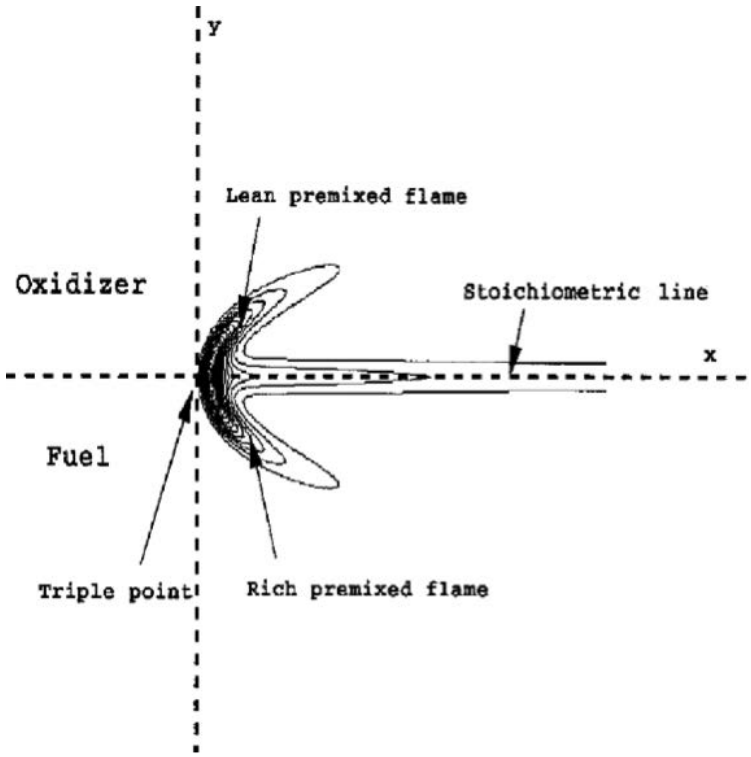

Figure 2.4: Schematic diagram of a propagating triple flame [38].

H_2O; and soot (which plays a key role in the flame radiation characteristics) [23, 39]. Furthermore, the degree and rate of mixing directly affect the mass transfer and reaction kinetics [40].

It was previously noted that the mixing efficacy in combustion systems is controlled, to a great extent, by large-scale vortex motions, which are commonly induced in the turbulent jet shear region [27]. Furthermore, these large-scale structures also play a role in determining the shape of the flame, stability and other combustion characteristics. Small-scale structures, on the other hand, bring the reactants together at microscopic level [18] and also influence the reactants' residence time through strain [23]. Heat release is also largely determined by the mixing intensity as intense reactions are commonly observed near high strain regions, induced by large vortices [27, 41].

The current study aims to enhance and quantify reactants mixing for combustion. Enhanced mixing of the initially separated reactants' streams in industry is required to burn efficiently to maximize heat release and to reduce residence time for advanced pollution control strategy [41]. The mixing intensity and range of scalar fluctuation decay are determined by molecular mixing and characterized by the scalar dissipation rate, $\chi_z[s^{-1}]$ [41, 42]:

$$\chi_z = 2\alpha_z|\nabla z|^2 \tag{2.1}$$

where α_z is the molecular diffusivity term for the mixture fraction, z.

Noteworthy that the characteristics of turbulent mixing are radically different from mixing by molecular diffusion. For example, increasing the flow velocity of a turbulent jet flame effectively increases the flow Reynolds Number, and hence turbulence, but it does not alter the flame length, in particular when the velocity is sufficient to produce a fully developed turbulent flow [43]. Therefore, this shows that without a specific reactant mixing technique, there is a limit to the extent of mixing that can be achieved by a simple turbulent jet flame, relying on the flow out of the nozzle itself.

2.1.3 Flame stability

Flame stability plays an important role in ensuring the continuity of the operation, safe operation and consistent heat generation, all which are critical to industry. Ensuring the continuity of the combustion reaction process is also a motivation to the conception of the multilateral jet burner in this thesis. Furthermore, a highly stable burner allows a more intense combustion and hence results in a higher burner capacity and load, for the same size [44].

Ignition of flames generally undergo a three-phase process [45]:

Phase (i) Flame pockets generated around a spark (ignition);

Phase (ii) Flame expansion and turbulent dispersion of the already ignited flame, and propagation of the flame front towards unburnt reactants;

Phase (iii) Flame stabilization, which is important for continuous operation of the burner, and is burner specific. Flame stabilization implies that the combustion reaches a statistical steady state condition for that particular flow rate.

Previously stated in Chapter 1, combustion instability refers to a coupling of heat release and acoustic waves, which result in damaging pressure oscillations within the combustion chamber. These oscillations can lead to intense pressure fluctuation level which may cause excessive structural vibrations and heat transfer to the system thus leading to failure [7, 46]. In addition, combustion instability may also lead to the decrease in the lean blow off limit or unsteadiness in thrust provided in propulsion devices [47]. Therefore, it is a challenge to design and develop combustors which suppress these combustion induced pressure oscillations and also extend the flame's flammability limits [48].

The study in this thesis also focuses on combustion instabilities in gaseous systems where hydrodynamic strain plays a dominant role. The combustion instability mechanism in gaseous turbulent jet combustion is complex and often involve coupling of flow-field conditions and thermo-chemical effects. Instability in a turbulent combustion system depends on various parameters [28], namely: thermochemical parameters; Damköhler number; fuel Lewis number; buoyancy; and co-flow.

The stabilization and emission characteristics of turbulent jet flame are also adversely

affected by local extinction [35], which is a result of localized flame instabilities. These instabilities occur when the flame is subjected to excessive strain or other limiting conditions [35]. This phenomenon contributes to the formation of "flame holes", often observed in an unstable jet flame [28]. These flame holes are separated by edge flames from regions of near-equilibrium flows.

Global flame extinction, meanwhile is generally attributed to interaction between excessive flow strain and reaction, which may be induced by large-scale eddies in the flow [27, 29, 46]. These eddies, typically in the scales equal to the flame thickness, can cause excessive flow fluctuation in the flame flow field that leads to quenching. This also happens when the Karlovitz Number, Ka of the flow is greater than one, i.e. $\tau_k \ll \tau_c$, where τ_k and τ_c denote the flow and chemical time scales, respectively.

The flame extinction, or blow off is often regarded as the "static stability" limit of the combustor design [46]. Flame blow off occurs when the flame detaches from its "anchoring position" and is physically blown out of the combustor. Flame blow off can also be considered as "consequences of finite-rate chemistry in competition of a finite-rate supply of cold reactants of the flame" [26]. Blow off can be costly to the industry as it requires lengthy and often expensive system shut down, purge and restart [46].

Another undesirable phenomenon in industrial flames is flame flashback. This is observed when flame propagates upstream of the anchoring point, breaching regions that are not designed to handle high temperature. Flame flashback poses serious safety risks to handling personnel and to the equipment and can be attributed to several mechanisms [46]:

- Turbulent flames propagation back into the core of the flow;

- Flashback due to combustion instabilities;
- Flashback in boundary layer; and
- Flashback in the core due to alteration of vortices breakdown.

A similarity can be discerned from these mechanisms, i.e. flashback occurs when the turbulent flame speed exceeds that of the flow velocity along some streamline, allowing flames to propagate back into the reactants premixing section. Therefore, it is a criterion to design a burner with high axial velocity to minimize the risks of flashback.

In addition, strong fluctuation in the flame due to large-scale vortices may also cause flame flashback in burners. The strong fluctuations emulate a pulsating mechanism that modulates the velocity field, causing periods of low flow velocity. If the velocity is low enough, flame flashback may take place.

Turbulent flames can exist in two states: burner attached and lifted-flame. Compared to attached-flames, lifted flames are more susceptible to flame blow off. At small primary flow to laminar flame velocity ratio (V_0/V_{SL}) values, i.e. in the order of unity, the flames generated remain attached and transit to being lifted-off after a critical value (which increases with jet velocity). The lifted-flame blows off when the jet velocity exceeds a critical value, and is dependent on the fuel mixture used (hence also dependent on laminar flame velocity (V_{SL})) [28]. Lifted-flames are governed by the local interactions of non-equilibrium chemistry and flow turbulence [49], and its blow-off characteristics depend on the ability of the triple flame and edge flame to propagate upstream, relative to the jet flow.

The stabilizing mechanisms for lifted-flames can be classified as: propagation of turbulent premixed flames, large-scale turbulence, and extinction of laminar diffusion

flamelets [35, 50].

The premixed flame theory argues that the lifted flame base is made up of premixed mixture that burns at local burning velocity, allowing the flame to stabilize at a statistically stable point [32]. The shortfall of this theory is that, the model used did not describe the flame dependence on the pre-existing large-scale flow structures induced in the flow. In summary, this theory attributes the flame stabilization to the equilibrium between the premixed turbulent burning velocity and flow velocity entering the flame base [51].

The critical dissipation concept associates the flame stabilization to the extinction of diffusion flamelets where the flame stabilizes when the scalar dissipation rate falls below a critical value [51]. The scalar dissipation rate increases downstream from the nozzle exit, along the stoichiometric contour of the flame, but falls off further downstream. This theory does not consider the premixing of fuel and air upstream of the flame front [32].

The turbulent intensity theory associates the propagation of the flame reaction zone to the impact of the turbulent burning velocity and turbulent intensity at the flame's leading edge.

The large eddy theory highlights the importance of large-scale structure in the flow. This theory stipulates that the flame's leading edge is attached to large-scale eddies and transferred to an upstream neighboring structure repeatedly in quick succession to stabilize the reaction zone. Furthermore, it also implies that there is a requirement to have hot combustion products constantly transported upstream in large-scale structures near the leading edge. This theory is not supported by experimental

results [32].

The edge flame theory assumes that the flame leading edge is partially premixed and propagates upstream to counter the local flow-field, whilst also augmenting the flow field through heat release.

These theories show that flow hydrodynamic i.e. flow turbulences and large-scale vortices, and fuel premixing both play a role in anchoring the flames to a “statistically" stable location. They also imply that the flow-field out of the nozzle, but ahead of the flame’s leading edge, is minimally affected by the heat release and flames downstream [50].

Flame stabilization is undoubtedly one of the most important subjects in combustion [52]. Much efforts and investments have been made to conceptualize flame stabilization strategies to ensure adequate time is available for the reactions to complete.

2.1.4 Flame stabilization strategies

Strategies, both aerodynamically and hydrodynamically, and sometimes through hot products recirculation [18], have been applied to further stabilize the flames generated. Devices with aerodynamic variability are generally designed to stimulate and excite the large-scale eddies that are embedded in the shear layer of the emerging jet. Examples of such devices in practice include: bluff-body burner, reverse/counter jet, wall recess, backward facing steps, and quarl/conical nozzle. The mechanisms and schematic diagram of bluff-body, counter jet, and cavity flame holders are illustrated in Figure 2.5, as summarized by Shimokuri and Ishizuka [52].

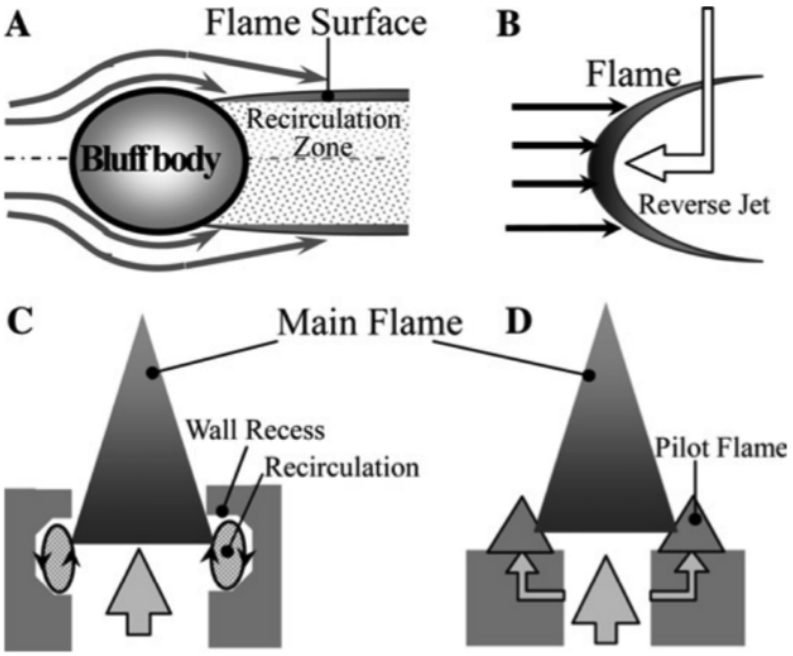

Figure 2.5: Flame stabilization techniques: (A) bluff body flame holder; (B) counter-flow; (C) cavity flame holder; and (D) piloted flame [52]

Flame stabilization can also be achieved by providing a continuous ignition source in the form of a piloted flame [53]. A pilot placed near the burner nozzle exit provides a high temperature reaction zone and a large radical pool that enhanced the stability for the combustion of fresh reactants from the main flow [54]. A shortfall is that, pilot flames are prone to blow-off as the flow is directly affected by the turbulence-field of the main flow stream [52].

Bluff bodies obstruct the flow-field thus generating a low velocity region in the rear of the object [55]. Mixing and reaction of the mixture is sustained in the low velocity region, assisted by the generation of large-scale structures. Prominent large-scale structures here include counter-rotating eddies, which recirculates the hot combustion product back into the fresh mixtures [52, 56]. The large-scale structures induced are influenced by blockage ratio, confinement, and most of all, the fuel

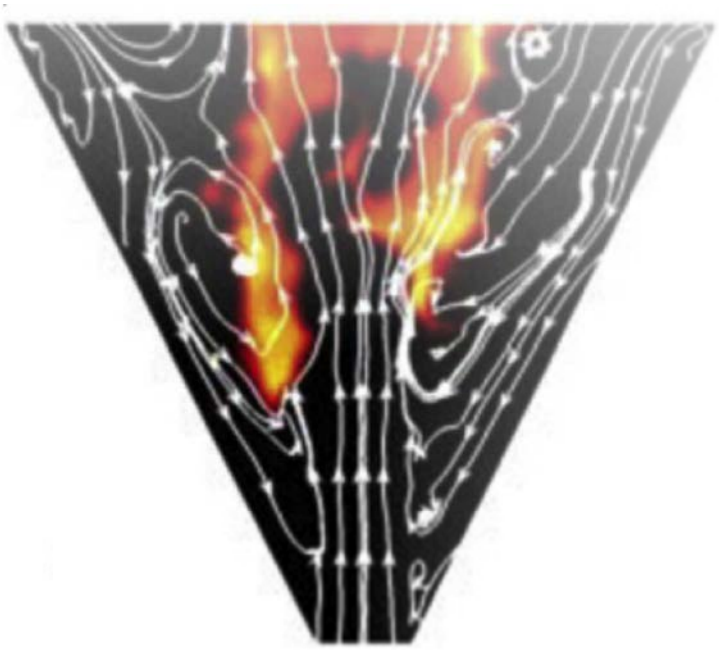

Figure 2.6: Instantaneous velocity streamline and temperature field inside a quarl[57].

to air velocity ratio [56]. Commonly used bluff-body burners are the disk-shaped and tulip-shaped bluff-bodies. The downfall of bluff-body burner includes pressure loss in the main stream due to drag which is proportional to the square of flow velocity and erosion and corrosion of the bluff-body due to its direct contact with high temperature flow [52].

Cavity flame holders involve a series of recesses in the wall and can sometimes feature a backward facing step. These type of flame holders provide a low-speed recirculation which assists in the establishment of the reaction zone. The recirculation reduces the bulk ignition delay time and stabilizes the flame at the nozzle exit [54]. However, these recesses can be damaged by strong velocity fluctuations in the flame [52].

The jet in counter-flow method injects flow (commonly oxidizer) in opposing direction to the fuel stream. This method is undesirable as it involves placing a

physical fixture into a fuel stream, which can also be damaged by high temperature, combustion and pressure oscillations in the system [52].

Figure 2.6 shows the velocity streamline and temperature inside a conical section (quarl) that is commonly used to stabilize jet flames and is perched at the nozzle exit. The quarl induces a flow recirculation and anchor the flames near the nozzle exit, thus stabilizing the flame [57, 58]. Furthermore, the quarl also entrains ambient air into the section, which further premixes with the reactants from the burner. An advantage of a conical section is that the flame stability is insensitive to the flame characteristics, mixture composition, flow velocity, and has a large operational range [57]. However, it is dependent on the cone angle.

To summarize, most of the combustion stabilizing devices have been successful in providing the functionality needed in certain applications. Invariably, they feature some physical fixtures or require modifications to the burner itself. Some of these fixtures require exposure and contact with the generated flame and sometimes in the fuel stream, which make it susceptible to damages caused by combustion instability. Furthermore, like a typical passive mixing device, they do not offer good control to help cater for fuel flexibility and flames' stability. However, these devices show that manipulation of aerodynamics/hydrodynamics is a viable combustion stabilization technique. This elevates the prospect of using multilateral jet as a stabilization method that also allows control towards reactants mixing.

2.1.5 Passive mixing devices

Due to rising commodity prices, it is a necessity for industry to adapt to alternative fuel blends, which range from coal-derived Syngas to biofuels and landfill gases. These fuels differ from natural gas in terms of physical and chemical properties, and

hence display markedly different combustion behaviour [7].

Common industry practices to beneficially modify the mixing rate typically involve having a near-field spreading rate that is dramatically different from that seen in the far-field [21]. This is achieved through stimulation of large-scale coherent motions to enhance the production of flow structures in the shear layer [8] and potentially increase the mixing rate between the reactants and increase the combustion intensity, whilst reducing volume. The application of "enhanced mixing" devices modifies the aerodynamics and increases the mixing rate between the jet and the ambient flow and the combustion intensity. Various combustion-mixing devices were conceived to accommodate the engineering challenge mentioned. These devices can be categorized into passive and active mixing devices.

Passive mixing devices generally require hardware and design modifications which are fixed in space and do not have explicit dynamic components or actuator [47]. The fuel nozzle itself is a critical element that can be controlled to modulate the flow field and combustion process leading to different flow features downstream [7, 59]. This includes inducing and destroying large-scale structures [48]. With these notions, that combustor geometries exert significant influences on the flow and flame structures [7], most passive control strategies involve modifications to the fuel injector itself. Modifications to the nozzle also influence acoustic properties of the burner, i.e. the pressure oscillations, which in turn affects the mixture flammability limit [7, 48]. Passive mixing devices are popular due to their simpler implementations and lower costs [60]. The variants in passive mixing devices are:

1. Non-circular nozzles

   Non-circular nozzles have been used for various purposes, which span from reducing jet noise to augmenting heat transfer between jet and flat plate [59].

Non-circular nozzles are effective in inducing large-scale flow structures and hence better flow entrainment. For combustion, continuous mixing between fresh mixtures and the hot products are required to sustain an on-going combustion. Combustion mixing can be broken down to a two stage process: (i) initial stage where large amounts are brought together through vortical action and (ii) the later stage involving small-scale turbulent mixing which accelerates molecular contact [59]. The application of non-circular nozzles enhances these processes by generating small-scale vortices directly from the nozzle vertices and sharp corners, hence increasing mixing rate, which directly increases the reaction rate [40]. However, there is a limit to how much mixing can be achieved, constrained to the burner geometry itself. Also, despite being effective in stabilizing jet flames, these devices provide little control over the mixing intensity achieved.

2. Mechanical tabs

   Mechanical tabs are physical fixtures that protrude into the flow-field and generate strong stream-wise vortices into the jet. Generally, more than one tab are placed around the jet periphery, which has been reported to be an effective method in enhancing near-field mixing, up to 10 jet diameters downstream [61]. The tabs placed around the jet exit distort the exiting flow cross-section profile, raising the level of turbulent stress in the flow, and this indirectly increases the entrainment of surrounding fluid into the jet. Like non-circular nozzles, they provide little control over the mixing intensity required, and are difficult to be removed once fitted.

3. Flow recirculation devices

   Recent fluid mechanics studies generated a 3-dimensional asymmetric flow structure, the Precessing Vortex Core (PVC), which is hypothesized to further enhance flow mixing and improve combustion efficiency [7]. These structures

are induced when the central vortex core is made to precess around an axis of symmetry at a well-defined frequency. This mode of mixing was generated via a swirling device [22] and a precessing nozzle [8]. The instability of flow generates large-scale structures in the shear region that sheds, leading to vortex breakdown due to Kelvin-Helmholtz instabilities [7, 22]. The precessing structures drastically affect the aerodynamics and flame evolution by modulating the mixing process of both reactants and hot products in a compact region within the combustion chamber [7, 22].

The core generates a strong adverse pressure gradient along the jet center axis, which lead to the formation of a recirculation structure, the central toroidal recirculation zone (CTRZ) [62]. This region is effective in recirculating heat and reactants to the root of the flame, hence anchoring the flame near the outlet, which generates a stable flame and provide a consistent flame establishment in regions of low velocity where flow and turbulent flame velocity are matched [62, 63]. However, in certain cases, precessing can contribute to undesirable combustion driven oscillations, which may cause damage to the combustion chamber [8].

A precessing jet nozzle generates fluid dynamic instability within an axisymmetric chamber following a large sudden expansion at its inlet. Within certain limits in the chamber geometry, the flow in the chamber reattached asymmetrically, which induces an azimuthal pressure field that drives a precession of the emerging jet from the nozzle [21].

Swirling jets in practical applications meanwhile, are often found in gas turbine combustors [62]. Swirl flows are defined as flows in a spiralling motion with

swirl velocity components (tangential and azimuthal components), and are commonly generated through swirl vanes or induced tangential jets [17]. The swirlers affect the flow-field jet growth, entrainment and decay, flame size, shape, stability and intensity [17]. Early studies in swirling flows show that the swirlers generate an azimuthal shear layer and centrifugal instabilities attributed to the PVC, which further enhance the asymmetric flow structures [7]. These characteristics have potential to enhance combustion mixing, in propulsion systems, and even in chemical reactors [64].

Both precessing jet nozzles and swirls are effective in reactants mixing by enhancing the production of large-scale vortices. The flow conditions are generally controlled by increasing the flow velocity whilst the jet geometry and vanes are physical fixtures that once implemented, are difficult to be removed or controlled. Therefore, it will be challenging especially when an instantaneous change to the mixing intensity is required.

4. Concentric tube burners

   Previous attempts to generate and control partial premixing have used the concentric tube burner [30, 44], previously presented in Figure 2.2. This partial premixing technique uses the jet in co-flow configuration, which is discussed in Section 2.3.3. Here, the exit of the inner tube is upstream of the outer tube and therefore allows a certain degree of partial premixing of reactants and allows the interaction between rich, lean and the diffusion structure in the flame [44]. Both fuel and air streams can be used interchangeably, i.e. fuel can be delivered via the inner tube and air through the outer tube, and vice versa [30].

   Recessing the central tube increases the flame stability and it has been

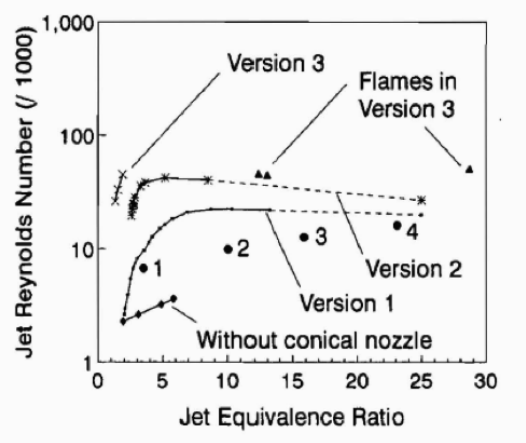

Figure 2.7: Stability characteristics of the concentric tube burner adapted from Mansour[44].

found that the optimum distance upstream is approximately 5 inner diameters upstream [30, 36]. By recessing the central tube also, different mixing intensity can be achieved and a uniform flow can also potentially be generated should the central tube be recessed beyond a certain distance [30]. Despite reporting increase in stability compared to a conventional non-premixed flame, owing to the partially premixed reactants and local velocity fluctuation [34], the concentric burner requires additional stabilizing mechanism, for example a conical nozzle [34] or a pilot co-flow [30]. The stabilizing effect of the conical section is clearly shown in Figure 2.7.

2.1.6 Active mixing

Active jet mixing and control systems depend on dynamic, or time varying hardware components, placed at strategic locations, to impart controlled and uncontrolled perturbations to the jet shear layer to achieve significant entrainment of ambient fluid into the jet [60]. Examples of active mixing techniques include servo valves to control combustor flow rates and acoustic drivers to excite acoustic waves in the flow [47]. A more comprehensive list of active mixing techniques and devices can be

found in work by Huang and Yang[7].

Actuators modify the pressure field in the combustion system and modulate the supply of reactants to suppress combustion oscillations. Sensors, typically used to monitor flame characteristics and through a feedback control loop, drive the actuator accordingly [48].

An active mixing method that has attracted much attention is jet excitation through acoustic input [61]. This technique aims to excite the instability modes of the flow within their most amplified frequency band to energize the large-scale coherent structures and enhance vortical interactions, which accelerates the decay to small-scale structures [61, 65]. Acoustic excitation has the potential to increase the coherence and intensity of large-scale motions in the near-field and is capable of increasing the combustion intensity (by reducing the flame volume) [8]. Acoustic excitation can also be used to destroy any span-wise structural coherence or disrupt any organized structures in the near-field to prevent flow induced resonance [65].

However, like most active mixing methods, the power requirement and weight implications of the systems outweigh that of the achievement by the system [61]. This dampens any further interest in this technique.

2.2 Overview of multilateral jet mixing

The previous section discusses the importance of a stable flame in industry and how reactants mixing play an important role in enhancing the flame stability. These mixing techniques to stabilize flames generally involve aerodynamic modifications, however current techniques are inadequate or expensive to answer the needs of industry. It is a challenge to conceive an idea that is simple and yet allows control to

the mixing intensity and flame characteristics. This thesis investigates the potential of multilateral jet configuration to answer the challenges in mixing and reliably stabilize turbulent jet flames. However, the fundamentals of multilateral jet mixing are not cohesive, and so require further investigations.

2.2.1 Multilateral jet mixing

Multiple lateral jets are often found within the same mixing systems in industry to enhance streams mixing [66]. Compared with single jets, the interactions between multiple jets in a confined cross-flow are more intense [67]. The mixing intensity, when coupled with the resulting flow structures' interactions, are believed to be responsible for much of the increase in mixing performance, which remained poorly understood [60].

Various design variables for the multilateral jet injection can be modified which will impact the jets' penetration and mixing characteristics differently, such as: jet to cross-flow momentum ratio, orifice spacing, confinement geometry, orifice diameter, orifice to confinement aspect ratio, and orifice angle [68, 69].

Side-jets injected into a confined round flow are typically dominated by counter-rotating vortex pairs (CVPs) (see Figure 2.8) [69]. The side-jets penetrate directly into the flow cross-section and stretches with increasing jet to cross-flow momentum ratio. Figure 2.8 also shows the connector ribbons for the vortex pairs propagate towards the confinement centreline with increasing momentum ratio, whilst the vortices tend to stay near the wall. This is attributed to the effect that a curved-wall has on the rotational vortices [70]. In addition, the side-jet penetration into the cross-flow also increases as an inverse function of the number of orifices within a cross-section [69].

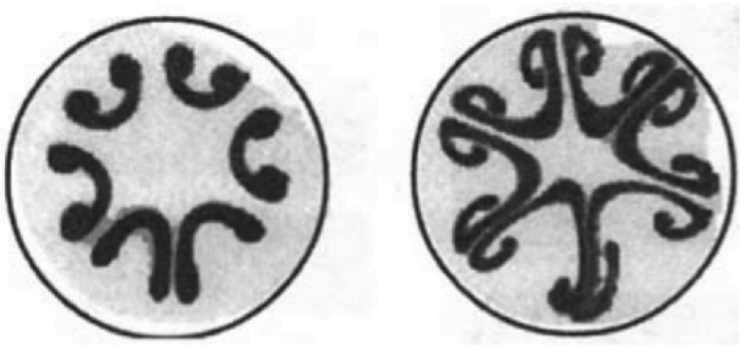

Figure 2.8: Modelled multilateral jet injection profile in low momentum ratio (left) and relatively higher momentum ratio (right) [69].

Limited studies have been conducted on multilateral jet injection into a confined round flow. Such configuration has direct application to the multilateral jet burner, which is the primary focus of the thesis. The majority of the studies into multilateral jet mixing were aimed at Rich burn/ Quick quench/ Lean burn (RQL) combustors. Although the intended applications may differ, the findings in these studies may be transferable.

RQL combustors are conceived as a low NOx solution to industrial burner. The rationale behind the conception includes the quenching of the hot combustion products within a short period, therefore lowering thermal NOx. This explains why most multilateral jet mixing studies uses flow temperature as a scale of measurement. This “unit of measurement” is not suitable for a purely fluid mechanics based investigations or for our purpose.

The RQL studies have made available an empirical scaling variable that correlates with “optimum mixing”. Do note that the optimum mixing here refers to the generation of a near-homogeneous mixture (based on temperature) at a certain downstream

distance from the side-jets. For example, an application which requires uniform mixing with optimum penetration at location "x" may see under-penetration at location "$x-s$" or over-penetration at "$x+s$" (s refers to an arbitrary distance) [69]. This may not be applicable for our purpose, i.e. combustion reactants mixing where other factors come into play (for example, mixture equivalence ratio).

Optimum mixing here is considered achieved when the side-jets penetrate the half-radius ($r_{1/2}$) at the required location. By considering cases with similar penetration distance and cross-sectional profiles, the parametric correlation, C was formed. It is defined as

$$C = \frac{\pi\sqrt{2J}}{n} \tag{2.2}$$

and has a constant value set to 2.5 [68]. The parameter n denotes the number of side-jets, and J denotes the flow momentum-flux ratio, which is represented by,

$$J = \frac{(MFR)^2}{(DR)(C_d)^2(\frac{A_J}{A_m})^2} \tag{2.3}$$

MFR denotes the jet to cross-flow mass-flow ratio:

$$MFR = \frac{w_j}{w_m} \tag{2.4}$$

DR represents the jet to cross-flow density ratio, C_d the orifice discharge coefficient, A_J/A_m the jet to cross-flow area ratio, and w_j and w_m the jet and cross-flow mass-flow rates, respectively . As a flow configuration derived from the well-studied jet in cross-flow (JICF), the parametric correlation agrees with the previous JICF scaling parameters on the importance of jet to cross-flow momentum ratio in JICF related flows. More on JICF will be discussed in Section 2.2.3.

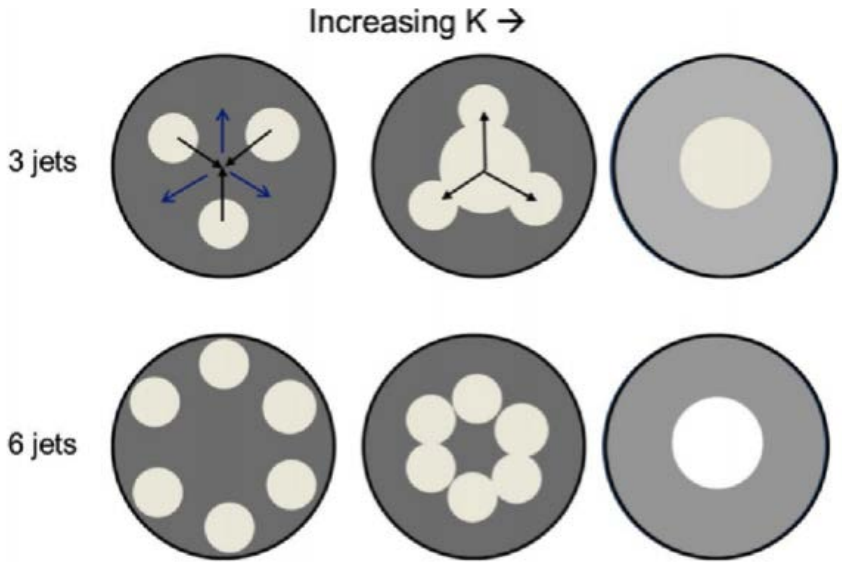

Figure 2.9: Schematic diagram for three and six transverse jets in a confined round cross-flow. K is a constant derived from the jet to cross-flow momentum ratio. Adapted from Forliti et al. [71].

Next, this parametric scaling method is reportedly to be only effective for the number of side-jets, $n \geq 6$, in particular within the range of 8 to 18 side-jets [71]. The large number of side-jets complicates further an already complicated flow. Therefore, a configuration with low number of side-jets is more suitable to further understand the side-jets and flow structures interaction. Furthermore, this scaling method is also dependent on the side-jets' configuration such as jet spacing, which makes it less reliable.

In addition, most studies done on multilateral jet mixing focus only on low jet to cross-flow momentum ratio (MR) flow, as high MR leads to the side-jets interacting, which allegedly leads to high flow unmixedness. This is further illustrated in Figure 2.9 by Forliti et al. [71]. For 6 side-jets configurations, low side-jets MR allows the vortices to expand and develop as they are carried downstream, hence forming regions of low unmixedness. At high MR however (here, represented by the factor

K), the side-jets penetrate the flow centerline forming a region of high unmixedness along the centerline, which is not desirable for the intended applications (for example, fume quenching). However, for lesser number of side-jets' configurations such as 3 side-jets, increasing the flow MR reduces the mixture unmixedness [71], which is in contradiction with that of higher side-jets number advantages mentioned earlier. Little explanations were provided for this phenomenon as there are very little data available for studies related to low number of side-jets flow configurations.

Other related studies involve placing side-jets directly at the turbulent jet nozzle exit, perturbing the flow exiting a nozzle, in place of mechanical tabs. These studies aim mainly to emulate flow of non-circular nozzles by placing the side-jets at locations that coincide with the vertices of a non-circular nozzle (for example, 4 side-jets equidistant to simulate a square nozzle). The side-jets here disrupt the shear layer of the turbulent jet in the immediate near-field and enhance the production of small-scale vortical roll-ups on the otherwise stable shear layer devoid of large-scale vortex structures. This should significantly increase the mixing of the flow out of the jet nozzle [72]. The vortical interactions corresponding to these findings are not well resolved.

Available data suggest that the side-jets generated vortices, in particular the CVPs distorts the cross-sectional flow profile of the exiting jet [60]. Furthermore, it has been suggested that the MR of the side-jets should be sufficiently high to influence the turbulent jet's potential core to produce better mixing [72]. Further, it was also suggested that a non-symmetrical side-jets configuration shows better mixing performance compared to the equi-spaced placed side-jets [72]. Despite these suggestions, not much data can be synthesized on the performance comparison between symmetrical and non-symmetrical side-jets configuration, and at different

side-jet's MR.

When multilateral jet mixing is applied to premixed flames (air injected via side-jets into premixed fuel mixture), it was found that different flame characteristics, that deviate from unmodified premixed flames, were achieved [25]. These include the reduction in the flame length and higher blow-off limit. However, note that the anatomy and characteristics of a premixed flame differs from that of a non-premixed flame and the effects that the side-jets have on non-premixed flame may differ, which was discussed in Section 2.1.1. Birzer et al. [73] show the potential of such multilateral jet burner in producing stable partially premixed flames (by injecting fuel into cross-flow of air). The work done in this thesis builds on this study with a systematic and in-depth investigation of the vortical interactions and effects that varying flow MR have on the flow and resultant flames.

2.2.2 Jet in a confined cross-flow

Multilateral jet configuration is a combination of multiple jets placed in a confined cross-flow. Traditionally, most JICF studies are carried out in unconfined conditions despite engineering applications involving JICF for streams mixing occur in a confined pipe or channel [67, 71, 74]. These applications span from chemical reaction to engines and cooling technologies [68, 74]. For this study, a confined JICF is defined as a condition where the span-wise dimensions of the duct/channel is of the same order as the jet exit, whilst unconfined JICF refers to the configuration at which the span-wise dimension of the duct is much larger, which has been previously defined by Fernandes et al. [74] and will be discussed in Section 2.2.3.

The inclusion of a confinement affects the JICF drastically, including the trajectory and CVP growth downstream [74]. In terms of CVP growth, the confining wall(s)

limit the spread of the CVP and hence the efficacy of momentum transport of the flow. Impinging the side-jet on the wall or an obstacle generates a complex flow and flow recirculation, which introduces favorable mixing structures thus enhance flow mixing [75, 76]. However, there are little studies that have been done which quantify the efficacy of jet impingement or effect of confinement on flow mixing, which is of importance to this study. Furthermore, placing multiple side-jets in a confinement is expected to alter the dynamics of the flow drastically.

In terms of combustion, reacting flow studies have also been conducted to study the flame stability for fuel that is injected into a confined cross-flow of air [39]. The motives of such studies are mainly for applications in refinery flare stacks or gas burners [39, 77]. The jet flames ignited in the cross-flow are stable, but is limited to low MR values [39].

Several characteristics define the flames ignited in a cross-flow. The physical flame length is up to 35% shorter than a vertical straight jet flame, which is attributed to the increase in air entrainment and enhanced mixing-rate that is commonly associated with the JICF configuration [78]. This shows the potentials that JICF configurations may have to partially premix combustion reactants to generate a stable flame.

Furthermore, the flames generated are anchored on the lee-side of the jet, where the flow recirculates, and is the region where the highest temperature in the flame is found [77]. In addition, at relatively higher MR, substantially less soot is formed within the flames, which lead to a hotter and less radiative flame. The downside to such combustion mode is the high unburnt hydrocarbon, CO emission, and NO_2 to NOx ratios observed within increasing MR, which is attributed to the fuel escaping the side-jet nozzle in the near-field region [78].

2.2.3 Jet in cross-flow: Introduction

Flow field of an unconfined jet in cross-flow has been investigated in depth by many researchers over a long period of time [79–81]. The data and information obtained, however, are motivated by the specific application in industry, from flow out of a chimney, to fuel injectors in an internal combustion engine [82].

In industry, the practicality of using side-jets[1] to enhance mixing, for example, in reactors and industrial burners, between two fluid streams remains undisputed [60, 83]. The efficacy of mixing for side-jets is commonly associated with its vortical entrainment properties, which brings the jet fluid in contact with the cross-flow fluid to create regions of high scalar gradients, hence promoting mixing on the molecular level [84]. Examples of engineering applications of side-jets include Vertical Take-Off and Landing (VTOL) aircraft propulsion systems, refinery and safety flaring operations, industrial burners, and secondary and dilution zones of gas turbines [78]. However, little attention has been given to the application of JICF in partial premixing of reactants in turbulent jet flames and it is not known if the mixing induced will be practical for such purposes.

A JICF is identified by the mutual deflection of both the jet and the cross-flow. Here, the jet is bent over by the momentum of the cross-flow and is deflected as if blocked by a rigid obstacle [83], which leads to the formation of a “bluff-body wake” in the cross-flow [76]. The presence of the cross-flow reduces the potential core of the turbulent jet and results in various distinct flow structures [60], which enhances mixing between the two flows. This feature of JICF is utilized in the current study.

The flow structures and vortices generated by JICF are attributed to two sources:

[1] JICF is used interchangeably with other terms commonly used in similar studies, including “lateral jets”, “side-jets” and “transverse jets”.

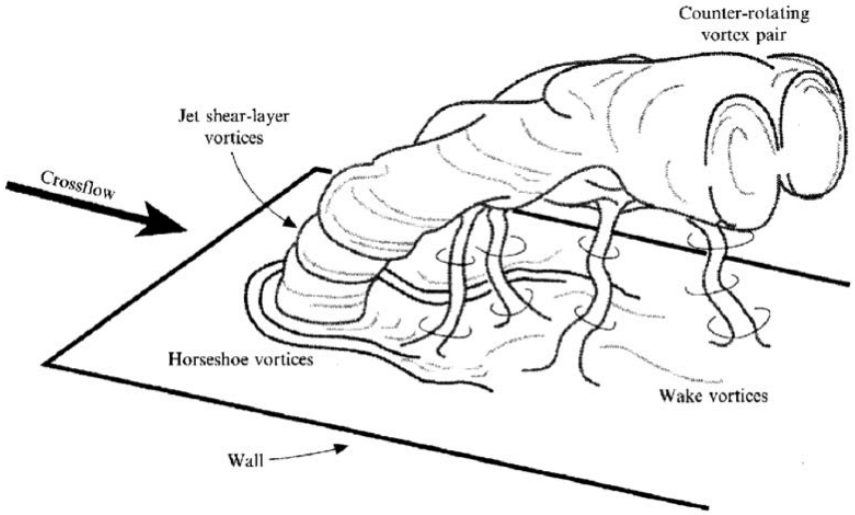

Figure 2.10: Schematic diagram depicting the vortices generated in a JICF system [79]

the cross-flow boundary layer and jet exit boundary layer [79, 85]. As a result, four main coherent structures can be discerned in the near-field of the side-jet, which is where the interaction and entrainment of fluid between jet and cross-flow is most intense [83]. They are [79, 85]:

i Jet shear layer vortices;

ii Horseshoe vortices;

iii Wake vortices; and

iv Counter-rotating vortex pair,

Figure 2.10 shows a schematic diagram, which summarizes the flow structures (i)-(iv) generated in JICF system of vortices. Here, it is immediately obvious that the Counter-rotating Vortex Pair (CVP) is the most prominent flow feature, which is also reported as a result of the impulse of the jet on cross-flow [79]. Counter-rotating vortex pair manifest itself as a kidney-shaped mean profile in both flow visualization studies and in time-averaged velocity fields [86].

Counter-rotating vortex pairs are products of shear between a side-jet's stream and a cross-flow [76] and originate from the process of shear layer roll-ups, tilting and folding motions [80]. They are formed immediately downstream in the near-field of the jet [79, 87] and then propagate and dominate the far-field of the flow [79]. Counter-rotating vortex pairs grow in size with propagation but diminished in strength due to the diffusion of vorticity across the symmetry plane [74]. However, as these studies are typically performed in large channels, the effect of a confinement (small aspect ratio channel) on the characteristics of a CVP is less well-understood or studied. This is also true on the effect of a circular confinement on the characteristics of a CVP.

Also observed in Figure 2.10 is the formation of horseshoe vortices (HSV), which are usually formed close to the wall immediately upstream of the jet exit [87]. The jet "column" blocks the oncoming flow and induces a reverse flow, which produces an adverse pressure gradient that contributes to the formation of the HSV structures [88]. The HSV develops, propagates and sheds around the side-jet, which is similar to those observed for a flow around a solid cylinder [87, 88].

Other vortices that are induced by the shear between the side-jet and the cross-flow are the unsteady transverse vortices [79] or shear layer ring vortices [80] at the interface between the side-jet and the cross-flow. These vortices are similar to those observed for turbulent jets and are attributed to Kelvin-Helmholtz instability [79, 80]. It has been deduced that the Kelvin-Helmholtz instability amplifies the small local disturbances in the shear flow, which may also be the precursor to the formation of three dimensional shear structures, such as CVPs [79].

Jets in cross-flow are generally generated via two different methods: net positive and

zero net mass-flux type injection. Zero net mass-flux jets are also known as synthetic jets, are produced using vibrating membranes or oscillating pistons to push fluid through an orifice [60]. The advantage of this set up lies in that it does not require additional fluid to impart additional vorticity into the flow field, by making use of the ambient fluid alone. The synthetic jets are an improved variant of the net-positive type jet, to be discussed next, and show improvement in terms of penetration and mixing [89].

The net-positive type jet, otherwise known as the continuous injection, bypasses small amounts of high-pressure fluid and exhausts them continuously into the flow [60]. This method is simple compared to the zero net mass-flux jets due to the absence of complex moving components and hence is picked to provide side-jets' flow to the current experimental outfit, shown in Chapter 3. A weakness to this method is that, it relies on the availability of fluid and sometimes requires an additional fluid reservoir. However, this method is particularly useful for mixing of multiple streams of different fluid, such as fuel and air.

A commendable effort has been put into studies of JICF trajectory especially that it will enable the prediction of the path followed by the jet, which is indirectly correlated to how efficiently the jet mixes with the ambient flow [84]. There are several ways of defining the jet trajectory, which include: jet centreline (for circular jets, this is the streamline starting at the center of the injection nozzle); the locus of the maximum velocity; and the locus for maximum concentration. Despite the variations in locating the flow trajectories, the behaviors displayed are essentially the same [86].

Side-jet penetration, trajectory and subsequently the CVP are sensitive to various parameters including: velocity ratio, injection length, Reynolds Number of both

jet and cross-flow, exit diameter of the jet, and the presence of a confinement, as discussed previously [86]. Some studies considered the boundary layer of the cross-flow to be of importance to jet penetration into the cross-flow [90]. An example of the argument is that jet injected into a cross-flow with a thicker boundary layer penetrates deeper compared to other jets with similar velocity ratios [75].

Jet to cross-flow MR has been considered as the primary parameter that controls the jet penetration and trajectories into a cross-flow [85, 86]. This ratio is defined as:

$$MR = \frac{\rho_J \bar{v_J}^2}{\rho_\infty v_\infty^2} \tag{2.5}$$

Where the subscript J denotes the side-jet flow parameters and ∞ denotes the cross-flow parameters, ρ denotes the media density, and v denotes the flow velocity. At low MR, the JICF behaves as if a partial inclined cover was positioned over the front part of the jet exit, causing the jet streamline to bend while still within the discharging jet itself [83]. At higher MR, the jet is minimally affected near the jet exit and penetrates to a certain distance into the cross-flow before being deflected. The role that the flow MR play in JICF study is further expanded into jet in confined cross-flow and multilateral jet in a cross-flow as discussed earlier.

Efforts to characterize JICF trajectories consider the jet to cross-flow velocity ratio:

$$r = \sqrt{(MR)} \tag{2.6}$$

by assuming that the flow has the conditions of $\rho_J = \rho_\infty$. The trajectory scaling parameters for jet in unconfined cross-flow established is simply by:

$$\frac{y}{d} = \alpha r^\beta (\frac{x}{d})^\gamma \tag{2.7}$$

where d denotes the diameter of the discharging jet, and the parametric constants, $\alpha = 0.527$, $\beta = 1.178$, and $\gamma = 0.314$ [90]. This is later refined to incorporate the length-scale of the side-jets [91]:

$$\frac{y}{rd} = A(\frac{x}{rd})^B \tag{2.8}$$

The scaling of the jet trajectory using the length-scale of the side-jets are well received and various experimental campaigns validated this scaling factor with the 1.2 < A < 2.6 and 0.28 < B < 0.34 [90]. The range of constants accommodates the differing experimental conditions. However, like most CVP studies, the scaling studies on JICF is mostly conducted in a large duct, therefore do not account for the effects of the duct, or additional jets in close proximity, that may impose on the characteristics of the jet. Very few investigations on the effect of a small duct on an injected jet exist.

Other factors that may influence the jet trajectory include the geometry of the jet exit and the cross-flow turbulence. Augmentation of the side-jet can also be achieved by manipulating the cross-flow's turbulence, however, the effects of turbulence and Re are small when the flows are fully turbulent [75].

2.3 Overview of jet fluid mechanics, turbulence and control

Evaluating the JICF derived multilateral jet mixing configuration shows the potential of this configuration to premix fluid injected through the side-jets with the fluid in the cross-flow. However, there is little information regarding the impact of placing the side-jets or premixing reactants upstream of the emerging jet flow, which affect the induced flame characteristics.

2.3.1 Turbulent jets

Turbulent jet flame is an example of the many applications of turbulent jets in industry due to their simplicity and efficacy in mixing different streams. Therefore, understanding the characteristics and features of turbulent jets is crucial for the current study on turbulent jet flames.

A prominent feature of turbulent jets, as mentioned previously, is the intrinsic large-scale coherent structures formed in the form of jet shear layer roll-ups [47]. These large-scale structures, a result of the initial flow hydrodynamics instabilities (Kelvin-Helmholtz type and Tollmien-Schlichting type), occur naturally at a frequency defined by the Strouhal Number, $St = fd/u$, where f represents the frequency of the vortices, d the diameter of the jet, and u the jet velocity [8, 47, 92]. Furthermore, they can also be caused by external perturbations, by introducing pressure oscillations or through structural vibration [47], and can be made more coherent and larger by forcing the flow acoustically at St = 0.3 [8].

In isothermal flows, modifications to the initial conditions of a turbulent jet (in the near-field) will most likely be reflected by the far-field flow conditions [92]. The near-field region, otherwise known as the region of flow establishment encompasses the region, $0 \leq x/D_P \leq 7$ while the far-field is defined as $x/D_P \geq 7$. The structures generated in the near-field degrade downstream beyond the first few diameters [93], however, any attempts to enhance the formation of large-scale structures in the jet shear layer indirectly affect the intensity of the turbulence in the flow [92]. Therefore, due to the interrelated nature of the shear layer and overall flow turbulence, modification to the shear layer are often considered a strategy for jet flow manipulation.

Another flow feature of a turbulent jet is the flow potential core as seen in the

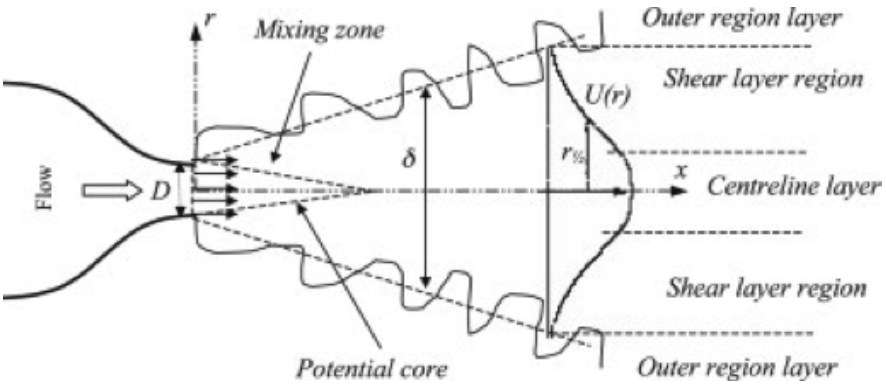

Figure 2.11: Schematic diagram depicting the jet potential core, mixing zone, and the near-field and far-field regions [92].

schematic diagram in Figure 2.11 [92]. This is a region where the centreline velocity remains constant and equal to the centreline velocity at the nozzle exit [94]. The potential core is formed regardless of the Reynolds Number in a turbulent jet, and it's length is proportional to the flow Reynolds Number in laminar jets. Immediately downstream of the jet potential core is the region of established flow and is characterized by the gradual decay in centreline velocity [94]. This region is also known as the near-to-intermediate field (NIF) and typically spans the region $7 \leq x/D_P \leq 30$ [92]. The decay of the potential core dampens the effect of the shear forces that supports the vortical structures and results in the decay of the large-scale vortical roll-ups into smaller structures, hence forming a region that is highly anisotropic [92]. It is possible to take advantage of the characteristics of this region to possibly enhance the flow mixing downstream, however, not many studies have shown the possibilities in doing so, in particular the effect of shortening or elongating potential core on reactants' mixing.

Attempts to modify the initial turbulent jet outflow profile have shown that the jet flow will asymptotically attains a self-similar state in the far-field [92, 95]. This asymptotic characteristic is independent of other initial conditions and positions [96],

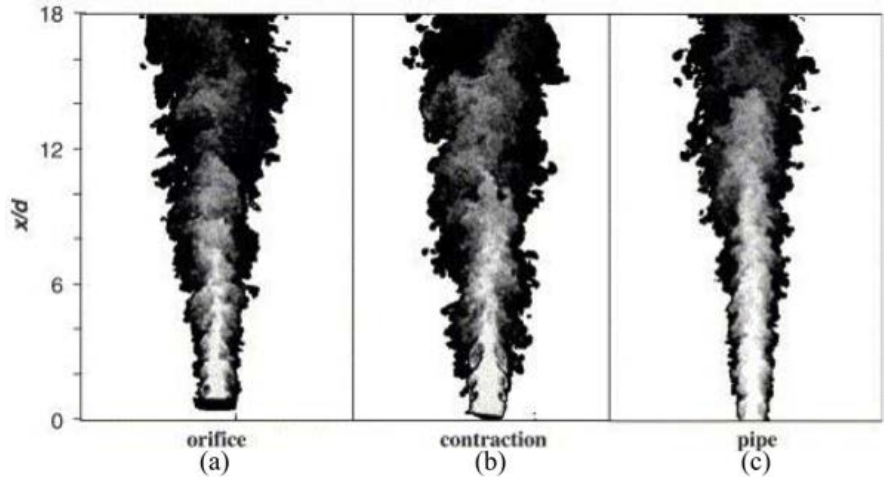

Figure 2.12: Differences in the underlying large-scale structures issuing out of: (a) an OP nozzle, (b) SC nozzle; and (c) an LP nozzle, adapted from Nathan et al.[8].

except for momentum addition [95]. Increase in the jet Reynolds Number, however, shifts the virtual origin upstream, which results in a longer flow distance required to achieve the asymptotic mixing behavior in the self-similarity region [96]. Therefore, minor changes to the flow are not expected to play a prominent role in the far-field.

Turbulent jets can be characterized by the geometries of their issuing nozzles, which are: long-pipe (LP); smooth-contracting (SC); and orifice plate (OP) nozzle. These jets have their respective distinguished characteristics, in particular the induced large-scale structures, as reviewed by Nathan et al.[8] and shown in Figure 2.12

In this study, the LP nozzle is chosen for its simplicity, well characterized flows and wide spread use in industry. The LP nozzle produces a predictable boundary layer, both upstream and downstream of the jet exit, i.e. produces a fully turbulent boundary layer within the pipe and a fully developed pipe flow at the exit plane, at appropriate length.

The velocity profile at the exit can be described empirically by a power law [95, 97]:

$$\frac{\bar{u}}{U_{max}} = (1 - \frac{r}{R})\frac{1}{n} \tag{2.9}$$

Here, U_{max} is typically the velocity at the flow centreline, r the local radius, R the radius of the exit pipe exit, and a constant n that is typically 7. Long-Pipe nozzles are known to generate the incoherent structures with its near-field dominated by small-scale turbulences [8, 95].

Compared to the LP nozzle, the SC nozzle generates a thin boundary layer and a uniform potential core. It produces the largest and most coherent near-field structures in low frequency, which is inferred to originate from initial shear layer instabilities [8]. The manufacturing of such nozzle is complicated by the smooth-contraction section upstream, where the contraction ratio may affect the flow structures generated. The OP jets are characterized by a complex converging and diverging flow profile and has a relatively more complex induced near-field structures compared to the other nozzles.

For flows in the LP nozzles, local entrainment of ambient fluid into the jet can be influenced by the pipe centreline mixing behavior [96]. Entrainment here is defined as the radial inward flux of ambient fluid drawn into the jet, which affects both the diffusion and turbulent mixing of jet fluid [81]. This opens the possibilities to manipulate these large-scale structures, which form the shear layer in reactants mixing (in particular non-premixed turbulent jet combustion). These flow structures entrain ambient air into the fuel stream, by impacting or manipulating the upstream pipe flow. Further research into flow structures manipulation is warranted due to its potential to perturb the jet outflow by manipulating the upstream flows.

Furthermore, modifications of the pipe flow will most probably induce drastic changes in the near-field region, before the jet flow reverts to a self-similar condition further downstream. In addition, these modified flows also provide an indication of the regions that need to be prioritized for both isothermal and reacting flow studies and subsequently for data collection.

2.3.2 Turbulent jet control

The characteristics of turbulent jets that allow efficient mixing between different streams of fluid have made it attractive for engineering applications. Modifications to the initial flow may cascade to influence other changes in the flow immediately downstream, such as heat, mass and momentum transfer. Placing multilateral jet upstream of the turbulent jet nozzle exit is also likely to impact the flow characteristics out of the nozzle exit.

Most attempts to manipulate turbulent jets aim to enhance jet entrainment by enhancing the generation of stream-wise vortex motions. This is encouraged by the hypothesis that: increasing the production of vortical structures and motions effectively distort the jet cross-section and increases the contact area between the jet and the ambient, and increases turbulence [98]. The results of these studies have also shown that the flow instabilities are governed by two different jet length scale: the initial momentum thickness (θ_0) which describes the near-field flow dynamics, and the jet diameter (D_P) which governs the flow evolution in the far-field [7]. The simplest example of jet modification is the application of the different types of nozzle geometries (LP, SC or OP nozzles), which produce different mean velocity profiles and turbulence conditions. However, there is a limit to how much flow can be augmented by merely changing the nozzle geometries, and is influenced by other factors such as practicality.

Various mixing methods have been attempted to further enhance jet mixing, from what was already achieved by the LP, SC and OP jets. These ranges from an array of simplistic nozzle additions to complex methods utilizing flow feedback and control to fluid mechanics manipulation, for example the multilateral jet mixing method studied in this thesis. Among these techniques is one simple, but yet effective technique to enhance jet mixing, by using non-circular nozzles. Studies on non-circular nozzles have shown that it is possible to reduce the potential core lengths, which is achieved due to the increase in centreline decay rate [72, 99]. The effects of non-circular nozzles are more prominent in the near-field, and have reportedly shown axis-switching phenomena, which so far, is unique to non-circular nozzles [72]. Axis-switching can potentially increase the contact area between the jet and the ambient flow and enhance the mixing between the jet flow and the surrounding fluid.

Axis-switching

Axis-switching is described as a phenomenon in which the cross-section of any asymmetric jet evolves in such a manner that, after a certain distance from the nozzle, the major and minor axes are interchanged [100]. Axis-switching has only been recorded for eliptical jets, triangular jets and square jets, attributed to the limited studies and interest on this phenomena. The switching of the major and minor axes is illustrated in Figure 2.13.

The jet cross-section expands in the direction of the minor axis and reduces in the direction of the major axis, which prompts a 90° switch (square, rectangular and elliptical nozzles) at a certain downstream distance. The axial location of the switch is relatively uncertain and is dependent on the aspect ratio of the nozzle geometry, jet

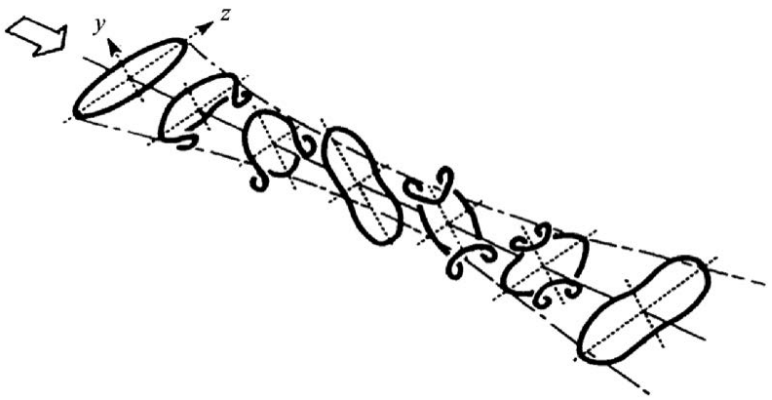

Figure 2.13: A depiction of axis-switching interaction for an elliptical jet [101].

initial conditions and compressibility [100]. It was also suggested that the contraction in an SC nozzle promotes axis-switching by directing the secondary flow towards the jet axis, along the corners of the jet [59]. The potential of generating axis-switching in LP jets are unclear.

Hypothetically, it is possible to emulate the axis-switching by strategically distorting or impacting the vertices of the jet either through mechanical tabs or side-jets (which was discussed earlier), which mimic the positions of the vertices on a non-circular nozzle. The prospect of generating axis-switching for Counter-rotating Vortex Pairs within a pipe flow and its effects on mixing is relatively unknown.

2.3.3 Jets: simple, co-flow, counter-flow, and cross-flow

Different variants of turbulent jets have been used in conjunction with various flow conditions, dependent on the applications and extent of mixing required. These flow conditions most commonly include: co-flow, counter-flow and cross-flow. This goes to show that turbulent jets are versatile and allows flow modifications through the introduction of different flow conditions to enhance mixing.

Jet in counter-flow describes a turbulent jet issuing into a uniform stream of ambient flow in the opposite direction. This results in the enhancement of mixing efficiency drastically, in particular when compared to both jet in co-flow and jet in cross-flow. The influence of the counter-flow include an enhanced spreading of the jet, which is dependent on the relative strength of the jet to counter-flow. At low velocity ratio, the jet forms one single vortex ring at the nozzle exit and produces a stable and regular shedding, whilst at higher velocity ratio, the jet becomes less stable and oscillates with a low frequency in a disordered fashion [102]. Despite the efficacy of jet in counter-flow in mixing different streams, it is counter intuitive to inject fuel in the opposite direction of air and in particular in the direction of flame propagation and for that reason, the applications of such configuration in industry is limited and difficult without proper flame arrestor in place.

Jet in co-flow is the most common form in industry. The interaction of the turbulent flow exiting the jet with the surrounding fluid creates a shear region that affects the entrainment efficiency and the mixing between the two streams. The velocity gradient between the jet and the co-flow affects the rate of centreline mixture fraction decay due to its effect on entrainment of the co-flow fluid [81, 103]. The co-flow, however does not alter the mean velocity profile of the central jet, but increases the turbulence in the far-field region (end of potential core) [104]. This jet configuration has been adopted by concentric tube burners to effectively partial premix reactants to generate a controlled partially-premixed combustion, discussed in Section 2.1.5.

Jet in cross-flow (JICF) meanwhile is an effective method to mix different streams of flow in less than tens of milliseconds [67] and has been discussed in-depth in Section 2.2.3. This mixing configuration is perceived to be a safer option than jet in counter-flow and is widely used in industry.

2.3.4 Turbulence

Flow turbulence is ubiquitous in both isothermal and reacting flows. Investigation into flow turbulence has led to the advancement of many combustion systems including air breathing propulsion systems, energy conversion power plants, and incinerators, to mention a few [19], as well as to increase fuel conversion rates, generate a compact flame, reduce emission or enhance stability [105].

Generally, manipulation of flow turbulence directly influences the amount of soot in hydrocarbon flames, due to the induced changes in the strain rate. Furthermore, due to the complex nature of turbulence-combustion interactions, the effect of turbulence manipulation can also lead to the change in temperature and mixture fraction distribution in the combustion zone [8, 23]. The increase in flame temperature also influences the flow viscosity and density, which in turn affects the flow turbulence, mainly at small-scales [31]. The increase in temperature also increases the specific volume and viscosity, typically by $\rho_r/\rho_p \approx 5-10$ and $\nu_T/\nu_p \approx 10$ (here subscripts r and p denote "reactants" and "products", respectively) [31]. The small-scale turbulence induced also bring together the different intermediate species in the mixture (including OH, H, CH, and etc.) which are essential for the reaction to proceed [106]. For combustion particularly, the underlying turbulence structures render the velocity field more sensitive to changes than the scalar field [95]. The ability to control these relationships will be highly valuable to manipulate the flame characteristics to the industry's requirements.

The flow turbulence conception of a jet exiting into an ambient surround is through shear between the jet with the ambient, giving rise to the production of large-scale coherent structures [59, 92]. These structures contain most of the energy in the flow and dominate the transport of momentum and mass, and heat [106]. These

large-scale structures break down to form smaller eddies and turbulence structures that diminish in scale, time and space [92]. This results in a chaotic flow that is orchestrated as an organized motion at the largest scale superposed on a fine grain random background of fluctuation in the small scale [27].

The unsteady nature of flow turbulence, in particular for a turbulent jets, is composed of a continuous spectrum of eddy length and velocity scales [27]. For example, despite the large-scale structures are often observed to dominate the shear region of both the turbulent jet and JICF's outflow, the smaller scale turbulent structures dominate the velocity fluctuations of the flow [59] and span the dissipative range responsible for most of the energy dissipation in the flow [106]. The smallest size of small-scale turbulence is characterized by the Kolmogorov length scale $l_k = (\nu^3/\epsilon)^{1/4}$ (here ν represents the medium's kinetic viscosity while ϵ represents the average rate of dissipation of turbulence kinetic energy per unit mass) [27, 31], which thickness is of the order of viscous layer developed during a time $\tau_k = (\nu/\epsilon)^{1/2}$. The Kolmogorov scale also features a characteristics velocity, $v_k = (\epsilon\nu)^{1/4}$. Meanwhile for reactants mixing, the mixing efficacy depends on the turbulent Damköhler Number, Da_t which measures the importance of the interaction between chemistry and turbulence. Here, Da_t is regarded as a ratio of characteristics mixing time to the reaction time, $Da_t = \tau_t/\tau_c$, where τ_t denotes the turbulent time scale and τ_c denotes the chemical time scale. A small Da_t indicates that turbulent mixing is much faster than the reaction time scale, whilst $Da_t \gg 1$ indicates combustion mixing dominated process (usually in scales of milliseconds) [67]. Therefore, increasing the flow turbulence reduces the Da_t of the flame. Since τ_c is dependent on the fuel composition in the reactants' mixture, changing the flow turbulence, τ_t by perturbing the pipe flow with side-jets can impact on the flame characteristics.

2.4 Summary of the literature and knowledge gaps

Based on the literature reviewed, the potential of muiltilateral jet in the mixing of two or more fluid streams for many applications including flames is shown to be tangible. The available studies regarding multilateral jet mixing are application specific mostly for fume quenching applications. The motive for these studies are mainly to achieve a homogeneously mixed flow in the shortest period of time possible, which differs from this study's objective to better control of turbulent flames using partial premixing.

It is clear that our knowledge of vortices structures, scaling and trajectory of Jets In Cross Flow (JICF), is well developed. Very few studies have considered the effects of confinement on the lateral jets and its impact on generating a mixture distribution at the primary nozzle exit that is conducive for stable and well-controlled flame. Therefore, it is not well understood how placing side-jets upstream of a burner nozzle exit will affect flame stability or control. The use of side-jets to induce a particular distribution of partial premixing for reactants is new and a deeper understanding of its feasibilities and the parameters that controls it under both isothermal and reacting conditions is needed.

The gaps from the published research on multilateral jet mixing is as follows:

1. Lack of fundamental knowledge pertaining the structural interactions between CVPs generated through JICFs. Most fundamental studies focus on deriving large-scale structures and characterizing jet streams that are issued through a single-jet in a cross-flow. Therefore, fundamental studies on the structural interactions between CVPs, in a confined circular geometry is required to further understand vortical interactions that may happen.

2. Most studies aimed at creating a homogeneous mixture involving 6 or more

multilateral jet for mixing. While the current study looks at creating favorable mixing distribution using three or four side-jets in order to have better control of the flow emerging from the nozzle exit.

3. Most studies in multilateral jet mixing favors non-interacting CVPs, i.e. the side-jets streams do not interact but are allowed to develop to a location far downstream. It has been implied that side-jets interaction reduces the mixing performances of the system, however, little information can be uncovered on results of such mixing regime or how the flow evolution takes place inside the nozzle.

4. There is currently no study that uses multilateral jet mixing method to partial premix combustion reactants. Current methods include using recessing concentric jet. Not much information can be synthesized from this method or other multilateral jet mixing methods. Therefore, the effect of injecting fuel a short distance upstream of the burner nozzle exit is relatively unknown. The structure and stability of the resulting flames with respect to the different mixing regimes inside the primary nozzle is also not known.

2.5 Research aims

The main aim of this thesis is to understand the underlying mechanism of multilateral jet mixing and its feasibility for reactants mixing of gaseous turbulent flames. The specific objectives of the thesis are as follows:

i To characterize the flow regime that can be achieved via multilateral jet mixing in a confined cross-flow and to identify its controlling parameters;

ii To quantify the effects of multilateral jet mixing on both the flow and scalar fields inside the nozzle and in the near-field;

iii To quantify and study the effect of lateral jets on non-premixed turbulent jet flame characteristics and flow-chemistry interaction in the flames.

Chapter 3 and Chapter 5 address Objective (i), which investigate the roles of momentum ratio and number of side-jets in controlling the flow and mixing field inside the nozzle. Objective (ii) is addressed in Chapter 4, which studies the effect of momentum-ratio on the flow and scalar field in the near-field region. The information compiled from Chapters 3, 4, and 5 are applied in Chapter 6 to address Objective (iii) of the thesis.

2.6 Measurement of passive and reactive scalars

The concept of creating and developing a new technology, here combustion burner, follows a generic trend of: ideation, laboratory scale testing, modeling of flow phenomena and characteristics, and lastly scaling up of burners through developed models [23]. Various tools have been developed for the purpose of advancing combustion science, both in diagnostic methodologies and numerical modeling. The advancement of computing has since provided sufficient processing power to model key phenomena in combustion, such as the complex turbulence-chemistry interactions [13]. This process of model development and validation, in turn, requires reliable experimental measurements in conditions where experimental and computational data can be directly compared [23]. Various experimental tools, intrusive and non-intrusive, have been developed for these purposes. The current study focuses on the applications of optical based and laser diagnostics techniques, which have been developed to provide unrivaled edge over intrusive probes.

2.6.1 Limitations in isothermal based experiments

As discussed in the previous sections, reacting flows generate localized heat release which affect the flow and differentiate it from an equivalent flow with no reaction. Certain flow mechanisms that may be dependent upon heat release are difficult to be replicated in isothermal flow studies. For example, the actual variations in the diffusion layer thickness expected in gaseous reactions as a result from variations in local strain rate are not observed in fluid experiments [27]. Furthermore, gas expansion and the increase in volume within flames tend to completely diminish the initial vortex generated.

Chen et al.[53] also reported significant differences in the velocity profiles between a chemically cold jet (no reaction) and a reacting jet. A chemically cold jet shows fast velocity decay with a sharp rise in turbulence towards the end of the jet potential core due to the shear layers merging. Therefore, both fluid mechanics and reaction based studies are required in order to probe the vortical interaction of the side-jets configuration and reacting flow to study the effects that such interactions have on the turbulent jet flames.

2.6.2 Planar and point measurements

Experimental methods and techniques have evolved over the years to accommodate the increasingly demanding scientific requirements: higher spatial resolutions; higher temporal resolutions; high repetition rate; and etc. The advancement of optical techniques has allowed for the interrogation of planar regions, and often, measuring different scalars simultaneously, and allowing the measurement of 3-dimensional distribution within a volume, which is a large step-up from point measurement techniques. Most importantly, it allows the determination of the instantaneous gradients of key scalars in a sheet.

Optical diagnostic techniques have been used to study combustion processes and fluid mechanics for many years. Current techniques allow the instantaneous and simultaneous measurement of key active and passive scalars including: specie concentration, temperature, and velocity [18]. Compared to point measurement techniques with similar capabilities, planar techniques offer further insights that are not possible with point measurement. However, collection of certain high temporal resolution or time-resolved data in flow fields are still dependant on point measurement techniques.

2.6.3 Planar Laser Induced Fluorescence

The Planar Laser Induced Fluorescence (PLIF) technique has been used to conduct flow visualization as it allows the quantitative, spatially, and temporally resolved scalar data to be collected [21].

In a typical PLIF set up, the flow is laced with molecular markers and then illuminated by a laser sheet of known wavelength [107]. The wavelength of the laser is tuned to excite a particular transition of the marking molecule, which could be a specie occur-

ring naturally in the flow (e.g. CH, OH, and NO in flames), or added specifically for diagnostics (diluted Rhodamine 6G in water). The laser radiation excite the specie's atom/molecule on the lower energy level, to a high quantum state, after which some of the excited atom/molecule will return to equilibrium by emitting fluorescent or by transferring the excess energy through non-radiative decay [18, 107]. The specie fluoresces spontaneously in a short time scale for laser-induced fluorescence, or on a longer time scale (for phosphorescence) when metastable electronic states are involved [107].

For quantitative measurements, various methods for PLIF calibration have been proposed and are currently in practice. The most common method involves acquiring images of varying dye concentration to construct a linear relation between dye intensity and the collected image's pixel intensity [108].

Using large quantity of fluorescent dye, for example lacing the whole test section with dye, poses significant absorption problems. This can be overcome by correcting the images to the intensity variation from background dye concentration in the image, by initially assuming that the light emitted from the fluorescent specie in the imaging region is linearly related to the total dye concentration and laser intensity at each point. Different PLIF users have adopted different correction algorithms, for example, Kalt and Nathan[109], Venderwel and Tavoularis[110], and Sarathi et al.[108].

Applying the PLIF technique to reacting flows, quenching effects need to be accounted for and that necessitates the measurement or the determination of the concentration of the other species in the volume control. Calibration is usually done in flat laminar flames with different equivalence ratios and the specie concentration is determined through modelling of the flames.

2.6.4 OH*-Chemiluminescence

Unlike optical diagnostic techniques which require source of illumination such as PLIF, chemiluminescence, or spontaneous emissions from certain chemical specie can be collected via intensified high speed cameras fitted with suitable filters.

The chemiluminescence from electronically excited CH*, OH*, NO* and CO* species are commonly used as markers for reaction zones in hydrocarbon based fuel combustion [111]. Chemiluminescence is a line-of-sight measurement technique collecting photon emissions from a volume, unlike planar techniques such as LIF. The electronically excited CH* and OH* species are commonly used in the study of flame reaction zones. This is owed to a thin CH layer (<1mm thick) and a thin peak OH layer (around 1mm thick) that exist on the fuel rich and the fuel lean side of the stoichiometric contour, respectively [32, 112]. The presence of CH signifies fuel decomposition and a region of rapidly reacting fuel, whilst OH signifies high temperature zone, and is a reasonable indicator of reaction zone and flame structure [113]. OH formation is fast ($\approx 1-5\mu s$) but elimination of OH is slow ($\approx 200\mu s$) and exists over a small temperature and mixture fraction range [23].

OH concentrations are particularly sensitive to fuel dilution and this affects the scalar dissipation rate and decreases significantly with axial distance in the upstream region of an unperturbed flame [27]. Also, in sooty, fuel-rich non-premixed flames, OH is generated in low concentration. Hence, this makes it a poor candidate for simultaneous measurements with soot, which is found on the fuel rich side of the stoichiometric contour [23].

2.6.5 Particle Image Velocimetry

Particle Image Velocimetry (PIV) is a technique developed to study the flow vector field quantitatively. PIV has become an important tool in fluid mechanics research, especially for turbulent flow studies [114], owing to the availability of high speed cameras, lasers with high repetition rate, and sufficiently high computer processing power [115]. PIV measurements are applied to obtain the mean flow-field and turbulence statistics, by ensemble averaging large numbers of vector images. The precision of the final result is dependent on the number of PIV vector images collected, among other things [116].

The targeted flow for PIV measurement is seeded with micron sized reflective particles of similar density to follow the flow. For measurement in air flows, micron sized particles or oil droplets can be used as seeds whilst polyamide and glass spheres are used in water-based measurements. A planar laser sheet is generated via a combination of optics to illuminate the region of interest for approximately 9 ns and the light reflected off the seeds are recorded onto a sensor array of high speed cameras. The laser is usually double pulsed at a required time delay (of the second laser pulse from the first) [117]. A charged-coupled device (CCD) camera capture the elastic scatter from the particles in the flow for each pulse and the resulting image pair is used to determine the velocity vectors.

Important parameters in the PIV technique are the time delay between two laser pulses and hence imaging frames, and the displacement of particles between two frames. Various types of PIV techniques have been developed and they are: stereoscopic PIV, which allows measurement of three velocity components; auto correlation, which require the particles image of two subsequent laser pulses within the same image frame; and cross-correlation, which correlates the particle images of

two consecutive image frames of two subsequent laser pulses. Each image collected is divided into interrogation areas of 2^n pixels × 2^n pixels. The interrogation areas for the image pairs are cross-correlated using correlation algorithms to generate displacement peaks. These correlation algorithms include: Parabolic and Gaussian curve fitting; centroid fitting; and Whittaker's reconstruction [114].

Of these, the Parabolic and Gaussian curve fits are commonly used due to the similar pofiles expected of the displacement peaks. Gaussian method is superior in estimating the displacement peak than the Parabolic algorithm as it has a good sub-pixel accuracy whilst Parabolic fit tends to be biased towards integer pixel values. The centroid fitting meanwhile relies on the center of mass at the peaks and hence presents errors for small displacements, that may sometimes lead to self-correlation. Whittaker's algorithm is commonly used to interpolate between discrete data samples [114].

There are other variants of optical measurement techniques that are being applied in fluid mechanics, combustion and other fields. This section discusses only techniques that are being used for the purposes of this thesis. The archive and performance of optical measurement techniques continue to grow daily.

The results from the study contained in this thesis is expected to transcend both the fluid mechanics and combustion fields, therefore is applicable to both mixing related and combustion applications.

Chapter 3

Effects of multilateral jets on mixing regimes, flow and mixing fields

3.1 Overview

From the background literature performed in Chapter 2, it can be concluded that there are scarce information on the flow regimes and mixing field characteristics in a confined pipe flow, affected by multi-lateral jet. This is so despite many practical applications in industry are based on the jet in a confined flow mixing technique. Furthermore, most studies reviewed in Chapter 2 are focused on achieving a homogeneous mixture, which might not be the aim of the current application.

To achieve homogeneous mixing within the shortest time span, numerical modelling has shown that Counter-rotating Vortex Pairs (CVPs) play a dominant role, hence studies with low momentum-ratio (MR) side-jets in a confined cross-flow (JICCF) are often prioritised. This further contribute to the scarcity of information regarding high MR JICCF cases and the corresponding flow structures that are induced. Therefore, the study presented in this chapter sets out to investigate the flow field characteristics influenced by a range of different MR.

To study the flow regimes inside the nozzle (Objective (i)), a primary acrylic pipe is fitted with four equi-spaced jets at 1 primary nozzle diameter (D_P) upstream of the pipe nozzle exit, and is placed in the working section of a closed-looped water tunnel. The mass-flows through the side-jets and the primary pipe are varied to achieve different MR. Simultaneous Planar Laser Induced Fluorescence (PLIF) and Particle Image Velocimetry (PIV) studies are conducted in the mixing region of the nozzle to study the effects of changing momentum ratio on both the scalar and flow fields inside the nozzle (Objective (ii)).

This study shows that

- Different mixing regimes are induced corresponding to different side-jet to primary flow momentum ratio, i.e. streaming flow regime, impinging flow regime, and backflow regime (with increasing MR);
- Impinging side-jets lead to the formation of a high side-jet mixture fraction region at the primary flow's centreline;
- The secondary flow streams formed in the backflow regime show flapping characteristics;
- Increasing the flow MR increases the centreline turbulence intensity.

The results of this study is published in a paper in the *Experiments in Fluids* journal, volume 56, issue 1, titled "Flow dynamics of multi-lateral jet injection into a round pipe flow" in 2015, authored by Chia X. Thong, Pater A.M. Kalt, Bassam B. Dally, and Cristian H. Birzer.

3.2 Manuscript

Statement of Authorship

Title of Paper	Flow Dynamics of Multi-Lateral Jets Injection into a Round Pipe Flow
Publication Status	☑ Published ☐ Accepted for Publication ☐ Submitted for Publication ☐ Unpublished and Unsubmitted w ork w ritten in manuscript style
Publication Details	Thong, C.X., Kalt, P.A.M., Dally, B.B., and Birzer, C.H. 2015, 'Flow dynamics of multi-lateral jets injection into a round pipe flow', *Experiments in Fluids*, vol 56, no 15, p1-p16.

Principal Author

Name of Principal Author (Candidate)	CHIA XIONG THONG
Contribution to the Paper	Conduct literature review, setting up and conduct experiments in the water tunnel, collect PIV and PLIF data, perform data processing and analysis, structure and write manuscript, and the corresponding author for the paper
Overall percentage (%)	65
Certification:	This paper reports on original research I conducted during the period of my Higher Degree by Research candidature and is not subject to any obligations or contractual agreements with a third party that would constrain its inclusion in this thesis. I am the primary author of this paper.
Signature	Date 15/12/2016

Co-Author Contributions

By signing the Statement of Authorship, each author certifies that:

i. the candidate's stated contribution to the publication is accurate (as detailed above);

ii. permission is granted for the candidate in include the publication in the thesis; and

iii. the sum of all co-author contributions is equal to 100% less the candidate's stated contribution.

Name of Co-Author	PETER KALT
Contribution to the Paper	Mentor and supervise experimental work and data processing, interpreting data, and edit manuscript.
Signature	Date

Name of Co-Author	BASSAM DALLY
Contribution to the Paper	Supervising development of work, interpreting data, and editing manuscript
Signature	Date 16-12-16

Name of Co-Author	CRISTIAN BIRZER		
Contribution to the Paper	Supervise experimental work, interpret data, and edit manuscript		
Signature		Date	15 DEC 16

Please cut and paste additional co-author panels here as required.

Exp Fluids (2015) 56:15
DOI 10.1007/s00348-014-1884-4

RESEARCH ARTICLE

Flow dynamics of multi-lateral jets injection into a round pipe flow

Chia X. Thong · Peter A. M. Kalt · Bassam B. Dally · Cristian H. Birzer

Received: 8 September 2014 / Revised: 6 November 2014 / Accepted: 7 December 2014 / Published online: 13 January 2015

Abstract Controlling the mixing field of turbulent jets is an important approach in optimizing practical combustion systems. The use of multi-lateral jets upstream from the nozzle exit to control mixing fields is one particular method. Existing studies have investigated jets into a confined cross-flow (JICCF) for dilution mixing, but there is a paucity of data available on the fundamentals for turbulent mixing capabilities of JICCF. The current study investigates the flow structures and Primary Reynolds number mixing characteristics within a round pipe flow modified by four equi-spaced, lateral side injectors. Experiments are conducted in a primary water jet flow that is modified with smaller jets located one central (axial) jet diameter upstream of the nozzle exit. Flow structures and mixing within the nozzle are non-intrusively characterized using simultaneous planar optical techniques. Planar laser-induced fluorescence is used to measure the scalar mixing of the side and axial jet streams, and particle imaging velocimetry is used to measure the planar velocities. Several cases are investigated with variable primary flow to explore the influence of cross-flow velocity on the induced mixing structures within the nozzle. By varying the momentum ratio, three characteristic flow modes are identified within the primary flow, namely streaming mode, impinging mode, and backflow mode. The impact of these modes on the flow and scalar fields is presented and discussed.

C. X. Thong (✉) · P. A. M. Kalt · B. B. Dally · C. H. Birzer
School of Mechanical Engineering, The University of Adelaide, Adelaide, SA 5005, Australia
e-mail: chia.thong@adelaide.edu.au

P. A. M. Kalt
e-mail: peter.kalt@adelaide.edu.au

B. B. Dally
e-mail: bassam.dally@adelaide.edu.au

C. H. Birzer
e-mail: cristian.birzer@adelaide.edu.au

1 Introduction

Combustion is a widely used method to convert the chemical energy that lies dormant within fuels into other usable forms of energy such as heat and light. However, the combustion of fuels can bring about adverse effects through pollutant emission such as greenhouse gases, and particulates such as soot. Therefore, combustion research is necessary both to increase combustion heat output and to reduce pollutant emissions.

Turbulent jet flames are widely used in industries requiring high-temperature applications such as mineral processing and power generation. Turbulent flames are usually categorized via two distinct combustion regimes: premixed and non-premixed flames. However, in practical turbulent flames, combinations of these regimes exist simultaneously with one dominating flame regime. Non-premixed flames are preferred in high-temperature applications in industry due to lower risks of flashback. The mixing mechanism of reactants for non-premixed flame is done by fluid entrainment at the nozzle exit (near-field region) by turbulent structures in the flow (Beer 2000).

Turbulent jet flows are known to have a wide range of scales: from the larger length-scales to the smallest turbulence scale which are characterized by the Kolmogorov Scale (Nathan et al. 2012). Pitsch and Steiner (2000) show that increasing the large-scale mixing contributes indirectly to the increase in fine-scale mixing which is necessary for combustion of the reactants. Enhanced turbulent mixing is also known to promote a more compact and stable flame, which leads to a higher heat release rate. Highly intense

turbulence, meanwhile, leads to an increase in the strain rate, which may lead to flame extinction. Currently, most flow mixing strategies to enhance combustion mixing aim to manipulate turbulent mixing in the near-field in order to influence combustion in the far-field of the jet. Active and passive mixing methods have been studied and applied in practical systems. Passive mixing that requires no energy input (Liu et al. 2000) can be cost-effective and efficient but is not adaptable to change in reactants' composition or flow rates. An example of passive mixing is by placing a mesh over a burner exit. Active mixing methods that allow control to the flame characteristics require moving parts or varying pressure gradients, which are more complex and costly (Liu et al. 2000). An example of active mixing includes acoustically induced flow mixing (Nguyen and Wu 2005). A challenge in combustion mixing is for there to be an active mixing method that is both simple and cost-effective.

The current study considers the application of jets in confined cross-flow (JICCF) technique as a combustion mixing method to address the above challenges. JICCF is an extension to the research in jets in cross-flow that has been widely studied and is considered as a classical fluid mechanics case-study due to its complex nature presented by a simple jet mechanism, e.g. chimney in crosswind (Hoult and Weil 1972). Most studies on JICCF focus on the effective dilution capabilities of the jets discharged into a cross-flow as reviewed by Holdemann et al. (1997). The dilution capabilities are often associated with the various induced vortices, namely the counter-rotating vortex pair (CVP). Similar to JICF, CVP is induced by the shear interaction of the injected jet with the cross-flow and has been regarded as the most important feature in rapid streams mixing applications and fume dilution. Unlike the unconfined domain, CVPs induced by multiple injections into a confined duct tend to develop close to the wall due to interactions with neighbouring vortices. The concept of JICCF has sprouted many applications particularly for turbojet fume dilution and for applications in quick quenching and mixing systems such as in the Rich Burn/Quick Quench/Lean Burn (RQL) combustors (Leong et al. 1999).

Studies into the mass addition and mass fraction distribution have been undertaken for various planar locations in order to optimize the different mixing systems (Sowa et al. 1994; Kroll et al. 2000; Leong et al. 2000). Studies have been conducted by injecting air into a heated cross-flow and combustion products by Leong et al. (1999, 2000). The temperature profiles at relevant axial planes have been published, but no comparison can be made with the current data (from this study) as mixing mechanism varies between isothermal- and temperature-affected flows. Besides, no flow structures are presented or described in detail in the previous studies.

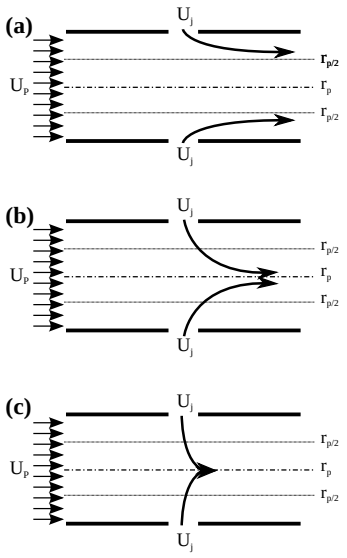

Fig. 1 Various characteristics of jet penetration into a confined cross-flow: **a** under-penetration; **b** over-penetration; and **c** jet impingement

Various terms have been coined to describe the jet trajectories such as under-penetration and over-penetration. Under-penetration is described as a jet trajectory that does not penetrates the half radius ($\boldsymbol{r}_\mathrm{P}/2$) of the primary/central flow, whilst over-penetration is described as a jet trajectory that penetrates over the half radius point at a given location as visualized in Fig. 1. An optimized flow is described as flow which penetrates the half radius of the central flow. Due to different applications in the industry, no single parameter can be used to depict an optimized flow and each flow cases have to be customized separately. For example, an application which requires optimized jet penetration at a location half central diameter downstream of the jet ($\boldsymbol{D}_\mathrm{p}/2$) will see under-penetration upstream of this location and over-penetration downstream of this location. However, the trajectory of the flow can be scaled with momentum ratio as described by Holdemann et al. (1997). Optimized mixing for most applications including RQL and fume dilution would mean homogenous mixture at a given location. Applying the same concept to fuel and air mixing would mean generating a premixed fuel field which could potentially lead to flame flashback.

Relying on vortices induced by the jet in cross-flow alone does not contribute much to the turbulent mixing required in the flow (Gosman and Simitovic 1986). A jet that impinges on the opposite wall or on other jets forms favourable large-scale mixing structures in the flow that can increase flow entrainment. Doerr et al. (1997) found that jets over-penetration into the cross-flow upstream of

targeted regions result in inhomogeneous mixing distribution and hence has not been explored further. However, this regime has the potential to generate favourable mixing distribution low number of side injectors ($n < 6$). Hence, there is a niche to study the mixing and velocity fields induced by impinging jets and its related potential for reactant mixing in jet flames. It is also not known whether the momentum ratio "rule" depicted above will hold for impinging jets, i.e. other quantifiable physical flow characteristics with regard to momentum ratio.

The current study examines the structures induced in a round pipe flow by multiple lateral jet injections and in particular the differences produced by impinging and non-impinging jets and the internal (upstream of nozzle exit) flow structures that can be achieved through lateral jets. The mixing between side injections and primary flow is examined using planar laser-induced fluorescence (PLIF). The 2D in-plane velocities are simultaneously resolved using particle imaging velocimetry (PIV). The optical techniques used in this study are non-intrusive, simultaneous and planar, therefore providing an insight into the instantaneous flow structures, which is not possible using point measurement alone.

2 Methodology

2.1 Experimental nozzle

The experimental nozzle is constructed of a 1-m long Perspex central cylinder with internal diameter (ID) of 56 mm (primary nozzle) and with four acrylic equi-distant, radially oriented side injectors of 150 mm long, ID of 6 mm (injection nozzles) placed at one central diameter upstream of the nozzle exit. The 1-m long pipe is equivalent to approximately 17 central diameter and is connected to the flow source via a diverging nozzle and a honeycomb structure of 3 mm × 30 mm dimension (cell size × length).

A four-jet configuration will be used for the current study. The jets' placement of one central diameter upstream of the nozzle exit is based on realistic estimation to perturb nozzle outflow for near-field mixing and also to ease quantification and result normalization.

2.2 Experimental apparatus

The Perspex nozzle is placed in the working section of the water tunnel facility in the School of Mechanical Engineering, the University of Adelaide, which is depicted in Fig. 2. The working section measures 500 mm × 500 mm wide and 1,800 mm in length. Water is used as the working fluid as it allows for a higher Reynolds number at a lower flow velocity.

Fluid for the primary flow is sourced from a 400 L capacity reservoir seeded with 0.1 g of rhodamine 6G dye, whilst fluid for the injection flow is sourced from a similar reservoir of clean water. Aqueous rhodamine 6G dye mixture was chosen as the fluorescent dye as its peak absorption is at about 530 nm, which is close to the emitted wavelength of the available Nd:YAG laser, whilst the emission of the dye is at about 560 nm (Tsunoda and Saruta 2002).

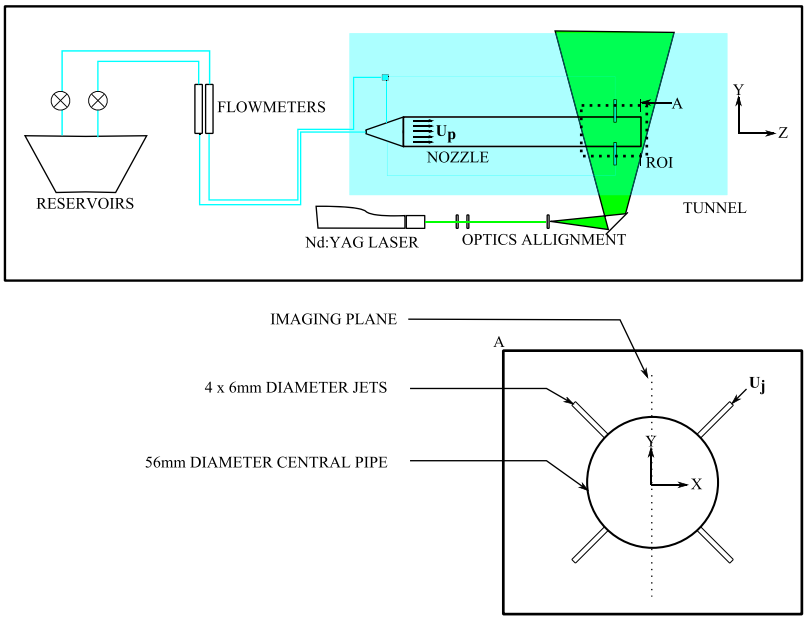

Fig. 2 Experimental set-up schematics

Both reservoirs are seeded with 50-μm Dantec Dynamic PSP-50 Polyamid Seeding Particles.

Light is sourced from a Quantel Brilliant B Nd:YAG laser frequency doubled to 532 nm and double-pulsed at 10Hz. The laser light sheet is formed using a combination of spherical (a plano convex length of *focal length* +100 mm, and a bi-concave lens of *focal length* −50 mm) and cylindrical (a plano concave of *focal length* −25 mm) optics to form a laser sheet of approximately 2 mm thick. The nozzle and the laser light sheet are aligned such that the sheet is incident on the nozzle centreline, illuminating the region of interest (ROI).

Image collection is done by a pair of Princeton Instruments' CCD Megaplus II ES4020 camera units. The CCDs feature 2,048 pixels × 2,048 pixels capability and is triggered by a Berkeley Nucleonics Corporation (BNC) 565 Delay Generator at a duty cycle of 2.5 Hz. The overall physical imaging region is estimated to be approximately 200 mm × 200 mm therefore giving an averaged spatial resolution of 10.2 px/mm. Both CCDs are fitted with Tamron lens sets of 50 mm, $\boldsymbol{f}1/4\boldsymbol{D}$ and filters. The CCD control and image collection are performed through the use of EPIX XCAP 3.8 software.

The flowmeters to monitor the primary flow rate consist of a Fischer & Porter tube FP-1-27-G-10 with a float 1-GNSVGT-68 which allows a maximum flow reading of 1,467.1 L/h. The side-injectors' flowmeter consists of a tube FP-3/4-21-G-10 with a float 3/4-GUSVT-510 which allows a reading of up to 1,438 L/h. The injection flowmeter is connected to a manifold which distributes the flow equally to the side jets via four flexible tubes of equal length.

2.3 Flow conditions

The flow conditions for this study are set up to allow for a large range of flow regimes to be studied which spans from under-penetrating flow to over-penetrating to impingement flow. A fixed-jet injection flow of 0.9985×10^{-6} m^3/s for each jet is applied, and primary flow rate is decreased gradually from 2.85×10^{-4} m^3/s to 0.61×10^{-4} m^3/s to observe and document the relevant changes in the flow characteristics. The current study emulates a condition whereby fuel is injected into a central flow consisting of air which is reduced gradually in response to different air-to-fuel ratio. The experimental flow parameters are presented in Table 1

2.4 Velocity and scalar measurement

The PIV image ensemble is batch processed on PIV view 2.3C. A single-pass, standard fast Fourier transform (FFT) was used to process the PIV images to obtain the raw vector field data. The single-pass 2D cross-correlation is calculated for a 32 pixels ×32 pixels interrogation window with 50 % overlap. The PIV vector data files are imported into freeware, OMA-X (Kalt and Long 2014), for further post-processing and analysis.

Table 1 Experimental flow parameters for flow cases

Parameters	Cases			
Primary Reynolds number (Re_P)	6,467	4,629	2,768	1,386
Injection Reynolds number (Re_{inj})	2,115	2,115	2,115	2,115
Primary flow rate ($Q_P \times 10^{-4}$) (m^3/s)	2.85	2.04	1.22	0.61
Injection flow rate ($Q_{inj/4} \times 10^{-6}$) (m^3/s)	0.9985	0.9985	0.9985	0.9985
Momentum ratio (G_{inj}/G_P)	0.1	0.2	0.6	2.3

The dye mixture concentration scalar measurements were taken using the PLIF technique. Instantaneous and ensemble averaged dye mixture fraction of the imaging plane is obtained from an ensemble of 212 images, which correlates to the image pairs collected simultaneously for PIV. The PLIF CCD is fitted with an OG orange glass filter to exclude elastic scattering from PIV particles at 532 nm. Dye is injected through the primary flow and is diluted with dye-free water from the jets. The imaged PLIF signal intensity is assumed to be linearly proportional to the concentration of the dye (rhodamine) in water which renders the region with the highest dye concentration the brightest (Shan et al. 2004).

The PLIF ensembles are processed in OMA-X for background removal, laser sheet profiling, and divergence, attenuation, and response correction in line with methods highlighted in Kalt and Nathan (2007) and Kalt et al. (2007).

2.5 Calibration, errors, and uncertainties

The PLIF images are predominantly calibrated with the unmixed dye solution (100 % dye mixture concentration). Each individual PLIF image for this study is calibrated with the upstream primary flow which remains unmixed with the injection stream. The PIV resolution is calibrated with a 2 mm × 2 mm grid resulting in a spatial resolution of 10.2 pixels/mm. The spatial resolution varies slightly from 10.2 to 10.5 pixels/mm depending on the flow case due to camera lens refocusing and repositioning.

Errors in the study could stem from random errors, systematic errors, interferences, and various uncertainties. Random error can be caused by foreign particles travelling in the tunnel flow which cast shadows over the ROI. The images are examined after every collection and are excluded from the ensemble.

Systematic errors in this study can stem from acrylic deformities, imperfections and grubs. These deformities cast "lines" into the ROI, consistently throughout the ensemble.

These are corrected through background and response correction methods during the image processing stages as mentioned in the previous subsection. Besides, some locations in the imaged region show physical obstruction by the side injectors' set-up components. These obscured regions are masked out of the final data during post-processing.

Bias errors in PIV measurements are usually associated with peak-locking. This phenomenon is kept to a minimum by ensuring that the imaged particles are larger than 2 pixels, which is confirmed by the 1D histogram obtained after every batch processing.

Tolerances and uncertainties from the study can result from the use of measuring equipment such as flowmeters and calibration grids for PIV. The errors contributed by the flowmeter tubes are measured to be $\pm 2\,\%$ of the maximum flow, whilst errors contributed by the calibrating grids for PIV are estimated to be ± 0.05 mm. Measurements are repeated and averaged to get to the final value.

The reason that small sets of images are used is to compromise between reliable results and an admissible run time. Owing to the high flow rate of the primary flow and size of the reservoir, a longer run time will deplete the reservoir of fluid. To evaluate the statistical and qualitative convergence, different ensemble sets with increasing numbers of images were acquired and evaluated.

The percentage uncertainty for the image sets is plotted in Figs. 3 and 4 to evaluate the confidence of the results acquired corresponding to the size of the samples. Random subsampling of an area within the region of interest is performed on the PLIF image ensemble and is plotted for an increasing size of samples.

Mean pixel values for the PLIF images in Fig. 3 (red circle) show a low-percentage uncertainty <1 % for the sample size larger than 80 images. The uncertainty for the PLIF RMS profile (black diamond) shows a plateau of uncertainty <10 % for sample size above 40 images up to and include 150 images before falling below 1 %.

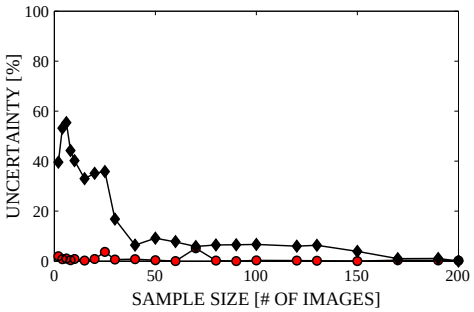

Fig. 3 Percentage uncertainty for the averaged pixel value (*red circle*) and the RMS (*black diamond*) corresponding to sample sizes of PLIF image sets

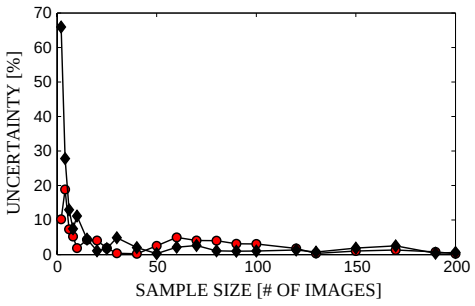

Fig. 4 Percentage uncertainty for the averaged velocity (*red circle*) and the RMS (*black diamond*) corresponding to sample sizes of PIV image sets

Plotting the percentage uncertainty for the PIV image sample sizes in Fig. 4 (red circle) shows the uncertainty converging to a level <5 % from a sample size of 10 images. The uncertainty dips and remains below 1 % from the sample sizes larger than 120 images. Uncertainty profile for the PIV RMS (black diamond) shows that the plotted uncertainty hovers around 2 % beyond the sample size of 40 images and remains around 1 % from a sample size of 80 images onward.

The profiles in Figs. 3 and 4 give sufficient confidence for the sample size of 212 images to be used to provide quantitative information for the current study with percentage uncertainty below 1 %.

3 Results and discussion

The coordinates used to describe the experimental results are $\boldsymbol{z}$-coordinate denotes the axial (stream-wise) direction, the $\boldsymbol{y}$-coordinate denotes the upwards radial direction, and the $\boldsymbol{x}$-coordinate denotes the direction into the page. The axial distance is normalized to the central pipe diameter, $\boldsymbol{z/D}$. The location of the jet injectors denotes the origin $\boldsymbol{z/D} = 0$, whilst $\boldsymbol{z/D} = 1$ denotes the nozzle exit. The primary flow propagates from the left to the right of the images. As mentioned previously, the fluorescent dye-laced water is pumped through the primary nozzle, rendering the brightest area in the figures as the region with the highest dye concentration and the least bright region the lowest (high injection fluid concentration). The decrease in primary velocity also corresponds to an increase in injection-to-primary momentum ratio,

$$\frac{\boldsymbol{G}_{\mathrm{inj}}}{\boldsymbol{G}_{\mathrm{P}}} = \frac{(\rho \boldsymbol{V}^2 \boldsymbol{A})_{\mathrm{inj}}}{(\rho \boldsymbol{V}^2 \boldsymbol{A})_{\mathrm{P}}} \tag{1}$$

$\boldsymbol{G}_{\mathrm{inj}}$ in the current study represents the side-injection momentum for a single jet. As such, the $\boldsymbol{V}_{\mathrm{inj}}$ and $\boldsymbol{A}_{\mathrm{inj}}$ represent injection velocity and side injection inlet area for a

single jet ,respectively, whilst $\boldsymbol{V}_{\mathrm{P}}$ and $\boldsymbol{A}_{\mathrm{P}}$ represent the primary flow velocity and central flow area, respectively, and ρ, the fluid density. To characterize the injection penetration in the current study, only momentum ratio from a single side injection will be considered.

3.1 Instantaneous flow characteristics

Random still images were selected from their ensembles and interrogated. Visual interrogation of the instantaneous images was carried out to qualitatively identify the mixing structures present in the flow. The instantaneous images for the axial position of $\boldsymbol{z}/\boldsymbol{D} = -1$ to $\boldsymbol{z}/\boldsymbol{D} = 1$ are compared for flow cases: $\boldsymbol{G}_{\mathrm{inj}}/\boldsymbol{G}_{\mathrm{p}} = 0.1$; $\boldsymbol{G}_{\mathrm{inj}}/\boldsymbol{G}_{\mathrm{p}} = 0.2$; $\boldsymbol{G}_{\mathrm{inj}}/\boldsymbol{G}_{\mathrm{p}} = 0.6$; and $\boldsymbol{G}_{\mathrm{inj}}/\boldsymbol{G}_{\mathrm{p}} = 2.3$. Dye mixture fraction is determined by normalizing the recorded signal with unmixed dye far upstream of the mixing region. Unmixed dye mixture is represented by a dye mixture fraction value of 1.0 and 0.0 for clean water (injector stream).

For the flow case of $\boldsymbol{G}_{\mathrm{inj}}/\boldsymbol{G}_{\mathrm{P}} = 0.1$ in Fig. 5a, large-scale mixing structures are evident. These are predominantly induced by CVPs which are well documented in other JICCF studies (for example Holdemann et al. 1997). Increasing the relative momentum ratio to $\boldsymbol{G}_{\mathrm{inj}}/\boldsymbol{G}_{\mathrm{P}} = 0.2$ (Fig. 5b) shows that relatively stronger injection fluid signals (darker region) can be detected in the region close to $\boldsymbol{z}/\boldsymbol{D} = 0$. The relatively darker region signifies a stronger presence of injection fluid, especially at the centreline of the primary nozzle. This is also an indication of the jet injections' impingement upon the primary flow centreline. Correspondingly, more large-scale mixing structures can also be detected.

The presence of injection fluid being convected upstream from the jets impingement region can be detected in Fig. 5c for case $\boldsymbol{G}_{\mathrm{inj}}/\boldsymbol{G}_{\mathrm{P}} = 0.6$ and Fig. 5d for case $\boldsymbol{G}_{\mathrm{inj}}/\boldsymbol{G}_{\mathrm{P}} = 2.3$. This phenomenon (fluid convected upstream) is identified as *backflow* throughout the remaining sections of this study. Comparison between Fig. 5c and d also shows that relatively more mixing structures can be detected in Fig. 5d than in Fig. 5c corresponding to a relatively higher momentum ratio.

It is also noted that some optical aberrations exist due to perspex refraction that can be seen most prominently at the near-wall region and lines evident in Fig. 5a, b as artefacts not successfully removed. These interferences have small impact on the results, and a large portion of the data remain unaffected.

3.2 Dye profile

Variation in the centreplane mean dye profile for the different cases can be observed by comparing Fig. 6a–d, which corresponds to the cases represented by Fig. 5a–d, respectively. Little jet impingement can be detected on average between location $\boldsymbol{z}/\boldsymbol{D} = 0$ to $\boldsymbol{z}/\boldsymbol{D} = 0.5$ in Fig. 6a as the injection flow streams are convected downstream due to the relatively high primary flow momentum. The averaged concentration in Fig. 6b indicates that the jet injections' impingement is centred around location $\boldsymbol{z}/\boldsymbol{D} = 0.25$ at the flow centreline and can be deduced from the darker "triangular"-like region. The flow downstream from this impingement region shows a higher jet injection fluid signal and is seen to be reducing radially away from the centreline. That is, at any axial position downstream of the injectors' location ($\boldsymbol{z}/\boldsymbol{D} > 0$), the dye mixture fraction increases from the centreline towards the wall, indicating a secondary stream of fluid on the centreline predominantly originating from the injectors. This flow region, the "secondary stream", is formed within the nozzle by the side injection jets impinging together in the centreline and is also apparent in similar axial positions in both Fig. 6c, d.

The side injection impingement can be more readily observed in Fig. 6c, d and is typically centred at an axial position of approximately $\boldsymbol{z}/\boldsymbol{D} = 0.1$. The presence of

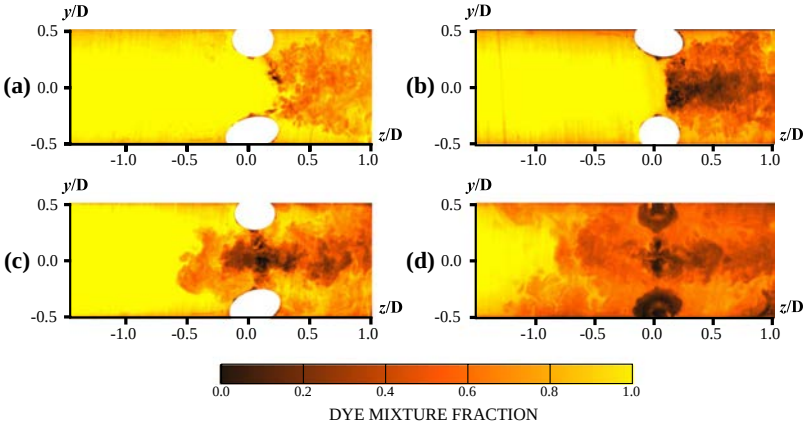

Fig. 5 Typical instantaneous dye mixture fraction image for flow cases: **a** $\boldsymbol{G}_{\mathrm{inj}}/\boldsymbol{G}_{\mathrm{P}} = 0.1$; **b** $\boldsymbol{G}_{\mathrm{inj}}/\boldsymbol{G}_{\mathrm{P}} = 0.2$; **c** $\boldsymbol{G}_{\mathrm{inj}}/\boldsymbol{G}_{\mathrm{P}} = 0.6$; and **d** $\boldsymbol{G}_{\mathrm{inj}}/\boldsymbol{G}_{\mathrm{P}} = 2.3$

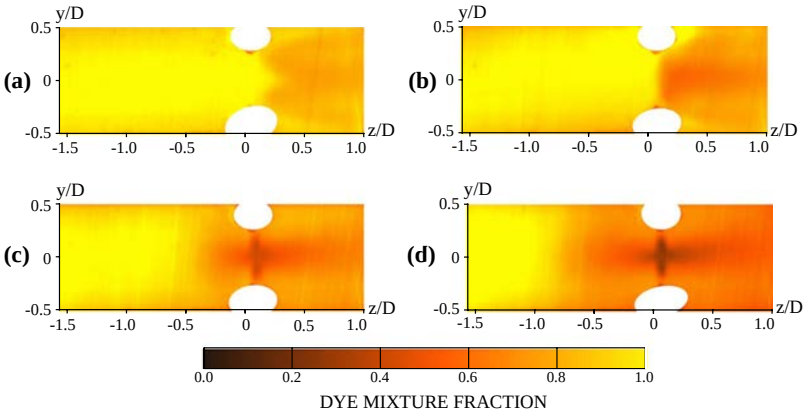

Fig. 6 Averaged dye mixture fraction images at the centre-plane for cases: **a** $G_{inj}/G_P = 0.1$; **b** $G_{inj}/G_P = 0.2$; **c** $G_{inj}/G_P = 0.6$; and **d** $G_{inj}/G_P = 2.3$

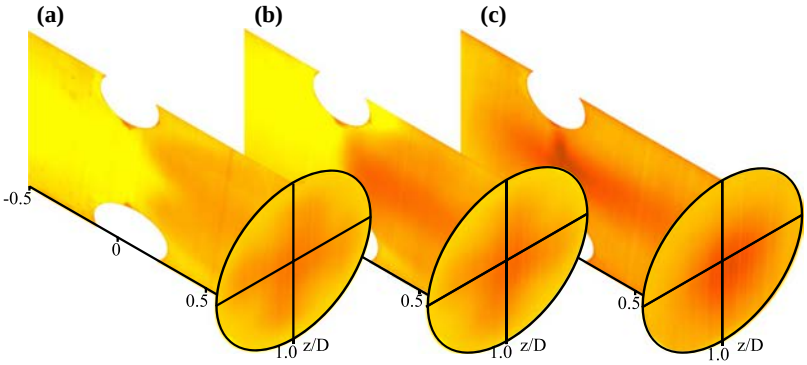

Fig. 7 Outlet dye profiles for cases: **a** $G_{inj}/G_P = 0.1$; **b** $G_{inj}/G_P = 0.2$; and **c** $G_{inj}/G_P = 0.6$

fluid originating from the side injectors can be detected upstream of the impingement region corresponding to the backflow seen in Fig. 6c, d. This backflow occurrence induced by the jet impingement is readily seen in the mean dye mixture fraction images (Fig. 6c, d) and suggests that the backflow occurs consistently and is in the same location. Another similarity between Fig. 6c, d includes the highly mixed regions surrounding the downstream secondary flow. These observations enable the categorizing of flows into various corresponding flow modes, namely streaming mode as seen in case $G_{inj}/G_P = 0.1$; impinging mode in case $G_{inj}/G_P = 0.2$; and backflow mode in both cases $G_{inj}/G_P = 0.6$ and 2.3. These characteristics modes are discussed in the subsequent sections (Sects. 3.4, 3.5 and 3.6, respectively).

The characteristic differences of the flow modes which are driven by the momentum ratio are also reflected in the dye distributions at the nozzle exit. A PLIF run is carried out to profile the dye mixture fraction for each characteristics mode at the nozzle exit and is presented in Fig. 7. The dye profile is calibrated using a "dye cell" of undiluted dye mixture (not in the figure) in the same image frame. Figure 7a, b shows the outlet profiles for cases $G_{inj}/G_P = 0.1$ and $G_{inj}/G_P = 0.2$, respectively, which demonstrate a "cruciform" averaged profile at the outlet. This shows that the structures of the side injectors persist in these cases to the emerging scalar field. Figure 7c, on the other hand, shows the outlet profile for case $G_{inj}/G_P = 0.6$ (with backflow) which shows a radially symmetrical dye profile. The dye profile in Fig. 7c is also expected to be similar to that of case $G_{inj}/G_P = 2.3$ which was not measured.

Despite the irregularities present for case $G_{inj}/G_P = 2.3$ in both the averaged dye mixture fraction in Fig. 6d and averaged velocity flow field in Fig. 12d, the lowest dye mixture fraction remains around the centreline at $y/D = 0$ (as shown in Fig. 10) which reaffirms the legitimacy of the flow centreline data values. In these figures, the dye profile near the outlet can be seen biased upwards away from the centreline. This is interpreted as the secondary stream flapping (Sect. 3.6) more frequently in the $+y$ direction than in the $-y$ direction.

Figure 8 shows the axial mean dye mixture fraction along the centreline for all investigated cases. For the streaming flow, $G_{inj}/G_P = 0.1$, and for the impinging flow, $G_{inj}/G_P = 0.2$, and the dye mixture fraction upstream of the injectors' location ($z/D < 0$) is 1.0 which indicates that

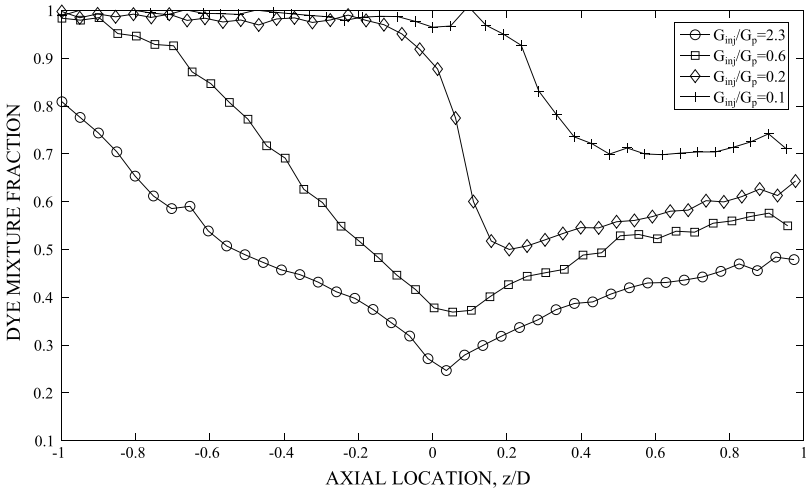

Fig. 8 Mean centreline dye mixture fraction profile from $\boldsymbol{z/D} = -1$ to $\boldsymbol{z/D} = 1$ for cases $\boldsymbol{G}_{\text{inj}}/\boldsymbol{G}_{\text{P}} = 0.1$; $\boldsymbol{G}_{\text{inj}}/\boldsymbol{G}_{\text{P}} = 0.2$; $\boldsymbol{G}_{\text{inj}}/\boldsymbol{G}_{\text{P}} = 0.6$; and $\boldsymbol{G}_{\text{inj}}/\boldsymbol{G}_{\text{P}} = 2.3$

the fluid on the centreline originates wholly from the primary stream. As the momentum ratio is increased (cases $\boldsymbol{G}_{\text{inj}}/\boldsymbol{G}_{\text{P}} = 0.6$ and $\boldsymbol{G}_{\text{inj}}/\boldsymbol{G}_{\text{P}} = 2.3$), the mean centreline dye mixture fraction upstream of the injectors' location begins to decrease as fluid originating from the side injectors starts propagating upstream. It is also noted that as the momentum ratio is further increased, the backflow increases accordingly.

Another observation from Fig. 8 is apparent in the profiles downstream of the injection. For the $\boldsymbol{G}_{\text{inj}}/\boldsymbol{G}_{\text{P}} = 0.1$ case, the minimum mean centreline dye mixture fraction occurs at $\boldsymbol{z/D} = 0.5$ and increases steadily towards the nozzle exit. For the impinging case represented by $\boldsymbol{G}_{\text{inj}}/\boldsymbol{G}_{\text{P}} = 0.2$, the centreline dye mixture fraction quickly drops to a local minimum dye mixture fraction of 0.5 at $\boldsymbol{z/D} = 0.1$ before increasing gradually to 0.65 at the exit. Further increase in the relative momentum ratio shifts the location of the dye mixture fraction's local minimum closer to the injectors' location. For the $\boldsymbol{G}_{\text{inj}}/\boldsymbol{G}_{\text{P}} = 2.3$ case, the local minimum occurs only slightly downstream of the injectors' location at $\boldsymbol{z/D} = 0$.

One final observation is that the emerging flow from the nozzle exit is not uniformly mixed that there remains some stratification between the primary and the injection streams. For all cases, the centreline mean dye mixture fraction is lower that a perfectly mixed flow of the corresponding relevant flow rates. That is, the centreline dye mixture fraction predominantly originates from the side injectors. On the basis of total mass-flow rate inside the pipe, a homogeneous flow for case $\boldsymbol{G}_{\text{inj}}/\boldsymbol{G}_{\text{P}} = 0.1$ will amount to a uniform dye mixture fraction of 0.88; however. only 0.73 is observed in the centreline. For the case of $\boldsymbol{G}_{\text{inj}}/\boldsymbol{G}_{\text{P}} = 0.2$, a homogeneous exit profile of 0.84 is expected compared to the achieved 0.64. For the case of $\boldsymbol{G}_{\text{inj}}/\boldsymbol{G}_{\text{P}} = 0.6$, a homogeneous dye mixture fraction of 0.75 would be expected for complete mixing compared to the dye mixture fraction of 0.56 observed at the centreline. Finally, for the case of $\boldsymbol{G}_{\text{inj}}/\boldsymbol{G}_{\text{P}} = 2.3$, homogeneous dye mixture fraction of 0.6 is expected in comparison with the value of 0.48 achieved at the centreline. It is also worth noting that for combustion applications, this can increase the flame surface density resulting in enhanced reaction close to the jet exit especially if the dye mixture fraction is close to stoichiometric conditions.

Mixedness shows the deviation of local mixing value from a homogeneous dye mixture fraction value. The degree of centreline mixedness for the investigated cases is defined by:

$$\textbf{\textit{Mixedness}} = \begin{cases} \dfrac{|(\boldsymbol{f}_{\text{local}} - \boldsymbol{f}_{\text{max}})|}{(\boldsymbol{f}_{\text{max}} - \boldsymbol{f}_{\text{mixed}})}, & \text{if} \quad \boldsymbol{f}_{\text{local}} \geq \boldsymbol{f}_{\text{mixed}} \\ \dfrac{\boldsymbol{f}_{\text{local}}}{\boldsymbol{f}_{\text{mixed}}}, & \text{if} \quad \boldsymbol{f}_{\text{local}} < \boldsymbol{f}_{\text{mixed}} \end{cases} \tag{2}$$

where $\boldsymbol{f}_{\text{local}}$[arbitrary unit a.u.] defines the local dye mixture fraction at an axial location, $\boldsymbol{f}_{\text{max}}$[a.u] defines the maximum dye mixture fraction which corresponds to the unmixed dye mixture fraction, and $\boldsymbol{f}_{\text{mixed}}$[a.u] is defined as:

$$\boldsymbol{f}_{\text{mixed}} = \frac{\dot{\boldsymbol{m}}_{\text{P}}}{\dot{\boldsymbol{m}}_{\text{P}} + \dot{\boldsymbol{m}}_{\text{inj}}} \tag{3}$$

where $\dot{\boldsymbol{m}}_{\text{P}}$ defines the primary flow rate and $\dot{\boldsymbol{m}}_{\text{inj}}$ defines the total injection flow rate.

Mixedness of 1.0 defines a well-mixed fluid mixture, whilst mixedness of 0.0 defines unmixed jet or purely primary flow fluid. Inspecting the mean centreline mixedness for the different flow cases in Fig. 9 shows similar trend for cases $\boldsymbol{G}_{\text{inj}}/\boldsymbol{G}_{\text{P}} = 0.2, 0.6$ and 2.3 at location $0.3 < \boldsymbol{z/D} < 1.0$. This cluster of data shows that cases with impinging flow have similar mixedness at around the

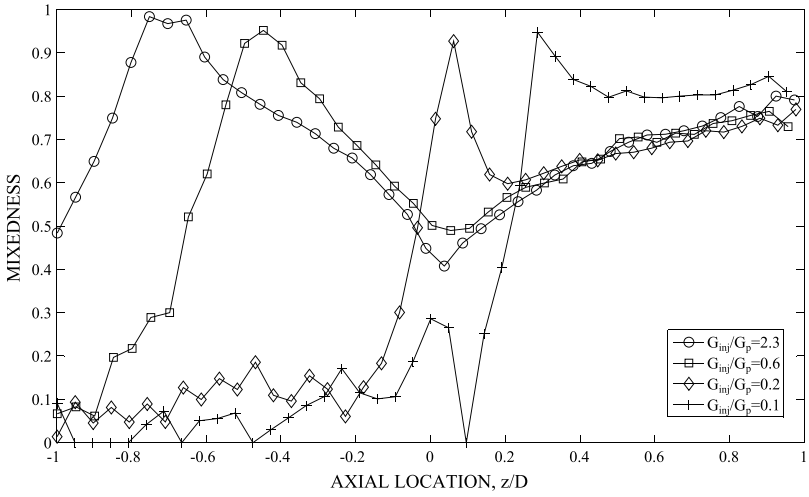

Fig. 9 Mean centreline mixedness profile from $\boldsymbol{z}/\boldsymbol{D} = -1$ to $\boldsymbol{z}/\boldsymbol{D} = 1$ for cases $\boldsymbol{G}_{\text{inj}}/\boldsymbol{G}_{\text{P}} = 0.1$; $\boldsymbol{G}_{\text{inj}}/\boldsymbol{G}_{\text{P}} = 0.2$; $\boldsymbol{G}_{\text{inj}}/\boldsymbol{G}_{\text{P}} = 0.6$; and $\boldsymbol{G}_{\text{inj}}/\boldsymbol{G}_{\text{P}} = 2.3$

centreline. Similar mixing trend upstream is noticeable for cases $\boldsymbol{G}_{\text{inj}}/\boldsymbol{G}_{\text{P}} = 0.6$ and 2.3 which corresponds to the backflow region. The jagged region that can be seen at locations $-1.0 < \boldsymbol{z}/\boldsymbol{D} < 0.8$ which fluctuates between mixedness of 0 and 0.1 is a product of errors posed by the "lines" (which forms local maximum and minimum)that are not eliminated during data reduction and the sensitivity posed by this method of calculation.

Figure 10 shows the radial dye mixture fraction distribution at the outlet for the mentioned flow cases whilst Fig. 11 shows the radial mixedness of the flow cases at the nozzle outlet. The cases with backflow $\boldsymbol{G}_{\text{inj}}/\boldsymbol{G}_{\text{P}} = 0.6$ and 2.3 display a similar trend, especially in the region close to the primary flow centreline despite the relatively large difference in flow momentum ratio. Case $\boldsymbol{G}_{\text{inj}}/\boldsymbol{G}_{\text{P}} = 0.2$ shows the lowest mixedness near the centreline which corresponds to the formation of the secondary stream in the nozzle as a result of upstream jet injections impingement. The relatively low mixedness of this particular case compared to the other cases has been reported in previous studies (Doerr et al. 1997) but the authors did not extend the study to include the backflow mode. Case $\boldsymbol{G}_{\text{inj}}/\boldsymbol{G}_{\text{P}} = 0.1$, meanwhile, shows an overall higher mixedness near the centreline flow region, but comparing with Fig. 7a shows regions of low mixedness at intervals. Overall, this figure summarizes that case of the impinging flow mode displays less mixing in the measured region in comparison with a streaming flow mode. However, cases with backflow show an improved mixing relative to that of the impinging flow mode.

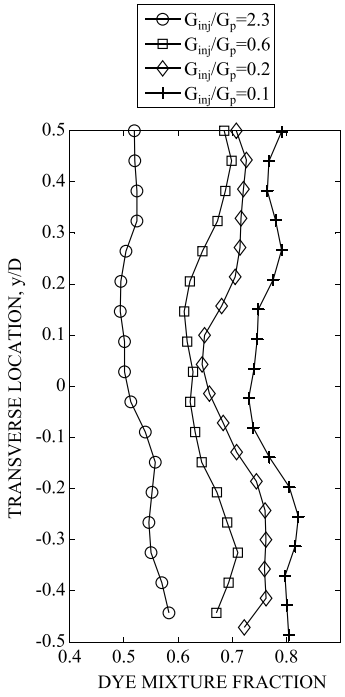

Fig. 10 Radial dye mixture fraction distribution for cases $\boldsymbol{G}_{\text{inj}}/\boldsymbol{G}_{\text{P}} = 0.1$; $\boldsymbol{G}_{\text{inj}}/\boldsymbol{G}_{\text{P}} = 0.2$; $\boldsymbol{G}_{\text{inj}}/\boldsymbol{G}_{\text{P}} = 0.6$; and $\boldsymbol{G}_{\text{inj}}/\boldsymbol{G}_{\text{P}} = 2.3$, from centreline ($\boldsymbol{y}/\boldsymbol{D} = 0$) to nozzle wall ($\boldsymbol{y}/\boldsymbol{D} = \pm 0.5$), and at the exit plane

3.3 Flow velocity field

The mean velocity data corresponding to the regions presented in Fig. 6 are presented in Fig. 12. The mean velocity results are presented in a colour contour which represents the velocity magnitude (red represents higher velocity and blue the lowest), whilst the vectors indicate the averaged flow direction.

A high-velocity region can be seen formed at $z/D > 0.3$ in Fig. 12a due to the jet injections' over-penetration, corresponding to the mean dye mixture fraction image in Fig. 6a. Also present within the same figure is a region of relatively low velocity preceding the high-velocity region. It is evident that the jets injections' over-penetration into the centre flow slows down the on-coming primary flow whilst the oncoming flow accelerates the injection streams. The adverse pressure gradient on the centreline acts like an obstruction to slow the oncoming primary flow. Figure 12b, meanwhile, shows a region of close to 0 velocity near $z/D = 0$ and a high-velocity flow stream downstream of this region, corresponding to the secondary flow seen in the dye mixture fraction diagrams. Examining the vectors in the blue region reveals the presence of a stagnation region and primary flow being deflected over and below the centreline. The flow deflection allows more contact for the primary flow fluid to mix with the injection fluid by shear and also causes a "shielding" effect which aided in the formation of the secondary stream as seen in Fig. 6b. Vectors in the negative direction seen in Fig. 12c, d correspond to the backflow region, and a region of low velocity can be seen at approximately $z/D = 0.1$ for both figures which indicates the impingement region. Despite the relatively higher momentum ratio in Fig. 12c as compared to Fig. 12b, lower downstream centreline velocity at locations $z/D > 0$ is observed in Fig. 12c. However, this trend does not persist in Fig. 12d as both upstream and downstream flow velocities increase corresponding to a relative increase in momentum ratio.

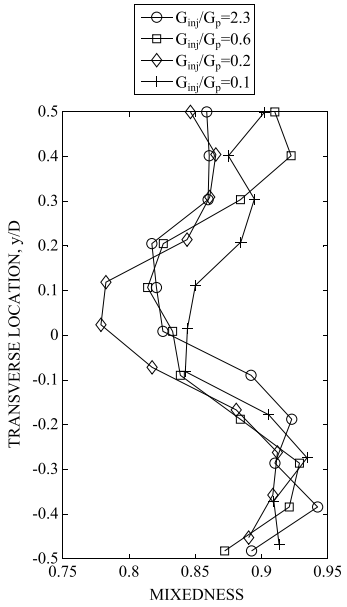

Fig. 11 Transverse mixedness for cases $G_{inj}/G_P = 0.1$; $G_{inj}/G_P = 0.2$; $G_{inj}/G_P = 0.6$; and $G_{inj}/G_P = 2.3$, from centreline ($y/D = 0$) to nozzle wall ($y/D = \pm 0.5$), and at the exit plane

The behaviour of the backflow being deflected from the impingement region can be observed from the vectors in Fig. 12c, d. Observing the backflow vectors in these figures shows that the edges of the backflow are sheared, on-average, by the on-coming primary flow which enhances mixing between both streams. Moving upstream to approximately $z/D = 0$ and $y/D = 0$ shows that the primary stream is recirculated into the backflow slightly upstream of the impingement region. Both Figs. 13 and 14 show the random instantaneous PIV vector field for case $G_{inj}/G_P = 2.3$ and $G_{inj}/G_P = 0.6$. As observed, the backflow captured in the mean velocity results is also observable in the instantaneous images. The flow trend in Fig. 13(i) followed by Fig. 13(ii) demonstrates what is known as the flow flapping which will be discussed in Sect. 3.6.

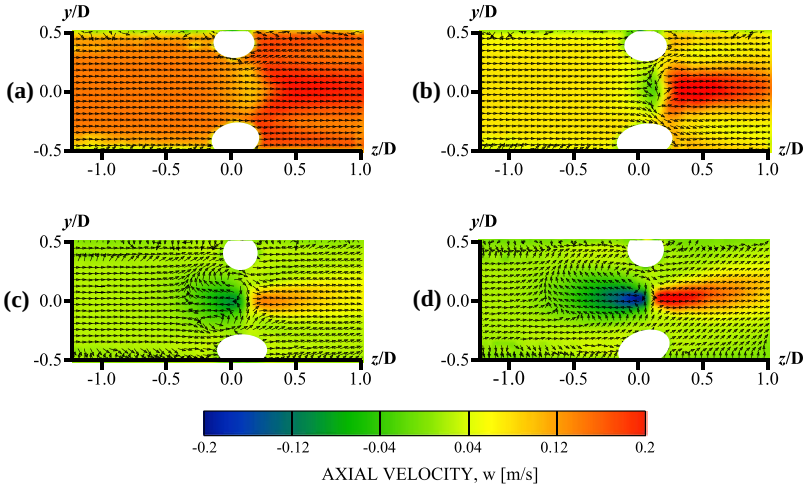

Fig. 12 Mean velocity magnitude contour and vectors in the axial plane for cases: **a** $G_{inj}/G_P = 0.1$; **b** $G_{inj}/G_P = 0.2$; **c** $G_{inj}/G_P = 0.6$; and **d** $G_{inj}/G_P = 2.3$

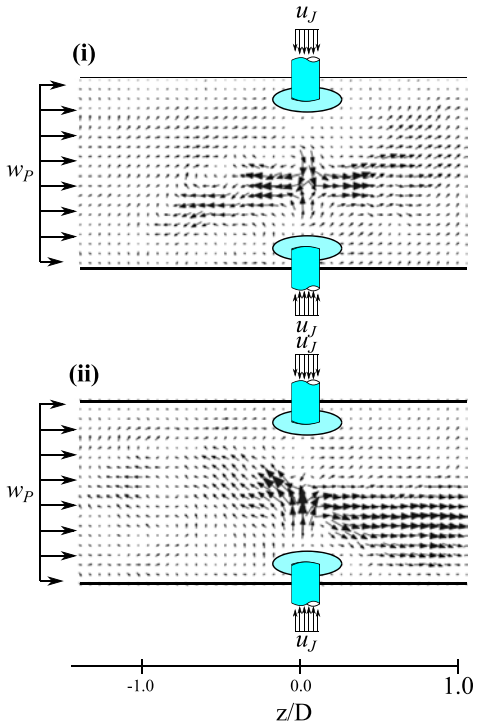

Fig. 13 Instantaneous PIV vector field for case $G_{inj}/G_P = 2.3$ for a local time **i** 0 s and **ii** 1.25 s overlaid on the nozzle schematics

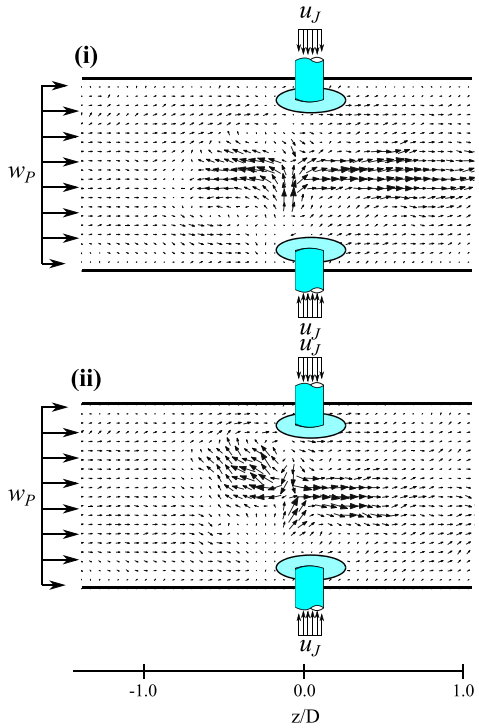

Fig. 14 Instantaneous PIV vector field for case $G_{inj}/G_P = 0.6$ for a local time **i** 0 s and **ii** 1.25 s overlaid on the nozzle schematics

Some anomalies are noticeable especially in Fig. 12d at which the vectors at locations $z/D < 0$ within the backflow region and downstream of the impingement at $z/D > 0$ are biased towards the positive y direction. The strong impingement of the side injection coupled with the flow flapping phenomenon amplifies the instabilities present in the flow any other instabilities caused by the slight misalignment of the injection jets (manufacturing defects). Some minor anomalies are also noticeable near the walls of the pipe and these errors are caused by the scattering of laser sheet by the Perspex and does not affect the results of this study.

The outlet flow radial profiles of the axial velocity corresponding to the change in momentum ratio are extracted from Fig. 12 to study the flow trends at the nozzle outlet and are presented in Fig. 15 (closed symbols with line) with their corresponding flow without injections (open symbols without line). Profile for the flow case $G_{inj}/G_P = 0.1$ shows a trough region of low-velocity flow between $y/D = \pm 0.2$ to $y/D = \pm 0.4$ with a maxima of 0.17 m/s at centreline. Profile for flow case $G_{inj}/G_P = 0.2$, meanwhile, shows a relatively higher peak (maxima) and shallow trough. The differences in these flow velocity profile relate a higher peak centreline velocity to the side injection impingement upstream. Figures 6 and 12 show flow cases $G_{inj}/G_P = 0.6$ and 2.3 to be in similar regime with a backflow; therefore, some similar velocity profile is expected. The trend of reducing peak velocity at the centreline with reducing primary velocity as witnessed for both case $G_{inj}/G_P = 0.1$ and case $G_{inj}/G_P = 0.2$ is not witnessed for case $G_{inj}/G_P = 0.6$ and $G_{inj}/G_P = 2.3$. Even though case $G_{inj}/G_P = 0.6$ has a relatively higher primary velocity than case $G_{inj}/G_P = 2.3$, a higher peak velocity is observed for case $G_{inj}/G_P = 2.3$ compared to case $G_{inj}/G_P = 0.6$. This trend goes to show that the backflow regime deviates strongly from and is categorically different from both the streaming and impingement flow modes. Besides, for the same mode, the velocity flow profile is similar to a core profile within the developed flow region. This figure demonstrates that the presence of the side injection modifies the "top-hat" profile present in most fully developed flow into different flow profiles corresponding to their respective flow modes.

The axial velocity root mean square profiles, RMS (U') at the centreline, for the different cases, are shown in Fig. 16. The unperturbed pipe section in the fully developed pipe flow is represented by the plateau observed upstream of the injectors at $z/D < 0$ in both cases $G_{inj}/G_P = 0.1$ and $G_{inj}/G_P = 0.2$. The backflow spotted in the previous figures for cases $G_{inj}/G_P = 0.6$ and $G_{inj}/G_P = 2.3$ is represented

by the positive slope gradient observed in the RMS plot at location $-1 < \boldsymbol{z}/\boldsymbol{D} < 0$. The location where the streams (injections) meet can be pinpointed by the local peaks in the RMS plot. The figure also shows a consistent increase in $\boldsymbol{U}'$ downstream of the jet injectors' location ($\boldsymbol{z}/\boldsymbol{D} > 0$) which also indicates that the placement of side injectors in the nozzle increases the turbulence intensity at the centreline of the primary flow. The increase in centreline turbulence intensity has consequences on the centreline mixing in the nozzle outflow.

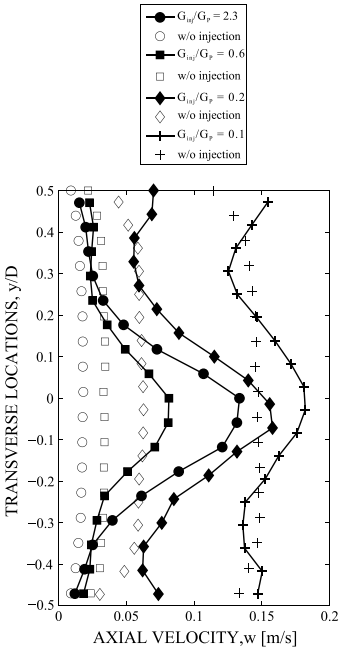

Fig. 15 Radial profile of the mean axial velocity for cases $\boldsymbol{G}_{\text{inj}}/\boldsymbol{G}_{\text{P}} = 0.1$; $\boldsymbol{G}_{\text{inj}}/\boldsymbol{G}_{\text{P}} = 0.2$; $\boldsymbol{G}_{\text{inj}}/\boldsymbol{G}_{\text{P}} = 0.6$; and $\boldsymbol{G}_{\text{inj}}/\boldsymbol{G}_{\text{P}} = 2.3$ with their respective flow profile without injection at the nozzle exit

3.4 Streaming mode

The streaming mode as mentioned in the previous sections has been well studied and documented (Leong et al. 1999; Holdemann et al. 1997). This mode is characterized by the individual jet injection streams that are convected downstream by the high-momentum primary flow rate. Application in practical combustion will give rise to separated streams of flame (Birzer et al. 2011).

Studies by Holdemann et al. (1997) have proposed a design equation for an optimum mixing

$$\boldsymbol{n} = \pi(\sqrt{2\boldsymbol{J}/\boldsymbol{C}}) \tag{4}$$

where $\boldsymbol{n}$ = the number of side injection, $\boldsymbol{J}$ = momentum-flux ratio, and $\boldsymbol{C}$ = constant which is proposed to be 2.5 for an "optimum mixing" condition. This equation, however, is geometrical dependant and is optimized for the geometry used in that particular study.

Applying the same calculation criteria to the current case of $\boldsymbol{G}_{\text{inj}}/\boldsymbol{G}_{\text{P}} = 0.1$ is equivalent to having $\boldsymbol{n} = 11$ or 11 side injection on the nozzle. Although the number of jets will most probably guarantee enhanced mixing between the streams, the shear amount of jets will make it impractical for high-fidelity measurements and reacting flow applications.

Besides, most of the conducted studies in the streaming mode involve injecting jets of fluid of relatively lower temperature into a high-temperature cross-flow or rich combustion product. No direct comparison can be made with the current study of impinging and backflow modes as these methods of flow mixing are adversely affected by the temperature and density gradient.

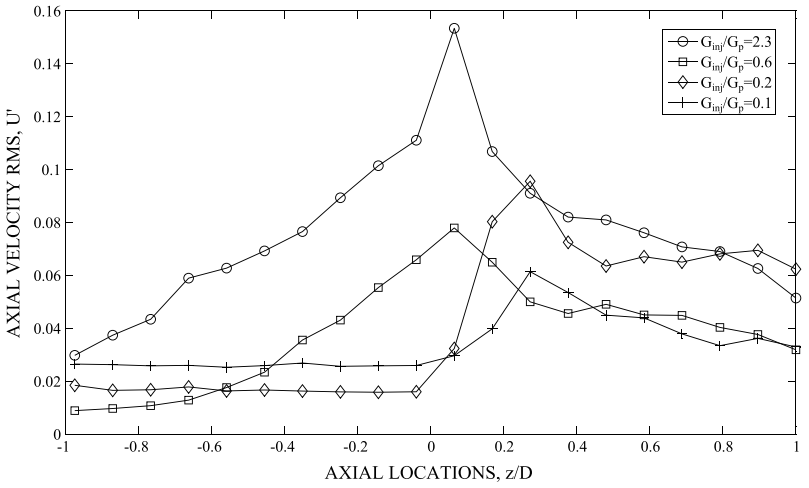

Fig. 16 Centreline velocity RMS for cases $\boldsymbol{G}_{\text{inj}}/\boldsymbol{G}_{\text{P}} = 0.1$; $\boldsymbol{G}_{\text{inj}}/\boldsymbol{G}_{\text{P}} = 0.2$; $\boldsymbol{G}_{\text{inj}}/\boldsymbol{G}_{\text{P}} = 0.6$; and $\boldsymbol{G}_{\text{inj}}/\boldsymbol{G}_{\text{P}} = 2.3$, from axial location of $\boldsymbol{z}/\boldsymbol{D} = -1$ to $\boldsymbol{z}/\boldsymbol{D} = 1$

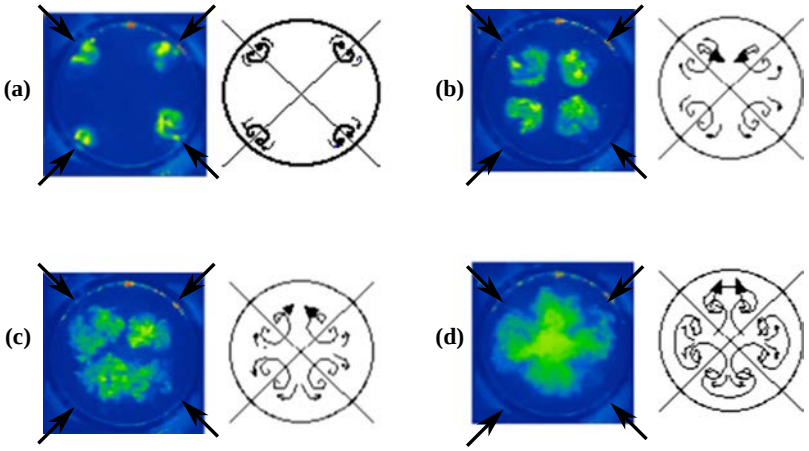

Fig. 17 Instantaneous cross-sectional PLIF image at location $\boldsymbol{z/D} = 0.5$ (*left*) for different flow conditions with increasing jet velocity and vortex flow schematics (*right*). The case flow parameters are converted as **a** $\boldsymbol{G}_{\text{inj}}/\boldsymbol{G}_{\text{P}} = 0.005$; **b** $\boldsymbol{G}_{\text{inj}}/\boldsymbol{G}_{\text{P}} = 0.04$; **c** $\boldsymbol{G}_{\text{inj}}/\boldsymbol{G}_{\text{P}} = 0.06$; and **d** $\boldsymbol{G}_{\text{inj}}/\boldsymbol{G}_{\text{P}} = 0.24$. *Black arrows* indicate the locations of the side-injection nozzles. Adapted from Birzer et al. (2011)

The current understanding of the flow characteristics of jets in cross-flow mixing suggests that the capacity of mixing in a streaming mode is reliant upon the induced vortical structures (for example, CVPs). The study into streaming flow mode by Birzer et al. (2011) provides a good understanding of the flow development in the primary nozzle.

Figure 17 shows various instantaneous PLIF images taken at location $\boldsymbol{z/D} = 0.5$ for experiments conducted in a nozzle of similar dimensions. A typical under-penetration case at location $\boldsymbol{z/D} = 0.5$ can be seen in Fig. 17a. Penetration to half radius distance $\boldsymbol{r}_{\text{P}}/2$ can be seen from Fig. 17b. The under-penetration cases are represented as the streaming mode in the current study. As observed in Fig. 17a, little interaction can be seen between vortices of different streams which are similar to separate jets in cross-flow mechanism albeit in a confined domain. Due to the lack of physical interaction between the individual streams, the mixing mechanism in this mode is reliant on the formation of shear vortices such as the CVPs.

The CVPs seen in Fig. 17a stay close to the wall due to influence of the vortex image in the wall Saffman (1979). At higher side injection momentum, the vortices form further from the wall that the CVPs are relatively less affected by the wall image and are acted upon more strongly by neighbouring CVPs which cause them to convect towards one another, as depicted by the accompanying schematics. Figure 17c, d shows over-penetration cases where the jets penetrate over $\boldsymbol{r}_{\text{P}}/2$ and towards the centre of the pipe. Axis switching of the vortices can be observed from the instantaneous images and more prominently from Fig. 17d which is manifested by the vortices forming new pairings as compared to the other figures. The figure also shows that the axis switching phenomena only takes place in cases with flow over-penetration where the CVPs form relatively further away from the pipe wall, so as to not be affected by the wall image. The axis switching phenomenon also improves the flow surface area of the streams and enhances mixing between streams.

The trajectory of the jets in a confined cross-flow can be scaled by momentum-flux ratio, $\boldsymbol{J}$, as proposed by the previous studies (Holdemann et al. 1997; Leong et al. 1999, 2000), and has been recorded for flows of the streaming mode. The characteristics of a jet trajectory in a streaming mode have not been used to characterize jets in the impinging mode.

3.5 Impinging mode

Increasing the jet momentum ratio relative to the cross-flow ratio will see the jets overcoming the primary flow momentum and impinge at the primary flow centreline close to the jet origins. The impingement of the jets generates turbulent structures which are transported downstream as evident from the increase in velocity RMS in the profile for $\boldsymbol{G}_{\text{inj}}/\boldsymbol{G}_{\text{P}} = 0.2$ in Fig. 16. The characteristics of this flow mode include a stagnation region near the origin ($\boldsymbol{z/D} = 0$). The comparison of the flow characteristics for this flow mode and that of the streaming mode reveals considerable differences between the two modes.

The stagnation region is formed as a product of jets impingement at the primary flow centreline, and the upstream deflection of the jets is convected downstream by the on-coming primary flow. The upstream jet deflection is sheared and mixed-in by the primary flow and forms a shielding effect which contributes to the formation of a secondary stream (downstream jet impingement deflection) as observed in the centreline downstream region ($0 < \boldsymbol{z/D} < 1.0$) in Figs. 6b and 12b. The secondary stream observed consists of relatively higher concentration and momentum jet fluid. The formation of such stream has consequences on the near-field outflow which will be the focus of a subsequent study. Despite the differences in the planar

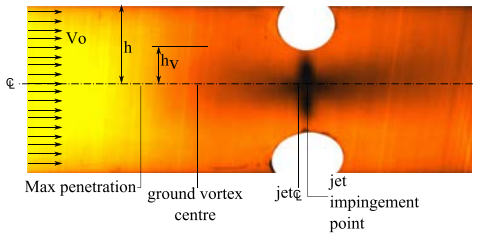

Fig. 18 Typical case of an oblique jet impinging on a flat plate

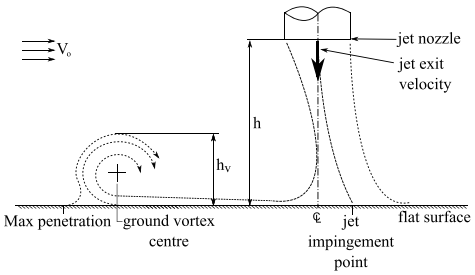

Fig. 19 Typical structural characteristics of a multi-lateral jet impingement in a confined cross-flow (backflow mode) case

flow characteristics observed, both impinging flow and the streaming flow modes display similar dye mixture fraction exit profile as can be observed from Fig. 7a, b.

3.6 Backflow mode

The flow enters the backflow mode when the jet impingement momentum overcomes the momentum of the oncoming flow. This class of flow has not been sufficiently documented and raises questions regarding its ability in promoting mixing in these type of flows. The flow structures observed in the current study is similar to those normally found in studies related to "oblique jets impingement on a flat plate" (Knowles and Bray 1993; Landreth and Adrian 1990; Goldstein and Behbahani 1982) albeit in a confined environment.

A comparison between an oblique jet impinging on a flat plate (Fig. 18) and case $\boldsymbol{G}_{\mathrm{inj}}/\boldsymbol{G}_{\mathrm{P}} = 2.3$ (Fig. 19) shows various similarities in the flow characteristics that can be distinguished which include: the location of the "vortex centre", max vortex penetration, jet centreline, and the jets impingement point. An important parameter in analysing measurements for this category of flow is the cross-flow velocity ratio, which is equivalent to $\boldsymbol{G}_{\mathrm{P}}/\boldsymbol{G}_{\mathrm{inj}}$ in the current study. In contrast, jet impingement on a plate does not take into account the complex dynamic flow vortex interactions of the impingements of four jets. Therefore, modifications to the scaling parameters are required to adapt it to the backflow mode of the current study. The study into "ground vortex" also found self-similarity laws applicable to quantify the location/position of the vortex. Due to the similarities between the backflow mode and that of the impinging jet study, it is also possible to quantify the length of the backflow on a self-similarity basis.

Despite the relatively large difference in momentum ratio between the two cases featured in the current study, relatively small differences can be seen in several flow trends, namely the backflow length, the centreline dye mixture fraction in Fig. 8, and the nozzle outlet velocity profile in Fig. 15. Therefore, it is deduced that large change in flow momentum ratio $\boldsymbol{G}_{\mathrm{inj}}/\boldsymbol{G}_{\mathrm{P}}$ is required in order to induce a small change in the flow characteristics in comparison with the other flow modes. Also, there are clear evidences that some primary flows are recirculated into the backflow and this encourages mixing in the nozzle by providing interactions between the two flow streams prior to being convected downstream.

The other phenomenon that is observed only in this flow mode is the existence of a flow oscillation. Observing the data collection in progress and visual inspection of the raw images ensemble indicates that both backflow and the secondary stream as a result of jets impingement oscillate at a random manner. Early observation shows that the backflow flapping frequency couples with that of the secondary stream in terms of frequency and flapping magnitude. Lateral jets misalignment has been ruled out as the cause of such flow flapping as a transient Reynolds Averaged Navier–Stokes (RANS) CFX model from the commercially available ANSYS Computational Fluid Dynamics (CFD) package (not shown) has captured similar flapping in cases of identical flow parameters. A more detailed study is underway to better understand this flapping phenomenon both experimentally and computationally and will be the focus of future publication.

Figures 13, 14, and 20 demonstrate the flow flapping phenomena in the backflow cases. In Fig. 20, the instantaneous PIV velocity vector field sequences selected at random are overlaid on instantaneous PLIF image to show the jet flow propagation after impingement. At $\boldsymbol{t} = 0$ s (top), the present velocity vectors indicate that the general backflow direction propagates diagonally downwards after impingement. At $\boldsymbol{t} = 1.25$ s, the velocity vectors indicate that the general backflow propagates diagonally upwards after impingement. This pattern can be observed throughout the ensemble and happens at a random manner.

The flapping mechanism encourages the impingement of the backflow onto the nozzle wall which creates favourable mixing structures. These structures are propagated a small distance upstream before being convected downstream by the primary flow. This phenomenon is deduced to be the

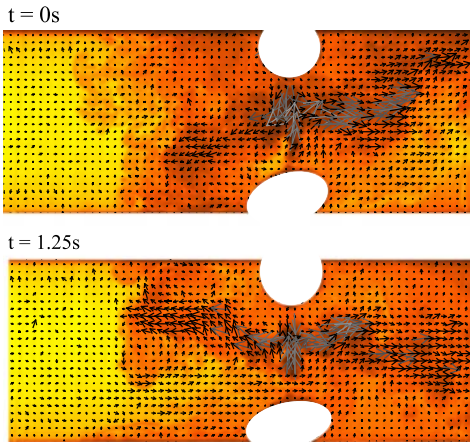

Fig. 20 Image sequence demonstrating the flapping motion in the flow. *Top* flow condition at time $\boldsymbol{t} = 0$ s; *bottom* flow condition at time $\boldsymbol{t} = 1.25$ s

contributing factor to the different exit profile as shown in Fig. 5c (rounded profile).

4 Summary and conclusions

The current study investigates the planar flow field and dye mixture fraction profile of multi-lateral jet in a round pipe flow with water as the working fluid. Experimental parameters such as jet to primary nozzle area ratio are kept constant, whilst primary flow velocity is varied relative to the jet flow. Scalar and flow fields are visualized and measured simultaneously using PLIF and PIV techniques, respectively.

Three different flow modes are identified: streaming flow mode; impinging flow mode; and backflow flow mode. Different flow characteristics are recorded and compared to previous studies on related flow phenomenon. The formation of different flow modes is found to have a large influence on the nozzle outflow conditions. Accordingly, the flow mode present has significant effects on the emerging flow field and is an important characterization of the mixing and turbulence in an emerging flow.

The streaming mode shows similarities with previous flow dilution studies; however, imminent differences are observed due to differences in geometric parameters and variances in measuring methods. Streaming flow mode is characterized by streams of jet fluid convected downstream by the primary jet and converging towards the primary flow centreline at a distance downstream (approximately $\boldsymbol{z}/\boldsymbol{D} = 1$). The streaming flow mode is also compared with the previous records (Birzer et al. 2011) in terms of primary outflow in a reacting flow condition. Unlike the impinging flow mode and backflow mode, streaming flow mode can also be found with variances in numbers of jets and momentum-flux ratio (Holdemann et al. 1997). Comparisons of the exit profiles for the streaming and impinging flow modes show observable similarities despite the differences of flow characteristics in the planar profile. The impinging flow mode can be characterized by lateral jets impinging close to the origin ($\boldsymbol{z}/\boldsymbol{D} = 0$). The flow impingement proceeds to form a stagnation region inside the nozzle, and the bulk of primary flow is convected around the central impingement region. The formation of a secondary flow can be observed downstream of the impingement region and is aided by the shielding effect induced by the stagnation region upstream. Incidentally, the secondary flow formation can also be found in the backflow mode. The backflow mode is similar to oblique jets impinging on a flat surface in terms of induced flow structures. The phenomenon that sets this flow mode apart is the existence of backflow and secondary flow stream flapping.

Scaling of the regimes with one common rule will be difficult. The results from the current study suggest that the different flow modes should be scaled differently due to the presence of different flow structures. Further study in this subject will most likely yield: a scaling law for the different flow modes; understanding of the structures formed due to jets impingement; and phenomenon behind backflow flapping and its consequences. The direction of this study will be extended to examine these flows under reacting conditions so as to investigate the consequences of multi-lateral jets in turbulent jet combustion.

Acknowledgments The help of Mr Marc Simpson, Thebarton Lab Manager, in assisting with the setting up of the experiment is gratefully acknowledged.

References

Beer JM (2000) Combustion technology developments in power generation in response to environmental challenges. Prog Energy Combust Sci 26:301–327

Birzer CH, Kelso RM, Dally BB (2011) Flame structure of jets in confined cross-flows. In: Proceedings of the Australian combustion symposium

Doerr TH, Blomeyer M, Hennecke DK (1997) Optimization of multiple jets mixing with a confined crossflow. J Eng Gas Turbines Power 119:315–321

Goldstein RJ, Behbahani AI (1982) Impingement of a circular jet with and without cross flow. Int J Heat Mass Transf 25(9):1377–1382

Gosman AD, Simitovic R (1986) An experimental study of confined jet mixing. Chem Eng Sci 41:1853–1871

Holdemann JD, Liscinsky DS, Dechsle VL, Samuelsen GS, Smith CE (1997) Mixing of multiple jets with a confined subsonic crossflow: Part I—cylindrical duct. J Eng Gas Turbines Power 119(4):852–862

Hoult DP, Weil JC (1972) Turbulent plume in a laminar cross flow. Atmos Environ 6:513–531

Kalt PAM, Nathan GJ (2007) Corrections to facilitate planar imaging of particle concentration in particle-laden flows using Mie scattering. Part 2: diverging laser sheets. Appl Opt 46(29):7227–7236

Kalt PAM, Long M (2014) Oma for Mac OS X. www.oma-x.org

Kalt PAM, Birzer CH, Nathan GJ (2007) Corrections to facilitate planar imaging of particle concentration of particle-laden flows using Mie scattering. Part 1: collimated laser sheets. Appl Opt 46:5823–5834

Knowles K, Bray D (1993) Ground vortex formed by impinging jets in crossflow. J Aircr 30(6):872–878

Kroll JT, Sowa WA, Samuelsen GS (2000) Optimization of orifice geometry for crossflow mixing in a cylindrical duct. J Propuls Power 16(6):929–938

Landreth CC, Adrian RJ (1990) Impingement of a low reynolds number turbulent circular jet onto a flat plate at normal incidence. Exp Fluids 9:74–84

Leong MY, Samuelsen GS, Holdeman JD (1999) Mixing of jet air with a fuel-rich, reacting crossflow. J Propuls Power 15(5):617–622

Leong MY, Samuelsen GS, Holdeman JD (2000) Optimization of jet mixing into a rich, reacting crossflow. J Propuls Power 16(5):729–735

Liu RH, Stremler MA, Sharp KV, Olsen MG, Santiago JG, Adrian RJ, Aref H, Beebe DJ (2000) Passive mixing in a three-dimensional serpentine microchannel. J Microelectromech Syst 9:190–197

Nathan GJ, Kalt PAM, Alwahabi ZT, Dally B, Medwell P, Chan Q (2012) Recent advances in the measurement of strongly radiating, turbulent reacting flows. Prog Energy Combust Sci 38:41–61

Nguyen NT, Wu Z (2005) Micromixers—a review. J Micromech Microeng 15(2):R1–R16

Pitsch H, Steiner H (2000) Scalar mixing and dissipation rate in large eddy simulation of non premixed turbulent combustion. Proc Combust Inst 28:41–49

Saffman PG (1979) The approach of a vortex pair to a plane surface in inviscid fluid. J Fluid Mech 92(3):497–503

Shan JW, Lang DB, Dimotakis PE (2004) Scalar concentration measurements in liquid-phase flows with pulsed lasers. Exp Fluids 36:268–273

Sowa WA, Kroll JT, Samuelsen GS, Holdeman JD (1994) Optimisation of orifice geometry for crossflow mixing in a cylindrical duct. In: 32nd Aerospace Sciences Meeting and Exhibit

Tsunoda H, Saruta M (2002) PLIF study on the diffusion field of a passive scalar in a round jet issuing into a uniform counter-flow. In: Rodi W, Fueyo N (eds) Engineering turbulence modelling and experiments, vol 5. Elsevier, pp 505–514

Chapter 4

Effects of multilateral jets on the near flow field

4.1 Overview

Chapter 3 discussed the effects of varying momentum ratios of side-jets to primary flow on the mixing field and flow regimes. The different flow regimes discussed there have implications on the mixing field within the confinement. However, the implications of the changes upstream of the nozzle exit on the near flow field is not known.

A previous study shows that placing opposing jets at the nozzle exit has drastic effects on the near flow field [60]. The results are compared, in this chapter, to the 4 side-jets configuration used in the current study. Despite the differences in nozzle configurations and experimental set up, resemblances in the near flow field can be observed.

Simultaneous PIV and PLIF studies are conducted to study the effects that varying MR of jets to cross-flow have on the near flow field (Objective (ii)), up to $3D_P$ downstream.

Here, increasing the MR has the following effects in the near-field:

- Increased frequency and reduces coherence of large-scale structures;
- Increased spread of the exiting jet;
- Increased velocity decay rate and turbulence intensity.

Furthermore, it was also found that the changes in MR upstream has prominent effects in the near flow field up to $2D_P$ downstream, while the flow beyond $2D_P$ exhibits similar behaviour.

The findings from this particular research are published in a paper, in the journal of *Experimental Thermal and Fluid Sciences*, volume 81 (in 2017) and is titled “An experimental study on the near flow field of a round jet affected by upstream multi-lateral side-jet", authored by Chia X. Thong, Bassam B. Dally, Cristian H. Birzer, Peter A.M. Kalt and Eyad R Hassan.

4.2 Manuscript

Statement of Authorship

Title of Paper	An Experimental Study on the Near Flow Field of a Round Jet Affected by Upstream Multi-lateral side-jet
Publication Status	☑ Published ☐ Accepted for Publication ☐ Submitted for Publication ☐ Unpublished and Unsubmitted work written in manuscript style
Publication Details	Thong, C.X., Dally, B.B., Birzer, C.H., Kalt, P.A.M., and Hassan, E.R. 2017, 'An experimental study on the near flow field of a round jet affected by upstream multi-lateral side-jet', *Experimental Thermal and Fluid Science*, vol 82, p198-p211

Principal Author

Name of Principal Author (Candidate)	CHIA XIONG THONG
Contribution to the Paper	Perform literature review, set up and conduct experiments in the water tunnel, collect PIV and PLIF data, performed data processing, structure and write manuscript, and the corresponding author for the paper
Overall percentage (%)	65
Certification:	This paper reports on original research I conducted during the period of my Higher Degree by Research candidature and is not subject to any obligations or contractual agreements with a third party that would constrain its inclusion in this thesis. I am the primary author of this paper.
Signature	Date 15/12/2016

Co-Author Contributions

By signing the Statement of Authorship, each author certifies that:

i. the candidate's stated contribution to the publication is accurate (as detailed above);

ii. permission is granted for the candidate in include the publication in the thesis; and

iii. the sum of all co-author contributions is equal to 100% less the candidate's stated contribution.

Name of Co-Author	BASSAM DALLY
Contribution to the Paper	Supervise development of work, interpret data, and edit manuscript
Signature	Date 16-12-16

Name of Co-Author	CRISTIAN BIRZER
Contribution to the Paper	Supervise experimental work, interpret data, and edit manuscript
Signature	Date 15 DEC 16

Name of Co-Author	PETER KALT		
Contribution to the Paper	Supervise and mentor experimental work, assist in data processing and interpret data, and edit manuscript		
Signature		Date	

Name of Co-Author	EYAD HASSAN		
Contribution to the Paper	Interpreting data, and editing manuscript		
Signature		Date	9/1/17

Please cut and paste additional co-author panels here as required.

Experimental Thermal and Fluid Science 82 (2017) 198–211

Contents lists available at ScienceDirect

Experimental Thermal and Fluid Science

journal homepage: www.elsevier.com/locate/etfs

An experimental study on the near flow field of a round jet affected by upstream multi-lateral side-jet

Chia X. Thong *, Bassam B. Dally, Cristian H. Birzer, Peter A.M. Kalt, Eyad R. Hassan

School of Mechanical Engineering, The University of Adelaide, SA 5005, Australia

ARTICLE INFO

Article history:
Received 30 June 2016
Received in revised form 10 November 2016
Accepted 10 November 2016
Available online 19 November 2016

Keywords:
Jets in confined cross-flow
Mixing
Turbulent jet flow
Multilateral jet

ABSTRACT

The application of lateral jets into a confined flow in industry is a common method for mixing of reagents. However, there is limited understanding of the fundamentals surrounding the flow structures, flow evolution and their respective effects on a downstream outflow of a round jet nozzle when there are multiple jets inside the nozzle. To address this, an experimental study of the near-field outflow of a turbulent round water jet affected by multiple side-jet injected laterally into the round flow upstream of the nozzle exit has been conducted. Planar Laser Induced Fluorescence and Particles Image Velocimetry were used to investigate the fluid mixing and velocity in the near-field, respectively. The influence of jet to cross-flow momentum ratio on flow characteristics; including mixing and turbulence intensity, were assessed by varying the primary jet and side injection flow rates. Results indicated that side injection has major effects on the resulting near-field region flow. Flow cases with side-jets show an increase in shear layer roll-ups and spread. Velocity decay rates and turbulence intensity within the jet core increase with increasing jet to cross-flow momentum ratio. However, these effects extend only to the near-field region, as no significant perturbations beyond two primary jet diameters downstream are observed. This indicates that the side injection has significant effect on the flow and mixing in the near-field region, but minor influences further downstream.

1. Introduction

Jets in cross-flow (JICF) have been used in various industrial applications, such as gas-turbine combustion chambers, stage combustors operating on the Rich Burn/Quick Quench/Lean Burn (RQL) mode, and reagents mixing. An everyday example of JICF can be seen in the dispersion of fumes from chimneys. The mixing and evolution of flow from a jet with a cross-flow has been subjected to many studies which are well documented in the literature [1–4]. However, in many industrial applications, JICF is often used in a confined environment. Fundamentally, JICF and jets in confined cross-flow (JICCF) are similar, however, the jets trajectories [5] and vortices [6] may be affected by the shape of the confinement and any opposing jets that may exist. Many studies undertaken to study JICF trajectories [7], flow-fields [1], and vortices are done in an unconfined environment, which negate the effects of parameters such as opposing jets and boundary layers [2]. However, there are limited available studies on JICCF, in particular on cases involving small aspect ratio JICCF (ratio of primary diameter to jet, $(D_P/D_{inj}) \leq 10$). In addition, whilst the vortical evolution for JICF flow cases are well studied and documented, little data can be found on jet evolution, development and vortical spreading in confined round jet flows.

One aspect of JICCF that has been recently investigated is flow regime scaling. Multiple jets injected into a confined round flow can be scaled with respect to the momentum ratio (MR) of jet to cross-flow [8], as expressed in the equation

$$\frac{G_{inj}}{G_P} = \frac{(\rho V^2 A)_{inj}}{(\rho V^2 A)_P} \quad (1)$$

where subscripts *inj* and *P* denote the injection flow and primary flow, respectively; ρ denotes the fluid density [kg m^{-3}]; and A denotes the hydraulic area [m^2]. Using Eq. (1), flows can be categorized into three regimes: streaming flow regime; impinging flow regime; and backflow regime [9].

JICF have also been investigated as a mean to control turbulent jets [10,11]. By placing side-jets near the nozzle exit (both laterally and at an angle), it has been demonstrated that the properties of the exiting turbulent jet can be manipulated, in particular, the potential core length and flow exit profile. They have also suggested that the increase in flow turbulence results in an increase in ambient fluid entrainment into the jet. However, the influence

* Corresponding author.
E-mail address: chia.thong@adelaide.edu.au (C.X. Thong).

http://dx.doi.org/10.1016/j.expthermflusci.2016.11.008
0894-1777/

of JICCF placed a short distance upstream of the nozzle exit on the outflow is less well understood. Part of the current work is to assess if placing the JICCF a short distance upstream of a nozzle exit will result in an increase in entrainment of fluid at the nozzle exit due to the hypothesized increase of turbulence in the flow. If such an increase in entrainment is possible, then there may be potential in using such method for turbulent jet flames stabilization, which is an additional aspect of the current study.

The efficacy of JICF in mixing is attributed to the induced vortices in the flow, which include Counter-rotating Vortex Pairs (CVPs), horse-shoe vortices, and other shear induced vortices [4]. New and Tay [10] has previously demonstrated the flow structures that can be generated by injecting single and opposing jets into a round flow. This study is conducted on an orifice flow with two side jets. However, the flow properties from both an orifice and smooth-contraction differs from that of a long-pipe [12], which is required for the current study. Furthermore, the effect of four side-jets is expected to differ from the two side-jets [13].

The application of the current study will ultimately be for the purpose of fuel-air mixing in turbulent jet flames. Current reactants mixing methods can be sub-categorized into passive and active mixing methods. While passive reactants mixing has been utilized extensively in the industry, it has limitations in adapting to different fuel blends and operating conditions. Active reactants mixing allows more flexibility with control, but are typically more expensive and complex. It is proposed that a JICCF method be used as an active mixing method, which can be more cost effective and simpler than other active methods available.

In terms of combustion systems, JICCF has been used extensively for hot fume quenching in combustion chambers. For example, JICCF has been adopted for use within the RQL burner systems as a solution for quick quenching of hot combustion product [14]. Cooler air is injected into hot combustion product via lateral jets to rapidly reduce the temperature of fumes. The development of RQL burners [15,14,16] have indirectly contributed to JICCF studies, in particular on the matter of enhanced mixing between lateral jets and confined cross-flows. There are no parameters which defines "enhanced mixing" and that the definition varies on a case-by-case basis [15]. Despite the exhaustive studies related to RQL, not much data can be synthesized to illustrate the mixing effect that JICCF has on reactants mixing for turbulent jet flames.

The current study investigates the influence of mixing from multiple side-jet injection into a symmetrical configuration upstream of the round nozzle exit on the near-field of the jet outflow. This study can also be viewed as the build-up on the results of a previous study [10] by assessing a four side-jets flow case, placed upstream of a long-pipe (LP) nozzle. The specific focus of this study is to better understand how side-jets and primary flow rates, therefore momentum ratio, influence the flow fields in the near-field outflow of the perturbed round LP flow.

2. Methodology

Particle Image Velocimetry (PIV) and Planar Laser Induced Fluorescence (PLIF) techniques were used simultaneously during the experiments. The experiments were conducted in a closed loop water tunnel with working section measuring 500 mm × 500 mm × 1800 mm. The tunnel walls are made from acrylic to enable optical access for laser-based and visual measurement techniques.

The experimental nozzle is constructed from a one meter long clear acrylic central pipe with nominal diameter (D_P) of 56 mm and with four clear acrylic, radially orientated side-jets, placed equi-distant at one primary diameter ($1D_P$) upstream of the nozzle exit. The side-jets each measure 150 mm long with nominal diameter of 6 mm. The one meter long pipe is equivalent to approximately 16 central diameters in length and is connected to the flow source via a smooth diverging nozzle. The flow is conditioned far upstream with a honeycomb section to provide a developed and predictable pipe flow. Despite the relatively short development length, the velocity and concentration profiles at the nozzle exit show an almost uniform profile and a top hat profile (as seen in Fig. 11), respectively.

Fig. 1 shows the schematic diagram to the four side-jets configuration used for the current study. As indicated by the section A-A in the figure, the nozzle was rotated 45 deg to its longitudinal axis simply to fit within the water tunnel.

Fluid for the primary and side-jets flow were sourced from two separate 400 L capacity reservoirs, both seeded with Dantec Dynamics PSP-50 Polyamide Seeding Particles for PIV data collection. One reservoir was dyed with aqueous Rhodamine 6G fluorescent dye for PLIF collection. The dye was chosen as its peak absorption is at approximately 530 nm [17], which is closed to the emitted wavelength of the available frequency-doubled Nd:YAG lasers, whilst the emission of the dye is in the visible range of approximately 560 nm. The dye mixture was produced by premixing 0.1grams of Rhodamine 6G solids into 400 L of clean water.

Light was sourced from a Quantel Brilliant B Nd:YAG laser, frequency doubled to 532 nm and pulsed at 10 Hz. The laser light sheet was formed using an optics train (combination of plano convex spherical lens of *focal length* 100 mm; a bi-concave spherical lens of *focal length* −50 mm; and a cylindrical plano concave lens of *focal length* −25 mm) to form a laser sheet of approximately 2 mm thick. A silvered mirror (reflectance ⩾ 97.5%) was placed downstream of the sheet forming optic to reflect the laser sheet to illuminate the region of interest. The nozzle and the light sheet were aligned such that the sheet was incident on the nozzle centreline, illuminating the region of interest (ROI).

Two Princeton Instruments CCD Megaplus II ES4020 camera units were used for image collection. Each of the CCDs feature 2048 pixels × 2048 pixels arrays and were triggered by a Berkeley Nucleonics Corporation (BNC) 565 Delay Generator at a duty cycle of 2.5 Hz. The overall physical imaging region is approximated to be 200 mm × 200 mm, which translates to a spatial resolution of approximately 10.2 pixels/mm. Both CCDs were fitted with Tamron lens sets of 50 mm with $f1/4D$. The CCD for PLIF collection was fitted with an Orange Glass (OG) filter to exclude elastic scattering from PIV particles at 532 nm wavelength. EPIX XCAP 3.8 software and suitable frame grabbers were used for image acquisition and for camera shutter control.

To collect cross-plane data, the sheet forming optic was rotated by 90 deg and the silvered mirror was moved to align the formed laser sheet with the ROI. An additional mirror was placed far downstream of the nozzle exit in the water tunnel, so not to disrupt the bulk of the jet outflow, and angled at 45 deg to allow imaging (access) into the pipe. Only PLIF data was collected for this region.

A Fischer and Porter rotameter tube FP-1-27-G-10 with float 1-GNSVGT-68 was used to monitor the primary flow and a FP-3/4-21-G-10 with float 3/4-GUSVT-510 was used for the side-jets' flow. The side-jets' rotameter was connected to a distribution manifold downstream that, ideally, distributes the flow equally to the side-jets via four flexible tubes of equal length. The flow conditions for the current study are as detailed in Table 1.

Primary flow and side-jets' injection flow are manipulated to achieve the differences in the flow momentum ratio (MR). The total bulk flow is not conserved for most cases, however is conserved for flow case MR = 0.03; MR = 0.08; and MR = 0.15.

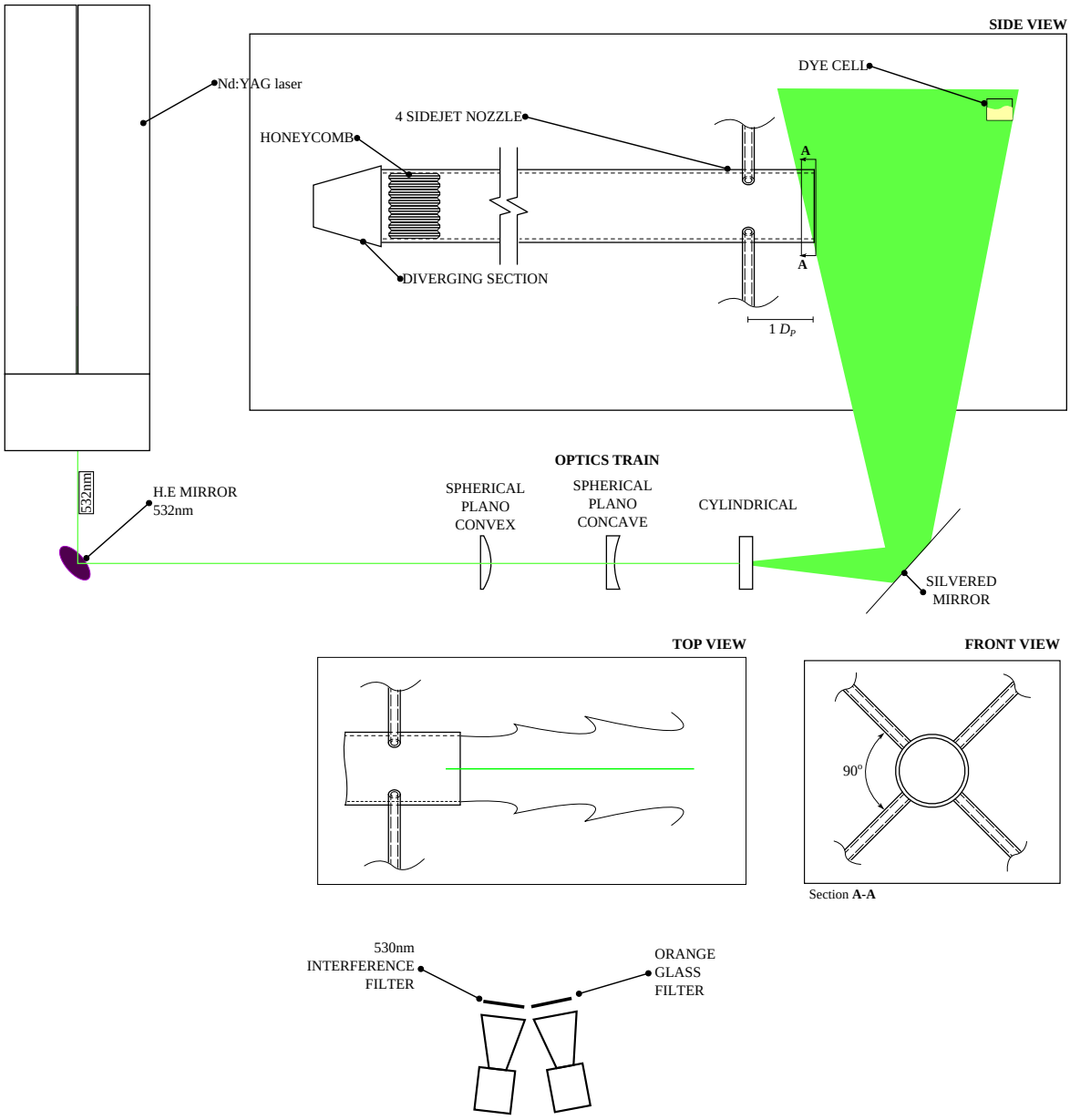

Fig. 1. Schematic diagram of the experimental set up.

Table 1
Experimental flow parameters.

Momentum ratio, G_{inj}/G_P (MR)	0.03	0.04	0.08	0.1	0.15	0.2
Primary flow rate, $Q_P[\times 10^{-4}$ m^3/s]	2.12	2.85	2.04	2.85	1.95	2.04
Injection flow rate, $Q_{inj}[\times 10^{-6}$ m^3/s]	3.99	5.99	5.99	9.97	7.99	9.97
Primary Reynolds number	4800	6500	4600	6500	4420	4600
Injection Reynolds number	840	1269	1269	2115	1680	2115
Primary velocity, V_P [m/s]	0.08	0.11	0.08	0.11	0.08	0.08
Injection velocity, V_{inj} [m/s]	0.14	0.21	0.21	0.35	0.28	0.35
Bulk velocity, V_b [m/s]	0.09	0.13	0.09	0.13	0.09	0.10

2.1. Velocity and passive scalar measurement

The PIV image ensembles were batch processed on PIVView 2.3C. A single-pass, standard Fast Fourier Transform was used to process the PIV images to obtain raw vector field data. The 2D cross-correlation was calculated for a 32 pixels × 32 pixels interrogation window with 50% overlap. The PIV vector data files were imported into freeware, OMA-X [18] for further post processing and analysis.

The measurement of the dye mixture concentration was conducted using the PLIF technique. The mean mixture fraction was obtained through ensemble average of over 200 images, which correlates to the number of image pairs collected for PIV. The imaged PLIF signal intensity, under ideal conditions, is linearly proportional to the concentration of the Rhodamine 6G in water, which renders the region with the highest dye concentration the brightest [19].

2.2. Image processing

The PLIF image ensembles were processed in OMA-X [18] for background removal; laser sheet profiling; and sheet divergence and response correction, in-line with methods highlighted in [20,21]. A dye tube was placed within the imaging region (as shown in Fig. 2(a)) to assess and acquire the virtual origin of the laser plane, and to acquire the response profile of the laser sheet (Fig. 2(c) accompanied by an approximately Gaussian profile plot of the beam). The laser divergence shown in Fig. 2(b) is acquired, corresponding to the virtual origin of the laser sheet. Fig. 2(d)(i) and (d)(ii) show the uncorrected ensemble mean and variance for the dye profile of a round jet with no side injection. Also shown is the variance profile (Fig. 2(d)(iii)) plotted at the marked line indicated in Fig. 2(d)(ii). As observed in Fig. 2(d), the dye profile displays eccentricities caused by the non-uniform laser sheet profile; divergence of the laser sheet; and absorption of the laser beam through the dye.

The mean profile in Fig. 2(d)(i) is first corrected for the sheet divergence and response (Fig. 2(b) and (c), respectively). The absorption for the laser is corrected by iterating the transmittance constant (C_K) value to compensate for signal loss due to absorption, until symmetry in the flow is achieved (similar to Fig. 2(f)(i)) and the loss in signal is compensated. An instance of the transmittance corresponding to the iterated C_K can be seen in Fig. 2(c). The correction algorithm, which consisted of divergence, transmittance and response correction is implemented on the instantaneous images in the ensemble, and the mean and image variance sets are acquired (as shown in Fig. 2(f)(i) and (f)(ii)). Comparing the variance image and profile for the uncorrected data (shown in Fig. 2(d)(ii) and (d)(iii), respectively) shows that the resolved variance is improved (with bias removed) and appears consistent to that of a symmetrical round jet.

The correction algorithm applied for the symmetrical flow in Fig. 2 is applied to the instantaneous images in the ensemble for the test cases. Fig. 2(g) shows a typical flow case with side-jets, which clearly shows eccentricities in the profile. A corresponding corrected image is shown in Fig. 2(h).

2.3. Calibration, errors and uncertainties

The PLIF images were calibrated with the unmixed dye solution (100% dye mixture concentration). The PLIF images were normalized by the calibration image from the dye cell (an acrylic cell with undiluted dye solution) on a shot-to-shot basis. The method for correcting PLIF images are detailed in Section 2.2.

The PIV spatial resolution is calibrated with a 2 mm × 2 mm grid and shows a spatial resolution of approximately 10.2 pixels/mm. The spatial resolution varies slightly between 10.2 pixels/mm to 10.5 pixels/mm depending on the flow cases due to camera lens refocusing and repositioning.

Acrylic deformities, imperfections, bubbles and other deformities can cast lines into the ROI consistently throughout the ensemble, which give rise to systematic errors. These were corrected through response correction methods during image processing. Some locations in the ROI show physical obstruction by the side-jets, which lie in the line of sight between the imaged area and the detectors. These obscured regions are masked out of the final data during post processing.

Using various measuring equipment such as rotameters and calibration grids for PIV brings rise to the issue of tolerances and uncertainties. The errors contributed by the rotameter tubes are measured to be $\pm 2\%$ of the maximum flow, whilst errors contributed by the calibration grids for PIV are estimated to be ± 0.05 mm. Measurements were repeated and averaged to obtained final values.

Ensemble sizes of 200 images provided a compromise between reliable results and available run time. Owing to the high flow rate of the primary flow and finite size of the reservoir, a longer run time depletes the reservoir fluid. To evaluate the statistical and qualitative convergence, different ensemble sets with increasing number of images were acquired and evaluated. The valuated statistics show that approximately 120 image pairs for PIV are required to achieve a confidence level of 99% (based on images average) whilst approximately more than 70 PLIF images are required to achieve a confidence level of above 95% (based on images average), both which were deemed sufficient for the current study.

3. Results and discussion

3.1. Initial flow condition and topology

Fig. 3 shows the evolution of multiple JICCF induced profiles within the flow development region (region inside the LP nozzle) for different jet injection to primary flow momentum ratios (MR). The dye mixture fraction images are acquired by injecting dye through the side injection into a primary cross-flow of clean water. The images are ensemble averaged from 200 instantaneous images. The dye concentration [mg/L] in each individual image is normalized to the concentration of a dye cell of unmixed dye within the same imaging frame in order to account for laser energy fluctuations on a shot-to-shot basis. Fig. 3(a), (b), (c) and (d) show the dye mixture fraction for the flow cases: MR = 0.04, MR = 0.08, MR = 0.1, and MR = 0.2, respectively. The dye mixture fraction are compiled for every subsequent $0.25D_P$ upstream of the nozzle exit (denoted as $z/D_P = 0$) up to $z/D_P = -0.75$ (side-jets located at $z/D_P = -1$). Each of the sub-figures are overlaid with a schematic diagram indicating the side-jets nozzles placement at $z/D_P = -1$ with respect to the induced flow profiles. The dye mixture fraction intensities for Fig. 3(a), (b), (c) and (d) are scaled to 0.5 to allow for better visual inspection. Note that the primary flow Reynolds number for flow cases MR = 0.04 and MR = 0.1 is 6500, and for flow cases MR = 0.08 and MR = 0.2 is 4600, and that these flows are within similar transitional turbulence regime. Furthermore, the flow features discussed here are not sensitive to the difference in primary flow Reynolds number and are dependent on the momentum ratio as discussed further on.

Fig. 3(a) shows the dye mixture fraction profile for the mean flow evolution inside the primary pipe, for the flow case MR = 0.04. The formation of kidney-like dye profiles and their progression downstream are clearly captured by the mean images. Progressing downstream to the nozzle exit at $z/D_P = 0$, the induced

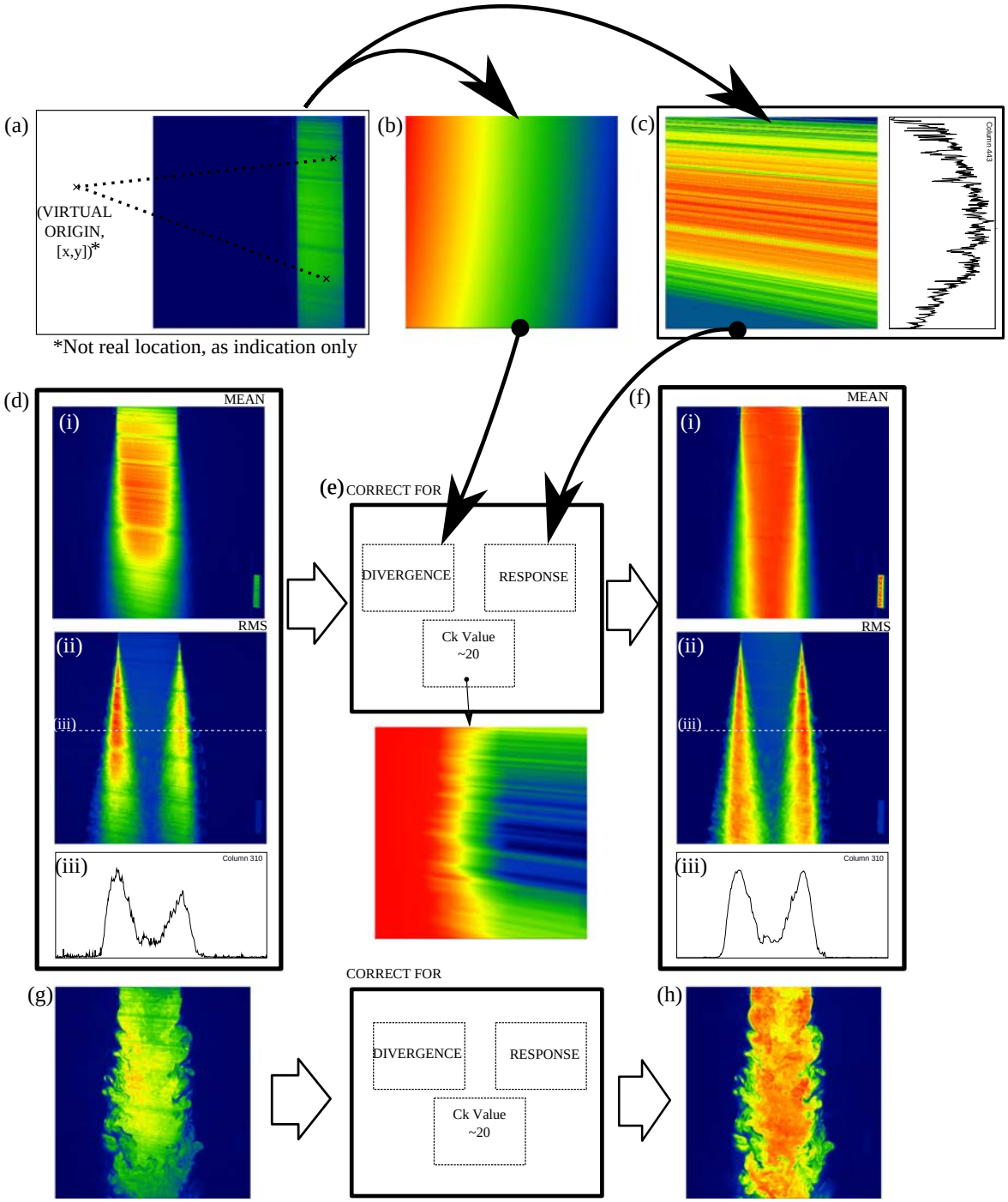

Fig. 2. Infographic on the PLIF image processing method adopted for the tested cases. (a) shows the uniform dye tube in the imaging region with the position of virtual origin indicated (not true location); (b) divergence profile; (c) response profile; (d) mean dye image, mean dye variance image, and variance for uncorrected dye images; (e) parameters that are corrected for a typical example of transmittance; (f) corrected mean dye image, mean dye variance image, and variance profile; (g) typical uncorrected instantaneous dye image; and (h) typical corrected instantaneous image.

kidney profiles remain separated from the neighboring profiles, although the mixture fraction of the profiles are observed to decrease as it progresses downstream, which indicates the mixing between the side-jets streams and the primary flow. Increasing the MR from 0.04 to 0.08 shows that the side-jets penetrate deeper into the primary flow, approaching the flow centreline (Fig. 3(b)), which eventually lead to the side-jets interacting as observed in $z/D_P = -0.5$.

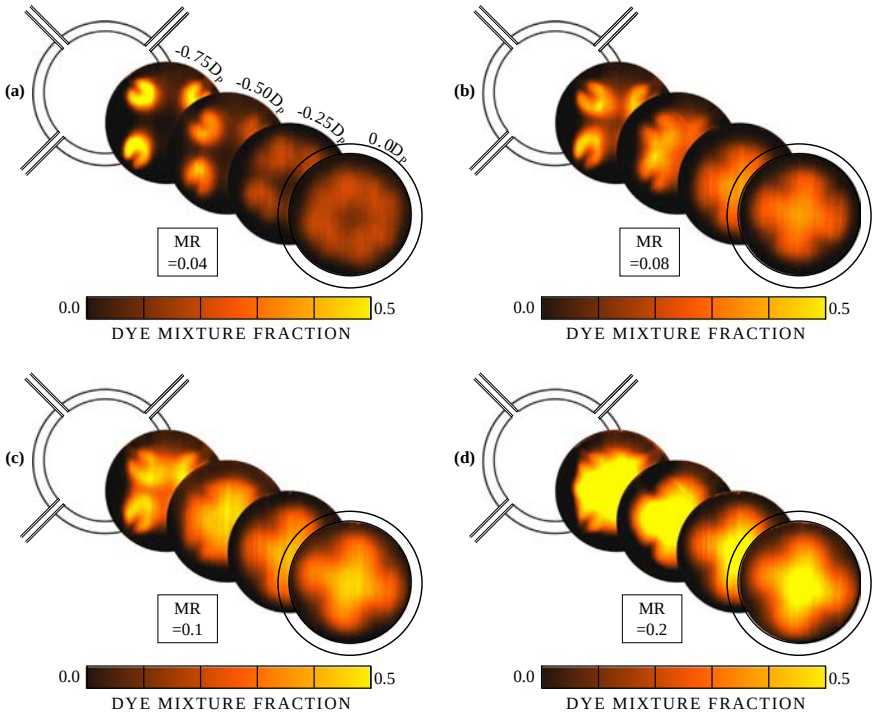

Fig. 3. Mean dye mixture fraction for multilateral jet injected into a round flow for momentum ratio: (a) MR = 0.04; (b) MR = 0.08; (c) MR = 0.1; and (d) MR = 0.2.

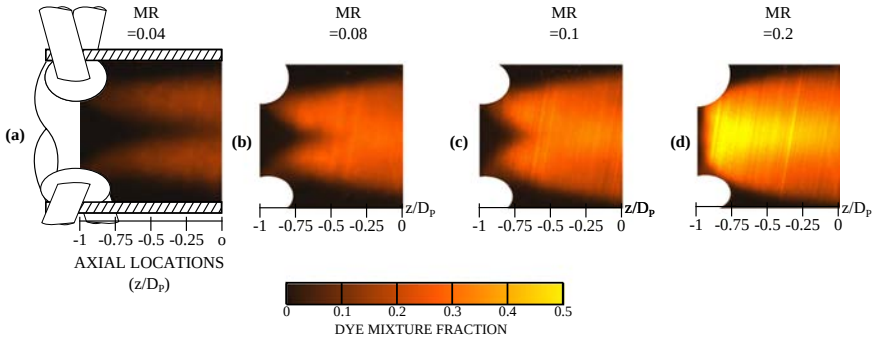

Fig. 4. Mean dye mixture fraction of the axial plane in the flow development region inside the nozzle for flow cases: (a) MR = 0.04; (b) MR = 0.08; (c) MR = 0.1; and MR = 0.2 [8].

The evolution of the four kidney-like dye profiles to a single cruciform profile is shown in Fig. 3(b) at $z/D_P = -0.25$. The discussion pertaining this change in dye profile is discussed further in Section 3.2. Likewise, increasing the MR from 0.08 to 0.1 increases the side-jets' penetration depth at $z/D_P = -0.75$ in Fig. 3(c). Both the dye profile and dye mixture fraction remain similar downstream at $z/D_P = -0.25$ and at $z/D_P = 0$.

Increasing the MR to 0.2 results in the impinging of the side-jets at the primary flow centreline. The dye mixture fraction image in $z/D_P = -0.75$ in Fig. 3(d) shows the mean flow structures immediately after the side-jets impinge. Little deviation in the dye mixture fraction profiles can be observed from $z/D_P = -0.5$ to $z/D_P = 0$. The flow profiles after impingement resembles a cruciform profile, which is not expected for this flow case where the side-jets impinge at a relatively higher momentum ratio.

Furthermore, cases which exhibit side-jets streams interaction, i.e. flow cases MR = 0.08; 0.1; and 0.2, display cruciform dye profiles at the nozzle exit ($z/D_P = 0$). This indicates that similar flow profile will be generated as long as the side-jets penetrate the flow centreline, be it in the impinging or streaming flow regime.

Fig. 4 shows the mean dye mixture fraction for the axial plane, recorded from the side-jets ($z/D_P = -1$) to the nozzle exit ($z/D_P = 0$). Schematic diagram of the nozzle configuration is overlaid on Fig. 4(a) to illustrate the side-jets' nozzle location relative to the imaging plane. The dye mixture fraction intensity is scaled to 0.5 for all cases, represented by the accompanying color bar, to

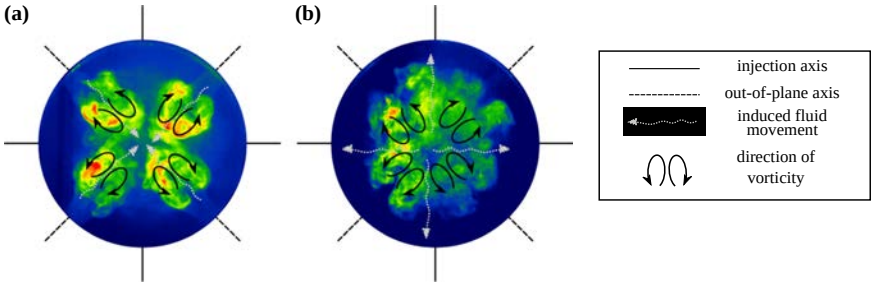

Fig. 5. Typical instantaneous PLIF images at (a)$z/D_P = -0.75$ and (b)$z/D_P = -0.5$ for flow case MR = 0.08. Black solid arrows indicate the direction of rotation of CVPs and white dashed arrows show the direction of induced fluid movement.

enhance visual representation of the figure. The direction of the primary flow is from the left to the right of the figures.

Weak dye mixture fraction is observed in Fig. 4(a) for flow case MR = 0.04 as there are only small quantities of side-jet fluid in the measured plane. This is caused by the side-jets' induced vortices' weak viscous interaction with the neighboring vortices. This can be further observed in Fig. 3(a). Higher dye mixture fraction intensity can be observed in Fig. 4(b) and (c) as a result of side-jets streams penetrating the primary flow centreline at approximately $z/D_P = -0.5$. Noteworthy is the central streak of relatively higher dye intensity around the flow centreline after the side-jets' penetration. Fig. 4(d) shows the side-jets impinging the primary flow centreline a short distance after injection, which leads to the formation of a high intensity central "core" region.

3.2. Counter-rotating vortex pairs interaction

The kidney profiles observed in the cross-sectional planar dye profiles in Fig. 3, in particular at $z/D_P = -0.75$, are results of an ensemble mean of Counter-rotating Vortex Pairs (CVPs) captured in the instantaneous images. CVPs are vortex structures that are developed in JICF due to the folding of injected lateral jet's shear layer by the cross-flow. The formation and development of CVPs in JICF are well documented [3]. Despite being in a different setting, here a confined round flow as opposed to an open channel or a square duct, there are clear signs that the CVPs are formed as a result of jets injected into a confined round flow.

If we consider the flow case of MR = 0.08 shown in Fig. 3(b), and in particular at locations downstream from $z/D_P = -0.75$, the four kidney profiles are observed to develop into a single cruciform profile, most prominent at $z/D_P = 0$. The mechanism behind such transformation is attributed to two proposed models, i.e. induced fluid convection by CVPs; and axis-switching of the induced CVPs. The former is illustrated in Fig. 5. Fig. 5(a) shows a typical instantaneous PLIF image for flow case MR = 0.08 at $z/D_P = -0.75$ with vortical direction of the CVPs overlaid. The vortices induce a velocity in the cross-section, which carries the fluid inside the pipe, in particular fluid near the pipe wall region, towards the pipe centreline. As the vortices move closer to the centreline of the pipe, the partially premixed fluid at the centreline of the pipe are transported outwards towards the pipe wall region, via the same method. This model also provides an explanation to why the core region, after the side-jets penetrated the centreline, has a higher dye intensity than the "arms" of the cruciform.

An alternative model is termed axis-switching. Fig. 6 shows instantaneous images for flow case MR = 0.08 at locations: (a) $z/D_P = -0.75$; (b) $z/D_P = -0.5$; (c) $z/D_P = -0.25$; and (d) $z/D_P = 0$, and accompanying schematic diagrams depicting the proposed axis-switching mechanisms of the induced CVPs. Studies on non-circular nozzles have indicated that it is possible to emulate the flow characteristics of non-circular nozzles by blowing at vertices of the corresponding nozzles [13]. Therefore, the current case of four side-jets blowing at equidistant locations around a round nozzle corresponds to that of a square jet.

Square jet nozzles demonstrate axis-switching characteristics [22], which is comparable to what is shown in Fig. 6. In a square jet, smaller vortex pairs are induced by the corners of the square jet nozzle, which in later stages undergo a 45 deg rotation of the vortex axis. The axis switch is not due to the helical turning of the vortices but is a result of interactions by adjacent vortices. The axis-switching here is attributed to the azimuthal vorticity (ω_θ) dynamics [23]. The ω_θ dynamics induced velocity, with respect to the azimuthal axis, is said to be the main contributors to axis-switching.

Fig. 6(a) shows similarities to vortical structures induced by a square jet [22]. A direct comparison to the flow structures generated by the square jet cannot be drawn due to the differences in the induced flow structures, which include ring vortices and horseshoe vortices. For a high injection momentum ratio (MR) case in the current study, it is believed that the CVPs generated are minimally affected by their wall images [6] and move towards the adjacent CVPs. The image sequence in Fig. 6(a)–(d) shows that as the CVPs move closer to the flow centreline, it is believed that the induced vortices turn towards the outer wall of the CVP (Fig. 6 (b)), which points away from the primary flow centreline. Fig. 6 (c) shows new pairings of the vortices as indicated by the schematic diagram. This is manifested as axis-switching [24] thus forming profiles similar to that observed in [22]. With increasing MR, the inception of axis-switching is brought upstream closer to the side-jets. The cross-sectional dye profile is projected to be carried downstream, however, additional investigations need to be carried out to verify this and to study the vortices dynamics within such flow.

3.3. Effect of side-jets on the outflow

The effect of MR on the flow structures at the nozzle near-field is presented in this section. Similar effects were reported earlier for 2 side-jets placed at an orifice nozzle exit [10].

Fig. 7 shows typical instantaneous dye profile sequences in the near-field out of the nozzle for flow cases: (a) MR = 0; (b) MR = 0.08; and (c) MR = 0.2. Unlike the aforementioned experiments, the current results are acquired by injecting clean water through the side-jets into a primary flow of dye. The flow proceeds from the left to the right of each image. Each image is normalized to the LIF signal from the dye cell. The intensity scale is represented by the accompanying color bar where the dye mixture fraction of 1.0 represents the undiluted dye mixture whilst region with dye mixture fraction of 0.0 represents clean water. The imaged

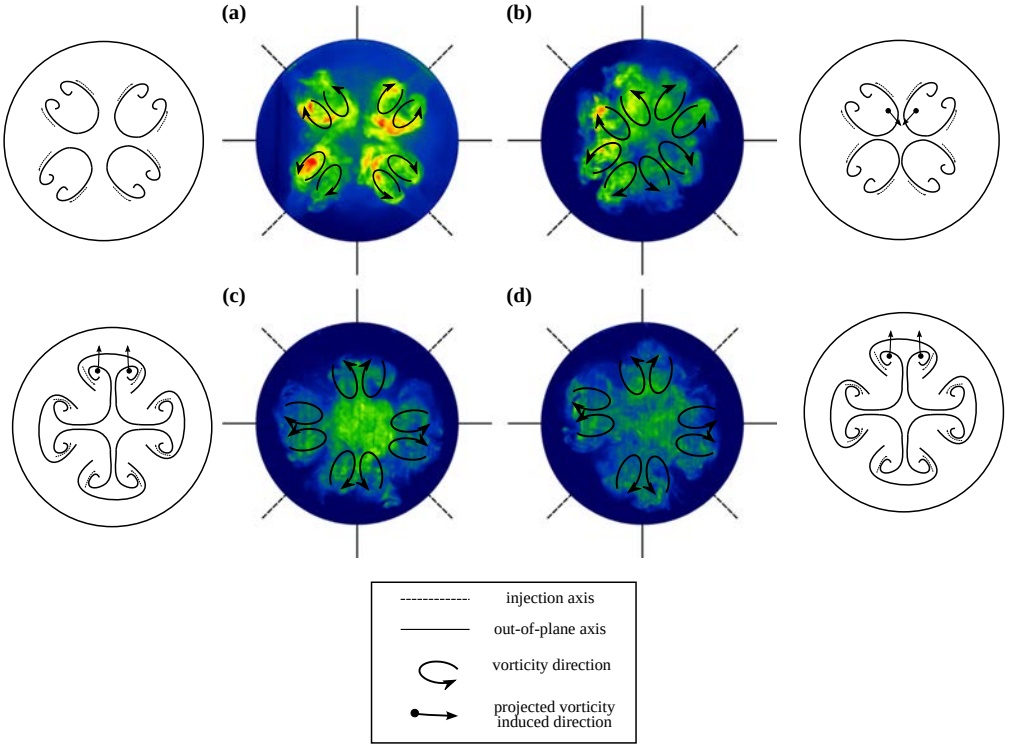

Fig. 6. Axis-switching model for the CVPs in the flow. (a)–(d) The sequence of flow interaction upstream of the nozzle exit and schematic diagram depicting the vortical interactions for flow case MR = 0.08 at locations: (a) $z/D_P = -0.75$; (b) $z/D_P = -0.5$; (c) $z/D_P = -0.25$; and (a) $z/D_P = 0$.

region spans from the nozzle exit ($z/D_P = 0$) up to $3D_P$ downstream.

Flow case MR = 0 shown in Fig. 7(a) has no side-jets, therefore, is an example of a typical round jet flow, exiting the LP nozzle at $Re_D \approx 4600$. The sequence of images from $t = 0.0$ s to $t = 1.6$ s show an intact jet profile up to $1D_P$ before the inception of shear layer roll-ups downstream. Also observed within the images sequence are large-scale flow structures that are typical of such flows.

By injecting water through the side-jets, an obvious dilution of the primary flow by the side-jets, in particular near the core of the flow can be observed (MR = 0.08) at the nozzle exit. It is also obvious from the image sequence in Fig. 7(b) that the side-jets affect the flow structure, most prominently the shear layer roll-ups. Here, it can be observed that the shear layer rolls up immediately after exiting the nozzle, unlike flow case MR = 0 which shows that the show layer rolls up only at approximately $z/D_P = 1$. Comparing this to the 2 side-jets flow case equivalent shown by [10] for 6% mass-flow, case MR = 0.08 does not show drastic narrowing of the primary jet upon exiting the primary nozzle. Furthermore, the same study [10] also show that the side-jets shorten the core of a round jet from approximately $5D_P$ to approximately $2D_P$, and initiated shear layer roll-up akin to that of a Kelvin-Helmholtz wake structures. However, the evolution of the jet profile upstream isn't described.

Placing the side-jets upstream of the nozzle exit shows that the drastic effects generated by the CVPs can be suppressed, and yet, is sufficient to affect the coherence of the jet shear region. The CVPs generated for flow case MR = 0.08 are transported into the body of the bulk flow, at an almost constant distance from the pipe wall (spatial location "restrained" by curved wall effect) compared to CVPs generated directly at the nozzle exit [10], which propagates along the edge of the bulk flow.

Likewise for flow case MR = 0.2, dilution effect of the side-jets on the primary flow can be observed quite clearly and consistently from each consecutive image in Fig. 7(c). Comparing the flow structures in this flow case to MR = 0 and MR = 0.08 show that the flow structures appear relatively less coherent. Furthermore, multiple shear layer roll-ups can sometimes be observed, in particular at $t = 0.8$ s at $z/D_P = 1.5$, while in subsequent images, various large and small-scale structures can also be observed in the flow. Compared to the 8% flow case in [10], noticeable differences can be observed in the jet shear layer where the CVPs propagate and seem to enhance the instability of the flow. Their cases differ to the flow cases tested in the current study, such that the side-jets fluid stream are propagated mainly along the central plane of the flow. A secondary stream consisting mainly of water from side-jets is observed propagating around the centreline. This stream is formed as a result of the impinging side-jets upstream (seen in Fig. 4(d)). Mixing in this flow case is attributed to the shear between this secondary flow stream and the primary flow, coupled with other effects related to the side-jets impingement [8].

Fig. 8 presents the Strouhal number, $Sr = fD_P/u_b$ variation with momentum ratio for two *Re* cases. The frequency of the large-scale vortical roll-ups frequency in the flow (f) is multiplied with the primary flow nozzle diameter (D_P) and normalized to the bulk flow velocity (u_b) for the respective flow MR. The flow cases with primary *Re* number of 4600 is plotted with ○-symbols while flow cases with primary *Re* number 6500 are plotted with the △-symbols.

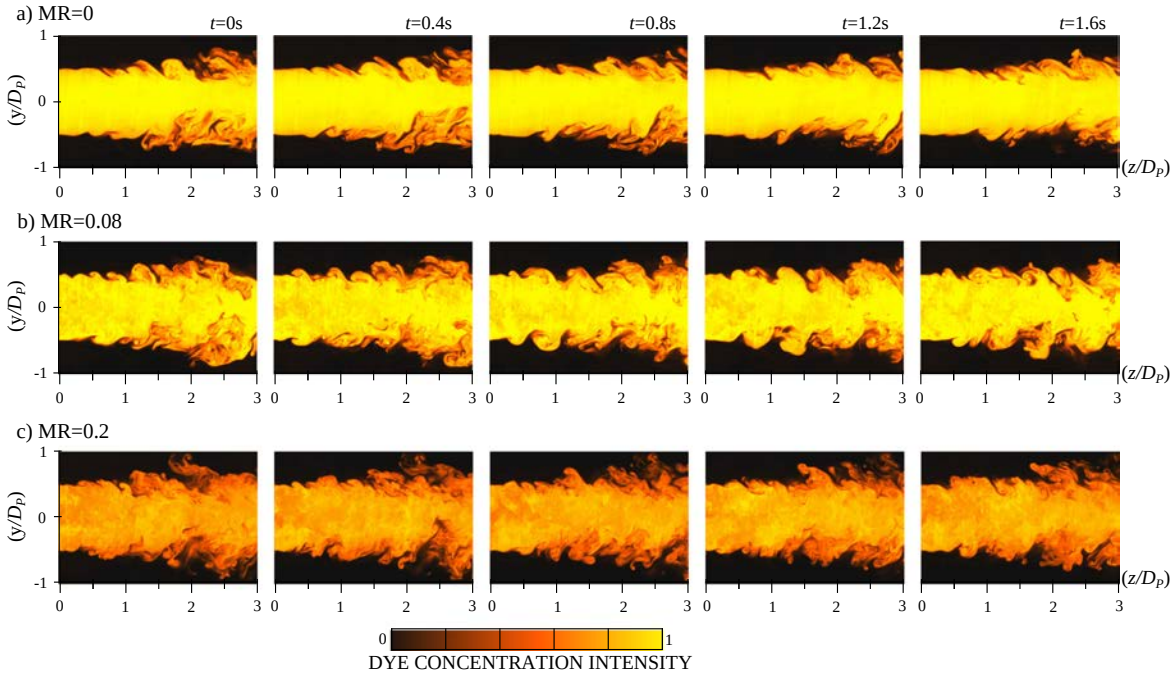

Fig. 7. Instantaneous dye mixture fraction image for flow cases: (a) MR = 0; (b) MR = 0.08; and (c) MR = 0.2, for five consecutive shots (from $t = 0$ s to $t = 1.6$ s, from nozzle exit ($z/D_P = 0$ to $3D_P$ downstream. The color bar shows the dye mixture fraction, where mixture fraction of 1.0 denotes the undiluted dye mixture, whilst mixture fraction of 0.0 represents clean water. (For interpretation of the references to color in this figure legend, the reader is referred to the web version of this article.)

Despite the small data points collected for the current study, an obvious trend in the results, plotted in Fig. 8, can be observed. Increasing the flow MR for the different tested cases lead to an increase in the Sr number. The increase in Sr is more prominent for higher MR flow compared to the lower MR cases, as observed for MR = 0.04. For the flow case *Re*4600, as the MR increase to 0.08, the frequency of the large-scale vortices roll-up increases by 1.2 times on average, which effectively increases the Sr number by 1.1. Whilst for MR = 0.2 case, the frequency of roll-up vortices increases by 1.6 times, while the Sr number increase by 1.4.

The addition of the side-jets upstream of the nozzle exit has inherent effects on the outflow of the primary jet. The affected characteristics of the jet include flow structure coherence and shear layer roll-up inception distance, as observed from the sequence of instantaneous images shown in Fig. 7. Perturbing the shear layer of the turbulent jet also enhances the mixing between the bulk of the jet with the surrounding flow [25,13]. In addition, the mean dye profile shown in Fig. 9 also captures the instantaneous images shown in Fig. 7.

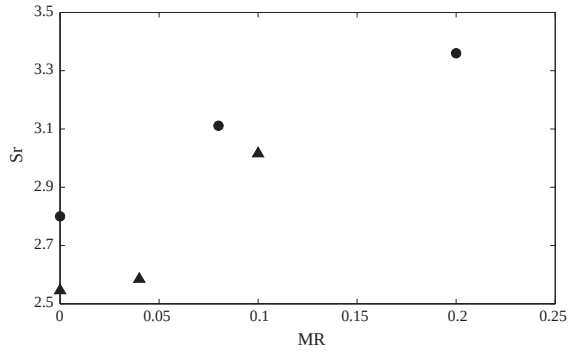

Fig. 8. Strouhal number plotted against momentum ratio, MR for the two primary flow *Re* numbers. Flow cases with primary *Re*4600 are plotted with the ○-symbols and flow cases with primary *Re*6500 are plotted with the △-symbols.

Fig. 9 shows the ensemble mean dye mixture fraction images for the near-field outflow for flow cases: (a) MR = 0; (b) MR = 0.08; and (c) MR = 0.2. These cases have the same primary flow Reynolds number of 4600. The mean dye mixture fraction images are averaged from an ensemble of 200 images and are normalized to the dye mixture fraction of unmixed dye. The images are scaled to 1.0 for unmixed dye mixture fraction and 0.0 for clean water. The flow arrangements are similar to those presented in Fig. 7. Dye concentration contours are superimposed on the dye mixture images to indicate the dye mixture fraction of the mean images.

Fig. 9 compares only the "out-of-plane" axis (refer to Fig. 5) centreplane visualized flow which has identical outflow pattern (according to Fig. 3) for flow case MR = 0.08 and MR = 0.2.

The dye mixture fraction of 0.1 is the lowest reliable dye mixture fraction count that can be measured before the data recedes below that of a tolerable noise and error level. The jet spread for flow case MR = 0.08, measured along the $C \geqslant 0.1(C_{0.1})$ at $z/D_P = 3$ in Fig. 9(b), is 16% wider than that measured for flow case MR = 0 in Fig. 9(a). Flow case MR = 0.2, measured at a similar region, shows similar growth in the jet's width. This implies that, despite the increase in flow MR, the spread of the jet from MR = 0.08 to MR = 0.2 is not significantly altered.

The unmixedness across the nozzle exit for flow case MR = 0.08 is 4.7% compared to 12.5% for flow case MR = 0.2. The higher unmixedness in MR = 0.2 is attributed to the impinging side-jets upstream, which lead to the formation of high side-jet concentricity mixture along the flow centreline region, which is consistent with the profiles shown later in Fig. 11(c). The unmixedness fur-

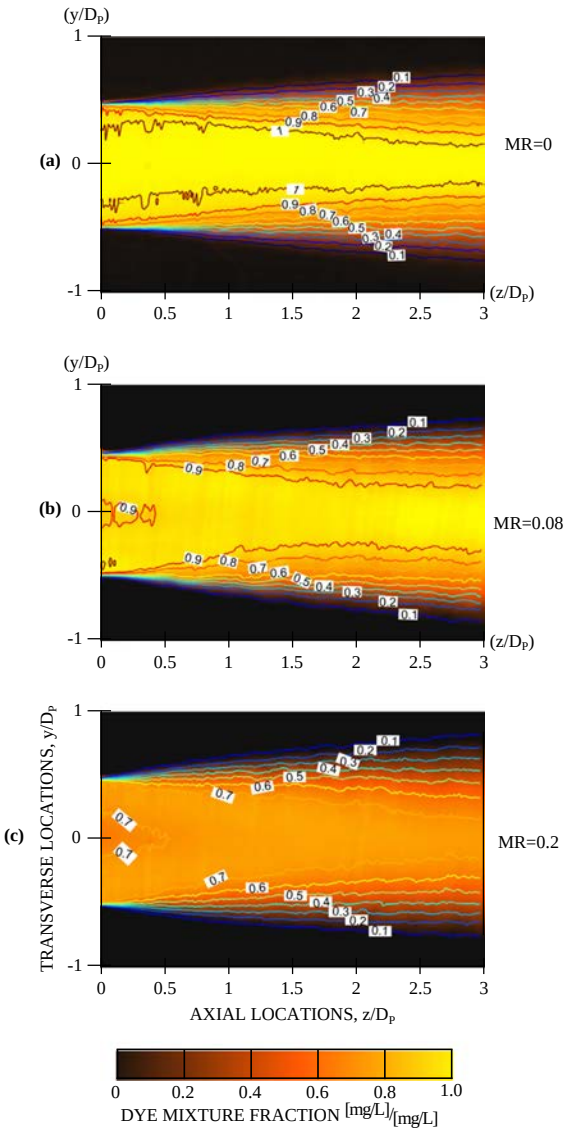

Fig. 9. Mean dye mixture fraction profiles and contours for flow cases: (a) MR = 0; (b) MR = 0.08; and (c) MR = 0.2 in the near-field region. The brighter region shows a region of higher dye mixture fraction whilst darker region shows region of low dye mixture fraction.

ther downstream in the near-field however, cannot be reliably determined due to the complications of mixing with water from the tunnel (ambient) transforming a 2-stream flow into a 3-stream one.

The cases compared in Fig. 9 involves only a single plane, further studies are required to ascertain the characteristics of the flow in the side-jets plane region.

Fig. 10 shows the modulus of the concentration gradient, Grad (C) from typical instantaneous images in the nearfield region. The Grad(C) intensity is scaled to 0.15, as indicated on the color bar, for enhanced visualization. The imaging region spans the nozzle exit at $z/D_P = 0$ up to $3D_P$ downstream and encompasses the radial region of $-1 \leqslant y/D_P \leqslant 1$, where $y/D_P = 0$ denotes the flow centreline.

Pockets of high gradient regions can occasionally be observed for flow cases MR = 0.08 and MR = 0.2 as seen in Fig. 10(b) and (c), respectively. These gradient pockets are rarely observed for the flow case with no side-jets, Fig. 10(a). This shows that the increase in shear layer roll-ups discussed previously in Fig. 7, also result indirectly in an increase in the ambient flow entrainment into the jet.

Fig. 10(b) and (c) shows the generation of moderately intense Grad pockets, which mostly indicates small-scale mixing of the side-jets and primary flow stream. The production of these structures is observed, qualitatively, to be more intense in Fig. 10(c) than in Fig. 10(b). This indicates that the impinging flow mode in Fig. 10(c) for MR = 0.2 is more efficient in converting large-scale structures generated via JICF into small-scale structures, which is beneficial for applications such as combustion fuel-air mixing.

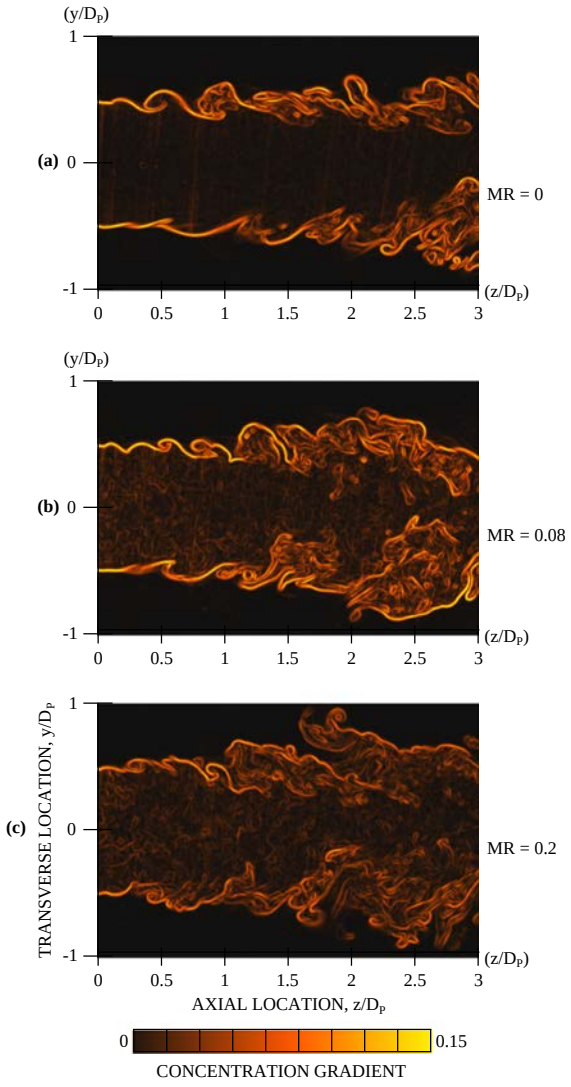

Fig. 10. Typical instantaneous concentration image gradients for flow case: (a) MR = 0; (b) MR = 0.08; and (c) MR = 0.2, scaled to 0.15 for the region encompassing $1D_P$ above and below the centreline, and spans the nozzle exit to $3D_P$ downstream.

3.4. Correlation of mixing and velocity field

The aforementioned results show how the outflow is affected, specifically the modification of the jet's shear layer flow characteristics, by altering the side-jets momentum ratios.

Fig. 11 compares the radial profiles for the normalized axial velocity (V/V_b) for flow cases MR = 0, MR = 0.08 and MR = 0.2, with their respective dye mixture fraction profiles at locations z/D_P = 0, 1, 2 and 3. The velocities are normalized to their respective bulk velocities (V_b) out of the nozzle exit.

$$V_b = \frac{Q_P + \sum_0^n Q_{inj}}{A_P} \tag{2}$$

Here, the total flow rate in the nozzle (total of primary flow rate, Q_P [m^3/s] and summation of the side-jets flow rate $\sum Q_{inj}$ [m^3/s]) is normalized to the hydraulic area of the primary jet, A_P.

The dye profile for the round jet outflow in Fig. 11(c) shows an almost uniform profile with a similar corresponding velocity, which shows a fully-developed flow exit. Less prominent mixing takes place within the body of the jet, also demonstrated in both Figs. 7 and 9, which incur a gradual reduction of the dye concentration profile from flow centreline towards the edge of the jet. Both the dye- and velocity- profiles developed gradually into a Gaussian-like profile at $z/D_P = 3$. This jet characteristic is expected as it is still within the round jet's potential core region [26].

The nozzle exit profiles for flow cases with side-jets (MR = 0.08 and MR = 0.2) show large perturbations. The velocity profiles for both MR = 0.08 and MR = 0.2 show lower normalized velocity on most parts of the profile, with the exception for a spike in velocity near the flow centreline for both cases. Referring to their respective dye profiles, it is clear that the high velocity spikes coincides with regions of low dye concentration (a reminder that clean water is injected through the side-jets), which indicates that the side-jets penetrating the flow centreline upstream of the nozzle exit increases the centreline velocity for these cases. The regions with uniform dye profile observed in these cases (around $\pm 0.3 \leqslant y/D_P \leqslant \pm 0.5$) are also lower than flow case MR = 0, which is expected. The application of these mixing characteristics in turbulent jet combustion will most probably indicate a fuel-rich region in the round jet centreline, which transits to a leaner mixture near the wall region of the pipe. Such configuration is likely to increase the stability of a round jet due to the decreased dependency on ambient air for mixing.

At $z/D_P = 1$, the increase in centreline velocity seen at the nozzle exit, for both flow cases MR = 0.08 and MR = 0.2, did not persist to this location and also display an overall lower normalized velocity, compared to flow case MR = 0. The modification in the velocity profiles observed at the nozzle exit is caused by the interaction between the side-jets and the primary flow. This modified profile is observed to be less prominent at $z/D_P = 1$ and is deduced to transition into a Gaussian-like profile, which is observed at $z/D_P = 2$ and at $z/D_P = 3$, for the respective cases. The dye profile observed, corresponding to the respective velocity profile plots, also transition into a Gaussian-like profiles. Noteworthy that the dye profile for flow case MR = 0.2 seem to have a flatter profile compared to both the MR = 0 and MR = 0.08 flow case. This is attributed to the formation of a core upstream near the side-jets, which is seen to have degraded at the nozzle exit, thus contributing to the shear mixing in the near-field outflow of the jet.

The observed modifications to the velocity profiles for both test cases, MR = 0.08 and MR = 0.2, which are clearly evident only at $z/D_P = 0$ and $z/D_P = 1$. This is similar to that shown in [10], which also reported that a stronger injection into the primary flow increases the velocity profile spread in the near-field. The differences in the flow profiles discussed in [10] and the current study stems mainly from the position of the side-jets upstream, relative to the nozzle exit. The side-jets in the current study are placed at approximately $1D_P$ upstream of the nozzle exit, as opposed to being at the nozzle exit [10]. The side-jets' streams in the current study does not immediately perturb the jet shear-layer in the outflow, but are allowed to develop within the "settling length" of $1D_P$ upstream of the nozzle exit before being expelled into the near-field. In contrasting fashion, placing side-jets at the nozzle exit directly perturb the near-field shear layer of the nozzle outflow. Furthermore, the different types of jets, i.e. LP nozzle compared to smooth-contracting and orifice flow, may also contribute to some contrasting data in both studies.

Comparison of the near Gaussian profiles for the flow cases at location $z/D_P = 2$ show that the normalized velocity profiles for flow cases MR = 0.08 and MR = 0.2 have a flatter profile compared to flow case MR = 0. This indicates the reduction in the potential core length of the bulk flow, which agrees with the findings by [13], despite having a different experimental set-up. The shortening of the potential core has an effect on combustion reactants mixing, as the flame lift-off height can be correlated to the potential core length of the jet [27,28]. The effect will be further investigated in a future study on reacting flow.

Examining the jets' half-width distance for the cases presented in Fig. 11 shows little changes in the distance leading up to $3D_P$ despite the changes in the flow MR. This in contrast to the results presented by [10] which shows observable differences in the jets' half-width in the near-field region. This suggest the suppression of jet spread and fluctuation in the near-field of the jet. The changes in the jets' half-width in the far-field could not be ascertained through the current range of data sets. Furthermore, it is also difficult to generate useful entrainment coefficient values which relies on the jets' half-width data.

3.5. Effects of momentum ratio on centreline flow

The centreline for a jet outflow is often used as a yardstick for enhanced mixing [29,30] and other turbulent jet parameterization studies. The changes in the flow centreline can be correlated to the changes in the flow characteristics, for example, flow decay.

The flow case MR = 0.08 is used as a reference for the case studies to compare the effect of flow MR on the near- velocity field. The side-jets' flow rate is increased whilst primary flow rate is decreased to compensate for the mass addition through side-jets, to achieve a side-jets to primary MR of 0.15, and to keep the bulk flow velocity, V_b out of the nozzle exit constant at 0.09 m/s. To achieve flow MR = 0.03, the side-jets are decreased and primary flow is increased correspondingly. The flow parameters of the tested cases are detailed in Table 1.

Fig. 12 shows the centreline velocity data for flow cases MR = 0.03; 0.08; and 0.15 plotted from the nozzle exit ($z/D_P = 0$) up to $3D_P$ downstream, and normalized to the bulk exit velocity of 0.09 m/s. The centreline velocity profiles are normalized per method highlighted in Eq. (2). MR = 0.03 shows the lowest normalized centreline velocity profile which plateaus at around 0.8 at $z/D_P \geqslant 2$. Flow case MR = 0.03 is categorized under the streaming flow regime, at which the side-jets' stream do not interact (lower MR than 0.04 shown in Fig. 3(a)), which contributes to the low exit velocity observed near the nozzle exit. The slight increase of velocity near $z/D_P = 0.2$ is deduced to be the effect of side-jets interacting and penetrating the primary flow centreline.

A higher MR is synonymous with strong side-jets. The velocity profile for flow case MR = 0.08 appears to have similar trend to the flow case MR = 0.03, albeit with a higher exit velocity. The velocity profile for flow case MR = 0.15 decays in similar fashion to the other two cases with a normalized exit velocity of ≈ 1.22.

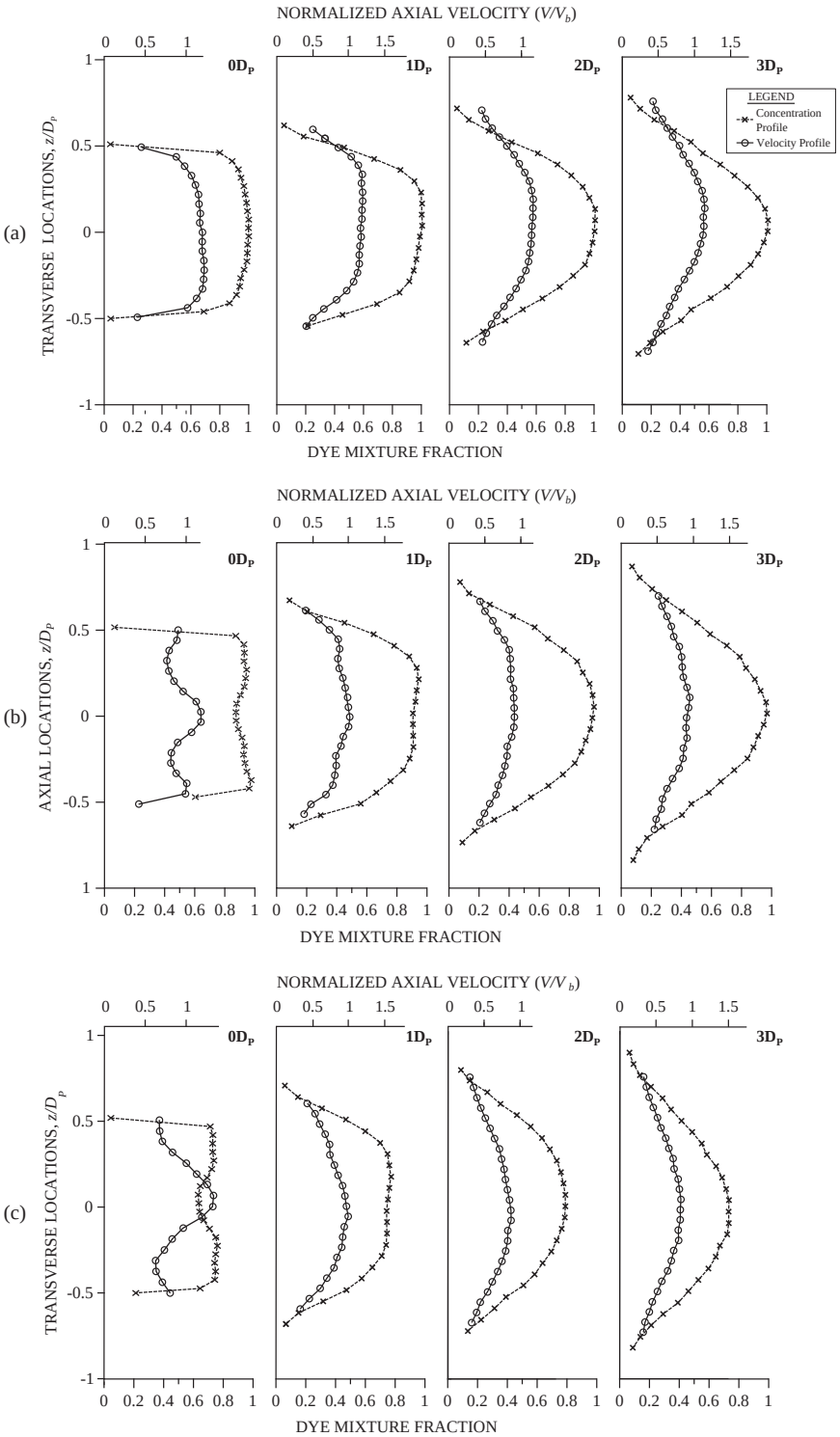

Fig. 11. Radial profiles for dye mixture fraction and normalized axial velocity (V/V_b) for flow case: (a) MR = 0; (b) MR = 0.08; and (c) MR = 0.2, at locations z/D_P=0; 1; 2; and 3, respectively.

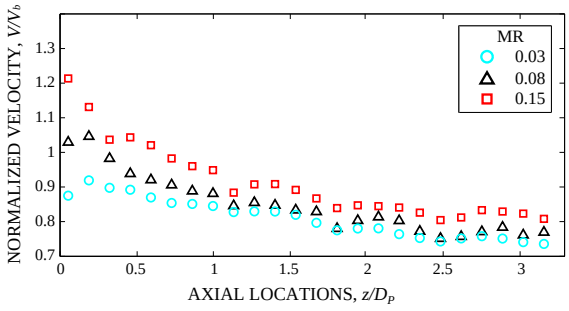

Fig. 12. Normalized centreline velocity profiles for flow cases: MR = 0.03 (∘-symbols); MR = 0.08 (△-symbols; and MR = 0.15(□-symbols).

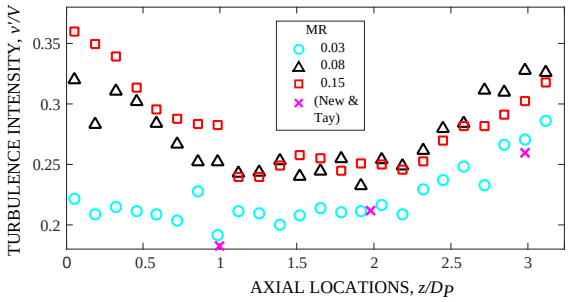

Fig. 13. Axial centreline turbulence intensity data for flow cases: MR = 0.03 (∘-symbols); MR = 0.08 (△-symbols; MR = 0.15(□-symbols); and 4% mass flow injection case from [10], which is equivalent to MR = 0.09 (×-symbols).

The observation for this flow case (MR = 0.15) is consistent with that of an impinging flow, which displays a higher centreline flow velocity. Similarity is observed for all tested cases where the normalized velocity decays to an almost plateau region around $z/D_P = 2$. This shows that any disruption in the flow through the change of the side-jets to primary flow MR, affects the flow centreline up to $2D_P$ downstream in the near-field.

Fig. 13 shows the axial centreline turbulence intensity, *T.I.*, profiles plotted from the nozzle exit location to $3D_P$ downstream. The *T.I.* is acquired by normalizing the axial velocity fluctuation, V'_Z [m s^{-1}] with the mean axial velocity, V_Z [m s^{-1}].

Flow case MR = 0.03 shows the lowest *T.I.*, at the nozzle exit compared to flow cases MR = 0.08 and MR = 0.15. The *T.I.* profile for this case remains almost constant at ≈ 0.22 up to $z/D_P = 2$ before increasing to 0.28 at $z/D_P = 3$. This shows the streaming flow regime has little effect on the centreline *T.I.* despite the side-jets interacting at around $z/D_P = 0.2$ as seen in Fig. 12. Increasing to MR = 0.08 shows a drastic increase in *T.I.* to approximately 0.32, at the nozzle exit. The *T.I.* profile decrease to 0.25 at around $z/D_P = 1$, plateaus, before increasing gradually after $z/D_P = 2$. Data presented earlier in Fig. 3(b) show that the side-jets stream for flow case MR = 0.08 penetrates the centreline, a short distance upstream of the primary nozzle exit before being expelled, which explains the drastic increase in centreline turbulence,

The *T.I.* profile for flow case MR = 0.15 almost mirrors the MR = 0.08 case, albeit with a higher *T.I.* at the nozzle exit at 0.37. It is interesting to note that despite almost doubling of the MR, the *T.I.* for MR = 0.15 case is quite similar to that of the MR = 0.08 case. This is an indication that the secondary core formed by the impingement of side-jets for flow cases MR = 0.15 and MR = 0.08 degrades at a similar rate to a similar distance downstream. The increase in *T.I.* downstream for all tested flow cases just downstream of $z/D_P = 2$ is attributed to the degradation of the primary jet's "potential core".

In addition, an extract from the 4% mass-ratio side-jets case from [10] is overlaid on Fig. 13. The study conducted involved two opposing side-jets, placed close to the nozzle exit of a converging jet. The selected flow case is equivalent to MR = 0.09 when scaled using Eq. (1). It is clear from Fig. 12 is that, despite the higher MR compared to flow case MR = 0.03, similar centreline *T.I.* can be observed. Furthermore, the trend of the *T.I.* also roughly follows that set by the current flow cases of MR = 0.03, 0.08 and 0.2. This shows that the number of side-jets and its respective placements play important roles in increasing the *T.I.* of the outflow in the near-field region.

Collating data shown in Figs. 11–13, it can be deduced that the side-jets are required to penetrate the primary flow centreline in order to increase the flow turbulence, in particular at the flow centreline. Inducing turbulence at the flow centreline may enhance combustion reactants mixing, which otherwise depends on turbulence induced by the large-scale coherent motions in the primary jet shear layer [31]. In addition, increasing the flow turbulence near the centreline also directly contributes to the generation of small scale reactants mixing, which is measured by the level of turbulence [32].

4. Conclusions

In this experimental study, the emerging flow and mixing fields from a 56 mm diameter round jet fitted with four lateral jets (of aspect ratio $D_{inj}/D_P \approx 0.1$), placed in a symmetrical configuration at approximately one diameter upstream of the primary round nozzle exit are reported. The primary flow and side-jets flow velocity is manipulated to alter the flow momentum ratio (MR) and flow pattern. Non-intrusive experimental techniques, Planar Laser Induced Fluorescence (PLIF) and Particles Image Velocimetry (PIV) are used to measure the mixture fraction and velocity field, respectively.

It is found that changing the MR between the side-jets and the primary flow affects the flow pattern and the interactions between the side-jets drastically. For flows with MR above 0.08, the side-jets penetrate the primary flow centreline, which results in the evolution of kidney-shaped profiles into a single cruciform profile. The formation of such profiles is attributed to fluid transport within cross-sectional region due to the vorticity induced by the Counter-rotating Vortex Pairs (CVPs) and also axis-switching of the vortices. Further increase of MR brings about the inception of the cruciform profile at an earlier point, which eventually causes the side-jets to impinge the primary flow centreline, forming a "core" region near the impingement point.

The increase in MR also affects the behavior of the outflow in the near-field, most notably, the shear layer roll-up. By placing the side-jets upstream, the length of the potential core is reduced, resulting in the appearance of coherent vortical structures closer to the primary nozzle exit. The flow structures appear more turbulent with large-scale vortex roll-ups as the MR increases. Flow cases with side-jets penetrating the primary flow centreline shows the formation of a secondary stream that propagates along the flow centreline. The secondary flow is especially obvious at the nozzle exit where high centreline velocity is observed for these flow cases. The modified flow and velocity profiles degrade to a Gaussian-like profile around $2D_P$ downstream of the nozzle exit.

Despite the differences in flow MR, the centreline normalized velocity profiles for both streaming and impinging flow cases reduce to similar levels at around $1D_P$ downstream. However, the

centreline flow turbulence intensity increases with increasing MR. A significant increase in turbulence intensity is recorded for the impinging case compared to the streaming flow cases.

Finally, the results in the current study indicate the possibilities of enhancing mixing in the near-field flow without significantly altering the jet spread. This is encouraging, in particular to enhance combustion reactants mixing to generate a stable turbulent jet flame. Future work will concentrate on the study of different number of jets and their orientations, as well as conducting similar study on reacting flow that focuses on flame stability and structures at the flame base.

Acknowledgement

The authors would like to gratefully acknowledge Mr. Marc Simpson, Thebarton Lab Manager, in assisting with the setting up of the experimental rig.

References

[1] Y. Kamotani, I. Greber, Experiments on a turbulent jet in a crossflow, AIAA J. 10 (11) (1972) 1425–1429, http://dx.doi.org/10.2514/3.50386.
[2] R.M. Kelso, T.T. Lim, A.E. Perry, An experimental study of round jets in cross-flow, J. Fluid Mech. 306 (1996) 111–114.
[3] R.J. margason, Fifty years of jet in cross flow research, in: AGARD Conference Proceedings 534, AGARD.
[4] S.H. Smith, M.G. Mungal, Mixing, structure and scaling of the jet in crossflow, J. Fluid Mech. 357 (1998) 83–122, http://dx.doi.org/10.1017/S0022112097007891.
[5] J.D. Holdeman, Mixing of multiple jets with a confined subsonic crossflow, Prog. Energy Combust. Sci. 19 (1993) 31–70, http://dx.doi.org/10.1016/0360-1285(93)90021-6.
[6] J.D.A. Walker, C.R. Smith, A.W. Cerra, T.L. Doligalski, The impact of a vortex ring on a wall, J. Fluid Mech. 181 (1987) p99–p140, http://dx.doi.org/10.1017/S0022112087002027.
[7] L.L. Yuan, R.L. Street, Trajectory and entrainment of a round jet in crossflow, Phys. Fluids 10. doi:http://dx.doi.org/10.1063/1.869751.
[8] C.X. Thong, P.A.M. Kalt, B.B. Dally, C.H. Birzer, Flow dynamics of multi-lateral jets injection into a round pipe flow, Exp. Fluids 26 (1) (2015) 1–16.
[9] E.V. Kartaev, V.A. Emelkin, M.G. Ktalkherman, S.M. Aulchenko, S.P. Vashenko, V.I. Kuzmin, Formation of counter flow jet resulting from impingement of multiple jets radially injected in a crossflow, Exp. Therm. FLuid Sci. 68 (2015) 310–321, http://dx.doi.org/10.1016/j.expthermflusci.2015.05.009.
[10] T.H. New, W.L. Tay, Effects of cross-stream radial injections on a round jet, J. Turbul. 7(57). doi:http://dx.doi.org/10.1080/14685240600847466.
[11] D.A. Tamburello, M. Amitay, Manipulation of an axisymmetric jet using continuous control jets, J. Turbul. 7(59). doi:http://dx.doi.org/10.1080/14685240600854892.
[12] J. Mi, G.J. Nathan, D.S. Nobes, Mixing characteristics of axisymmetric free jets from contoured nozzle, an orifice plate and a pipe, J. Fluid Eng. 123 (4) (2001) 878–883, http://dx.doi.org/10.1115/1.1412460.
[13] J.F. Seidel, C. Pappert, T.H. New, H.M. Tsai, Effects of multiple radial blowing around a circular jet, in: Proceedings of 43rd AIAA Aerospace Sciences Meeting and Exhibit, Nevada, 2005, http://dx.doi.org/10.2514/6.2005-866.
[14] M.Y. Leong, G.S. Samuelsen, J.D. Holdeman, Optimization of jet mixing into a rich, reacting crossflow, J. Propul. Power (2000) 729–735, http://dx.doi.org/10.2514/2.5643.
[15] J.D. Holdeman, D.S. Liscinsky, V.L. Oechsle, G.S. Samuelsen, C.E. Smith, Mixing of multiple jets with a confined subsonic crossflow: Part 1 – Cylindrical duct, J. Eng. Gas Turb. Power 119 (4) (1997) 852–862, http://dx.doi.org/10.1115/1.2817065.
[16] J.T. Kroll, W.A. Sowa, G.S. Samuelsen, J.D. Holdeman, Optimization of orifice geometry for crossflow mixing in a cylindrical duct, J. Propul. Power (2000) 929–938, http://dx.doi.org/10.2514/2.5669.
[17] H. Tsunoda, M. Saruta, Plif study on the diffusion field of a passive scalar in a round jet issuing into a uniform counter flow, Eng. Turbul. Model. Exp. 5 (2002) 505–514, http://dx.doi.org/10.1007/s00348-014-1884-4.
[18] P.A.M. Kalt, M. Long, Oma for Mac OS X, website, 2014. <www.oma-x.org>.
[19] J.W. Shan, D.M. Lang, P.E. Dimotakis, Scalar concentration measurements in liquid-phase flow with pulsed laser, Exp. Fluids 36 (2004) 268–273, http://dx.doi.org/10.1007/s00348-003-0717-7.
[20] P.A.M. Kalt, C.H. Birzer, G.J. Nathan, Corrections to facilitate planar imaging of particle concentration of particle-laden flows using mie scattering, Part 1: Collimated laser sheets, Appl. Opt. 46 (2007) 5823–5834, http://dx.doi.org/10.1364/AO.46.005823.
[21] P.A.M. Kalt, G.J. Nathan, Corrections to facilitate planar imaging of particle concentration of particle-laden flows using mie scattering, Part 2: Diverging laser sheets, Appl. Opt. 46 (2007) 7227–7236, http://dx.doi.org/10.1364/AO.46.007227.
[22] W. Quinn, Streamwise evolution of a square jet cross section, AIAA J. 30 (12) (1992) 2852–2857, http://dx.doi.org/10.2514/3.48973.
[23] K.B.M.Q. Zaman, Axis switching and spreading of an asymmetric jet: the role of coherent structure dynamics, J. Fluid Mech. 316(1–27). doi:http://dx.doi.org/10.2514/6.1995-889.
[24] C.H. Birzer, R.M. Kelso, B.B. Dally, Flame structure of jets in confined cross-flows, in: Proceedings of the Australian Combustion Symposium, 2011.
[25] M. Davis, Variable control of jet decay, AIAA J. 20 (5) (1981) 606–609, http://dx.doi.org/10.2514/3.7934.
[26] P.O.A.L. Davies, M.J. Fisher, M.J. Barratt, The characteristics of the turbulence in the mixing region of a round jet, J. Fluid Mech. doi:http://dx.doi.org/10.1017/S0022112063000306.
[27] Y. Wu, I.S. Al-Rahbi, Y. Lu, G.T. Kalghatgi, The stability of turbulent hydrogen jet flames with carbon dioxide and propane addition, Fuel 86 (2007) 1840–1848, http://dx.doi.org/10.1016/j.fuel.2006.11.032.
[28] C.M. Coats, H. Zhao, Transition and stability of turbulent jet diffusion flames, Proceeding of the Twenty-Second Symposium (International) on Combustion (1988) 685–692, http://dx.doi.org/10.1016/S0082-0784(89)80076-1.
[29] P. Zhang, Y. Zhou, Jet flow structure under the perturbation of two unsteady microjets, in: Proceedings of the 19th Australasian Fluid mechanics Conference, Melbourne, 2014.
[30] Y. Zhou, C. Du, J. Mi, X.W. Wang, Turbulent round jet control using two steady minijets, AIAA J. 50 (3) (2012) 730–740, http://dx.doi.org/10.2514/1.J050838.
[31] C.G. Ball, H. Fellouah, A. Pollard, The flow field in turbulent round free jets, Prog. Aerospace Sci. 50. doi:http://dx.doi.org/10.1016/j.paerosci.2011.10.002.
[32] K.R. Sreenivasan, R.A. Antonia, The phenomenology of small-scale turbulence, Ann. Rev. Fluid Mech. 29 (1997) 435–472, http://dx.doi.org/10.1146/annurev.fluid.29.1.435.

Chapter 5

Impact of 3 and 4 side-jets on the flow and mixing fields

5.1 Overview

The background literature in Chapter 2 shows that most studies are focussed on the effects that the number of side-jets have on the mixing field. However, little systematic studies have been found that investigate the effects of asymmetrical and non-symmetrical multi-lateral jet have on the mixing and flow field. In addition, there are also little studies that investigate the mixing structures as a result of the side-jets interactions within the confined pipe flow.

To investigate the effect of the different momentum ratio and number of side-jets on the mixing field (Objective (i)), the flow cross-section at every 0.25 D_P downstream from the side-jets, up to the nozzle exit was investigated with PLIF. Furthermore, PIV was also conducted to compare the flow fields of both the 3SJ and 4SJ configurations, with similar MR.

The results in this chapter indicate that:

- CVPs dominate the planar flow field in low MR, streaming flow regime flow cases.
- Backflow regime in high MR forms a high concentricity flow at the primary flow centreline
- Axis-switching is observed for both 3SJ and 4Sj flow case
- The trajectory of the side-jets in a confined flow cannot be scaled by conventional JICF scaling methods
- Higher flow turbulence is achieved in the 4SJ configurations due to the higher blockage ratio.

The findings from this study has been submitted for publication in *Experimental Thermal and Fluid Sciences* in September 2016 in a paper titled “On the impact of 3 and 4 multilateral jet injection on the flow and mixing fields inside a round pipe flow", authored by Chia X. Thong, Bassam B. Dally, and Cristian H. Birzer.

5.2 Manuscript

Statement of Authorship

Title of Paper	On The Impact of 3 and 4 Multilateral Jet Injection on the Flow and Mixing Fields Inside a Round Pipe Nozzle
Publication Status	☐ Published ☐ Accepted for Publication ☑ Submitted for Publication ☐ Unpublished and Unsubmitted w ork w ritten in manuscript style
Publication Details	Submitted to Experimental Thermal and Fluid Science journal

Principal Author

Name of Principal Author (Candidate)	CHIA XIONG THONG
Contribution to the Paper	Performing literature review, setting up and conducting water tunnel experiments, collecting PIV and PLIF data, performed data processing, structuring and writing manuscript, and the corresponding author for the paper
Overall percentage (%)	70
Certification:	This paper reports on original research I conducted during the period of my Higher Degree by Research candidature and is not subject to any obligations or contractual agreements with a third party that would constrain its inclusion in this thesis. I am the primary author of this paper.
Signature	Date 23/12/2016

Co-Author Contributions

By signing the Statement of Authorship, each author certifies that:

i. the candidate's stated contribution to the publication is accurate (as detailed above);

ii. permission is granted for the candidate in include the publication in the thesis; and

iii. the sum of all co-author contributions is equal to 100% less the candidate's stated contribution.

Name of Co-Author	BASSAM DALLY
Contribution to the Paper	Supervising development of work, interpreting data, and editing manuscript
Signature	Date 02 FEB 2017

Name of Co-Author	CRISTIAN BIRZER
Contribution to the Paper	Supervising experimental work, interpreting data, and editing manuscript
Signature	Date 23 DEC 16

Please cut and paste additional co-author panels here as required.

On the impact of 3 and 4 multilateral jet injection on the flow and mixing fields inside a Round Pipe Nozzle

Chia. X. Thong • Bassam. B. Dally • Cristian. H. Birzer

Abstract

The paper reports on an experimental and numerical study of the flow and mixing fields inside a long round pipe nozzle after it was mixed with flows from an equi-spaced 3 (3SJ)and 4 side-jets (4SJ) mounted one diameter upstream of the pipe exit. The nozzle was mounted horizontally in a water tunnel with a slow-moving co-flow. Dye was injected through the side-jets into clean water carried by the primary nozzle. Planar Laser Induced Fluorescence was used to image the mixing field and Particle Image Velocimetry was used to study the flow field. Measurements were conducted at different side-jet to primary flow momentum ratios at values representing the three flow regimes: streaming, impinging and backflow. The flow for both 3SJ and 4SJ configurations, show the phenomenon of axis-switching of Counter-rotating Vortex Pairs. The backflow length is found to scale with the momentum ratio and the number of side-jets whilst the jet trajectories do not scale with the conventional scaling laws of a jet in a cross-flow. Higher momentum ratio flows display higher vorticity and turbulence in the flow cross-section, with slight differences found between the 3SJ and 4SJ configurations.

1 Introduction

Controlled partial-premixing of reactants has been shown to enhance flame stability when compared to conventional non-premixed turbulent jet flames [14]. Partial premixing of reactants can be achieved through simple premixing in the supply lines, or just before the reactants are introduced into the combustion zone. While the former can introduce a flashback hazard, the latter has been explored more closely in recent years. Most studies on partial premixing is carried out on concentric tube nozzles, at which the inner fuel-jet is recessed to generate the required level of partial premixing [13, 15]. The approach investigated in the current study utilizes multilateral jet injection into a flow inside a round pipe to achieve partial premixing as close to the jet exit as possible.

The mixing technique discussed here considers injecting fuel via lateral jets into a confined cross-flow of air, before being issued out of the nozzle to be combusted. Similar techniques were widely used for combustion quenching

via the Rich Burn/Quick Quench/Lean Burn (RQL) combustors [3, 12].

A review, which was published by Holdeman et al., [3], reported that multi-lateral jet studies for RQL combustors typically involve the arrangement of 6 or more lateral jets injected into a confined round cross-flow. The studies established that Counter-rotating Vortex Pairs (CVPs) dominate the mixing processes in the flow cross-section, however, the consequences of adjacent CVPs in the cross-section in a confinement are not well resolved due to the large number of lateral jets used. Furthermore, most multilateral jet studies focus on the development of multiple individual CVPs in the confined cross-flow [12] that do not penetrate far into the flow [16], hence the effects of jets penetration into the cross-flow, which are vital for the intended application, are not well quantified.

Earlier studies [23, 22] involving 4 equi-spaced lateral jets injection into a confined round flow have identified momentum ratio (MR) as the controlling parameter, in-line with studies by Holdeman [4] and Kartaev et al., [10]. Momentum ratio is defined as:

$$MR = \frac{(\rho V^2 A)_J}{(\rho V^2 A)_P}$$

where J and P denote jet (a single jet) and primary confined cross-flow, respectively. The symbol ρ denotes the media density, V denotes the bulk flow velocity, and A the hydraulic area. Also found are flow regimes within the confined flow which conform to specific MR ranges, and they are:

- Streaming flow regime (MR < 0.2);
- Impinging flow regime (MR ≈ 0.2); and
- Back flow regime (MR $>> 0.2$).

The impacts of the different flow regimes on the flow mixing pattern and the resulting turbulence field are discussed in detail by Thong et al., [23]. The study also found that the investigated 4 lateral-jets configuration creates a large blockage which impacts on the flow pattern for MR ≥ 0.2. Hence, a 3 lateral-jets configuration, which has less blockage ratio is also investigated in the current study. Furthermore, the evolution of a streaming flow regime into an impinging flow regime is also not well understood.

The current study compares the flow features generated in a confined round nozzle configured with either 3 lateral-jets or 4 lateral-jets with similar MR.

Water is used as the working fluid. The cross-section and axial planes from the lateral-jets to the nozzle exit are investigated with non-intrusive optical diagnostic techniques. Planar Laser Induced Fluorescence (PLIF) is used to infer scalar mixing while Particle Image Velocimetry (PIV) is used to measure the velocity field. A CFD study was also conducted to help shed more light on the flow inside the nozzle.

2 Methodology

Two different nozzles were constructed: a 3 lateral-jets nozzle (3SJ) and a 4 lateral-jets nozzle (4SJ), out of acrylic to allow for optical access, for the current study. The primary nozzles were constructed out of 1-m long acrylic pipes with nominal diameter (D_P) of 56-mm while the lateral-jets were constructed out of 150-mm long acrylic tubes with nominal diameter (d) of 6-mm. The tubes were mounted $1D_P$ upstream of the primary nozzle's exit and arranged in equidistant pattern on the circumference of the primary nozzle.

Water was used as the working fluid to allow Reynolds Number matching with lower flow velocities. The experiments were conducted in a closed-looped water tunnel where the working section dimensions were: 500-mm $\times$ 500-mm $\times$ 1800-mm.

Fluid for the primary nozzle were fed through a diverging nozzle upstream followed by a honeycomb section for flow conditioning. The fluid were sourced from a reservoir of clean water laced with seeding particles 50μm in diameter (Dantec Dynamics PSP-50 Polyamid Seeding Particles) for PIV. The lateral-jets were connected to a manifold via flexible tubes of equal length. Fluid for the lateral-jets were sourced from a second reservoir of water laced with seeding particles and 0.1-g of Rhodamine 6G dye for PLIF signal. Each reservoir has a capacity of $400L$.

A schematic diagram of the experimental set up is shown in Figure 1. Illumination was sourced from a Quantel Brilliant B (Twin) Nd:YAG laser, frequency doubled to 532-nm and pulsed at 10Hz. The laser beam was routed through a Galilean Telescope set up and a 150-mm cylindrical lens to form a laser sheet of approximately 2-mm in thickness. A silvered mirror (reflectance $> 97\%$) was set up below the tunnel to illuminate the axial and cross-sectional planes of interest.

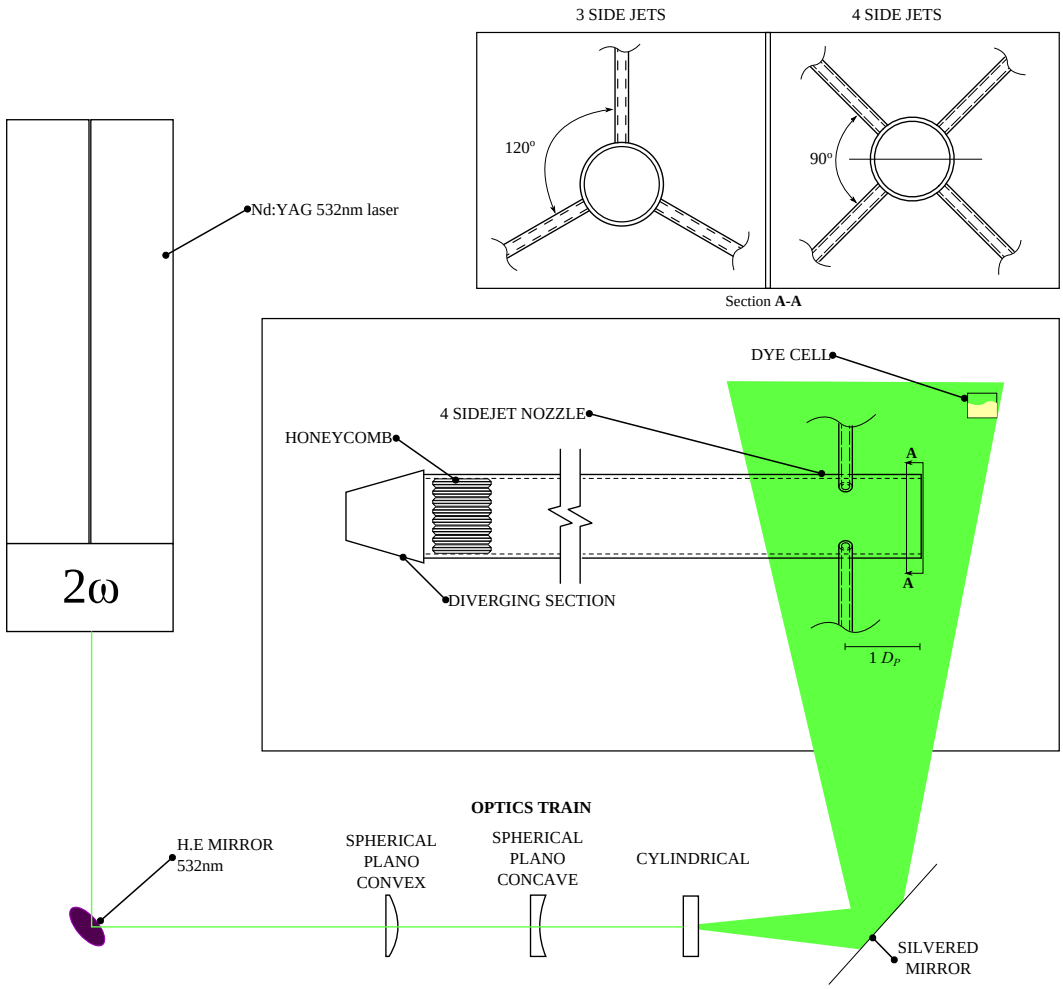

Figure 1: Schematic diagram for the experimental set up.

Two Princeton Instruments CCD Megaplus II ES4020 camera units with 2048 pixels $\times$ 2048 pixels array were used for imaging. The CCDs were triggered by a Berkeley Nucleonics Corporation (BNC) 565 Delay Generator, set at a duty cycle of 2.5Hz.

2.1 Dye Concentration Measurements

Rhodamine 6g(s) was mixed with water and its fluorescence was used to quantify mixing. The peak light absorption of the dye is at a wavelength of approximately 530-nm, which is close to the emitted wavelength of the second harmonics of the available Nd:YAG laser of 532-nm. The emitted fluorescence from the excited dye is in the visible range of 560-nm. Mixing 0.1-g of Rhodamine solid into $400L$ of water in the reservoir produces an aqueous dye concentration of 0.25 mg/L and this corresponds to 0.5×10^{-6} Molarity. This value is within the range of $0.1]times10^{-6} \leq$ concentration, $[M] \leq 1.0 \times 10^{-6}$, which ideally, according to Shan et al., [20], provides a linear increase of fluorescence intensity with dye concentration.

Planar images of the nozzle cross-section were obtained by placing a mirror angled at 45^o downstream of the nozzle exit. The angled mirror was placed at approximately $6D_P$ downstream to allow access into the nozzle and to avoid interference with the flow inside the nozzle. A CCD camera fitted with orange glass filter and a Tamron lens set (50mm f/14D) was placed normal to the region of interest, facing the angled mirror. The spatial resolution of the cross-sectional planar images was approximately 16.9 pixels/mm. Images in the axial planes were acquired by placing the camera normal to the region of interest

Approximately 200 instantaneous images were obtained for each flow case via the trigger programmable mode on EPIX XCAP 3.8. The raw data in TIF format were imported into OMA-X [7] for background removal, laser sheet profiling, sheet divergence and response correction; in-line with methods highlighted in Kalt and Nathan [6] and Kalt et al., [8]. The number of images required to achieve statistically independent results was discussed in Thong et al., [23], and found to be adequate.

Figure 2 shows the infographic to the data processing sequence, from raw images (Figure 2(f)) to the final instantaneous (Figure 2(g)) and mean (Figure 2(e)) results. A dye tube was placed within the imaging region (Figure 2(a)) to acquire the virtual origin of the laser plane and to acquire the response profile of the laser sheet (Figure 2(c)). Also shown in Figure 2(c) is

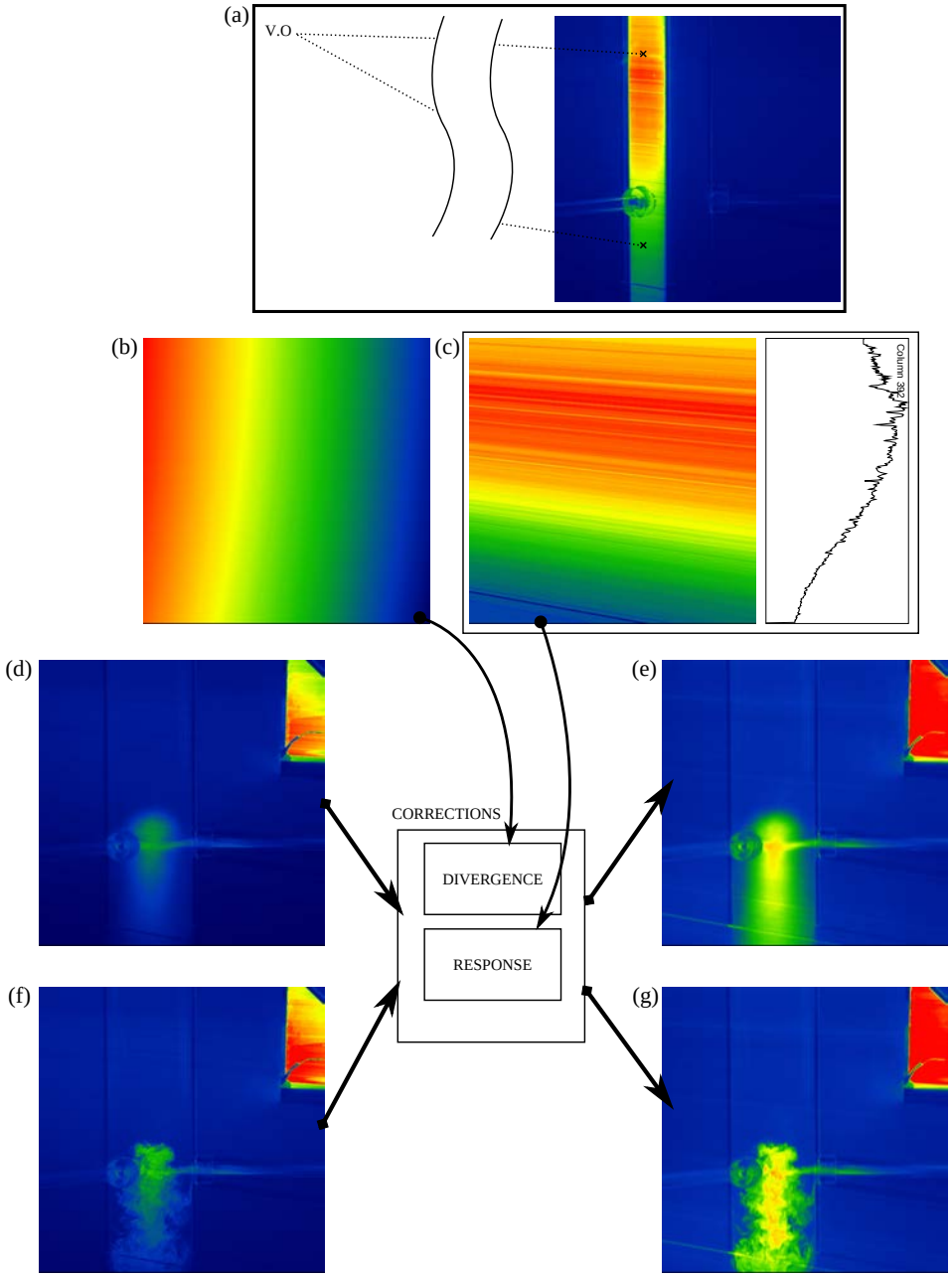

Figure 2: Infographic on the PLIF image processing method adopted for the tested cases. a) shows the uniform dye tube in the imaging region with indication of the position of the virtual origin (not real location); b) divergence profile; c) response; d) mean image for the uncorrected dye images; e) corrected mean image; f) typical raw uncorrected instantaneous image; and g) corrected instantaneous image.

Table 1: Flow parameters for the 3SJ and 4SJ flow configurations

Parameters	Three/Four side-jets cases, 3SJ/4SJ				
Momentum Ratio, MR [-]	0.04	0.08	0.1	0.2	0.6
Primary flow rate, $Q_P[\times 10^{-4} m^3/s]$	2.86	2.04	2.86	2.04	1.22
Injection flow rate, $Q_{inj}[\times 10^{-6} m^3/s]$	4.49/5.99	4.49/5.99	7.48/9.98	7.48/9.98	7.48/9.98
Primary Velocity, $V_P[m/s]$	0.12	0.08	0.12	0.08	0.05
Injection Velocity, $V_{inj}[m/s]$	0.21	0.21	0.35	0.35	0.35

the Gaussian profile of a typical laser plane. Figure 2(b) shows the divergence profile acquired corresponding to the virtual origin of the laser sheet. The instantaneous image profiles were corrected for obvious aberration caused by the non-uniformity and the divergence of the laser sheet. The lowest measured dye mixture fraction is capped to 0.1, which corresponds to the maximum allowable signal-to-noise ratio of 1%.

2.2 Velocity Field Measurement

The velocity field was measured with the PIV technique. The CCD camera was equipped with a Tamron lens set and a 532nm with FWHM 10nm interference filter. Image pairs were collected via double exposure mode on the XCAP camera software. The time delay between images was set to 300μs, controlled by the delay generator.

The image pairs collected were imported into PIVView 2C for PIV processing. The interrogation window was set to 32 pixels by 32 pixels, with 50% overlap. The overall physical imaging region was estimated to be approximately 200 mm $\times$ 200 mm, which translates to an averaged spatial resolution of approximately 10.2 pixels/mm. Cross-correlation of the image pairs was done with the Gaussian algorithm. The datafiles generated were imported into OMA-X for filtering and to compute the ensemble mean and r.m.s. velocity data. The velocity measurements provide a precision of up to 98% confidence, as previously discussed in detail in Thong et al., [23].

2.3 Studies Flow Cases

Both the side-jet and the primary flow momentums were manipulated to achieve the required jet to cross-flow momentum ratio (MR). Shown in Table 1, are the flow parameters for the cases studied in both the 3SJ and 4SJ configurations. The Reynolds Number (Re) of the primary pipe flow for most cases are within the turbulent flow regime. Flow cases with MR = 0.08 and 0.2 were tested in a primary flow of Re = 4500, whilst flow cases MR = 0.04 and 0.1 were tested in a primary flow of Re = 6700. Flow cases MR = 0.6 was conducted with primary flow of Re = 2800.

2.4 Computational Model and Domain

Commercial Computational Fluid Dynamics (CFD) package ANSYS CFX was used to model the flow inside and outside the nozzle. These runs are used to better understand the flow structures and behaviour not possible through experimental methods, by using a validated numerical representation of the flow. In particular, the model is used to better understand the axis-switching phenomenon caused by the vortical interactions inside the pipe. The domain tested included a 1000mm long, 56mm nominal diameter primary pipe, and lateral jets with nominal diameter of 6mm, to match the experimental rigs' dimensions. Both primary and side-jets' inflows were treated as inlets, pipe wall treated as non-slip wall, and region outside the pipe treated as entrainments.

Unstructured tetrahedral meshes were used for the 3-D models to better capcute the feature of the flow. The SST-kω turbulence model was used due to its applicability to many turbulent flows [18]. the calculation was done on a steady-state mode and the solutions deemed to converge when the RMS error values for all variables were reduced below 10^{-6}. A grid independence study was conducted and it showed that the model reaches 0.5% of uncertainty (based on centreline mean velocity) with $4{\times}10^6$ elements, which is within the acceptable range of confidence for the purpose of this study.

3 Results

3.1 Streaming flow regime

Shown in Figure 3, are the instantaneous and mean dye mixture fraction images for the 3SJ flow cases: (a) MR = 0.04; (b) MR = 0.08; and (c) MR = 0.1 at planar locations z/D_P = 0.25; 0.5; 0.75; and 1, as indicated on the

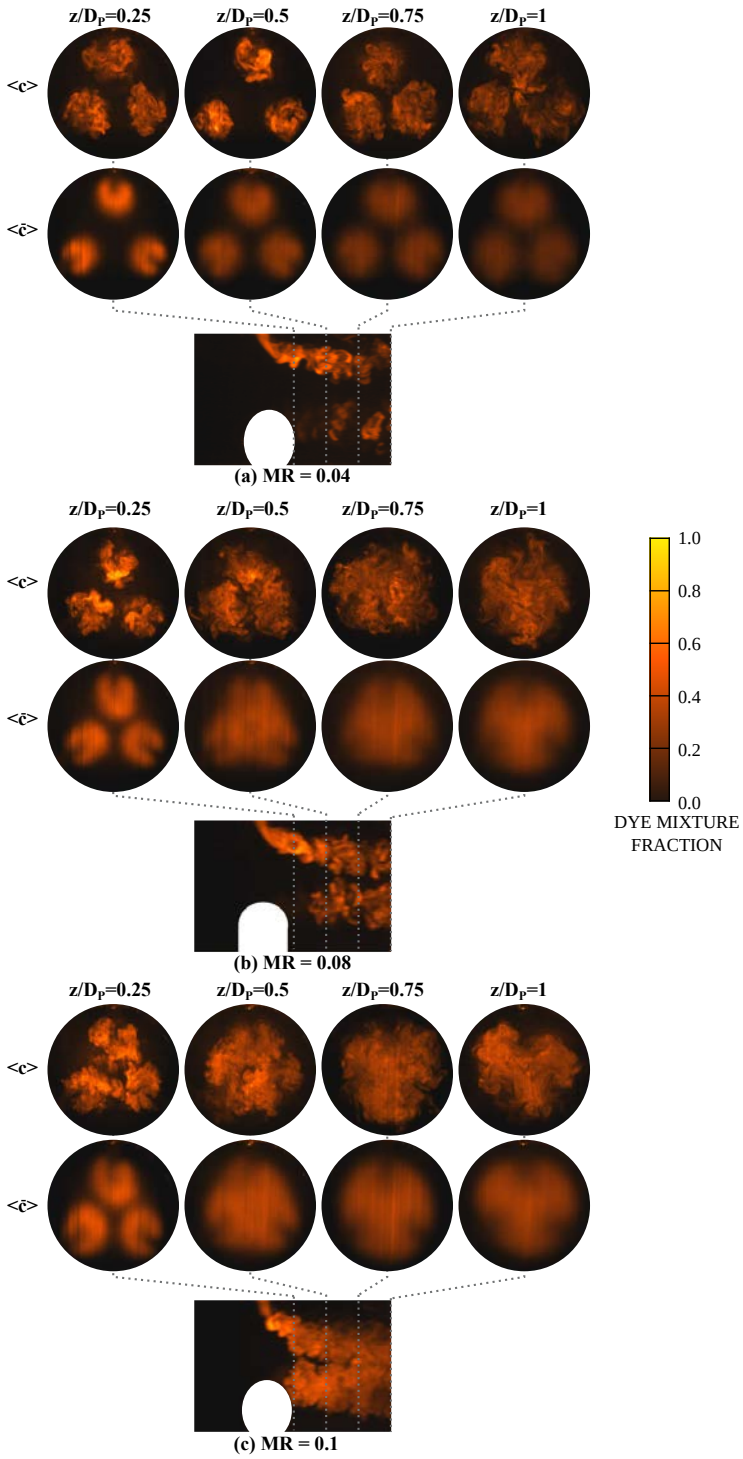

Figure 3: Instantaneous $< c >$ and ensemble mean $< \bar{c} >$ dye mixture fraction at planar locations $z/D_P = 0.25$, 0.5, 0.75 and 1 for 3SJ flow cases: (a)MR = 0.04; (b) MR = 0.08; and (c) MR = 0.1. Also shown are the instantaneous axial dye mixture fraction image for the corresponding cases. The images are scaled to the unmixed dye mixture i.e. 0.0 for clean water (darker regions) and 1.0 for unmixed dye mixture (brighter regions), shown by the accompanying colormap.

typical axial plane dye mixture fractionimage. The side-jets are placed at $z/D_P = 0$ whilst $z/D_P = 1$ indicates the primary nozzle exit. The flow in the typical axial plane dye mixture fraction image flow from left to right of the image. Here, the positioning of the side-jets are as indicated in Figure 1. The images are scaled to the unmixed dye mixture where brighter region indicates heavier presence of dye and darker region lower presence of dye.

Counter-rotating vortex pairs (CVPs) are observed, in particular at z/D_P = 0.25 in all three cases shown in Figure 3(a), (b), and (c). CVPs are commonly found in jets in cross-flow arrangement [2] and they resemble a 'horse-shoe' profile in the mean dye mixture fraction profile $< \bar{c} >$, as seen in the aforementioned locations.

The MR = 0.04 case shows the CVP profiles development of a typical multi-lateral jet flow, i.e. CVPs freely develop downstream with little interaction. Progressing downstream, the dye mixture fraction of the CVP profiles reduces as they are gradually being mixed by the cross-flow. The CVPs are expected to further expand downstream, out of the nozzle.

The increase in the momentum ratio to MR = 0.08 and MR = 0.1 is reflected by the proximity of the CVPs in Figure 3(b) and 3(c), in particular in the mean images at location $z/D_P = 0.5$. Further downstream, it is observed that the dye profiles gradually morphed into a "Y" profile, with branches formed at spaces in between side-jets (where no physical side-jets are placed). This morphine phenomenon is regarded as a subset of 'axis-switching' commonly found in studies related to non-circular jet studies [24, 5].

The axial planes for the typical instantaneous dye mixture fraction images shown in Figures 3(a), 3(b) and 3(c) capture the coherent large-scale structures formed through the interaction of the side-jets with the cross-flow. Coherent large-scale structures are more prominent in the axial plane presented in Figure 3(a) due to the low penetrating MR of the side-jet. The formation of these large-scale structures were previously correlated to Kelvin-Helmholtz wake structures in a study by Kelso et al., [11].

Figure 4 shows the instantaneous ($< c >$) and mean dye mixture fraction ($< \bar{c} >$) images for the 4SJ flow cases: (A) MR = 0.04; (b) MR = 0.08; and (c) MR = 0.1 at planar locations, z/D_P = 0.25; 0.5; 0.75; and 1, as indicated on the axial plane dye mixture fraction image. The side-jets are placed at $z/D_P = 0$ whilst $z/D_P = 1$ indicates the primary nozzle exit. The flow in the typical axial plane dye mixture fraction image flow from left to

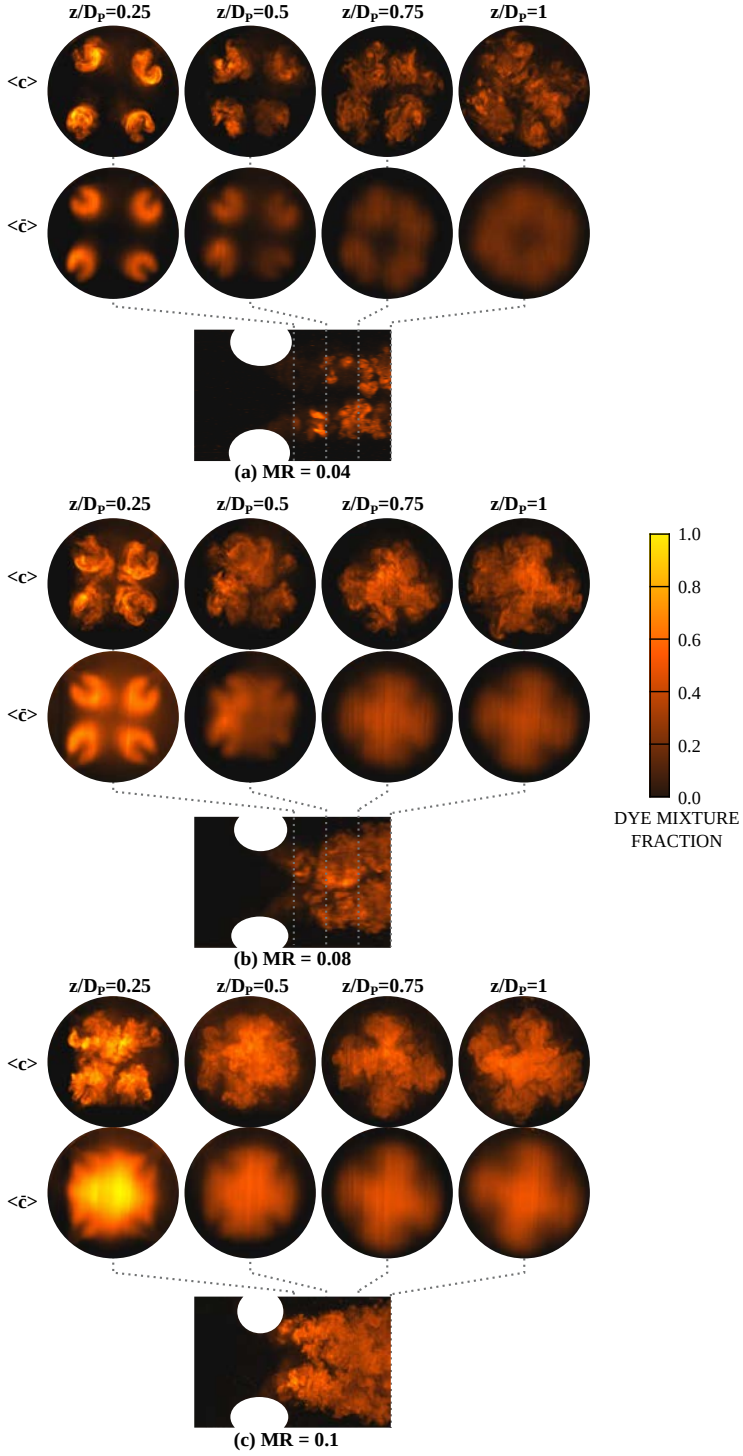

Figure 4: Instantaneous $< c >$ and ensemble mean $< \bar{c} >$ dye mixture fraction at planar locations, $z/D_P = 0.25$, 0.5, 0.75, and 1 for 4SJ flow cases: (a) MR = 0.04; (b) MR = 0.08; and (c) MR = 0.1. Also shown are the instantaneous axial dye mixture fraction image for the corresponding cases. The images are scaled to the unmixed dye mixture i.e. 0.0 for clean water (darker regions) and 1.0 for unmixed dye mixture (brighter regions), shown by the accompanying colormap.

the right of the image. The planar locations of the 4 side-jets are indicated in Figure 1. The images are scaled to the unmixed dye mixture where brighter region indicates heavier presence of dye and darker region lower presence of dye.

At MR = 0.04, the mean dye mixture fraction at the planar locations, z/D_P = 0.25 to z/D_P = 1 resembles the corresponding MR = 0.04 flow case in 3SJ configuration shown in Figure 3(a), both in terms of penetration into the confined flow, and dilution of the CVP progressing downstream. This shows that, albeit the additional mass-flow contributed by the additional side-jet, the flow still conforms to the momentum-ratio dependency. Furthermore, large-scale coherent structures are also obvious in the axial plane.

Counter-rotating vortex pairs are also observed in the instantaneous mixture fraction images at z/D_P = 0.25 in both flow cases MR = 0.08 and 0.1 in Figures 4(a) and 4(c), respectively. Progressing downstream, a cruciform profile is formed, and is more prominent near the nozzle exit at z/D_P = 1. However at MR = 0.1, the side-jets are observed to converge at the centreline at around z/D_P = 0.5, which is at an earlier stage compared to similar flow case in the 3SJ configuration.

3.2 Impinging flow regime

Figure 5 shows the instantaneous and ensemble mean planar dye mixture fraction at axial locations, z/D_P = 0.25, 0.5, 0.75, and 1, of flow case MR = 0.2 for the 3SJ (Figure 5(a)) and 4SJ (Figure 5(b)) configurations. The axial locations of the planar cross-section images are marked on the instantaneous dye mixture fraction image in the axial plane, in the corresponding sub-figures.

The flow case in this MR is characterized as impinging flow as the stream issued out of the side-jets impinge on the flow centreline a short distance downstream. The impinging points are usually close to the side-jets, as seen in the axial dye mixture fractions images in Figures 5(a) and 5(b). The effects of impingement are also observed in the cross-section images at z/D_P = 0.25, where high dye concentration is observed near the centreline of the flow.

Impingement of the side-jets hastens the development of the “Y” and cruciform profiles as is abundantly clear in both the instantaneous and mean profiles at z/D_P = 0.25. Therefore, it is hypothesized that the precursor of the axis-switching in such a geometrical configuration is the initial rolling of the side-jets by the primary flow, similar to that commonly seen in jets in

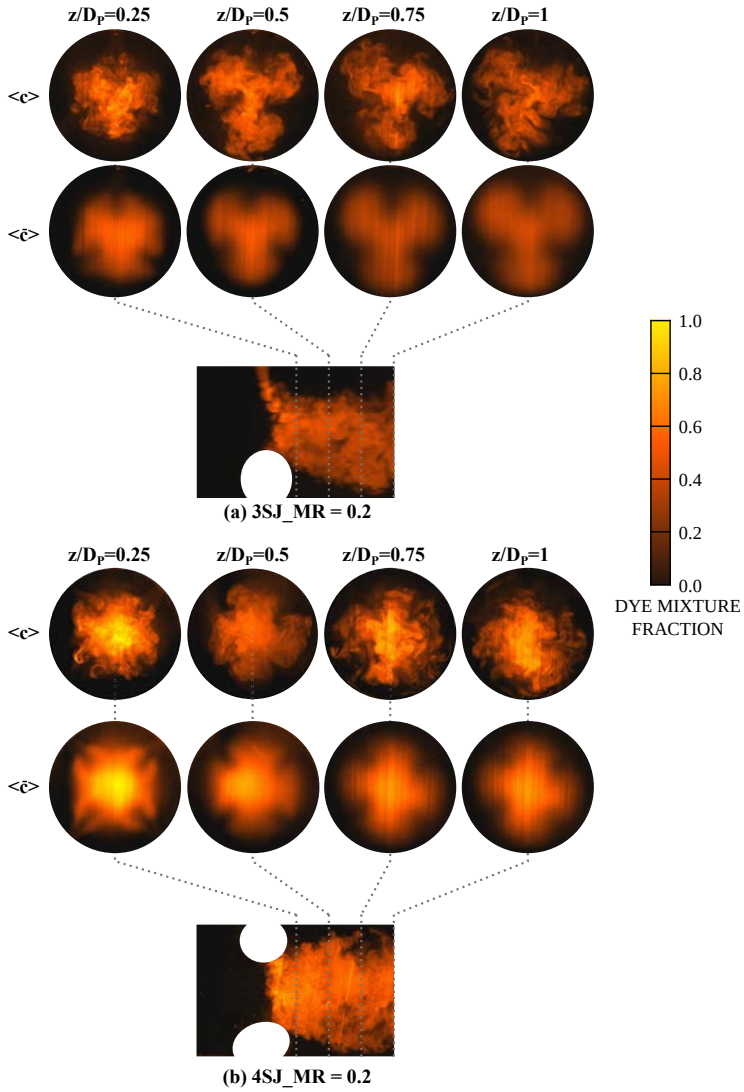

Figure 5: Instantaneous $< c >$ and ensemble mean $< \bar{c} >$ dye mixture fraction at planar locations, $z/D_P = 0.25$, 0.5, 0.75, and 1 for (a) 3SJ MR = 0.2 and (b) 4SJ MR = 0.2 flow cases. Also shown are the instantaneous axial dye mixture fraction image for the corresponding cases. The images are scaled to the unmixed dye mixture i.e. 0.0 for clean water (darker regions) and 1.0 for unmixed dye mixture (brighter regions), shown by the accompanying colormap.

cross-flow studies. Progressing downstream, up to the nozzle exit, the profiles remained unchanged.

Impinging flow regime for both the 3SJ and 4SJ configurations shows axis-switching phenomenon, with distinct differences in the resulting profiles for each configuration. The profile after axis-switching for the 3SJ configuration shows a relatively uniform dye distribution in the branches and in the centre-line. Comparatively, the 4SJ configuration shows higher dye mixture fraction near the centreline compared to the dye mixture fraction in the branches (approximately 20% higher). This will be further discussed in the coming sections using the numerical results from the CFD study.

3.3 Backflow regime

Increasing the flow momentum-ratio past the impinging flow regime results in an impingement point on the centreline, near $z/D_P = 0$, and a deflection of the side-jets flows in both downstream and upstream directions. The flow deflected upstream is carried downstream by the primary flow. Some details pertaining the backflow regime were previously discussed in Thong et al., [23].

The instantaneous cross-sectional dye mixture fraction for both 3SJ and 4SJ in Figures 6(a) and 6(b) show a chaotic flow at all axial locations down-stream. The mean images capture an intense stream propagating along the centreline of the primary flow, up to the nozzle exit at $z/D_P = 1$, which can also be observed in the axial plane. Unlike the flow regimes in the lower MR, no coherent flow profiles, i.e. both the "Y" or cruciform profiles are observed in the backflow regime.

3.4 Effect of MR on axial flow

Figure 7 shows the ensemble mean dye mixture fraction in the axial plane for: (i) 3SJ and (ii) 4SJ configurations for flow cases: (a) MR = 0.04; (b) MR = 0.08; (c) MR = 0.1; (d) MR = 0.2; and (e) MR = 0.6. These dye mixture fraction distributions are scaled to the undiluted dye mixture, i.e. mixture fraction of 1.0 represents the undiluted dye and 0.0 represents clean water. Dye mixture fraction for flow case MR = 0.04 in Figure 7(a) is scaled to 0.5 for clarity.

The mean PLIF images are ensemble averaged from 200 PLIF images. Physical fixtures in the imaging planes are masked off. The locations of the laser sheet and imaging plane with respect to placement of the side-jets are as

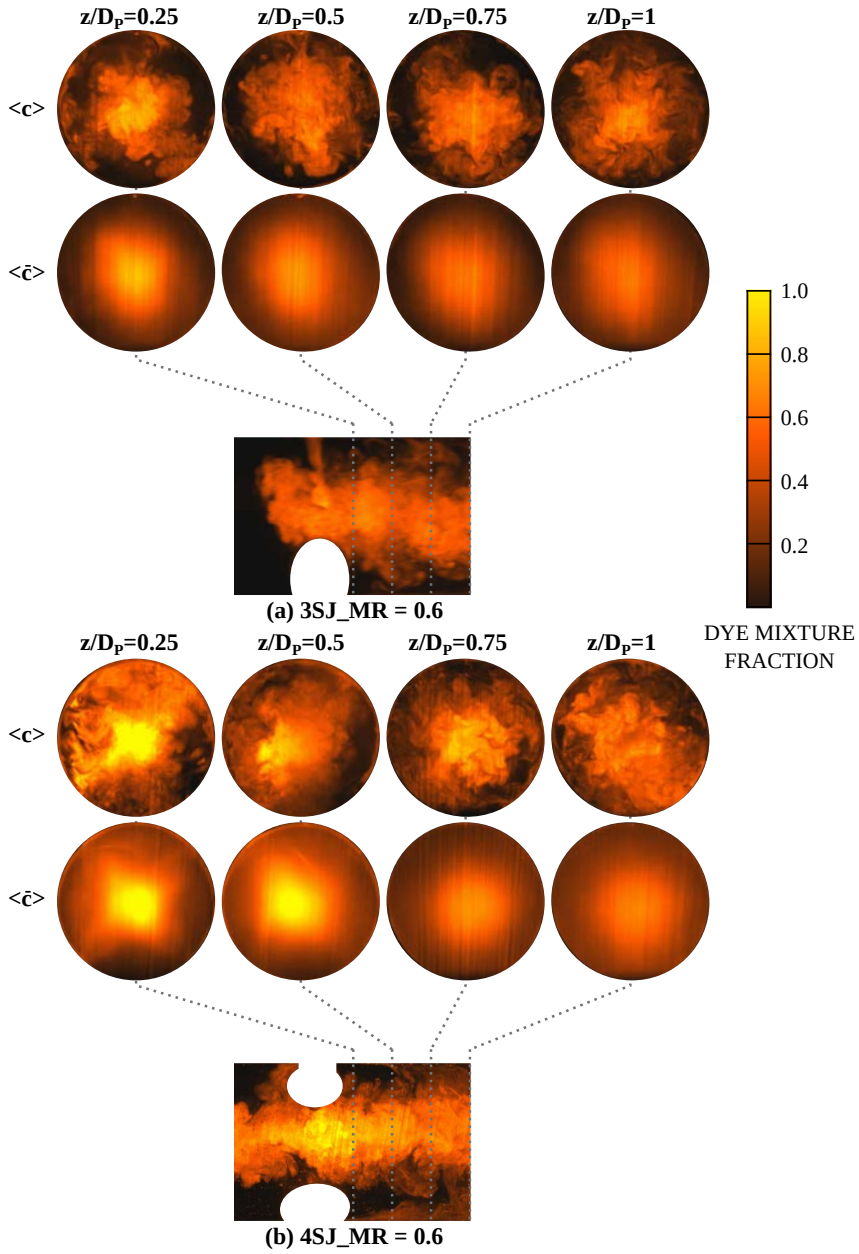

Figure 6: Instantaneous $< c >$ and ensemble mean $< \bar{c} >$ dye mixture fraction at planar locations, $z/D_P = 0.25$, 0.5, 0.75, and 1 for: (a) 3SJ MR = 0.6 and (b) 4SJ MR = 0.6 flow cases. Also shown are the instantaneous axial dye mixture fraction images for the corresponding cases. The images are scaled to the unmixed dye mixture i.e. 0.0 for clean water (darker regions) and 1.0 for unmixed dye mixture (brighter regions), shown by the accompanying colormap.

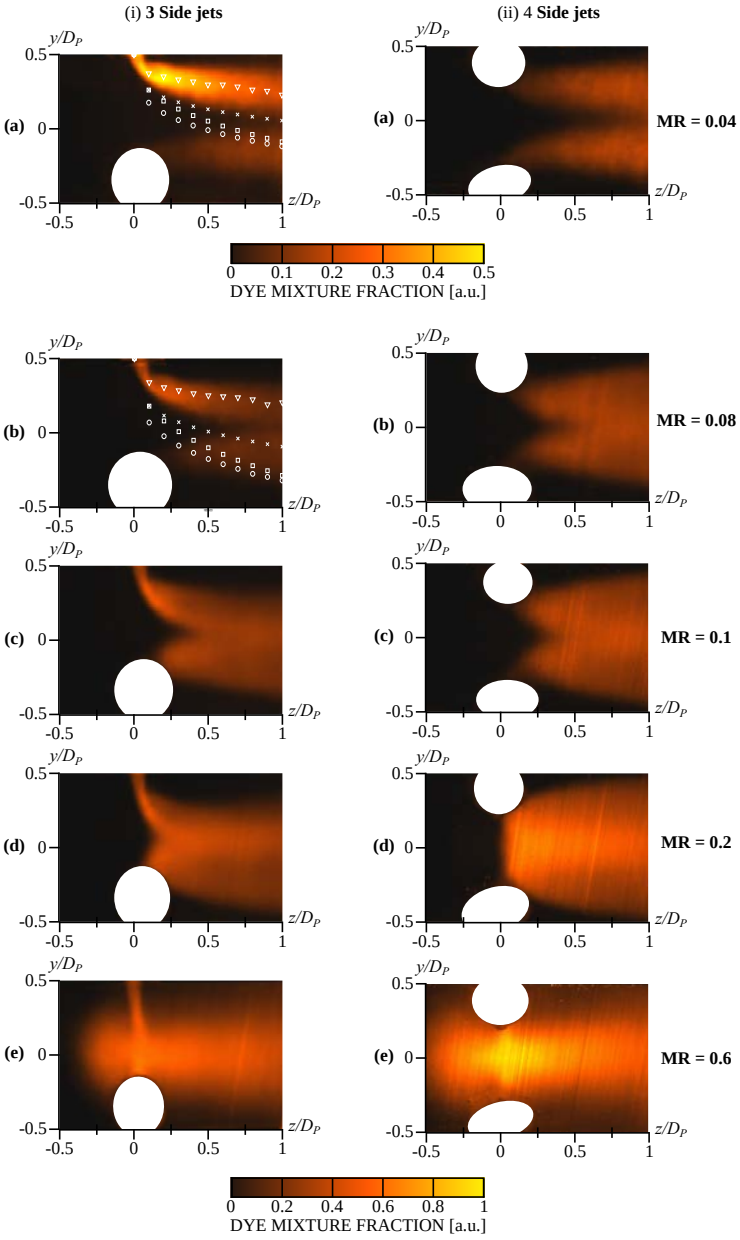

Figure 7: Ensemble mean dye mixture fraction of the axial plane for both 3SJ and 4SJ flow cases of: (a) MR = 0.04; (b) MR = 0.08; (c) MR = 0.1; and (d) MR = 0.2; and (e) MR = 0.6. The mean images are scaled to the unmixed dye mixture i.e. 0.0 for clean water and 1.0 for dye mixture. Figure 7(a) is acaled to 0.5 for clarity. △ marks the trajectory of the side-jet (based on local maxima) whilst '×', '□', and '○' marks the predicted trajectories by Smith and Mungal [21], Camussi et al., [1], and Pratte and Baines [19], respectively.

indicated in the schematic diagram for the experimental set up in Figure 1.

Progressing through the increase in flow MR, from Figure 7(a) to Figure 7(e) shows the change in the flow regime. Figure 7(a), (b), and (c) shows the dye interacts only at a distance downstream of the side-jets position axially, whilst Figure 7(d) shows the side-jets impinging on the centreline and are carried downstream by the main nozzle flow. The backflow regime is clearly demonstrated at MR = 0.6 shown in Figure 7(e), at which the backflow of the impinging jets is clearly observable.

As mentioned in Section 1, both jet in cross-flow and multi-lateral jet in cross-flow have direct applications in industry and scaling of both the flow trajectories and backflow length have previously been attempted. The trajectory of the streaming flow regime for flow cases MR = 0.04 and MR = 0.08 are plotted and marked in Figure 7(a)(i) and 7(b)(i), respectively with $\triangle$ - symbol, based on the local maxima. The trajectories of the side-jets are compared against common transverse jet scaling methods by: Smith and Mungal [21]($\times$ - symbols); Pratte and Baines [19] ($\circ$ - symbols); and Camussi et al [1] ($\square$ - symbols). The transverse jet scaling methods by Smith and Mungal [21] and pratte and Baines [19] are commonly referred to for most scaling studies, while Camussi et al [1] scales the side-jets for very low momentum-ratio.

Here, it is clear that common jet trajectory methods for unconfined flow are not suitable to scale the side-jets trajectory in a confined flow, let alone one with multiple side-jets. The conventional scaling methods over-predict the jets' trajectories, as they do not take into consideration the confinement geometry and the primary flow's centreline. The discrepancy highlights the need for further work to quantify the side-jets' trajectories in a confined cross-flow, whilst keeping the number of jets and the confinement geometry in consideration.

Figure 8 shows the normalized axial velocity w/w_p for the: (i) 3SJ and (ii) 4SJ configurations, and for flow cases: (a) MR = 0.04; (b) MR = 0.08; (c) MR = 0.1; (d) MR = 0.2; and (e) MR = 0.6. The velocity images are acquired by ensemble averaging a set of 220 PIV image pairs. The normalized axial velocity is scaled to the range of -2 $\leq w/w_p \leq$ 2, where $w/w_p = 1$ denotes the axial velocity of the primary flow velocity.

For the streaming flow regime cases of MR = 0.04 and MR = 0.08, the side-jets do not impact on the primary flow significantly. This is intuitive as

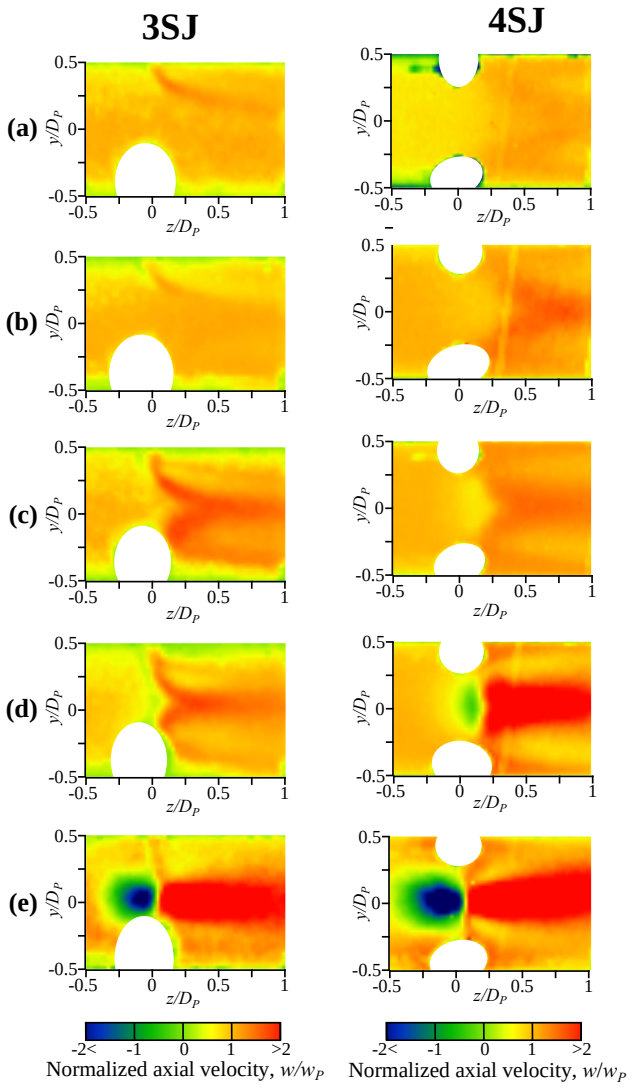

Figure 8: Normalized axial velocity in the axial plane for both 3SJ and 4SJ flow cases (experimental) of: (a) MR = 0.04; (b) MR = 0.08; (c) MR = 0.1; (d) MR = 0.2; and (e) MR = 0.6. The colour contour representing the velocities are as denoted by the colour bar.

the bulk flow is dominated by the strong primary flow momentum. Earlier in the previous sub-sections, it was established that increasing the flow MR results in the side-jets breaching the primary flow, which is also reflected in the axial velocity, seen in Figure 8(c) and Figure 8(d). At higher momentum ratio, addition of side-jets in a confined flow increases the centreline axial velocity, up to the nozzle exit. Furthermore, for impinging regime flow case, MR = 0.2 for both configurations in Figure 8(d), shows that the impingement of the side-jets reduces the velocity of the oncoming flow, in particular in the region immediately upstream of the impingement point. The backflow region in flow case MR = 0.2 is also clearly represented by the negative velocity region upstream of the impingement point.

The scaling of the backflow length in multilateral jet cases had also been conducted recently due to its importance in mixing applications. Study by Kartaev et al., [10] shows that the backflow penetration length upstream of the impingement point, measured by normalizing backflow length to the confinement diameter (h_v/D_P), is proportional to the mass-flow ratio.

Through observation of Figure 7, the length of the backflow can be scaled via dye mixture fraction and through the flow velocity methods. From the backflow regime of MR = 0.6 shown in Figure 7(e), the normalized length of the backflow is observed to be proportionate to the number of side-jets and MR,

$$\frac{h_{v-c}}{D_p} = knMR$$

HEre, n represents the number of side-jets and MR represents the flow momentum ratio. By conserving the flow MR and changing n, the constant, k, is calculated to be ≈ 0.18. The normalized backflow length here is measured at the point where the dye mixture fraction is half of the maximum dye mixture fraction at the impinging point.

Adopting the velocity scaling method from Kartaev et al., [10] results in the following scaling equation

$$\frac{h_v}{D_p} = kn\sqrt{MR}$$

where from the data presented in Figure 8(e), k is deduced to be around 0.16.

Shown in Figure 9, are results from the CFD study. Presented are the cross-sectional mixture fraction at axial locations, z/D_P = 0.25, 0.5, 0.75,

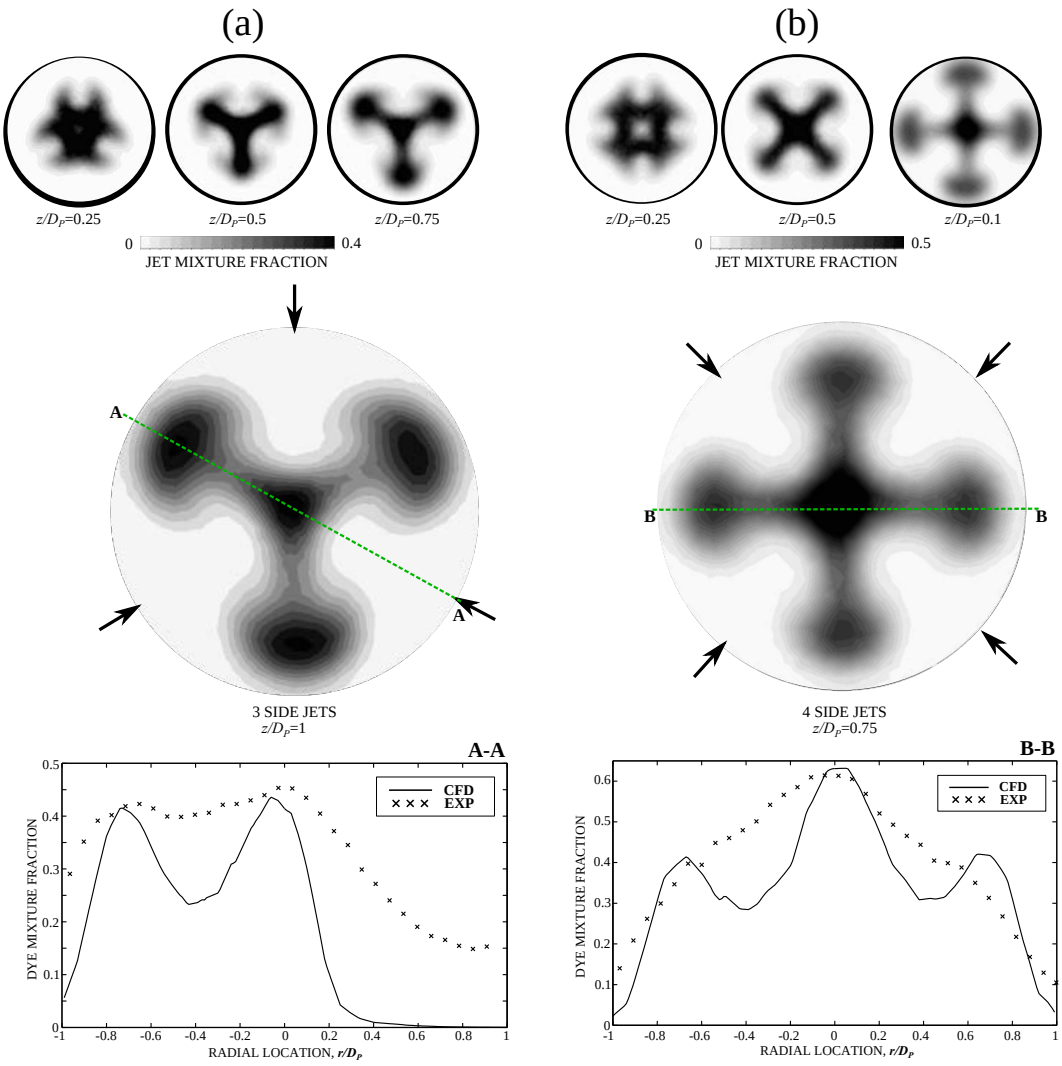

Figure 9: Modelled planar volume fraction profiles for flow case MR = 0.2: (a) 3SJ and (b) 4SJ, at axial locations, $z/D_P = 0.25$; 0.5; 0.75; and 1. The computed radial profiles at the exit plane, $z/D_P = 1$ and at $z/D_P = 0.75$, along line A-A (3SJ) and B-B (4SJ), respectively, are plotted (solid line) against experimental results (× - symbols).

and 1.0 for flow case MR = 0.2 for: (a) 3SJ and (b) 4SJ configurations. Also shown in the figure are the mixture fraction, radial distribution, at the measured planes, as indicated by the green dashed lines, whilst the arrows indicate the position of the side-jets upstream at $z/D_P = 0$. The dye mixture fractions from the experimental data for the same radial position are also plotted with the computed data.

Qualitatively, the volume fraction profiles for both 3SJ and 4SJ at z/D_P = 0.25; 0.5; 0.75 and 1 agree well with the mean dye mixture fraction at the corresponding locations previously discussed in Figure‘5. SImilar to the 3SJ flow profiles in Figure 5(a), the modelled 3SJ flow shows the profile after axis-switching and also equal distribution of volume fraction at the "branches". This is also true for the 4SJ profiles shown in Figure 9(b), which also indicate a higher volume fraction along the centreline compared to its branches, similar to that seen in Figure 5(b).

The comparison of the measured and computed radial profiles at the nozzle exit plane shows qualitative agreement for both A-A and B-B cross-sections. The model predicts the peaks in mass fraction well for both 3SJ and 4SJ configuration but over-predicts the trough region along the profile. The reason for such discrepancy may be due to the effect of dye diffusion at these positions in the experiments, which is not accounted for in the model. Nonetheless, for the purposes of the current study, the integrity of the model should be sufficient to assist in the understanding of related flow characteristics, especially axis switching.

Figure 10 shows the axial velocity profiles plotted at locations, z/D_P = 0; 0.5; 0.75; and 1, for flow case MR = 0.2 and for: (a) 3SJ and (b) 4SJ configurations. In this figure, solid line represents computational results, whilst the × - symbol represents experimental data. While the computational model is showing similar features to those measured experimentally, there are distinct differences especially at $z/D_P = 0.0$. These differences are more pronounced in the 4SJ case than the 3SJ case. The agreement close to z/D_P = 1 is reasonable for all cases, which will help us shed more light on the axis switching phenomenon.

4 Discussion

Figure 11 shows the modelled velocity curl $[s^{-1}]$ profiles for both (a) 3Sj and (b) 4SJ configurations at $z/D_P = 0.25$ and 1. The velocity curl at $z/D_P =$

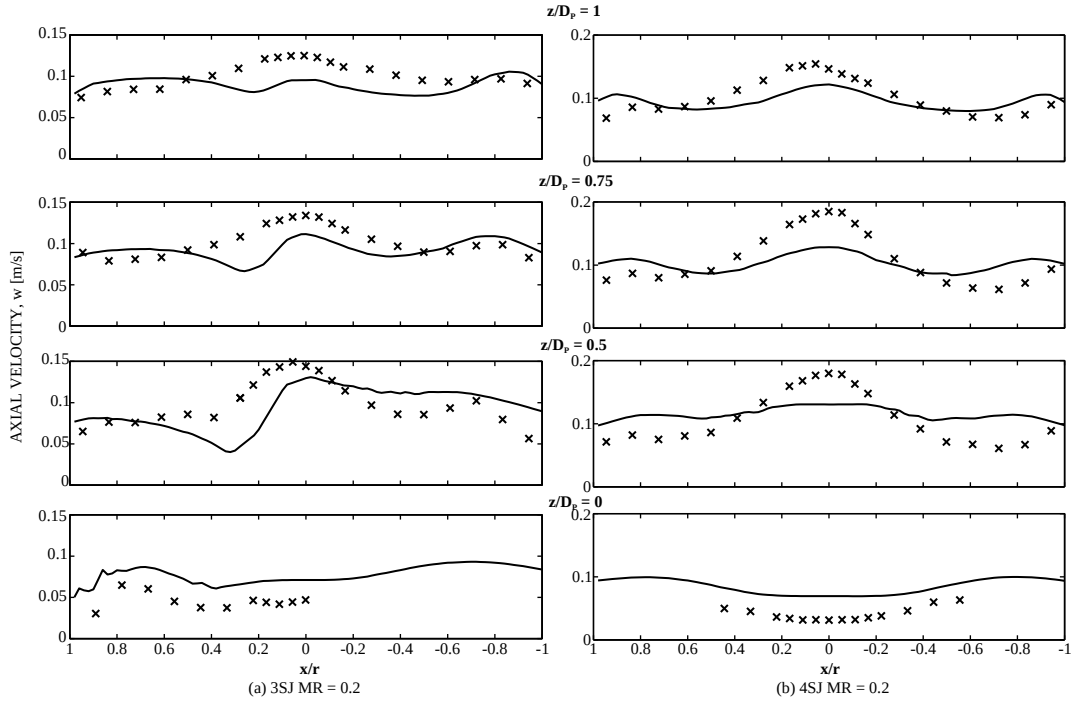

(a) 3SJ MR = 0.2 (b) 4SJ MR = 0.2

Figure 10: Axial velocity profiles of flow case MR = 0.2 from model (solid line) and experiment (× - symbols) plotted at $z/D_P = 0$; 0.5; 0.75; and 1, for (a) 3SJ and (b) 4SJ configurations.

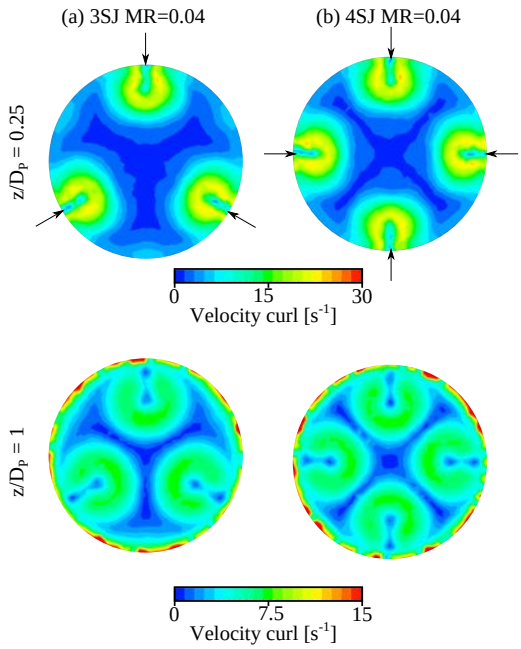

Figure 11: Modelled velocity curl $[s^{-1}]$ contours for the streaming flow case MR = 0.04 for (a) 3SJ and (b) 4SJ configurations at $z/D_P = 0.25$ and $z/D_P = 1$. The velocity curl at $z/D_P = 0.25$ and $z/D_P = 1$ are scaled to $30S^{-1}$ and $15s^{-1}$, respectively, for clarity.

0.25 and $z/D_P = 1$ is scaled to 30 s^{-1} and 15 s^{-1}, respectively. The relative location of the side-jets placed upstream at $z/D_P = 0$ is indicated by the arrows in the $z/D_P = 0.25$ row.

High velocity curl here indicates vorticity in the flow, where $\vec{\omega} = \nabla \times \vec{u}$, and are caused by both rotational and shearing motions. Figure 11(a) and Figure 11(b) show regions of high velocity curl is generated in the regions occupied by the CVPs (refer to Figure 3(a)). This is intuitive as CVPs are vortices that dominate the near flow-field, and induce vorticity in the flow [21]. Despite the additional side-jet in the 4SJ configuration, the region of high velocity curl of similar "sizes" can be observed. This shows that the presence of additional side-jet and hence vortex, in low momentum ratio does not drastically influence the vorticity in the flow.

At $z/D_P = 1$, the magnitude of the velocity curl in both 3SJ and 4SJ configurations diminishes. Here, the centreline of the flow shows low velocity curl (both at $z/D_P = 025$ and $z/D_P = 1$), which indicates an irrotational flow. This may be attributed to the evenly placed vortices cancelling out the vorticity closer to the centreline.

Figure 12 shows the modelled velocity curl contours for the impinging flow case MR = 0.2 for configurations: (a) 3SJ and (b) 4SJ, at locations $z/D_P =$ 0.25 and 1. The velocity curl for this figure is scaled to 30 s^{-1} for $z/D_P =$ 0.25 and 15 s^{-1} for $z/D_P = 1$, respectively.

Higher velocity curl is calculated in both 3SJ and 4SJ configurations at MR = 0.2, compared to MR = 0.04, in general. This is expected due to the higher momentum ratio presented in this flow case. Also, the 4SJ velocity curl profiles at $z/D_P = 0.25$ in Figure 12(b) appear "smaller" and stay relatively distant from the centreline as compared to the 3SJ configuration in Figure 12(a). Here, the "vortices" shown in the 4SJ configuration penetrate approximately 50% of the confinement's radius whilst in the 3SJ configuration, the penetration is a little more than 75% radius.

Velocity curl profiles at $z/D_P = 1$ show distinct differences to that seen in $z/D_P = 0.25$. Compared to MR = 0.04, flow case MR = 0.2 shows relatively higher velocity curl magnitude downstream at the nozzle exit. This shows that higher flow momentum ratio induces a higher vorticity into the flow, both in the near-field and in the far-field (approximately 9 side-jet's diameters downstream). Despite the higher flow momentum ratio and the side-jets impinging the centreline, the vorticity near the centreline remains low.

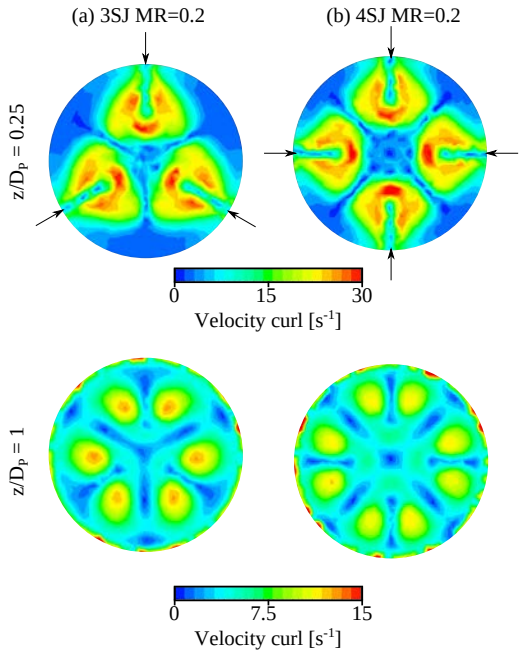

Figure 12: Modelled velocity curl $[s^{-1}]$ contours for the impinging flow case MR = 0.2 for (a) 3SJ and (b) 4SJ configurations at $z/D_P = 0.25$ and $z/D_P = 1$. The velocity curl at $z/D_P = 0.25$ and $z/D_P = 1$ are scaled to $30s^{-1}$ and $15s^{-1}$, respectively, for clarity.

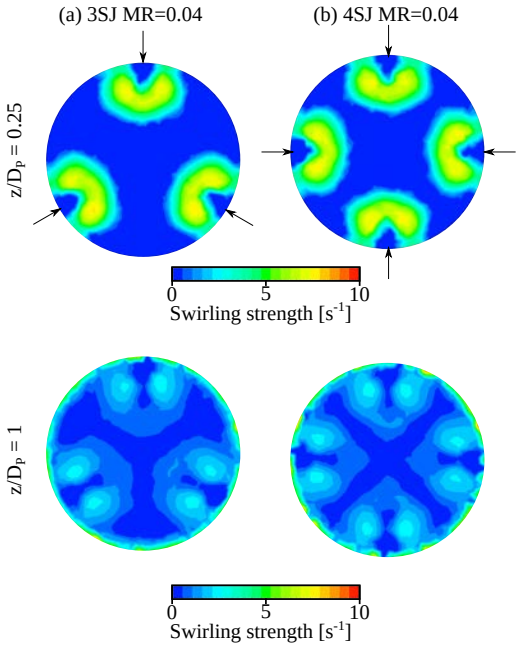

Figure 13: Modelled swirling strength $[s^{-1}]$ contours for the streaming flow case MR = 0.04 for (a) 3SJ and (b) 4SJ configurations at $z/D_P = 0.25$ and $z/D_P = 1$. The swirling strength at $z/D_P = 0.25$ and $z/D_P = 1$ are scaled to $10s^{-1}$.

Noteworthy that regions of high vorticity or velocity curl in the 4SJ configuration advect closer to the confinement walls compared to that in 3SJ. The regions of high vorticity in 4SJ being further away from the flow centreline is hypothesized to contribute to the more intense dye mixture fraction presence near the flow centreline, as seen in Figure 5(b). The relatively lower flow recirculation is hypothesized to cause a reservoir of dye travelling along the centreline. The region of high vorticity in 3SJ travels closer to the flow centreline, which assist in the almost equal dye distribution seen in Figure 5(a).

Figure 13 shows the modelled planar swirling strength contours at axial locations $z/D_P = 0.25$ and 1 for both the 3SJ and 4SJ configurations. The swirling strength for both locations are scaled to $10s^{-1}$ according to the attached colour map.

Figure 13 shows the magnitude of the swirling component in the vorticity, previously shown in Figure 11. Counter-rotating Vortex Pairs formed at $z/D_P = 0.25$ generates a strong swirling component at $z/D_P = 0.25$, which is intuitive, and diminishes as they advect downstream to $z/D_P = 1$. This

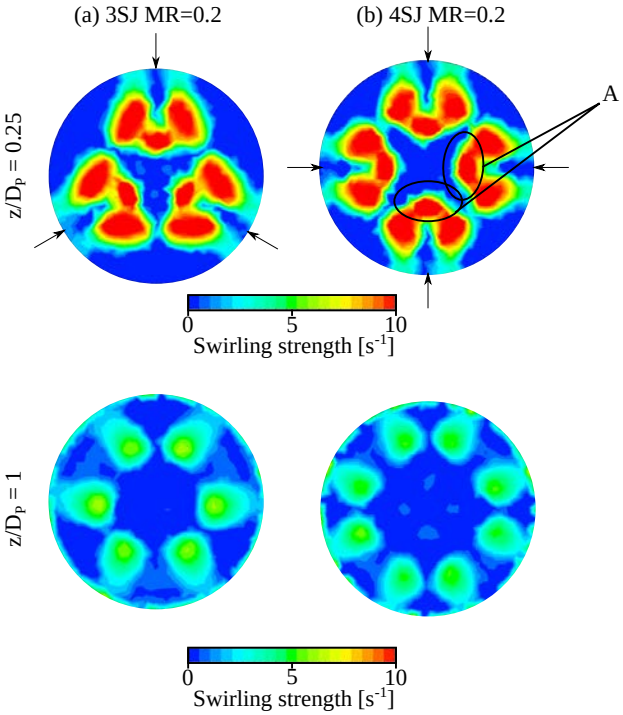

Figure 14: Modelled swirling strength $[s^{-1}]$ for the impinging flow case MR = 0.2 for (a) 3SJ and (b) 4SJ configurations at $z/D_P = 0.25$ and $z/D_P = 1$. The swirling strength is scaled to $10s^{-1}$.

further confirms that the dye mixture fraction profile and features seen in Figure 4(a) ($z/D_P = 1$) are not "frozen" and carried downstream by the initial CVP generation, but is rotational as well. Also, comparing the swirling strength profile at $z/D_P = 1$ to the corresponding location in Figure 11 shows that shearing components do exist in the flow, despite being dominated by the strong primary flow momentum. These shearing motions also promote small-scale mixing in the flow [17].

Figure 14 shows the modelled swirling strength for the impinging flow case MR = 0.2 for both 3SJ and 4SJ configurations. The swirling strength for both locations are scaled to 10 s^{-1}.

Higher swirl strength is achieved by flow case MR = 0.2 at $z/D_P = 0.25$ and 1 locations, compared to flow case MR = 0.04. Despite the impinging jets upstream, strong swirling motions are still predicted downstream at the nozzle exit, compared to the streaming flow. A more intense swirling component in

the flow promotes mixing between the different streams, and may be beneficial for partial-premixing applications.

The CVPs initially generated at $z/D_P = 0.25$ for this flow case induce a strong swirling component into the flow, which is expected. At $z/D_P = 1$, regions with strong swirling components overlap with regions where the vortices are "stationed". Compared to the corresponding velocity curl profiles in Figure 12, the regions outside these vortices show swirling components of low magnitudes (close to 0), which shows that the regions with high velocity curl in Figure 13 ($z/D_P = 1$) has high shearing motions.

Noteworthy, the regions with high swirling strength in between the vortex pairs (an example would be region A in Figure 14), diminishes downstream. The jets impinging immediately downstream diminishes the region, and hence is not visible further downstream, i.e. at $z/D_P = 1$.

The regions out of the vortices at $z/D_P = 1$ shows weak swirling components, despite the reasonably high velocity profiles, previously shown in Figure 12. This goes to show that the regions near and around the flow centreline is mainly dominated by shearing motions as a result of flow impingement upstream. This is beneficial for the flow mixing, in particularly to enhance small-scale mixing between the streams.

Figure 15 shows the modelled turbulent kinetic energy, TKE, which indicates the level of turbulence in the flow. Figure 15 shows the modelled TKE for flow case MR = 0.04 and scaled to 0.001 m^2s^{-2} and 0.0004 m^2s^{-2} at $z/D_P = 0.25$ and 1, respectively, for clarity.

Literature on side-jets have shown that JICF induces a region of high turbulence immediately downstream [9], which is consistent with the region of high TKE seen at $z/D_P = 0.25$, in both Figure 15(a)and Figure 15(b). The regions with high TKE at $z/D_P = 0.25$ dissipate as they progress downstream at $z/D_P = 1$. The TKE profiles at $z/D_P = 1$ in Figure 15 shows that the 4SJ configuration has a wider coverage of high TKE regions. This corroborates earlier findings [3] where mixing efficiency increases with the number of side-jets. However, as shown in Figure 15, the efficacy of turbulent mixing in the streaming flow regime is limited to the immediate near-field.

Figure 16 shows the modelled TKE for the impinging flow of MR = 0.2 for: (a) 3SJ and (b) 4SJ configurations, at $z/D_P = 0.25$ and 1. The TKE at $z/D_P = 0.25$ and 1 are scaled to 0.001 m^2s^{-2} and 0.0004 m^2s^{-2}, respectively.

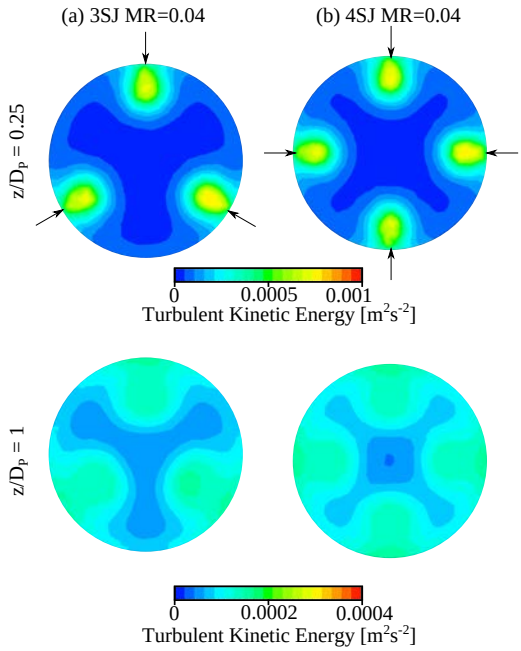

Figure 15: Modelled turbulent kinetic energy (TKE)$[m^2s^{-2}]$ for the streaming flow case MR = 0.04 for (a) 3SJ and (b) 4SJ configurations at $z/D_P = 1$. The TKE at $z/D_P = 0.25$ and $z/D_P = 1$ is scaled to 0.001 m^2s^{-2} and 0.0004 m^2s^{-2}, respectively, for clarity.

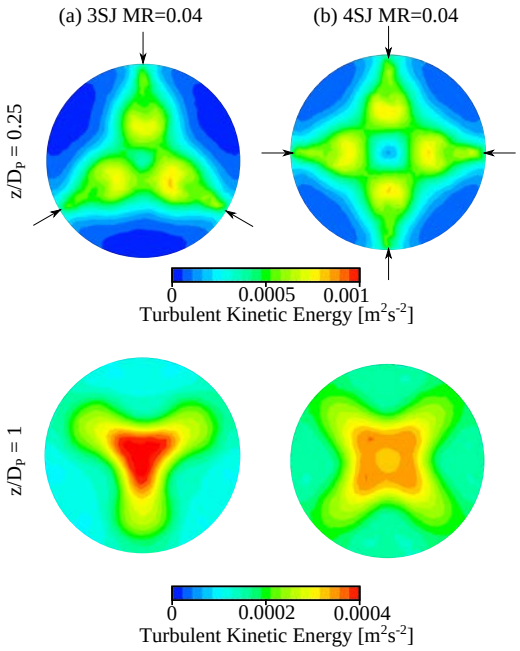

Figure 16: Modelled turbulent kinetic energy (TKE)$[m^2s^{-2}]$ for the impinging flow case MR = 0.2 for (a) 3SJ and (b) 4SJ configurations at $z/D_P = 1$. The TKE at $z/D_P = 0.25$ and $z/D_P = 1$ is scaled to 0.001 m^2s^{-2} and 0.0004 m^2s^{-2}, respectively, for clarity.

Higher momentum ratio leads to flow impingement increases the flow turbulence, in particularly at $z/D_P = 0.25$. Turbulent mixing is also seen over a wider region compared to the localized regions previously seen in Figure 15. Also, like the MR = 0.04 flow case, the region with higher TKE seen at $z/D_P = 0.25$ in Figure 16 coincides with the locations with high dye concentration seen previously in Figure 5(b) and Figure 9(b). Furthermore, despite the different number of side-jets, both 3SJ and 4SJ configurations show similar TKE magnitudes at $z/D_P = 0.35$.

Drastic differences in TKE profiles at $z/D_P = 1$ for the 3SJ and 4SJ configurations are observed. The 3SJ configuration induces a region of high TKE along the centreline and a "Y" profile in the cross-section corresponding to the dye mixture fraction images. Comparatively, the 4SJ configuration generates a slightly less intense TKE profile along the centreline, however, has a relatively higher TKE in the cross-section compared to the 3SJ. This is attributed to the higher blockage ratio that a 4SJ configuration has over the 3SJ (approximately 30% higher).

Comparing the streaming flow regime (MR = 0.04) to the impinging flow regime (MR = 0.2), it is obvious that the impinging flow regime promotes a more effective turbulent mixing. Instead of TKE dissipating, like that seen in Figure 15, the axis-switching of the vortices increases the TKE coverage (enhances TKE at both near wall regions and in the flow centreline)at $z/D_P = 1$, which is beneficial for flow mixing.

5 Conclusions

The current study focuses on the mixing of two streams, emerging from lateral jets into a confined cross-flow. Two configurations were studied, one with three equally spaced lateral jets (3SJ) and one with four equally spaced lateral jets (4SJ). The lateral-jets were placed 1 primary diameter upstream of the primary nozzle exit. The jet to cross-flow momentum ratios (MR) were varied to better understand the effect on mixing for both 3SJ and 4SJ configurations. Both PIV and PLIF techniques were used to measure the mixture fraction and the velocity fields, respectively. Computational Fluid Dynamics (CFD) method was also utilized to predict cross-sectional flow characteristics, that are not possible through experimental means.

The main findings of this study are:

- Both 3SJ and 4SJ follow similar regimes corresponding to the flow MR, i.e. streaming flow regime, impinging flow regime, and backflow regime;
- The Counter-Rotating Vortex Pairs (CVPs) in both configurations undergo axis-switching albeit with slight differences in mixture fraction distribution profiles, i.e. 3SJ configuration shows a more evenly distributed profile in a "Y" profile whilst 4SJ configuration shows a cruciform profile which consists of a more intense dye signal at the flow centreline;
- The vortices generated in 4SJ cases after axis-switching travels closer to the wall, which causes the more intense dye mixture presence near the centreline;
- The vortices generated in 4SJ cases after axis-switching travels closer to the wall, which causes the more intense de mixture presence near the centreline;
- The presence of side-jets increases the flow centreline velocity, both in 3SJ and 4SJ;
- Conventional scaling methods for jet in cross-flow do not scale the jet trajectories of a jet in a confined flow, which is limited to the primary flow centreline. The backflow length can be scaled to momentum ratio and the number of side-jets in the configuration adequately;
- CFD calculations show that jet impingement increases the vorticity, turbulent kinetic energy and the shearing components in the flow, which enhances mixing between the two streams.

Acknowledgements

The authors would like to acknowledge the contributions of the Australian Research Council for funding this project through a Discovery Grant DP110104410.

References

[1] R. Camussi, G. Guj, and A. Stella. Experimental study of a jet in a crossflow at very low reynolds number. *Journal of Fluid Mechanics*, 454:113–144, 2002.

[2] L. Cortelezzi and A. R. Karagozian. On the formation of the counter-rotating vortex pair in transverse jets. *Journal of Fluid Mechanics*, 208:347–373, 2001.

[3] J. D. Holdeman, D. S. Liscinsky, V. L. Oechsle, G. S. Samuelsen, and C. E. Smith. Mixing of multiple jets with a confined subsonic crossflow: Part 1 - cylindrical duct. *Journal of Engineering for Gas Turbines and Power*, 119:852–862, 1997.

[4] J. D. Holdeman, R. Srinivasan, and A. barenfeld. Experiments in dilution jet mixing. *AIAA Journal*, 22(10):1436, 1984.

[5] F. Hussain and H. S. Husain. Elliptic jets. part 1. characteristics of unexcited and excited jets. *Journal of Fluid Mechanics*, 208:257–320, 1989.

[6] P. A. M. Kalt, C. H. Birzer, and G. J. Nathan. Corrections to facilitate planar imaging of particle concentration of particle-laden flows using mie scattering, part 1: Collimated laser sheets. *Applied Optics*, 46:5823–5834, 2007.

[7] P. A. M. Kalt and M. Long. Oma-image processing for mac os x. www.oma-x.org, 2013.

[8] P. A. M. Kalt and G. J. Nathan. Corrections to facilitate planar imaging of particle concentration of particle-laden flows using mie scattering, part 2: Diverging laser sheets. *Applied Optics*, 46:7227–7236, 2007.

[9] Y. Kamotani and I. Greber. Experiments on a turbulent jet in a cross flow. *AIAA Journal*, 10(11):1425–1429, 1972.

[10] E. V. Kartaev, V. A. Emel'kin, M. G. Ktaklherman, V. I. Kuz'min, S. M. Aul'chenko, and S. O. Vashenko. Analyis of mixing of impinging radial jets with crossflow in the regime of counter flow jet formation. *Chemical Engineering Science*, 119:1–9, 2014.

[11] R. M. Kelso, T. T. Lim, and A. E. Perry. An experimental study of round jets in cross-flow. *Journal of Fluid Mechanics*, 306:111–144, 1996.

[12] M. Y. Leong, G. S. Samuelsen, and J. D. Holdeman. Optimization of jet mixing into a rich reacting crossflow. *Journal of Propulsion and Power*, 16(5):729–735, 2000.

[13] M. S. Mansour. A concentric flow conical nozzle burner for highly stabilized partially premixed flames. *Combustion Science and Technology*, 152:115–145, 2000.

[14] A. Masri. Partial premixing and stratification in turbulent flames. *Proceedings of The Combustion Institute*, 35:1115–1136, 2015.

[15] S. Meares and A. R. Masri. A modified piloted burner for stabilizing turbulent flames of inhomogeneous mixtures. *Combustion and Flame*, 161:485–495, 2014.

[16] T. H. New and W. L. Tay. Effects of cross-stream radial injections on a round jet. *Journal of Turbulence*, 57, 2006.

[17] W. R. Peltier and C. P. Caulfield. Mixing efficiency in stratified shear flows. *Annual Review of Fluid Mechanics*, 35:135–167, 2003.

[18] I. D. Piazzo and M. Ciofalo. Numerical predictions of turbulent flows and heat transfer in helically coiled pipes. *International Journal of Thermal Sciences*, 39:653–663, 2010.

[19] B. D. Pratte and W. D. Baines. Profiles of the round turbulent jet in a cross flow. *Journal of Hydronaulics Division*, 93:53–64, 1967.

[20] J. W. Shan, D. B. Lang, and P. E. Dimotakis. Scalar concentration measurements in liquid-phase flows with pulsed lasers. *Experiments in Fluids*, 36:268–273, 2004.

[21] S. H. Smith and M. G. Mungal. Mixing, structure and scaling of the jet in crossflow. *Journal of Fluid Mechanics*, 357:83–122, 1998.

[22] C. X. Thong, B. B. Dally, C. H. Birzer, P. A. M. Kalt, and E. R. Hassan. An experimental study on the near flow field of a round jet affected by upstrema multilateral side-jet. *Experimental Thermal and Fluid Science*, 82:198–211, 2017.

[23] C. X. Thong, P. A. M. Kalt, B. B. Dally, and C. H. Birzer. Flow dynamics of multi-lateral jets injection into a round pipe flow. *Experiments in Fluids*, 26(1):1–16, 2015.

[24] K. B. M. Q. Zaman. Axis switching and spreading of an asymmetric jet: the role of coherent structure dynamics. *Journal of Fluid Mechanics*, 316:1–27, 1996.

Chapter 6

Impact of multilateral jet on turbulent jet combustion

6.1 Overview

Chapter 3 and Chapter 5 show that varying the jet to cross-flow momentum ratio in the pipe induced different flow regimes: streaming flow, impinging and backflow. The different side-jets configurations (3 side-jets and 4 side-jets), generate different flow structures and different planar flow profiles in the pipe, upstream of the nozzle exit. Chapter 4 shows the effects the momentum-ratio have on the jet outflow.

However, flow structures and hydrodynamics of flow vary vastly for both isothermal and reacting conditions, owing to the heat release from the reactants' chemical reaction. Despite the drastic effect seen in the isothermal studies, it is unknown if these effect will be carried downstream, out of the nozzle, into the reaction zones. The study in this chapter focuses in the effects of MR and the different side-jets configurations on the flame characteristics (Objective (iii)), in particular in the near-field.

Here, a stainless steel long pipe nozzle was fitted with two multilateral jet configurations, a 3 side-jets and a 4 side-jets. Natural gas was injected through the side-jets into the cross-flow air in the primary nozzle to induce partial premixing, before exiting the nozzle. Bulk flow out of the nozzle exit was maintained at Re_b=7000. The same reactants mixture equivalence ratio is tested for both the 3 side-jets and the 4 side-jets configurations. OH*-chemiluminescence and Particle Image Velocimetry studies are conducted in the region immediately downstream of the nozzle exit to study the flame structures and flow-field, respectively.

This study shows that:

- Lifted flames and attached flames are generated corresponding to the upstream mixing regimes, impinging and backflow regimes, respectively. This directly affects the flame length;
- A stable flame cannot be stabilized under the streaming flow regime at this Reynolds Number;
- The effect of momentum-ratio and side-jets configuration extend up to $1D_P$ downstream, and is observed mostly on the radial v_{rms} and OH* chemiluminescence profiles.

The results of this study have been written in a paper which was submitted for publication in the journal *Flow, Turbulence and Combustion* in January 2017. The paper is titled “Effects of multilateral jet mixing on the stability and structure of turbulent partially-premixed flames", authored by Chia X. Thong, Bassam B. Dally, Paul R. Medwell and Cristian H. Birzer.

6.2 Manuscript

Statement of Authorship

Title of Paper	Effect of Multi-lateral Jet Mixing on Stability and Structure of Turbulent Non-premixed Flames
Publication Status	☐ Published ☐ Accepted for Publication ☑ Submitted for Publication ☐ Unpublished and Unsubmitted work written in manuscript style
Publication Details	Submitted to Flow, Turbulence, and Combustion Journal in January 2017

Principal Author

Name of Principal Author (Candidate)	CHIA XIONG THONG		
Contribution to the Paper	Performed literature review; designed and manufactured test burner; set up and conducted PIV and OH*-chemiluminescence; performed data processing, analysis and interpretation; structured and drafted manuscript		
Overall percentage (%)	65		
Certification:	This paper reports on original research I conducted during the period of my Higher Degree by Research candidature and is not subject to any obligations or contractual agreements with a third party that would constrain its inclusion in this thesis. I am the primary author of this paper.		
Signature		Date	30/01/2017

Co-Author Contributions

By signing the Statement of Authorship, each author certifies that:

i. the candidate's stated contribution to the publication is accurate (as detailed above);

ii. permission is granted for the candidate in include the publication in the thesis; and

iii. the sum of all co-author contributions is equal to 100% less the candidate's stated contribution.

Name of Co-Author	BASSAM DALLY		
Contribution to the Paper	Supervised development of work, interpreted data, and edited manuscript		
Signature		Date	02 FEB 2017

Name of Co-Author	CRISTIAN BIRZER		
Contribution to the Paper	Edited manuscript		
Signature		Date	30 JAN 17

Please cut and paste additional co-author panels here as required.

Name of Co-Author	PAUL MEDWELL		
Contribution to the Paper	Mentored and assisted in experiment work, data interpretation and edited manuscript		
Signature		Date	30-JAN-2017

Effect of multilateral jet mixing on stability and structure of turbulent partially-premixed flames

Chia. X. Thong • Bassam. B. Dally •Paul R. Medwell •Cristian. H. Birzer

Abstract

An experimental study was conducted to investigate the effects of multilateral jet mixing, using both three and four side-jets, on the structure and stability of turbulent partially-premixed flames. Particle Image Velocimetry and OH*-chemiluminescence were used to study the effects of geometry and operating conditions on the resulting flow-field and reaction zone structures, respectively. These effects were compared under varying ratios of side-jet to primary flow momentum, whilst keeping the bulk flow constant. It was found that the mixing regimes upstream of the nozzle exit affect the flame characteristics, i.e. an impinging regime is likely to generate a lifted flame whilst a backflow regime is likely to generate an attached flame. Unlike the 4 side-jets cases, the OH* images and v_{rms} profiles for the 3 side-jets cases show distinct asymmetry, with intense OH* and low velocity fluctuations on the opposite sides of the fuel injection. It was also found that the flow and scalar fields become independent of the upstream conditions, for both 3 and 4 side-jets, after one diameter downstream of the nozzle exit.

1 Introduction

Mixing of reactants affects flame characteristics, combustion efficiency, pollutants emission (including soot generation), and flame stability, hence is commonly manipulated to adapt to different fuel compositions in burners [26]. The interactions between flow turbulence, reaction kinetics, and heat transfer are complex and often coupled [33]. This is particularly true for turbulent jet flames, which are commonly used to achieve the high temperatures required for practical applications [12]. Mixing of reactants for combustion is usually modified by altering the jet burners' aerodynamic features, which is effective in changing the outflow profile and flow turbulence [11].

Enhanced mixing of reactants affects the stability of flames, which is vital to ensure process quality, safety and operational continuity. Flames can be statistically stable, either being attached or lifted off the burner exit [23]. The stability mechanism behind lifted-flames has been widely discussed and can be correlated to: large-scale structures in the flow; flamelets theory;

and generation of partial premixing upstream of the flame front [18]. Of these, partial-premixing based techniques are relatively new and require more research.

Partial premixing involves the addition of air to the fuel stream (at a level below the fuel-rich extinction limit), and can sometimes be achieved through stratification of flow, as reviewed by Masri [20]. The generation of partially premixed flames can be done by inducing inhomogeneity at the fuel inlets, or generated between the injector exit plane and flame base. An example of recent laboratory-scale generated partially premixed flames is the modified University of Sydney piloted flame [21] and the Concentric Flow Conical Nozzle (CFCN) burner [19]. These burners demonstrated enhanced stability compared to simple turbulent jet burners.

Both Meares and Masri [21] and Mansour [19] designed concentric tube burners. The enhanced stability in these devices (around 40% more stable than a conventional non-premixed turbulent jet flames [2]) is attributed to shear mixing and partial premixing characteristics. Despite the enhanced stability, an external stabilizing mechanism is still required to stabilize these flames at high Reynolds Number. it was hypothesized by Masri [20], that by partial premixing the reactants a short distance upstream of the nozzle exit, a stable and cleaner flame can be generated, due to the mixed mode combustion induced. The same principle will be attempted in the current study via jet in cross-flow technique via multilateral jet burner, as opposed to the concentric tube flows attempted in the mentioned studies.

The jet in cross-flow (JICF) configuration is practical in applications that require enhanced mixing between two streams. Jets placed laterally to the oncoming flow generate large-scale structures [8] to induce strong entrainment, thereby increasing turbulence which indirectly enhances the generation of small-scale structures and eventually molecular-scale mixing of the reactants, subsequently combustion [32]. Various industrial applications have been developed employing the characteristics of JICF, in particular for chemical mixing and to rapidly quench rich flames. Jet in cross-flow have been shown to benefit combustion systems [14, 3], however, a greater understanding of JICF mechanisms is still needed for further optimization and utilization.

Jet in cross-flow, when placed in a confinement, has limited mixing abilities due to the restricted growth of the counter-rotating vortex pair (CVP), which dominates the flow mixing. Therefore, to compensate for the reduction in mixing efficiency, more than one side-jet is usually used within the

confinement for example the Rich Burn/ Quick Quench/ Lean Burn (RQL) combustors which use between 6 and 18 side-jets for enhanced mixing [13]. To mitigate the complications to this fundamental study that may arise from the large number of jets used, the multilateral jet burner described in this manuscript uses three and four lateral jets placed a short distance upstream from the nozzle exits to premix combustion reactants before being combusted.

Multilateral jet mixing studies have been carried out in isothermal conditions, to understand the mixing mechanisms for a range of different applications. Various studies [13][17][22] have identified the counter-rotating vortex pairs (CVPs) generated within the flow as a dominant flow feature, which influence the mixing process. Different mixing regimes may be encountered in the multilateral jet configuration, which can be related to the jet to cross-flow momentum ratio (MR)

$$MR = \frac{(\rho V^2 A)_{inj}}{(\rho V^2 A)_P} \tag{1}$$

where the subscripts inj and P refer to the side-jets and the primary flow, respectively. Here, ρ denotes the density $[kg/m^3]$, V the velocity $[m/s]$, and A the hydraulic area of the side-jet and cross-flow $[m^2]$. Based on the relative momentum of the two streams, three regimes may be identified:

- **Streaming flow regime**, which is found in low MR cases where the side-jets injected are advected downstream by the strong primary flow momentum and may penetrate the flow centreline further downstream (shown in Figure 1(a)). This mixing in this flow regime is dominated by CVPs and other shear-induced structures.

- **Impinging flow regime**, which is the result of increasing side-jets MR where the side-jets impinge upon the flow centreline immediately downstream (Figure 1(b)). The impingement forms a stagnation region upstream and form a secondary stream of premixed fluid along the centreline.

- **Backflow regime**, which is formed by increasing the side-jets MR past the point of the impinging flow regime, presented in Figure 1(c). This flow regime creates a backflow upstream of the impinging point in addition to a secondary stream that propagates downstream. The backflow premixes with the primary flow and propagates downstream around the secondary stream (represented by the region with a lighter shade of grey in Figure 1(c)).

Isothermal studies conducted previously on an acrylic replica of the multilateral jet burner used in the current study show that by injecting dye (fuel)

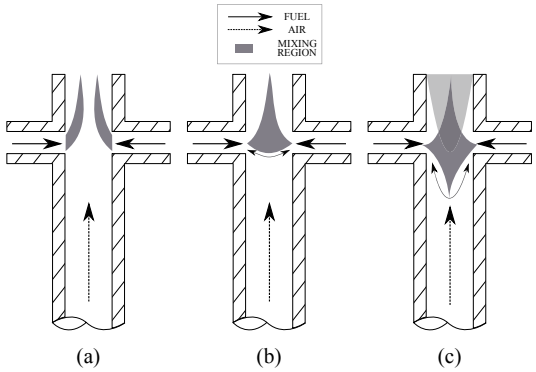

Figure 1: Representation of typical multilateral jet mixing flow regimes: (a) streaming flow; (b) impinging flow; and (c) backflow.

through strategically placed side-jets around a confined flow, an asymmetric flow field can be generated that closely emulate the profile from non-circular jets [27]. Placing three equi-spaced side-jets in a round flow emulates a triangular jet whilst four equi-spaced side-jets emulate a square jet [24, 27]. Generating small-scale eddies, similar to that found for non-circular nozzles, further stabilized the generated jet flames [10]. However, it is unclear how injecting fuel through the side-jets into a confined cross-flow of air, in the different configurations, will impact on the flames generated at the nozzle exit.

The current study investigates the flame stability, characteristics, and features under the multilateral jet injection mode. The study reports on the flow-field and flame structures in the near-field of the nozzle exit for different multilateral jet configurations. Non-intrusive optical diagnostic techniques, namely OH*-chemiluminescence and Particle Image Velocimetry (PIV), are used to study the flame structures and velocity field vectors, respectively.

2 Methodology

2.1 Multilateral jet burner

Figure 2 shows the schematic diagram of the multilateral jet burner used in the current experiment. The burner featured a primary long-pipe nozzle jet with equi-spaced side-jets attached laterally, at 1 primary diameter (D_P) upstream of the primary nozzle exit. Fuel was injected through the side-jets and partially-premixed with air carried through the 1.5-m-long primary jet inside the nozzle, before issuing out of the nozzle into an open environment, at room

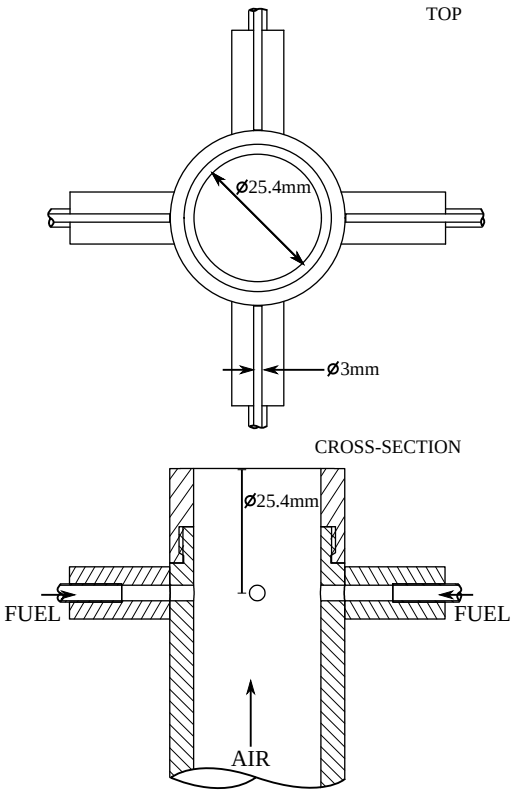

Figure 2: Schematic diagram of the multilateral jet burner: top view and cross-sectional view.

temperature and atmospheric pressure. Two side-jets nozzle configurations were considered: a three side-jets (3SJ) and a four side-jets (4SJ) configuration.

The primary nozzle was manufactured from a stainless-steel pipe with an internal diameter (D_P) of 25.4 mm. The side-jets were manufactured from stainless-steel tubes with an internal diameter (d) of 3 mm. The fuel used in this study is natural gas (NG) which contains approximately, 92.0% CH_4, 4.3% C_2H_4, 2.6% CO_2, and 0.9% N_2, supplied at room temperature.

2.2 Optical diagnostics set up

The experimental configuration is shown in Figure 3. A frequency-doubled 532-nm Nd:YAG laser (Quantel Brilliant B/Twins) was operated at 100mJ/pulse with a repetition of 10 Hz. The laser pulses were triggered by a Stanford Instruments DG535 delay generator with time delay of 70 μs between pulses.

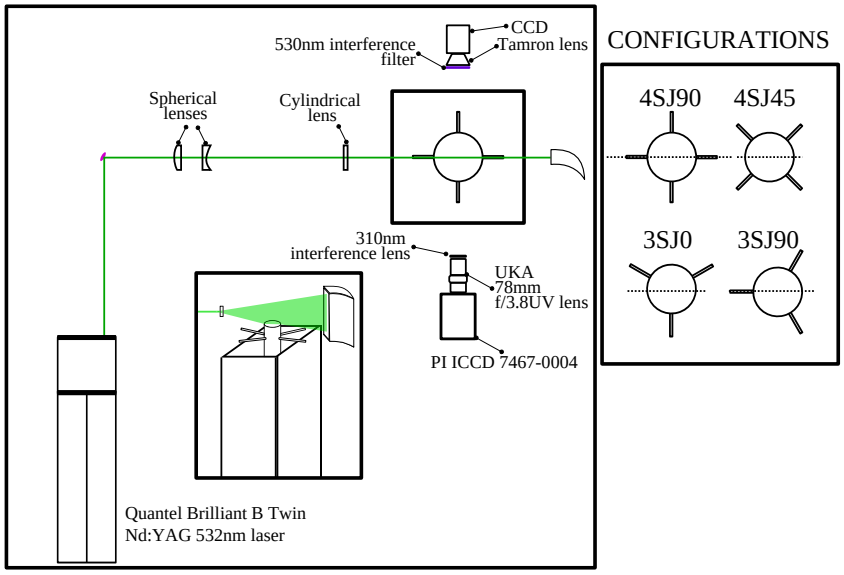

Figure 3: Schematic diagram for the PIV and OH*-chemiluminescence experimental set up and nozzle configurations.

A -100mm focal length cylindrical lens and a pair of spherical lenses were used in order to form a collimated laser sheet with thickness of approximately 1mm, aligned to the nozzle centreline. It should be noted that the OH*-chemiluminescence and Particle Image Velocimetry (PIV) were not conducted simultaneously, to avoid interference on the OH* signal collection.

PIV was used to assess near-field centre-plane planar velocity field at the nozzle exit. The air through the primary nozzle was seeded with Sigma-Aldrich titanium (IV) dioxide (rutile powder) particles ($< 5\mu m$ diameter), via a cyclone seeder.

A Princeton Instruments Megaplus II ES4020 CCD camera was operated in double-exposure mode and triggered by the delay generator. The camera resolution of 2048 pixels $\times$ 2048 pixels corresponds to 80mm $\times$ 80mm in physical space, giving a spatial resolution of $\approx$13 pixels/mm. The camera was fitted with a Tamron 50-mm compound lens, operated with an aperture f/1.4 and 530nm bandpass filter with a full width at half maximum (FWHM) of 10 nm to collect Mie-scattered light from the seed particles.

For each case, 600 planar velocity field image pairs were collected and processed with PIVView 2C for cross-correlation PIV processing. The interrogation win-

dow size was 32 pixels × 32 pixels, with 50% overlap. The cross-correlation is performed using the Gaussian algorithm. The generated data files are imported into OMA-X for post-processing, ensemble averaging, and removing outliers.

The OH*-chemiluminescence images of the flame structures were recorded with an intensified CCD camera (Princeton Instruments ICCD, 7467-004), fitted with a UKA 78-mm UV lens operated with f/3.8 aperture, and a band-pass filter centered at 310nm with 10 nm FWHM to collect signal from the OH*. The ICCD camera resolution of 1024 pixels × 1024 pixels corresponds to 150mm × 150mm in physical space, giving a spatial resolution of ≈6.8 pixels/mm. The exposure time of the camera is set to 10ms. The collected line-of-sight OH* images were imported into freeware OMA-X software [15] for further processing. Each individual image was corrected for vignetting, background and dark-charge. Ensemble mean and variance of the images were calculated. OH*-chemiluminescence is employed in this study to give information on the size and position of the flame zones. OH*-chemiluminescence is the radiative emission from the electronically excited OH* species formed by chemical reactions in the reaction [7]. The intensity of the chemiluminescence signal is affected by the flame temperature and local composition. The signals acquired were line-of-sight spatially integrated as signal from the entire reaction zone was collected [16].

2.3 Flame cases

Two sets of flames were measured in this study. The first flame had a Reynolds Number, based on bulk flow (b) velocity and main nozzle diameter, Re_b=5000 and the second with Re_b=7000. Stable flames with higher Reynolds Number were not possible without additional stabilization. The primary nozzle and side-jets flow rates were adjusted accordingly, after ignition, to maintain the total bulk flowrate constant. The change in the relative flow rates of the primary jet and the side-jets impacts on the ϕ at the burner exit. Noteworthy is that the range of ϕ considered in this study exceeds the upper flammability limits for methane [5]. Hence, the small variation in mixture strength, while important, is expected to have secondary effects in these flames.

The burner was mounted in a low turbulence intensity wind tunnel with a co-flow of ≈ 1 m/s. For PIV, the co-flow was seeded to better resolve the flow regions of interest. Flame cases with similar fuel-to-air ratio were tested for both 3SJ and 4SJ configurations, albeit at different side-jets to cross-flow momentum ratio (MR) due to the differing number of inlets. Flow conditions

Table 1: Flow parameters for the 4SJ flame cases with Re_b=5000.

Cases	Equivalence ratio, ϕ	Jet to cross-flow momentum ratio, MR	Primary jet velocity, $V_P[m/s]$	Side-jet velocity, $V_{inj}[m/s]$	Bulk flow rate, $\dot{m}_b[g/s]$	Bulk jet exit velocity, $V_b[m/s]$
4SJFA	2.6	0.19	2.51	17	1.7	3.1
4SJFB	3.2	0.29	2.41	20	1.7	3.1
4SJFC	3.8	0.41	2.30	23	1.7	3.1
4SJFD	4.6	0.59	2.20	26	1.7	3.1
4SJFE	5.3	0.80	2.09	29	1.7	3.1

Table 2: Flow parameters for the 3SJ and 4SJ flame cases with Re_b=7000.

Cases		Equivalence ratio, ϕ	Jet to cross-flow momentum ratio, MR		Primary jet velocity, $V_P[m/s]$	Side-jet velocity, $V_{inj}[m/s]$		Bulk flow rate, $\dot{m}_b[g/s]$	Bulk jet exit velocity, $V_b[m/s]$
			3SJ	4SJ		3SJ	4SJ		
3SJF1	4SJF1	3.4	0.59	0.31	3.56	32	24	2.6	4.6
3SJF2	4SJF2	3.9	0.76	0.43	3.45	35	26	2.6	4.6
3SJF3	4SJF3	4.4	0.96	0.54	3.35	38	29	2.6	4.6
3SJF4	4SJF4	4.9	1.18	0.66	3.24	41	31	2.6	4.6
3SJF5	4SJF5	5.4	1.44	0.81	3.14	44	33	2.6	4.6

pertaining to the flame cases, for both the 3SJ and 4SJ configurations are shown in Tables 1 and 2 below. Each flame is photographed with a standard Nikon DSLR camera.

3 Results and discussion

3.1 Flame characteristics at $Re_b = 5000$

Figure 4 presents the photographs (with a 1.0s exposure time at f/32 with ISO400 sensitivity) of the flames at bulk Re_b=5000, and arranged in order of increasing side-jet to cross-flow momentum ratio (MR): (a) 4SJFA with MR = 0.19; (b) 4SJFB with MR = 0.29; (c) 4SJFC with MR = 0.41; (d) 4SJFD

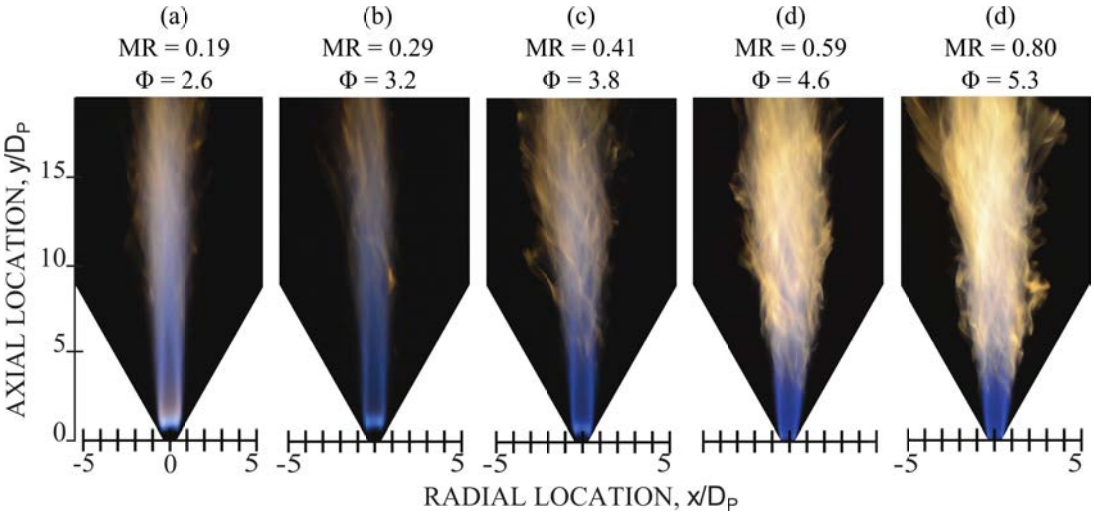

Figure 4: Photographs of flames taken with a standard Nikon DSLR at 1.0s exposure, ISO400 and f/32 under different MR: (a) 4SJFA; (b) 4SJFB; (c) 4SJFC; (d) 4SJFD; and (e) 4SJFE. The bulk Reynolds Number for the flow cases is Re_b=5000.

with MR = 0.59; and (e) 4SJFE with MR = 0.80. The flow parameters are detailed in Table 1. The MR values for flame cases 4SJFA and 4SJFB correspond to the impinging flow regimes while MR values for flame cases 4SJFC, 4SJFD and 4SJFE correspond to the backflow regimes (the flow regimes were previously described in Section 1). The correlation between the flow regimes and the flame characteristics will be further discussed in Section 4. The photographs in Figure 4 show that increasing MR, and therefore increasing the mixture equivalence ratio (ϕ), reduces the flame lift-off height. The increase in ϕ is associated with the increase in flame luminosity due to the richer mixture, promoting more soot within the flame. Note that the mixture in the tested cases here are all fuel rich and that the bulk flow exiting the nozzle is similar. Figure 5 presents the ensemble mean velocity profiles at the burner centreplanes: 45° offset (left) and at 90° offset (right) from the adjacent side-jet, respectively, for flame cases: (a) 4SJFA; (b) 4SJFB; (c) 4SJFC; (d) 4SJFD; and (e) 4SJFE. Axial distance y/D_P=0 marks the nozzle exit and the measurements here are taken up to y/D_P=2.5, downstream. Radially, the measurements include $\mathrm{x}/D_P = \pm 1.0$ from the centreline, and $\mathrm{x}/D_P = \pm 0.5$ mark the inner edges of the primary nozzle. The images in Figure 5 show velocity profiles, in both planes, to be similar for either the lifted or the attached flame cases.

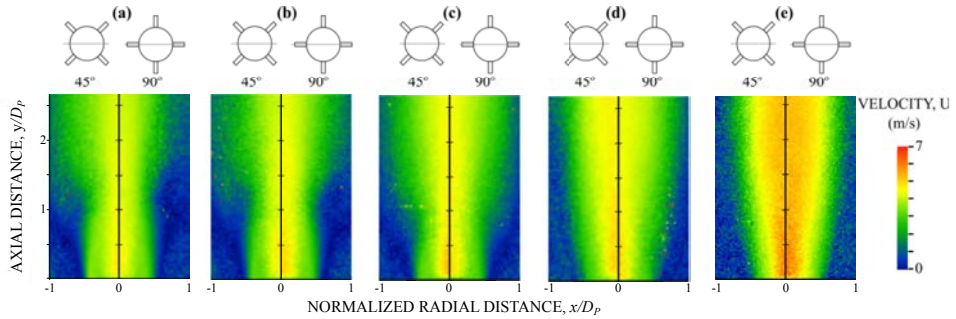

Figure 5: Mean velocity magnitude at the 45° and 90° plane relative to the adjacent jets (laser sheets indicated by the dotted lines in the schematic diagram) for the Re_b=5000 flame case: (a) 4SJFA; (b) 4SJFB; (c) 4SJFC; (d) 4SJFD; and (e) 4SJFE.

Velocity profiles for flame cases 4SJFA (Figure 5(a)) and 4SJFB (Figure 5(b)) show converging sections downstream of the jet exit at y/D_P=0, which then diverge around 1D_P due to thermal expansion as a result of ignition. The "neck" from this converging-diverging profile corresponds to the statistically stable lift-off height for the lifted flames of 4SJFA and 4SJFB visibly seen in Figure 4(a) and Figure 4(b), respectively.

The velocity profiles for flame cases 4SJFD and 4SJFE expand uniformly from the nozzle exit, consistent with the velocity profile shown by an attached flame, as seen in Figure 4(d) and Figure 4(e). The image in Figure 5(e) shows relatively higher velocity, in particular near the exit plane. This is attributed to the strong impingement MR upstream that forms a secondary stream along the centreline, which is minimally affected by the heat release in the shear region of the issuing jet.

3.2 Flame characteristics at Re_b=7000

Figure 6 shows the flame photographs (taken at 2s exposure with f/14 and at ISO500) for the 4SJ flame cases: (a) 4SJF1 at MR = 0.31; (b) 4SJF2 at MR = 0.43; (c) 4SJF3 at MR = 0.54; (d) 4SJF4 at MR = 0.66; and (e) 4SJF5 at MR = 0.81. The field-of-view of the flame photorgraphs are at 45^o-offset from the adjacent side-jet. The flames have similar bulk flow at Re_b=7000.

Similar to the previous 4SJ flame cases with Re_b=5000, the transformation of the flames from lifted to being attached, with increasing MR, is

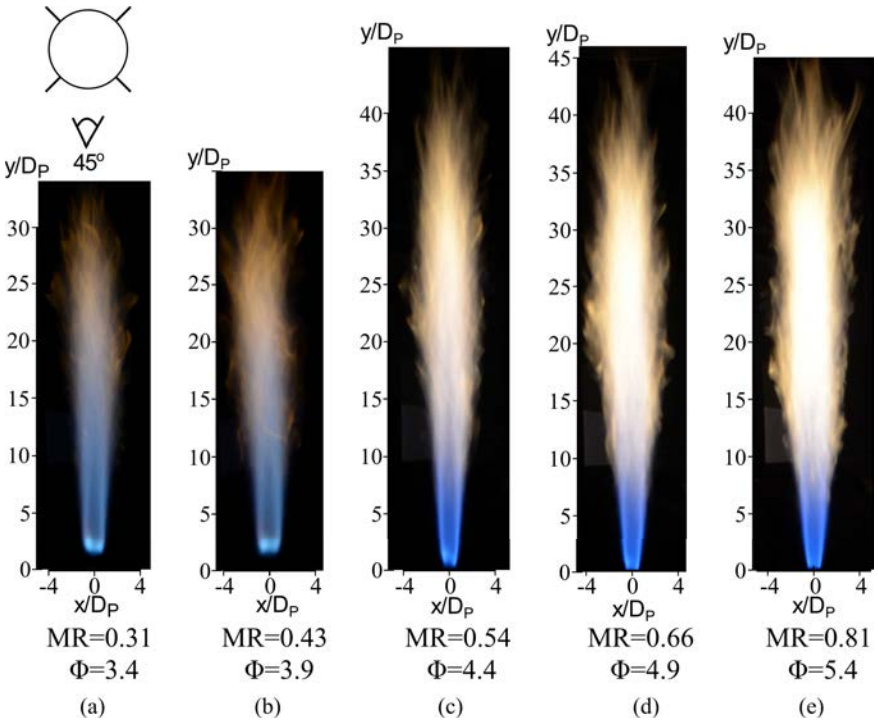

Figure 6: Flame photographs for the 4SJ flow at 45°-offset and 90°-offset planes for flames: (a) 4SJF1; (b) 4SJF2; (c) 4SJF3; (d) 4SJF4; and (e) 4SJF5. The flames are photographed with a standard DSLR camera at 2s exposure time for f/14 and at ISO500.

clear. Here, flames 4SJF1 and 4SJF2 are less stable and eventually blow off. Attached flames, meanwhile are stable for cases 4SJF3 through 4SJF5. Figure 7 presents the flame photographs taken for the 3SJ cases: (a) 3SJF1; (b) 3SJF2; (c) 3SJF3; (d) 3SJF4; and (e) 3SJF5. The field-of-view of the flame photographs are at 0°-offset from the adjacent side-jet, with the same camera settings as the 4SJ flame cases shown in Figure 6.

Here, the 3SJF1 flame is lifted, and similar to 4SJF1 and 4SJF2, is less stable and cannot be sustained over a prolonged period. Flames generated for 3SJF2 are observed to display a bimodal characteristics,that is, they alternate between being attached and lifted. Flames 3SJF2 through 3SJF5 are stable attached flames.

The attached flames have an approximate visible length of $40D_P$, whilst the lifted flames have an approximate visible length of $30D_P$. Despite the different side-jets configurations and further changes in both ϕ and MR, the

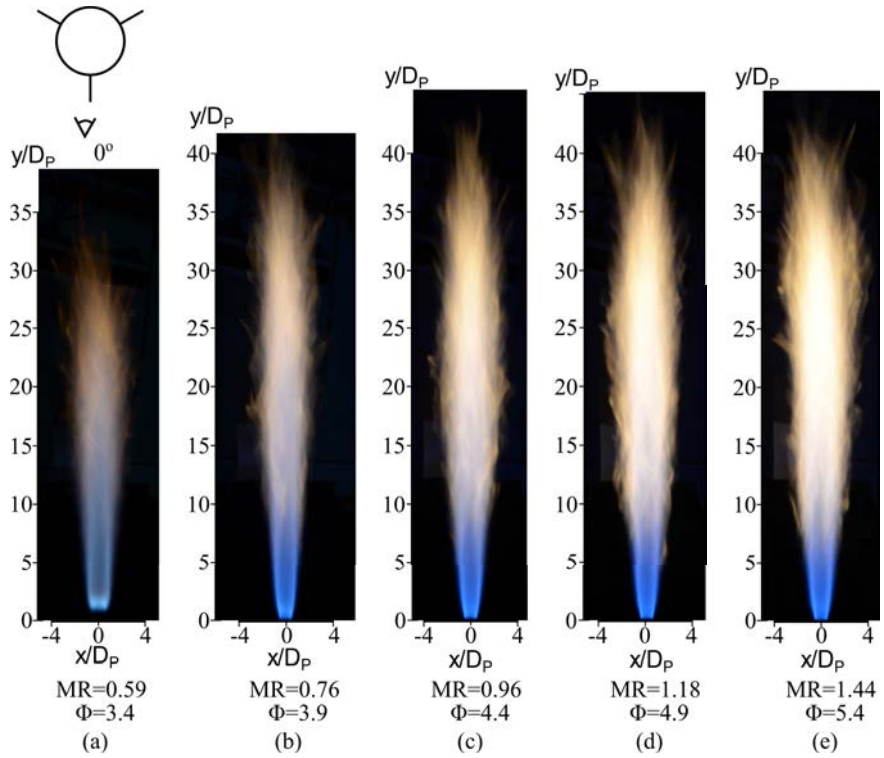

Figure 7: Flame photographs for the 3SJ flows at 0°-offset and 90°-offset planes for flames: (a) 3SJF1; (b) 3SJF2; (c) 3SJF3; (d) 3SJF4; and (e) 3SJF5. The flames are photographed with a standard DSLR camera at 2s exposure time for f/14 and at ISO500.

physical flame lengths for both lifted and attached flames remain unchanged. This shows that flame length is still dominated by the bulk flow issued out of the nozzle exit [9].

The formation of lifted-flames and attached flames in both Figure 6 and Figure 7 follows a trend: the lifted-flames are observed to form in the range $0.3 \leq MR \leq 0.6$ categorised as the impinging flow regime, whilst the attached flames form in the range $MR \gg 0.6$, considered as the backflow regime. Coupled with the results shown previously in the Re_b=5000 cases, a correlation between the flames' characteristics to the flow MR can be established. In addition, the F2 cases, which have similar fuel-to-air ratio (hence similar ϕ) show different characteristics, i.e. lifted-flame displayed by 4SJF2 (which MR lies within the impinging flow regime) and attached flame by 3SJF2 (which MR is within the backflow regime range).

A little disagreement is observed between the flame cases with MR = 0.66, i.e. 4SJF4 in Figure 6(d) and MR = 0.59 3SJF1 in Figure 7(a). Despite both being characterized within a similar mixing regime upstream, the 3SJF1 generates a lifted-flame, as opposed to the attached flame that is associated with the generation of a backflow upstream. This could be attributed to the higher blockage ratio posed by the 4SJ configuration upstream compared to the 3SJ configuration, which leads to more intense turbulent mixing or the leaner fuel mixture in the 3SJ configuration. Blockage ratio here defines the flow-facing planar area ratio of the side-jet columns to the primary flow cross-section. More intense turbulent mixing indirectly enhances the molecular-scale mixing, which contributes to more stable combustion. Also note that highly intense mixing contributes to high strain rate, which leads to flame extinction.

3.3 Effect of upstream MR on OH* profiles

Figure 8 shows the ensemble mean OH*-chemiluminescence ($< \bar{c} >$) for the field-of-view 45°-offset from the adjacent side-jets and OH* variance ($< c' >$) for flame cases: (a) 4SJF1; (b) 4SJF2; (c) 4SJF3; (d) 4SJF4; and (e) 4SJF5. The mean OH* is ensemble-averaged from 300 instantaneous OH* images and encompasses the region up to approximately $6D_P$ downstream of the burner nozzle exit and spans $1.5D_P$ in the transverse direction. $x/D_P = \pm 0.5$ marks the inner edge of the nozzle.

The mean OH* profiles for flame cases 4SJF1 and 4SJF2 in Figures 8(a) and 8(b) show some asymmetric behavior, probably caused by the sensitivity of lifted flame to flow conditions. Nevertheless, this sensitivity has no impact on the generality of the findings. For these two flames, the OH* variance profiles show similar asymmetry and two stabilization heights, as evident by the bimodal intensity profile in the axial direction. The two distinct regions with intense OH* seen in the mean image at the leading edges of the lifted-flame around x/$D_P = \pm 0.7$. The locations of these regions indicate the mean lift-off height of flames around $1D_P$ downstream, similar to the Re_b=5000 cases. Furthermore, the instantaneous chemiluminescence profiles for the lifted flames, an example presented in Figure 9, show the formation of 4 distinct regions of intense OH*. This corresponds to the formation of reaction zones around $1D_P$ downstream, which is associated with the 4SJ in the tested configuration.

With increasing MR, the mean OH* chemiluminescence intensity increases progressively. The highly intense flame leading edge in the lifted-flame becomes a compact structure anchored to the nozzle exit, as seen in 4SJF3 flames in Figure 8(c). The OH* intensity in similar regions is lower than

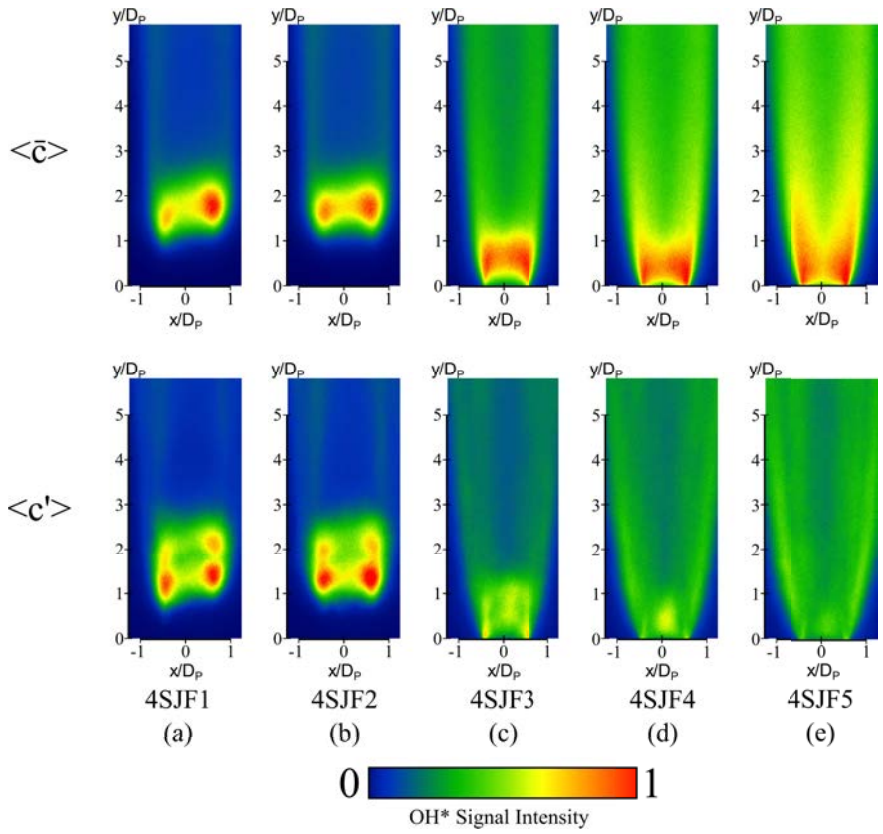

Figure 8: Mean OH*-chemiluminescence (OH*) profiles (top) and OH* variance profiles (bottom) for 4SJ flame cases at 45°-offset for flame cases: (a) 4SJF1; (b) 4SJF2; (c) 4SJF3; (d) 4SJF4; and (e) 4SJF5.

that presented in 4SJF4 and 4SJF5. This shows that higher temperatures, corresponding to premixed mixtures, in flame cases 4SJF1 and 4SJF2 are at the flame leading edges, whilst the OH* profiles for the attached flames show a more uniform OH* distribution which may be attributed to a more homogeneous partial premixing.

Figure 10 shows the OH* ensemble mean ($< \bar{c} >$) and variances ($< c' >$) for the 3SJ flames: (a) 3SJF1; (b) 3SJF2; (c) 3SJF3; (d) 3SJF4; and (e) 3SJF5. The 0°-offset field-of-view is shown in the top two rows and the 90°-offset field-of-view in the bottom rows.
The OH* mean and variance profiles for the lifted-flame case 3SJF1, in Figure 10(a), show similar characteristics to that observed previously for flame case 4SJF1 (Figure 8(a)) and 4SJF2 (Figure 8(b)), i.e. distinct intense OH* (mean) and high variance regions. The 0°-offset field-of-view shows nearly

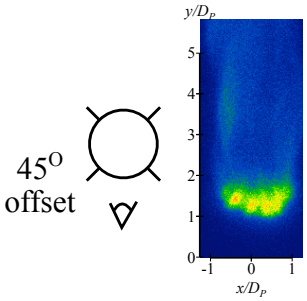

Figure 9: Typical instantaneous OH*-chemiluminescence profile for 4SJF1 at 45°-offset.

symmetrical OH* profiles, however, the effect of the asymmetry is evident in the 90°-offset field-of-view OH*, where the region not aligned with the side-jets shows a more intense OH* signal. This is attributed to axis-switching phenomenon where the fuel-rich regions issued out of the side-jets are translated by 60° (45° for 4SJ cases) due to vortical interactions, resulting in high fuel mixture concentration in regions between adjacent side-jets. The axis-switching process for both 3SJ and 4SJ configurations are described more in-depth in Thong et al., [27].

The lifted-flames presented by flame case 3SJF1 in Figure 10(a) show consistent characteristics with that shown previously with flame cases 4SJF1 and 4SJF2 in Figure 8(a) and Figure 8(b), respectively. Similarly, transitioning to an attached flame in 3SJF2 shown in Figure 10(b) shows increases in the global chemiluminescence intensity.

Flame cases 4SJF3 and 3SJF3, despite having similar ϕ, show obvious differences in the mean chemiluminescence profile. The OH* chemiluminescence profile in Figure 8(c) shows a compact reaction region near the nozzle exit whilst thin reaction regions are formed near the edge of the flames for both the 0°- and the 90°-offset field-of-view. The effect of ϕ is minimal here as the ϕ for both cases are conserved [16] and the difference in the chemiluminescence profiles here are attributed to the difference in jet to cross-flow MR upstream. Similarly, this is also observed when comparing the F4 and F5 for both the 3SJ and 4SJ cases.

Figure 11 shows the normalized maximum OH* signal intensity plotted against the normalized axial distance (y/D_P) for both the 3SJ (closed symbols) and 4SJ (open symbols) flame cases. The lifted-flame profiles for 3SJF1,

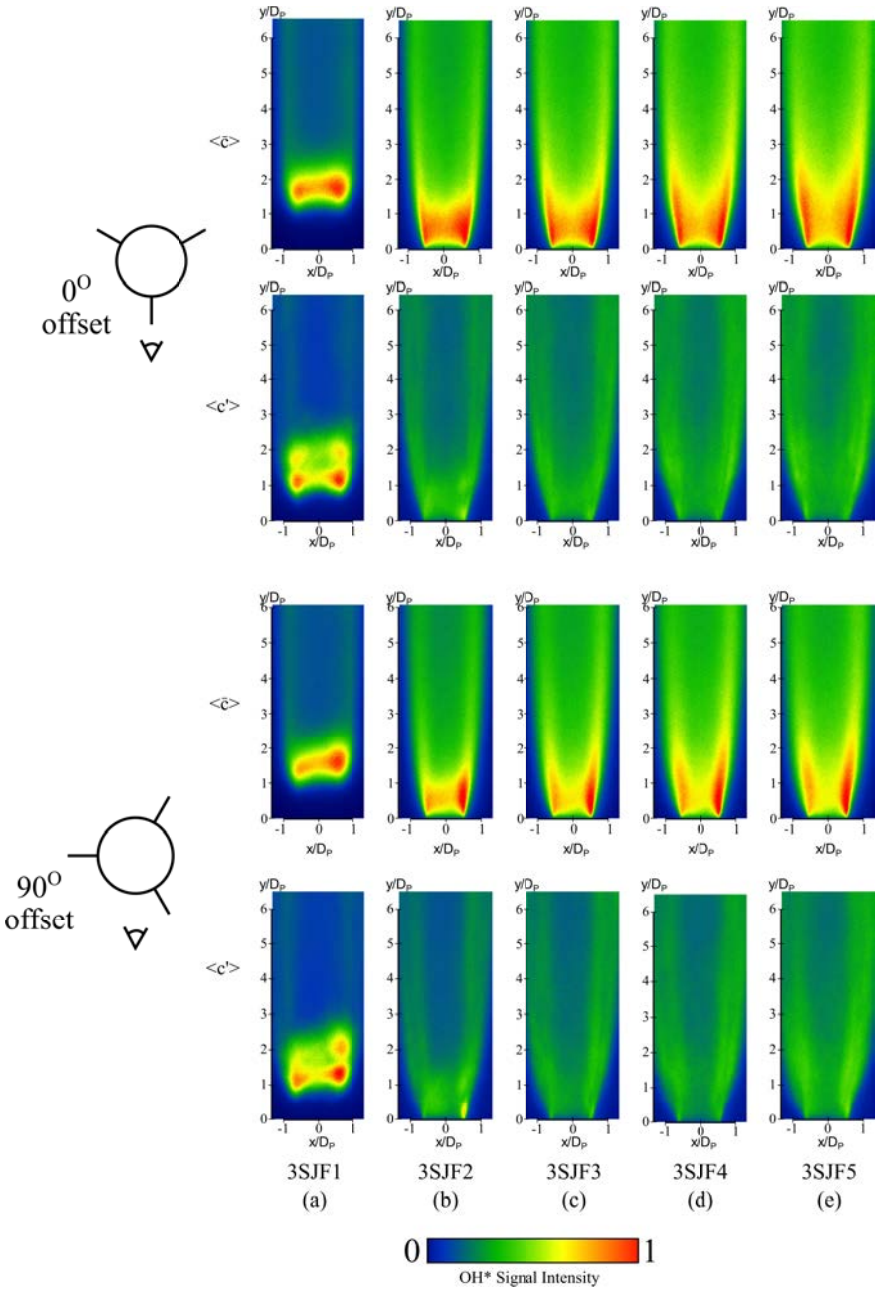

Figure 10: Mean OH* ($< \bar{c} >$) profiles and OH* variance ($< c' >$) profiles for 3SJ flame cases at 0°-offset and 90°-offset field-of-view for cases: (a) 3SJF1; (b) 3SJF2; (c) 3SJF3; (d) 3SJF4; and (3) 3SJF5.

4SJF1, and 4SJF2 show the maximum OH* peak around $2D_P$, and follow a similar trend. The lifted-flame profiles reduce to similar OH* signal level around 20% of the maximum downstream. Despite the difference in MR

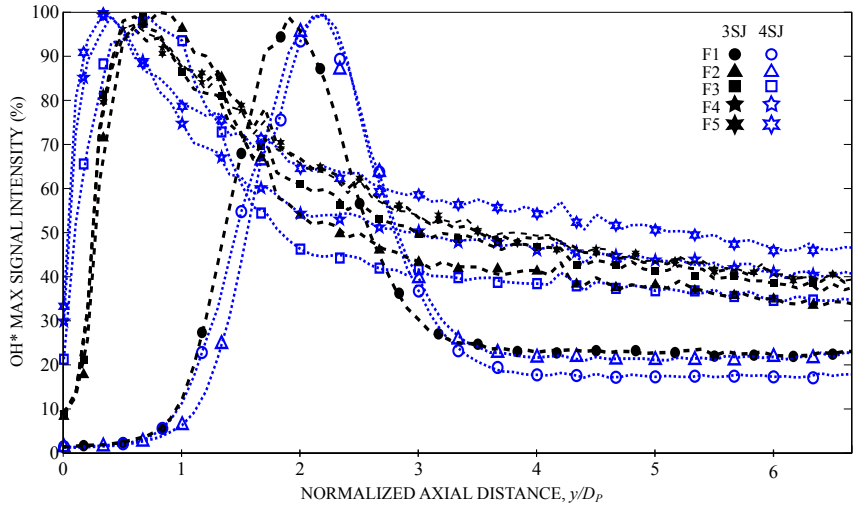

Figure 11: Maximum OH* signal from the flame cases normalized to their respective maximum, plotted to the normalized axial distance. The 3SJ flames (90° offset field-of-view) are plotted with closed symbols while the 4SJ (45° offset field-of-view) flame cases are plotted with open symbols.

upstream and ϕ, there are little changes in the max OH* profile to suggest any drastic effects on the heat release rate or temperature.

The peak in the OH* profiles downstream for the attached 4SJ cases increase from F3 to F4 and F5, which is consistent with the increase in ϕ. However for the 3SJ cases, the attached flame cases F3 to F5 seem to collapse despite the increase in MR and ϕ. This could possible mean that neither the value of MR or ϕ has significant bearings on the peak OH* profile at sufficiently high MR values.

3.4 Effect of MR on centreline velocity

Figure 12 presents the mean centreline velocity profiles for the 3SJ (open symbols) and 4SJ (closed symbols) flame cases: 3SJF2 ($\times$-symbols); 3SJF3 and 4SJF3 ($\circ$-symbols); 3SJF4 and 4SJF4 (Δ-symbols); and 3SJF5 and 4SJF5 ($\square$-symbols). Figure 13 shows the corresponding centreline axial velocity fluctuation component. The cases shown here are all attached flames only.

The most important result from Figure 12 and Figure 13 supports the previous finding, such that the attached flames are independent of the upstream mixing

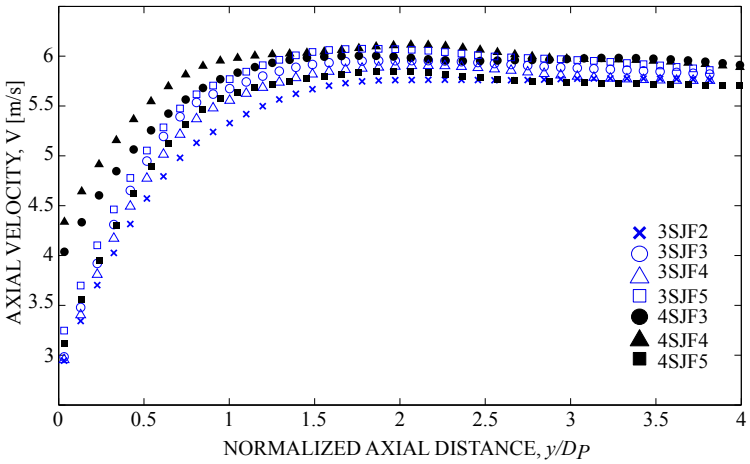

Figure 12: Mean centreline axial velocity profile for the tested flame cases.

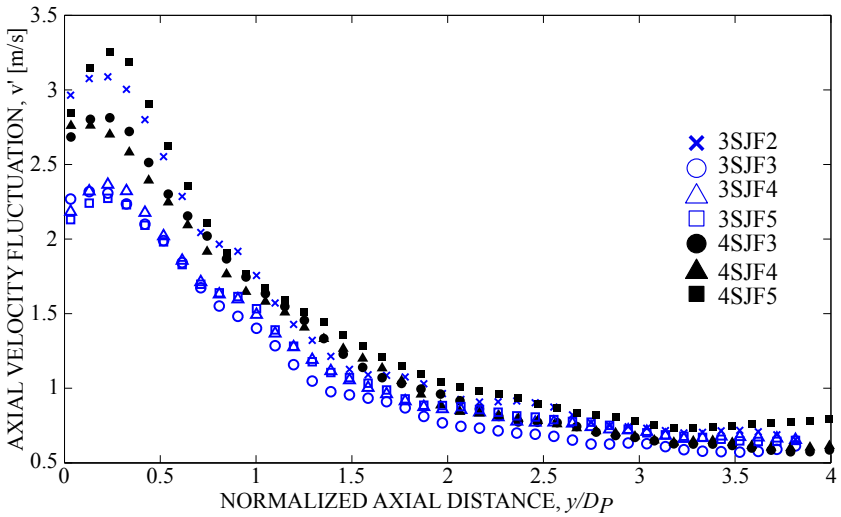

Figure 13: Centreline axial velocity fluctuation (r.m.s) for the tested flame cases.

regimes' MR after $1D_P$ downstream. The mean velocity profiles for 4SJF5 and 3SJ cases collapse in the region upstream of 1 D_P, whilst 4SJF3 and 4SJF4 do not due to lower MR upstream. This shows that cases with jet to cross-flow MR>0.6 with similar bulk velocities typically exhibit similar centreline velocities.

The 4SJ cases have higher centreline v_{rms} (around 25% higher) out of the nozzle than the 3SJ cases, except for 3SJF2, which still displays bimodal characteristics. This is expected as 4SJ cases pose a higher blockage ratio upstream than the 3SJ of equal MR. v_{rms} for 4SJF5 is relatively higher than the other 4SJ cases which is attributed to the higher MR upstream.

The convergence of the velocity profiles downstream is attributed to the conserved total bulk flow out of the nozzle. Therefore, it can be surmised that the flow regimes inside the nozzle have direct impact on the centreline velocity magnitude and the turbulence intensity at the primary nozzle exit. Both the centreline velocity magnitudes and turbulence intensity change markedly between cases and eventually converge and dissipate to similar values in the downstream direction.

3.5 Effects of the number of jets on flow and scalar fields

Figure 14 presents typical radial profiles for mean axial velocity [m/s], velocity fluctuation (V_{rms})[m/s], and mean OH* profiles [arbitrary unit a.u.] for axial locations in the near flow field $y/D_P = 0.25$, 0.5, 0.75, and 1.0 for: (a) 3SJ flame case 3SJF2 (in the 90°-offset) and (b) 4SJ flame case 4SJF5 (in the 45°-offset). Here, both the 3SJF2 and 4SJF5 flame cases represent the typical attached 3SJ and 4SJ flame cases, respectively. For the 3SJ configuration profiles, the side-jet is located $1D_P$ upstream on the right side of the figure.

Despite the introduction of multi-lateral jet and variations in MR upstream, no obvious distortions can be observed in the velocity profiles when compared to flames generated from a round jet, for example the piloted turbulent jet flames reported by Barlow [1]. The axial velocity profile for the 4SJF5 flame case shown in Figure 14(b) shows a slight bulge near the centreline, that is most prominent at $y/D_P = 0.25$. This is attributed to the strong secondary flow stream, which is formed by the strong side-jets injection into the cross-flow, upstream of the nozzle exit. This will be further discussed in Section 4 of this manuscript. The modifications to the near-field velocity

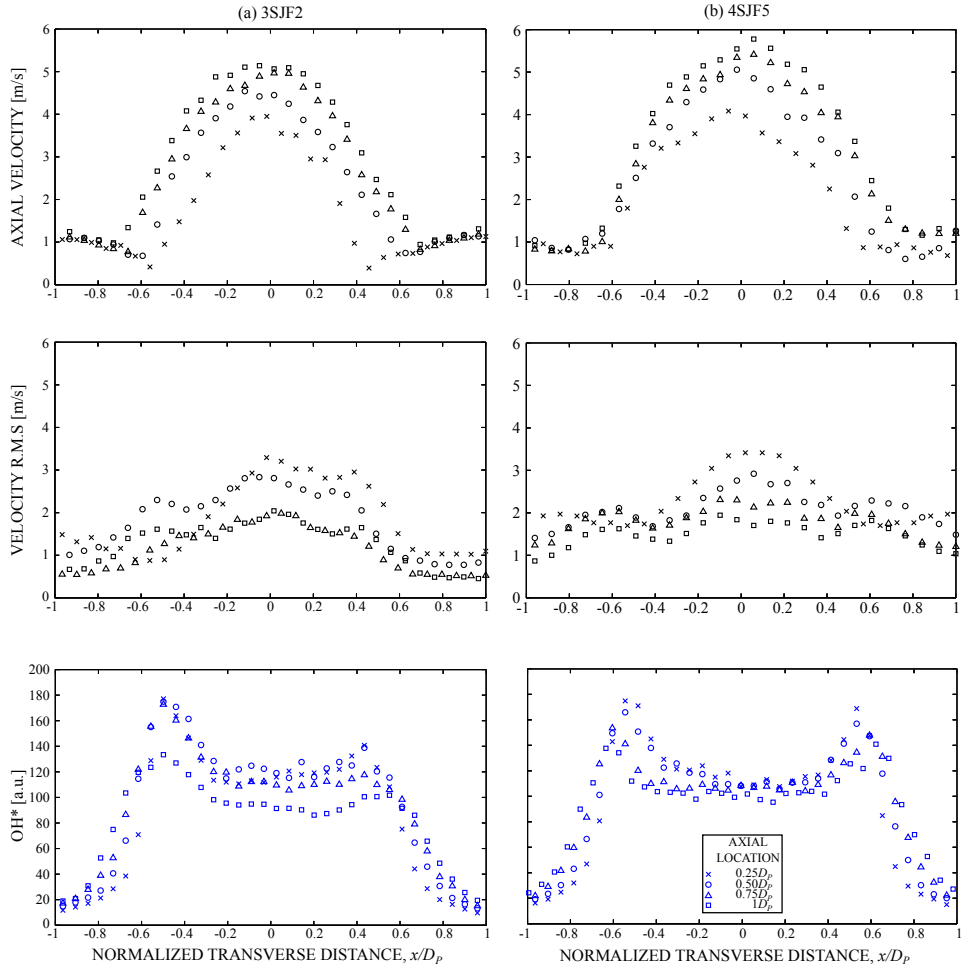

Figure 14: Radial mean axial velocity profiles (to), axial velocity fluctuation (V_{rms}) profiles (middle), and mean OH* profiles (bottom) for axial locations downstream, y/D_P=0.25, 0.5, 0.75 and 1.0, for flame cases: (a) 3SJF2 (90°-offset) and (b) 4SJF5 (45°-offset)

profiles diminish downstream. Similarly, despite the asymmetry posed by the 3SJ configurations, no obvious distortions are observed. From the centreline, the velocity profile reduces almost linearly towards the left side and show steps-like profiles as it reduces towards the right, which is attributed to the flow disruption upstream by the side-jet.

Comparing the V_{rms} profiles for both 3SJ and 4SJ profiles in Figure 14(a) and Figure 14(b) show similar peaks in r.m.s near the flow centreline at x/D_P=0. This peak in centreline, most prominent in the region immediately downstream of the nozzle exit at y/D_P=0.25, is deduced to be unique to multilateral jet burners as this region is absent in the r.m.s profiles typical of a round jet flame [1].

Comparing the symmetrical configuration for 4SJ to the asymmetrical 3SJ configuration shows a profound difference in the V_{rms} profile. Compared to the symmetrical profile presented for 4SJ, peaks in the V_{rms} profiles can be observed near the centreline and towards the right side of the profile at $x/D_P = 0.4$. The peak towards the right of the profile coincides with the placement of the side-jet while the side without shows a low V_{rms} region. The effects of the asymmetrically placed side-jets upstream also extend to the OH* chemiluminescence profile where higher chemiluminescence is observed on the region to the left where no side-jet is placed.

The effects of the asymmetrical configuration are less prominent proceeding downstream from the nozzle exit. The distortion in the V_{rms} profile, which is obvious within $0.5D_P$ downstream, reverts to a symmetrical profile at $0.75D_P$. Similarly for the 4SJ case, the high turbulence region near the centreline recedes progressively downstream into a trough at both $0.75D_P$ and $1.0D_P$ downstream.

To summarise, the results presented here show that the placement of the side-jets have effects on the flow-field and flame structures downstream, most prominently within $0.5D_P$ downstream, before being corrected by the combustion heat release. Also, the effects of placing side-jets upstream have effect on the near-field, most prominently shown by the V_{rms} profiles.

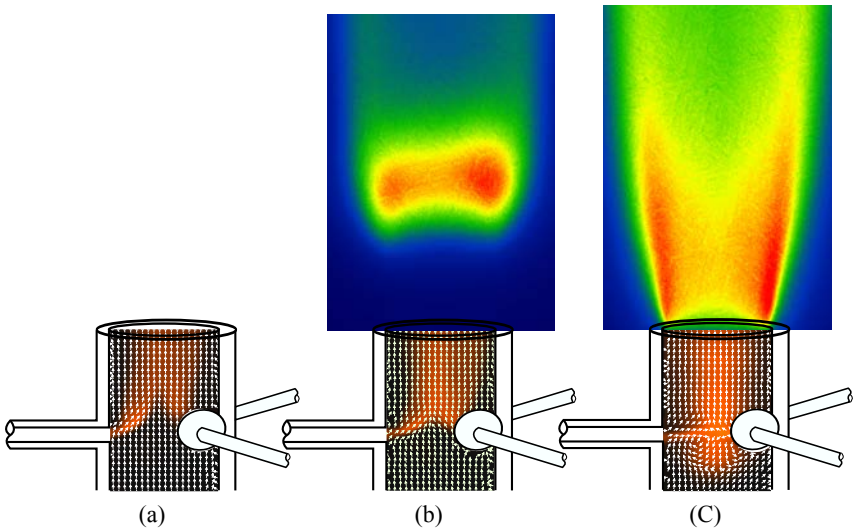

Figure 15: OH* images for a typical lifted and attached flames, collated with mean PLIF images of isothermal flow regime for 3SJ superimposed on a vector plot of the velocity inside the primary nozzle. The bright region represents the mean "fuel" profile injected from the side-jets into the primary flow. The flow vectors show the flow directions and are not scaled.

4 Discussion

4.1 Flow regimes and flames

The three different flow regimes previously shown in Thong et al., [28] can be associated to the respective flames' stabilizing characteristics, via the side-jet to cross-flow momentum ratio. The flow regimes previously identified via isothermal methods are expected to be achieved here, in the unreacted section upstream of the combustion zones.

Figure 15 and Figure 16 show the mean "fuel" Planar Laser Induced Fluorescence (PLIF) images overlapped with the flow velocity vectors inside the primary nozzle (obtained from cases of similar flow regime in non-reacting flow) for the different regimes typically achieved by changing the MR: (a) streaming mode; (b) impinging mode; and (c) backflow mode, for 3SJ and 4SJ cases, respectively. Here, the brighter regions denote the mixture fraction of side-jets' injected "fuel", whilst the darker region represents air, similar to the schematic diagram shown in Figure 1. Also shown in Figure 15 and Figure 16 are the corresponding flame characteristics that are matched to the corresponding momentum ratio, represented by the OH* chemiluminescence

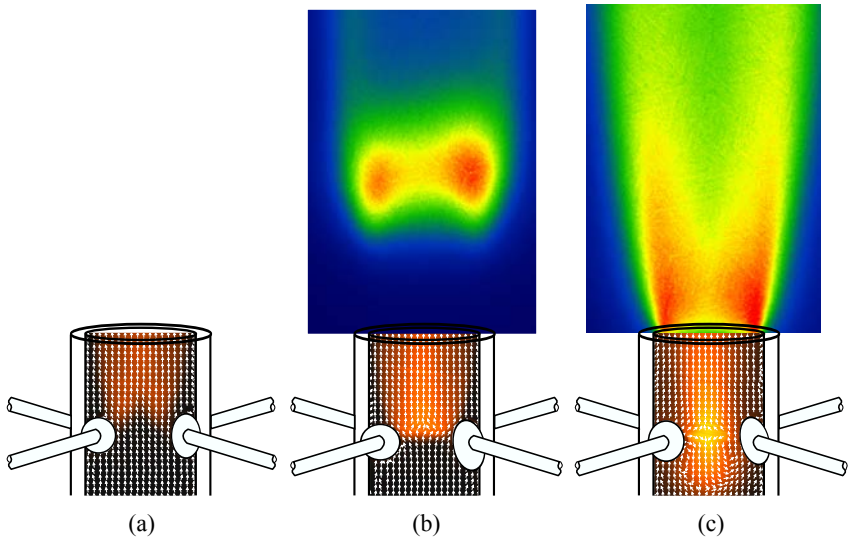

Figure 16: OH* images for a typical lifted and attached flames, collated with mean PLIF images of isothermal flow regimes for 4SJ superimposed on a vector plot of the velocity inside the primary nozzle. The bright region represents the mean "fuel" profile injected from the side-jets into the primary flow. The flow vectors show the flow directions and are not scaled.

profiles. Note that both the PLIF and vector images were acquired from isothermal experiments previously conducted using water as medium and are only used here for illustration purposes

Figure 15(b) and Figure 16(b) shows the scalar and vector fields for the isothermal impinging flow case MR=0.2. This mixing regime is associated to the lifted flames, formed in conjunction with similar flow MR, in both the 3SJ and 4SJ configurations.

Here, the injected fuel side-jets impinge upon the primary flow centreline. This forms rich premixed parcels, which are advected out of the nozzle along the centreline, which sustain the combustion downstream. The impinging fuel streams form a stagnation point inside the nozzle, which is expected to enhance fuel-air premixing through increased shear. The large-scale mixing induced contributes directly to small-scale mixing production, and produces a flame more stable than that produced by a streaming flow.

The fuel mixture fraction appears symmetrical in the 4SJ mixing region (Figure 16(b)) compared to the 3SJ in Figure 15(b), which is observed to be

skewed towards the region with no side-jet. The result of this asymmetric fuel distribution upstream is prominent and is evident in the accompanying OH* profile. The flame generated downstream shows slightly more intense OH* signal near the region with no side-jet. This is consistent with a region of higher fuel mixture fraction produced by the axis-switching of vortices upstream.

In the impinging regime, despite the reactants premixing induced by the impingement, the flames remain lifted. The lifting of flames here can be explained via several conjectures adopted from already-formed theories related to statistically-stable lifted flames theories. Firstly, it is apparent from the the vector-field in Figure 15(b) and Figure 16(b), that despite obstructing the flow via impingement, the bulk flow inside the nozzle is still dominated by the primary flow. Therefore, the primary flow velocity (V_P) inside the nozzle is expected to still be higher than the typical NG turbulent burning velocity (V_T), therefore stabilizing the flame at a distance downstream at which $V_P = V_T$ [30, 18]. For example, the turbulent burning velocity for methane-air mixture of $\phi = 1$ at $Re \approx 7500$ is around 2.8 m/s [25], compared to the $V_P \approx 3.5$ upstream, inside the pipe, for the F1 lifted-flame cases.

The impinging side-jets generate small-scale structures along the flow centreline. Despite coupling with the fuel mixture gradient across the nozzle exit, the flow is still primarily dominated by large-scale structures (largest being the integral scale of the nozzle) and also as a result of the sudden expansion out of the nozzle. According to large eddy theorem [18], the flame's leading edge is anchored upon these large-scale eddies as hot combustion products are transported upstream via these large-scale structures.

Figure 15(c) and Figure 16(c) show the attached flames generated, corresponding to the backflow mixing regime upstream. The fuel injected through side-jets impinge at the primary flow centreline and splits into two different streams: (a) stream propagated downstream to form a rich fuel stream along the flow centreline and (b) stream propagated upstream into the oncoming primary flow, premixes, and propagated downstream shrouding the centreline stream. This results in rich partially premixed mixture flowing along the centreline and a lean partially premixed mixture in regions away from the centreline. The variation in fuel concentration gradient expected and small-scale mixing structures induced by this mixing regime provide an advantage in stabilizing flames, compared to lower MR mixing regimes, and a typical non-premixed turbulent jet flame.

The impinging zone which generates a backflow mixing regime provides a larger stagnation effect, more so in a 4SJ configuration compared to 3SJ due to larger blockage ratio. The anatomy of backflow deflected upstream is similar to a jet injected into a counter flow, i.e. the near-field immediately upstream of the impingement where the deflected side-jets are dominant, and the region further upstream where the primary flow is more dominant. Jet injected into a counter-flow shows superior mixing enhancement when compared to jet into a stagnat flow, co-flow, and into cross-flow [29, 31]. The mixing by such mechanism is enhanced through the counter-mixing layer, which leads to the amplification of the jet shear layer instability [31, 6], which increases with momentum ratio.

In the impinging flow regime, the fuel mixture issued out of the nozzle cannot be ignited in both the $Re_b = 5000$ and $Re_b = 7000$ conditions for both 3SJ and 4SJ configurations, despite the mixture being within the reactants flammability limits. The isothermal scalar field and flow vectors for 3SJ and 4SJ, shown respectively in Figure 15(a) and Figure 16(a), show that the side-jets' streams are deflected by the higher primary flow momentum and then advected out of the nozzle exit as individual streams (flow dominated by primary flow). Ignition of the mixture in a streaming flow mode, however, has been achieved in lower Reynolds Number.

Figure 17 shows the flames previously generated by Birzer et al., [4] in a multilateral jet burner at lower primary flow Reynolds Number ($Re_{CEN} = 1005$ and $Re_{CEN} = 2009$). Note that the burner used in the study was in a 4SJ configuration and has geometries (D_P=50.8mm and d_{jet}=4.5mm) different from that used in the current study. These photographs were taken at 45°-offset field-of-view.

Individual flames are observed, formed for the flame cases $Re_{SIDE} = 300$ and 543 for $Re_{CEN} = 1005$ (shown in Figure 17). Increasing the Re_{CEN} from 1005 to 2009 increases the primary flow turbulence and decreases the momentum ratio of jet to cross-flow. At low MR, in the streaming flow regime, shown in Figure 1, there are little interactions between the side-jets within the confinement. Therefore, considering the flames generated as 4 individual jet flames in cross-flow, the flames shortened with increasing primary flow and eventually blows off. The flames in the streaming flow regime can be stabilized via external stabilization mechanism, for example the conical nozzle section [19].

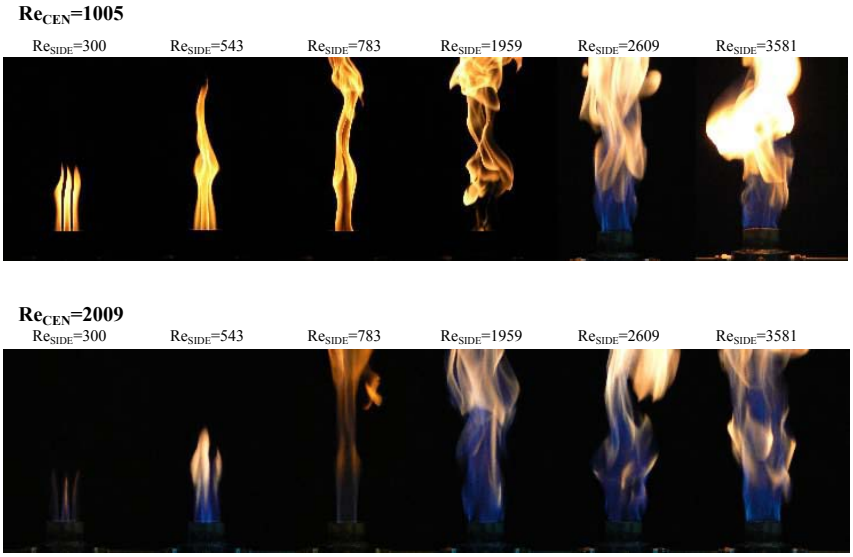

Figure 17: Flame photographs for primary flow (air) $Re_{CEN} = 1005$(top) and $Re_{CEN} = 2009$(bottom) with increasing fuel input (NG) from left to right

4.2 Concentric tube flow and multilateral jet flow

Figure 18 shows the conceptual representation of the cross-sectional views for a concentric tube burner (Figure 18(a)) compared to the multilateral jet burner (Figure 18(b)) in the current study. The figures are not drawn to scale. The solid arrows in the figure indicate the direction at which fuel is injected into the system while the dashed arrows indicate the direction of injected air. The greyed regions indicate the mixing regions where fuel and air are partially premixed. The different shades of grey represents the intensity in the mixing region.

The Concentric Flow Conical Nozzle (CFCN) Burner [19] was introduced as a proof of concept for a partial premixing device whilst the modified Sydney Burner [21] was introduced as a suitable platform to understand the complexity of such flow. The fuel and air streams are interchangeable and both configurations have been tested and contrasted. The central jet is recessed to increase the flame blow-off limits for the burner.

Despite both the concentric tube burner and the multilateral jet burner partial premix reactants before issuing out of the nozzle, different flame structures are generated. The flames generated from the concentric burner are sooty near the nozzle exit, and blue at most regions with the visible flame

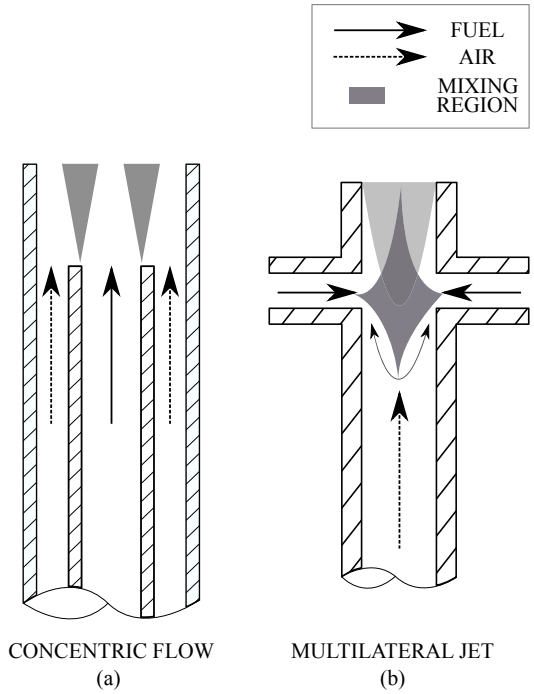

Figure 18: Comparison of partial premix burner configurations: (a) Concentric tube burner and (b) Multilateral jet burner.

length around $100D$ [21], which is longer than the flames generated by the multilateral jet burner. The flames from the Sydney Burner are externally stabilized by a pilot co-flow [21] and the CFCN is stabilized with a conical section [19]. This shows that despite the level of partial premixing achieved by the burners, they are reliant on external stabilization mechanisms to be reliable.

The stability map plotted by Mansour [19] for the CFCN burner, as presented in Figure 19 (blow-off Reynolds Number plotted against mixture equivalence ratio) provides an overview on the capabilities of the concentric tube burner (without conical nozzle for stabilization). Placing the conical nozzle improves the flame stability markedly. Overlapping the flow parameters investigated in the current study (Re_b=7000) allows a direct comparison with the "unstabilized" concentric tube burner, which shows that at similar mixture equivalence ratio, the flame's stability (in particular flame cases F3, F4 and F5) exceeds that of the concentric tube burner without a conical nozzle. A similarity between the multilateral jet burner and the concentric tube burner is that, the flame stability increases with increasing jet equivalence ratio.

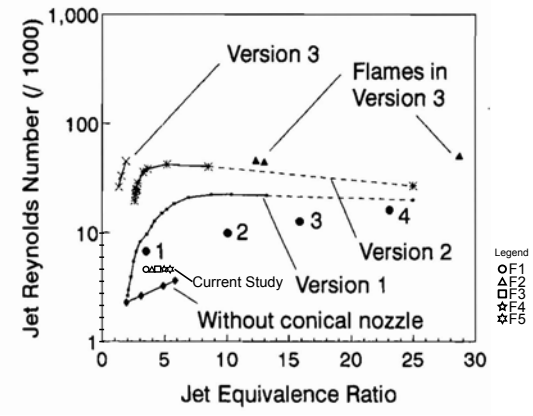

Figure 19: The blow-off jet Reynolds Number of the different CFCN configurations tested, plotted against fuel equivalence ratio, adapted from Mansour [19]. The current flame cases for Re_b=7000 cases are overlaid.

5 Conclusion

The current study focuses on the combustion characteristics of a multilateral jet burner in both 3 side-jets (3SJ) and 4 side-jets (4SJ) configurations. The side-jet to cross-flow momentum ratio (MR) in the burners was manipulated while maintaining the total bulk flow exiting the nozzle constant at two values corresponding to $Re_b = 5000$ and $Re_b = 7000$. Experimental results from PIV and OH* measurements lead to the following conclusions:

- Lifted flames and attached flames are generated corresponding to the upstream mixing regimes, impinging regime and backflow regime, respectively. Therefore, the changes in upstream mixing indirectly affect the length of the flames;

- The momentum ratio, MR, inside the primary nozzle has direct impact on the flame characteristics, as opposed to the conventional mixture equivalence ratio, ϕ. It is found to affect the flame and flow characteristics within the first nozzle diameter downstream. Further downstream, flames are dominated by combustion heat release;

- The asymmetrical configurations impact on the V_{rms} and OH* chemiluminescence profiles and found to be more prominent within the first diameter downstream.

References

[1] R. Barlow and J. Frank. Piloted ch4/air flames c, d, e, f - release 2.1. *Sandia National Laboratories*, 2007.

[2] R.S. Barlow, S. Meares, G. Magnotti, H. Curcher, and A. R. Masri. Local extinction and near-field structure in piloted turbulent ch4/air jet flames with inhomogeneous inlets. *Combustion and Flame*, 162:3516–3540, 2015.

[3] A. Ben-Yakar and R. K. Hanson. Experimental investigation of flame-holding capability of hydrogen transverse jet in supersonic cross-flow. *Symposium (International) on Combustion*, 1998.

[4] C. H. Birzer, R. M. Kelso, and B. B. Dally. Flame structure of jets in confined cross-flows. *Proceedings of the Australian Combustion Symposium*, 2011.

[5] K. L. Cashdollar, I. A. Zlochower, G. M. Green, and M. Hertzberg. Flammabilit of methane, propage and hydrogen gases. *Journal of Loss Prevention in the Process Industries*, 13(3):327–340, 2000.

[6] C. H. C. Chan and K. M. Lam. Centreline velocity decay of a circular jet in a counterflowing stream. *Physics of Fluids*, 1998.

[7] D. S. Dandy and S. R. Vosen. Numerical and experimental studies of hydroxyl radical chemiluminescence in methane-air flames. *Combustion Science and Technology*, 1992.

[8] T. F. Fric and A. Roshko. Vortical structure in the wake of a transverse jet. *Journal of Fluid Mechanics*, 279:1–47, 1994.

[9] T. Gautam. Lift-off heights and visible lengths of vertical turbulent jet diffusion flames in still air. *Combustion Science and Technology*, 41(1-2):17–29, 1984.

[10] E. Gutmark, K. C. Schadow, T. P. Parr, D. M. Hanson-Parr, and K. J. Wilson. Noncircular jets in combustion systems. •, 7(4):248–258, 1989.

[11] E. J. Gutmark and F. F. Grinstein. Flow control with noncircular jets. *Annual Review of Fluid Mechanics*, 31:239–272, 1999.

[12] D. Han and M. G. Mungal. Simultaneous measurements of velocity and ch distribution. part ii: deflected jet flames. *Combustion and Flames*, 133:1–7, 2003.

[13] J. D. Holdeman, D. S. Liscinsky, V. L. Oechsle, G. S. Samuelsen, and C. E. Smith. Mixing of multiple jets with a confined subsonic crossflow: part 1-cylindrical duct. *Journal of Engineering for Gas Turbines and Power*, 119:852–862, 1997.

[14] R. F. Huang and J. M. Chang. The stability and visualized flame and flow structures of a combusting jet in cross flow. *Combustion and Flame*, 1994.

[15] P. A. M. Kalt and M. B. Long. Oma - image processing for mac os x. www.oma-x.org, 2008.

[16] D. G. Lee and D. A. Santavicca. Experimental diagnostics for the study of combustion instabilities in lean premixed combustors. *Journal of Propulsion and Power*, 19(5):735–750, 2003.

[17] M. Y. Leong, G. S. Samuelsen, and J. D. Holdeman. Optimization of jet mixing into a rich, reacting crossflow. *Journal of Propulsion and Power*, 16(5):729–735, 2000.

[18] K. M. Lyons. Towards an understanding of the stabilization mechanisms of lifted turbulent jet flames: Experiments. *Progress in Energy and Combustion Science*, 33(2):211–231, 2007.

[19] M. S. Mansour. A concentric flow conical nozzle burner for highly stabilized partially premixed flames. *Combustion Science and Technology*, 152:115–145, 2000.

[20] A. R. Masri. Partial premixing and stratification in turbulent flames. *Proceedings of the Combustion Institute*, 35:1115–1136, 2015.

[21] S. Meares and A. R. Masri. A modified piloted burner for stabilizing turbulent flames of inhomogeneous mixtures. *Combustion and Flame*, 161:485–495, 2014.

[22] T. H. New and W. L. Tay. Effects of cross-stream radial injections on a round jet. *Journal of Turbulence*, 7, 2006.

[23] N. Peters and F. A. Williams. Lift-off characteristics of turbulent diffusion jet flame. *AIAA Journal*, 21:423–429, 1983.

[24] J. F. Seidel, C. Pappert, T. H. New, and H. M. Tsai. Effects of multiple radial blowing around a circular jet. *43rd AIAA Aerospace Sciences Meeting and Exhibit*, 2005.

[25] S. S. Shy, W. J. Lin, and J. C. Wei. An experimental correlation of turbulent burning velocities for premixed turbulent methane-air combustion. *Proceedings of the Royal Society A: Mathematical Physical and Engineering Science*, 456:1997–2019, 2000.

[26] T. H. Song and R. Viskanta. Interaction of radiation with turbulence - application to a combustion system. *Journal of Thermophysics and Heat Transver*, 1(1):56–62, 1987.

[27] C. X. Thong, B. B. Dally, C. H. Birzer, P. A. M. Kalt, and E. R. Hassan. An experimental study on the near flow field of a round jet affected by upstrema multilateral side-jet. *Experimental Thermal and Fluid Science*, 82:198–211, 2017.

[28] C. X. Thong, P. A. M. Kalt, B. B. Dally, and C. H. Birzer. Flow dynamics of multi-lateral jets injection into a round pipe flow. *Experiments in Fluids*, 56(15), 2015.

[29] H. Tsunoda and M. Saruta. Planar laser-induced fluorescence study on the diffusion field of a round jet in a uniform counter-flow. *Journal of Turbulence*, 4, 2003.

[30] K. A. Watson, K. M. Lyons, J. M. Donbar, and C. D. Carter. On scalar dissipation and partially premixed flame propagation. *Combustion Science and Technology*, 175(4):649–664, 2003.

[31] M. Yoda and H. E. Fiedler. The round jet in a uniform counterflow: flow visualizationand mean concentration measurements. *Experiments in Fluids*, 21(6):427–436, 1996.

[32] L. L. Yuan and R. L. Street. Trajectory and entrainment of a round jet in crossflow. *Physics of Fluids*, 10:2323, 1998.

[33] M. J. Zimberg, S. H. Frankel, J. P. Fore, and Y. R. Sivathanu. A study of coupled turbulent mixing, soot chemistry and radiation effects using the linear eddy model. *Combustion and Flames*, 113(3):454–469, 1998.

Chapter 7

Summary, Conclusions and Future Work

The work presented in this thesis examines the feasibility of using multilateral jet injection to partially premix the reactants of turbulent jet flames as a means to enhance their controllability and increase stability. The side injection results in a flow configuration termed 'jet in a confined cross-flow', and it resembles the well-studied 'jet in a cross-flow', albeit with major differences in the flow and scalar field. This study is focussed on better understanding the main controlling parameters, such as number of side-jets and momentum ratio, on the flow and mixing fields, and its influence on the flow both inside and in the near-field of the primary nozzle. The effects on flame structures and characteristics are also investigated in this study.

This study is conducted in two parts. The first part aimed at understanding the interaction of the side-jets with the primary jet flows, internally and externally. For this, water is used as the working fluid inside an acrylic pipe mounted in a water tunnel. The flow and mixing fields were measured and analysed under different operating conditions and geometry configurations, both inside and outside the primary nozzle. The second part involved reacting gaseous flows where the flow field

and the general features of the flame were investigated. In the isothermal studies, a closed-looped water tunnel was used where acrylic primary nozzles (D_P=56 mm) were fitted with 3 side-jets (3SJ) or 4 side-jets (4SJ) (each side-jets with d = 56 mm), which were placed equi-spaced at around $1D_P$ upstream, of the primary nozzle exit. The use of water allowed optical access and reasonable Reynolds Number with low flow velocity. Two laser diagnostics techniques, Planar Laser Induced Fluorescence and Particle Image Velocimetry (PIV), were used to study the mixing and flow fields, respectively. These techniques allow spatially and temporally resolved planar measurements, inside and outside the nozzles. Commercially available Computational Fluid Dynamics (CFD) package ANSYS CFX was validated and used to model the various cases and to interrogate flow regions in order to supplement our understanding of the flow from the experimental data.

The reacting flow cases utilized Natural Gas (NG) as fuel, and air as oxidizer. Stainless steel side-jets and primary nozzles, with internal diameter of 3 mm and 25.4 mm, respectively, were fabricated and were placed centrally in a vertical wind tunnel operating at low speed. Both 3SJ and 4SJ configurations were tested at varying primary flow Reynolds Number, fuel equivalence ratio, and jet to cross-flow momentum ratio. PIV and OH*-chemiluminescence techniques were used to study the velocity field and structures of the reaction zones.

The following is a summary of the research findings that were detailed in Chapters 3, 4, 5 and 6. This summary is followed by a list of the main conclusions and suggestions for future work.

7.1 Research Outcome Summary

The results and discussion presented in Chapters 3 to 5 have deepened the understanding of the fundamentals of the flow and mixing structures that are induced both inside and outside a nozzle, for a range of momentum ratios and side-jets' parameters, hence meeting Objectives (i) and (ii) (refer to Section 2.6). Chapter 6 applies the knowledge and information gained from the previous chapters to reacting flows, and has provided insights on the flame characteristics affected by different flow momentum ratio, mixing regimes, and side-jets' distributions, to address research Objective (iii) shown previously.

7.1.1 Effect of momentum ratio on flow regimes

In Chapters 3 and 5, PIV and PLIF techniques were applied to an isothermal study of flows emerging from either a 3SJ or 4SJ configuration. It was found that the side-jets to primary flow momentum ratio (MR) controls the type of flow regimes inside the primary nozzle. This ratio is defined as:

$$MR = \frac{G_{inj}}{G_P} = \frac{(\rho V^2 A)_{inj}}{(\rho V^2 A)_P}$$

where the subscripts *inj* and *P* represent the side-jet and primary flows, respectively, ρ denotes the flow density, V denotes the velocity, and A denotes the jet hydraulic area.

The range of flow regimes can be categorised into: streaming flow regime, impinging flow regime, and backflow regime. These regimes are determined by evaluating the side-jets' trajectories and the mean flow profiles in the axial plane. These regimes are also reflected in the planar vortical evolutions. The applications for the streaming flow regimes are mainly found in reactants mixing and in combustion fuel quenching

[118] due to their efficacy in generating a homogeneous flow. Impinging flow and backflow regimes are undesirable for most mixing applications due to their tendency in forming a secondary stream of high side-jets concentricity that propagates along the primary flow's centreline. However, this has been proven to be desirable for reactants' partial premixing

Streaming flow regime is observed in the lower MR range and is often characterized by the obvious formation of Counter-rotating Vortex Pairs (CVPs) in the flow cross-section, in particular immediately downstream of the side-jets' exit. An increase in MR results in the further penetration of side-jets into the primary nozzle's flow centreline and eventually interact with adjacent streams near the primary flow centreline. This flow regime characterizes side-jets that do not interact in the flow, to side-jets that later on (further downstream) penetrate the primary flow centreline. This flow regime is experimentally found to exist in the range $0 < MR < 0.2$

For both 3SJ and 4SJ configurations, increasing the flow MR to approximately 0.2 results in the side-jets impinging at the primary flow centreline, and hence the impinging flow regime. The impinging jets increase the centreline flow turbulence intensity, which enhances the flow turbulence mixing. The side-jets that impinge at the primary flow centreline undergo axis-switching and form a cruciform profile for 4SJ and a "Y" profile for 3SJ. This is also true for streaming flow cases which penetrates the primary flow centreline downstream of the side-jets' injection point. This phenomenon will be further discussed in Section 7.1.4.

Once side-jet impingement has commenced, further increase in MR leads to part of the impinging flow being deflected upstream and advect against the primary flow, akin to that of an "oblique jet impingement on a flat plate" [119]. The deflected

flow upstream is observed to be recirculated and carried downstream by the strong primary flow around the side-jets' impingement point, whilst the flow deflected downstream is carried along the flow centreline, effectively forming a "secondary flow" within the primary flow. This regime is observed for flows with a range of MR >> 0.2. Compared to the impinging regime discussed previously, the backflow regime further increases the flow turbulence, both upstream and downstream of the side-jets' impingement point, which further enhances the turbulent flow mixing in the confinement.

7.1.2 Effects of momentum ratio on mixing

In the streaming flow regime (MR<0.2), the CVPs induced via the individual jets in cross-flow are carried downstream by the stronger primary flow momentum. The mixing in this flow regime is mainly done via large-scale shear induced mixing structures in the flow, including CVPs and horse-shoe vortices, which are well established in the literature [79]. The turbulence strength in the flow is increased slightly and plateaus out of the nozzle exit in the near-field to around $2.5D_P$, or up to the end of the round jet's potential core. The centreline flow velocity decay is not greatly affected despite a spike in velocity, downstream in the near-field, as a product of the side-jets' streams interacting in the near-field of the nozzle. In the flow cross-section, this mixing regime is efficient in generating a flow close to homogeneous with low unmixedness, in particular near the nozzle exit. This also explains why most practical mixing and fume quenching studies mainly focus on optimizing flow parameters within this flow regime [69]. In the axial centreplane profile, the side-jets streams in the streaming regime reduce the velocity along the path of the side-jets stream and increases the velocity in the regions surrounding it to compensate. In occasions where the side-jets penetrate the primary flow centreline, the primary flow centreline velocity is increased.

For MR=0.2, the side-jets for both 3SJ and 4SJ impinge the primary flow centreline a short distance from injection. Both 3SJ and 4SJ flows undergo axis-switching after impingement. Small-scale structures are generated within the flow as a result of the side-jets impingement, which is not observed with the streaming flow regime. However, the result of the side-jets' impingement for 4SJ result in the formation of a secondary stream of high concentricity near the primary centreline, which consists mostly of side-jet fluid. The axial profile for the 3SJ is more uniformly distributed with a less visible secondary stream compared to 4SJ. This shows that an asymmetrical configuration of low number of side-jets (<6 side-jets) provides a relatively more even mixing compared to symmetrical configurations.

The secondary stream formed within the nozzle persists into the near-field and decays. The turbulence induced in the flow by the impingement decays to around $1D_P$ downstream of the nozzle exit, before plateauing, and increasing again in the regions nearing the end of the potential core (outside of the jet).

Furthermore, the side-jets penetrating the primary flow form a stagnation point upstream of the side-jets' impinging point. Primary flow is diverted over this region, before being carried downstream by the strong primary flow momentum. This regime generates an increase in the flow turbulence, in particular radial turbulence at the side-jet' impinging point, and axial turbulence downstream in the flow.

Despite increasing the flow turbulence and enhancing the generation of both large- and small-scale mixing structures, this flow regime is not as effective in generating a homogeneous flow as the streaming flow regime, which explains the lack of interest/study in this flow regime.

Backflow is formed for both the 3SJ and 4SJ configurations at the MR >> 0.6. The strong impingement by the side-jets leads to flow being deflected both upstream and downstream. These upstream and downstream flows induce a strong turbulence, which lead to increased mixing between the side-jets and the primary flow. The backflow regime also shows the highest increase in flow turbulence (by a factor of 7) compared to the impinging and streaming flow regime. The backflow generated both large- and small-scale mixing structures which are advected downstream by the strong primary flow. As a result of the strong impingement backflow, the cross-section of the primary flow shows a primary centreline of strong side-jets concentricity (secondary stream) with a well-mixed surrounding flow. Also prevalent in the backflow regime are flow flapping characteristics by the backflow, in particular at high MR, 4J backflow cases.

The backflow length in the current study is a function of the flow MR and number of side-jets, *n*. The length of the backflow (see Chapter 5), is scaled to the function

$$\frac{h_v}{D_P} = kn\sqrt{MR}$$

where $h_v[m]$ represents the velocity backflow length, normalized by the primary pipe diameter $(D_P)[m]$, and k denotes the scaling constant used in this expression. The scaling through velocity is done by measuring the distance between the two stagnation points: stagnation points caused by the side-jets impinging; and stagnation where the primary flow meets the backflow. The k for the studied cases is deduced to be 0.16.

Furthermore, the backflow length, when scaled to the half concentration length,

follows the expression

$$\frac{h_{vc}}{D_P} = knMR$$

where $h_{vc}[m]$ denotes the length of the backflow measured up to the point where the concentration is half of that at the impinging point, normalized to the primary flow confinement. k, n and MR denote the constant, number of side-jets, and momentum ratio, respectively. The k of this scaling method is deduced to be around 0.18.

The side-jets regimes reported above modify the round jet profile at the nozzle exit. The side-jets of a non-interacting flow reduces the velocity along its path, and increases the velocity around it as a compensation, and hence acting as a blockade to the primary flow. The flow progression, from side-jets interacting, to impinging, and to the backflow mode, increases the centreline velocity and the concentricity of side-jets flow along the primary flow centreline. However, these modified profiles diminish downstream at around $2D_P$ out of the nozzle exit, into a Gaussian profile, similar to a round jet.

The near-field outflow is also affected by the change in MR upstream. Increasing the side-jets MR reduces the coherence of the bulk flow shear layer roll-up and increases the frequency of the shear layer roll-up. The inception of the shear layer roll-up in a long-pipe round flow is typically $1D_P$ downstream of the nozzle exit, as reported in Chapter 4. The introduction of side-jets, with increasing MR, brings the shear layer roll-up inception closer to the nozzle exit, generates less coherent structures, and increases the Strouhal number, St of the round jet flow. At high MR flow cases, overlapping and more chaotic roll-ups are generated.

7.1.3 Effects of momentum ratio on combustion

Birzer et al., [73] showed that ignition of a turbulent jet nozzle in multilateral configuration is possible, which is also shown in the current study. Results reported in Chapter 6 show that flame characteristics generated downstream from the nozzle exit can be correlated to the change in jet to cross-flow MR upstream. In the current study, the ignition of the reactants exiting the burner at bulk Reynolds Number, Re_b = 5000 and Re_b = 7000 are achieved for both 3 side-jets (3SJ) and 4 side-jets (4SJ) configurations, albeit only for impinging and backflow mixing regime MR range.

The results reported in Chapter 6 shows that lifted flames are formed at the MR range of 0.2 up to 0.6, which coincides with the MR range of the impinging flow regime. The flames are stabilized at a statistically stable location approximately $1D_P$ downstream of the jet nozzle exit. Furthermore, a region of intense OH*, which translates to the region of high heat release, is observed at the leading edge of the flame front, which indicates that most reactions in the lifted-flames happen around this region.

Attached flames are formed for flame cases with MR above 0.6, which coincides with the backflow mode achieved in the isothermal flow studies. It is observed that the mean OH* profile peaks at edges of the jet close to the shear layer.

The jet to cross-flow MR upstream also appears to dominate the flame characteristics that are formed outside the nozzle, as oppose to the reactants mixture equivalence ratio. Comparing two flame cases of similar mixture equivalence ratio and different flow MR reveal that the flame with a higher MR, in the backflow regime, forms an attached flame whilst a flame with lower MR, in the impinging regime is lifted. The significance of this finding is the potential to manipulate the flame characteristics by

changing the MR upstream without changing the equivalence ratio.

The 4SJ nozzle generates similar velocity profiles in both 45° and 90° planes offset from the adjacent side-jet. However, the profiles generated for the 3SJ, reflects the asymmetric configuration upstream of the nozzle exit. The flames generated show that the flame-edge region that are not aligned with the side-jet generates a more intense OH* signal, which correlates to higher heat release than the region aligned with the side-jet. This is attributed to the uneven distribution of the fuel upstream as seen in the cross-section profiles presented in Chapter 5, at which regions opposite the side-jet have higher fuel mixture fraction compared to the region aligned with the side-jets.

The centreline velocity and turbulence profiles for the attached flames plateau at similar values beyond $2D_P$ downstream of the nozzle exit, despite the varied values at the nozzle exit. This indicates that the MR upstream has little unfluence beyond $2D_P$ downstream, which is deduced to be dominated by the reaction heat release. The centreline OH* profile for the lifted flame cases show peaks at similar region and subsequently plateaus at similar OH* intensity. However, for the attached flame cases, the OH* profiles peak at similar distance immediately downstream of the nozzle exit, but reaches different values in the plateau region.

The radial profiles for both 3SJ and 4SJ flame cases are similar such that they both display high turbulence intensity at the flow centreline immediately downstream of the nozzle exit. The 4SJ flame cases generate a symmetrical profile with high centreline turbulence. The 3SJ cases however generate turbulence profile which are skewed towards the side-jets' regions and a peak at the centreline. The distortion in flow profiles generated by both configurations become less obvious downstream

of $1D_P$. However, unlike the 3SJ, the 4SJ flame cases generate a more persistent turbulence profile which is observable up to $2D_P$ downstream, consistent with that shown in isothermal studies shown in Chapter 4. This shows that the mixing upstream of the nozzle has drastic effect of the flames' flow profile up to $1D_P$ downstream before the flow field gets dominated by convective effects as a result of the combustion heat release. No drastic changes are observed in the velocity profiles.

7.1.4 Axis-switching induced by side-jets injection

As presented in Chapter 4 and Chapter 5, CVPs in both the 3SJ and 4SJ configurations (for most streaming and impinging flow cases) undergo similar axis-switching induced by the same mechanisms widely reported in the literature [100, 101]. Axis-switching in such flows work on the underlying principle of azimuthal vorticity. Here, adjacent vortices from different pairs of CVPs induce fluid motions in the opposing direction as seen in the schematic diagram shown in Figure 7.1.

Figure 7.1 shows the sequence of the vortical interactions which lead to axis-switching inside the nozzle, and schematic diagrams which show the proposed axis-switching mechanisms. Figure 7.1(a) shows distinct CVPs formation immediately downstream of the side-jet's exit. The CVPs are advected towards the centreline further downstream and the adjacent vortices start interacting (Figure 7.1(b)). Figure 7.1(c) and Figure 7.1(d) show the new vortical pairings that form as a result of axis-switching. The new vortical pairings have implication downstream in the reacting flow and is deduced to contribute to the four distinct reaction zones observed periodically in the lifted-flames in Chapter 6.

The axis-switching mechanism manifests itself the same way in both the 3SJ and 4SJ configurations. In the 3SJ configurations, it was found that a "Y" profile is induced in

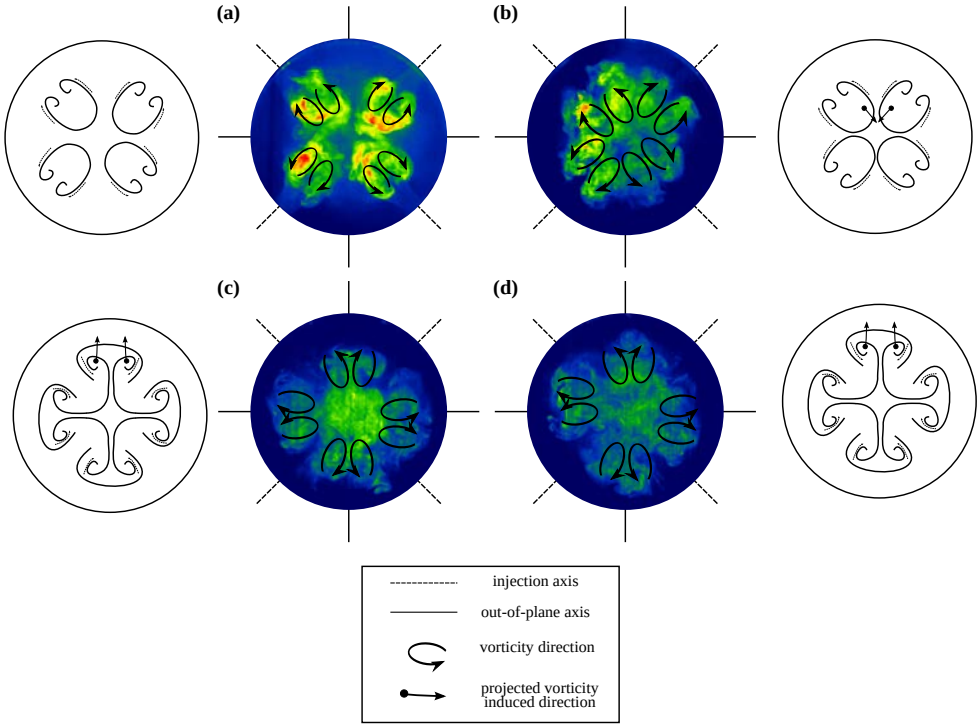

Figure 7.1: Proposed axis-switching mechanism in a 4 side-jets configuration (excerpt from Chapter 4).

the cross-section of the flow after the CVPs interaction. While in the 4SJ, a cruciform profile is formed. Similarly for both configurations, the dye ribbon that connects the CVPs are propagated towards the flow centreline, which remain relatively unaffected by the axis-switching mechanism, and form a region with moderate dye concentricity at the primary flow centreline.

The axis-switching in the studied flow case have similar precursor as the formation of CVP. This is deduced from the impinging flow cases at which axis-switching still happens in cases of side-jets impingement. The flow stream exiting the side-jets' exit is curved by the oncoming cross-flow resulting in the induction of CVPs, which subsequently lead to axis-switching of the vortices. However, a stronger side-jets impingement, seen in the backflow regime, suppresses the formation of these CVPs and hence axis-switching.

The CVPs generated in a jets in cross-flow (JICF) study is generally rotational, one that rotates clockwise and the other counter-clockwise. The rotational profiles entrain the cross-flow into the centre of the CVP and induces fluid movements away from the side-jets, deeper into the cross-flow. Axis-switching induces a vortical pair switch, which remain counter-rotating after switching. The vorticity is deduced to be weaker than the original CVP, and coupled with the curved wall effect, no further axis-switching within the flow is observed. Axis-switching of the vortices promote a larger area for interaction and enhances mixing via shear action of the profiles (cruciform for 4SJ and "Y" profile for the 3SJ) with the primary flow. This enhances mixing between the streams and increases the centreline turbulence, which enhances mass transport within the flow, as compared to conventional jets which largely relies on the shear between the primary jet and the ambient flow.

7.2 Conclusions

Multilateral jet mixing technique has been adopted as a means to enhance the controllability and stability of turbulent jet flames, by partial premixing the reactants of the turbulent jet flames. Despite being an extension to jet in a cross-flow, which is well-studied due to their applications in industry, little information can be synthesized from the literature for the required application. Isothermal experiments, aided by laser diagnostic measurement techniques PIV and PLIF, were conducted to provide a better understanding of the fundamentals of such mixing technique. The laser diagnostic techniques provide a higher temporal and spatial resolution compared to traditional point measurement methods, and have provided reliable planar measurements of the flow-field and flow structures induced by the multilateral

jet under the influence of a range of MR. The results from this study has cross-field applications. The findings from the isothermal component are incorporated into the reacting flow component of this study, which were carried out on a laboratory-scale, stainless steel burner. The flame structures and characteristics, and near flow field were investigated with OH*-chemiluminescence and PIV, respectively. The following conclusions can be drawn from the findings of this study:

1. The non-dimensional ratio of the side-jet's momentum to the primary jet's momentum, termed momentum ratio, was found to be the main controlling parameter to characterize the flow regimes inside the primary nozzle. Experimental study has helped define three distinct regimes as function of the momentum ratio, MR, and those are:

    - Streaming flow regime ($0 < MR < 0.2$)
    - Impinging flow regime ($MR \approx 0.2$)
    - Backflow regime ($MR >> 0.2$)

2. Streaming flow regime is dominated by the primary jet flow momentum. The side-jets injected into the primary flow do not augment the mean axial flow vectors considerably. The flow cases in this flow regime is effective in generating near homogeneous mixing at the exit plane, which is dominated by large-scale mixing, a result of the developing CVPs. This regime is suitable, and has been used in many practical engineering applications such as reactants mixing and fume quenching.

3. The trajectories of the side-jets in the streaming flow mode cannot be scaled via conventional jet in cross-flow scaling methods. The side-jets trajectories influenced by the confinement geometry, the location of the adjacent side-jets and is limited to the primary flow's centreline. The prediction of side-

jets trajectory via these conventional methods over-predicts the side-jets' penetration by at least 50%, for 3SJ cases.

4. Flow cases in the impinging flow regime generate an obvious secondary stream around the primary flow centreline. The secondary stream is more obvious in the 4SJ configuration compared to the 3SJ, attributed to the lack of space for vortical expansion in the cross-section. The side-jets in this flow regime impinge at the primary flow centreline and form a stagnation point upstream. This stagnation point acts as a pseudo-bluff body for the primary flow, which is routed around this region. This induces mixing between the side-jets streams and the primary flow stream. Downstream of the side-jets impingement, a secondary stream which consist mostly of side-jets fluid is carried out of the nozzle along the centreline, forming a core structure in the axial plane, which extends out of the nozzle exit. The impingement also induce a strong flow turbulence at the impinging point, which is sustained up to around $1D_P$ downstream.

5. Axis-switching of the CVPs, induced by the side-jets, are observed for most streaming flow and impinging flow cases for both 3SJ and 4SJ configurations. The impinging jets show that no obvious CVPs needed to be formed in the flow cross-section for axis-switching to take place. The axis-switching mechanism is deduced to rely on the folding of the exiting side-jets induced by the shear of the primary jet flow on the side-jets. The side-jet with CVPs that are carried downstream by the primary flow are advected towards the centreline by the velocity induced by the CVPs. Axis-switching takes place when adjacent CVPs are advected close to each other, which results in the pairing of adjacent vortices. This new vortical pairings induce a velocity to the opposing direction, and in our case, away from the centreline towards the pipe wall. The vorticity for the new vortices are relatively weaker than the original induced CVPs, and

coupled with the "curved-wall image" of the vortices, locks the vortices in space at a fixed distance away from the nozzle wall. The new vortices pairings remain rotational.

6. In the backflow regime, the side-jets impinge the primary flow centreline at a high momentum and a fraction of the side-jets' fluid are propagated upstream. The length of the backflow is a function of the side-jets to primary flow momentum ratio and number of side-jets. Both increasing the MR of the flow and the number of side-jets increase the length of the backflow. The flow characteristics of a backflow regime include a primary centreline of high side-jets' fluid concentricity, a well-mixed flow surrounding the secondary jet formed, and high flow turbulence, in particular in the region around the primary flow centreline. At higher momentum ratio, some flapping characteristics can also be observed.

7. The side-jets in a 4SJ configuration penetrate the primary flow sooner than in a 3SJ flow. The vortices induced in a 4SJ flow have less space to develop due to the increase of flow blockage, thus advecting the flow towards the centreline. Moreover the side-jets in the 3SJ flows are more uniformly mixed than the 4SJ.

8. Using ANSYS CFX commercial code, a CFD model was developed to predict the multilateral jet flows. Good agreement was found between a model utilizing the $SST-k\omega$ turbulence model and experimental. The CFD model was able to capture the flow physics, in particular the axis-switching phenomena within both 3SJ and 4SJ configurations. The model showed that the flow remains rotational in the cross-sectional flow after axis-switching.

9. Application of side-jets upstream of the nozzle exit influences the shear region downstream of the nozzle exit. Increasing the flow MR reduces the coherence of the large-scale structures in the jet shear layer and enhances the formation

of small-scale structures within the region.

10. Impinging jets increase the round jet turbulence intensity which decays up to approximately $2D_P$. Both the turbulence intensity and velocity decay show similar trends despite significantly different flow MR.

11. Compared to a normal round jet, the jet outflow for flow cases with side-jets show a shorter "potential core" region. This is in-line with findings by other side-jets studies [60].

12. The flame stability and appearance are affected by the mixing regime upstream of the nozzle exit. Streaming flow regime generates individual flames which are anchored to the side-jets exit at low flow Re number. At $Re_b = 5000$, flames in the streaming flow regime cannot be sustained and is blown out. Impinging flow regimes generate mostly lifted-flames which is stabilized at approximately $1D_P$ downstream of the burner nozzle exit, whilst flames in the backflow mode is stabilized at the nozzle exit and did not propagate back into the nozzle. The flame length generated by the attached flames are longer and more luminous than the lifted flame.

13. Flames and flow profiles generated by the 4SJ burner nozzle are similar both in the 45° and 90° offset planes. This also applies to the impinging flow (lifted-flames) which shows obvious differences at the nozzle exit due to the vortical pairing resultant from axis-switching.

14. The asymmetric side-jets configuration for 3SJ affects the near flow field (turbulence profile skewed towards the side-jets' aligned region) and has a more intense heat release in regions opposite the side-jets.

15. The mixing regimes upstream of the nozzle exit has drastic effects up to $1D_P$ downstream in the flames before being dominated by the combustion heat

release.

7.3 Recommendations for future work

This thesis provides a better understanding towards the fundamentals of multilateral jet mixing technique for partial pre-mixing. However, some cross-stream applications may also be synthesized from the findings. There are, however some outstanding issues that require further investigations, improvements and optimizations. The following recommendations are made to elevate this mixing technique beyond the scope of this thesis.

1. The flame characteristics of the nozzle should be tested for a varied locations upstream of the nozzle exit, and for different fuels. The integration of the side-jets location upstream of the nozzle exit is suggested to optimize and to identify a "sweet spot" for the placement of the side-jets for the optimal mixing which still generate a stable flame. it has been deduced that the mixing intensity of the mixture at the nozzle exit increases as the side-jets are placed closer to the nozzle exit, which needs to be verified. Different fuel needs to be injected into the nozzle to study the adaptability of such nozzle and mixing technique on different fuel variant.

2. It will be worthwhile to study the characteristics of the flame when the side-jets are placed in a non-symmetrical configuration. In addition, the effect of this configuration on the side-jets' penetration into the primary flow and axis-switching of the vortices is not known. The non-symmetrical placements of the side-jets will likely induce an instability due to the non-symmetrical vortical interaction that may take place in the flow.

3. In-depth CFD modelling and simulation should be conducted incorporating more in-depth combustion kinetics. The cross-validation of the combustion

model and the experimental outcomes will be beneficial for any future applications in practical burners.

4. The study of side-jet's trajectory in a confined cross-flow needs to be undertaken with systematic increment of the confinement size. It has previously been deduced that the side-jets penetration into the primary flow is influenced by the existence of the confinement and of adjacent jets, but to what extent? This study will potentially provide for a reliable scaling of the side-jets in a confined environment, which will benefit future studies which relies on such mixing technique for applications in the industry.

References

[1] V. Smil. 21st ventury energy: Some sobering thoughts. *OECD Observer*, (258/259), 2006.

[2] N. Clark and K. Yusoff. Combustion and society: a fire-centred history of energy use. *Theory, Culture and Society*, 31(5):203–226, 2014.

[3] C. D. Keeling. Global observation of atmospheric co2. *Global Environmental Change*, 15, 1993.

[4] C. B. Field, V. R. Barros, K. J. Mach, M. D. Mastrandrea, M. van Aalst, W. N. Adger, D. J. Arent, J. Barnett, R. Betts, T. E. Bilir, J. Birkmann, J. Carmin, D. D. Chadee, A. J. Challinor, M. Chatterjee, W. Cramer, D. J. Davidson, Y. O. Estrada, J.-P. Gattuso, Y. Hijioka, O. Hoegh-Guldberg, H.Q. Huang, G. E. Insarov, R. N. Jones, R. S. Kovats, P. Romero-Lankao, J. N. Larsen, I. J. Losada, J. A. Marengo, R. F. McLean, L. O. Mearns, R. Mechler, J. F. Morton, I. Niang, T. Oki, J. M. Olwoch, M. Opondo, E. S. Poloczanska, H. O. Pörtner, M. H. Redsteer, A. Reisinger, A. Revi, D. N. Schmidt, M. R. Shaw, W. Solecki, D. A. Stone, J. M. R. Stone, K. M. Strzepek, A. G. Suarez, P. Tschakert, R. Valentini, S. Vicuña, A. Villamizar, K. E. Vincent, R. Warren, L. L. White, T. J. Wilbanks, P. P. Wong, and G. W. Yohe. Technical summary. *Climate Change 2014: Impacts, Adaptation and Vulnerability. Part A: Global and Sectoral Aspects*, 2014.

[5] Energy Information Administration. The international energy outlook 2013. *US ENergy Informatiin Administration*, 2013.

[6] R. Wilson. The future of energy: why power density matters. *The energy collective*, 2013.

[7] Y. Huang and V. Yang. Dynamics and stability of lean-premixed swirl stabilized combustion. *Progress in Energy and Combustion Science*, 35:293–364, 2009.

[8] G. J. Nathan, Z. T. Alwahabi, G. J. R Newbold, and D. S. Nobes. Impacts of a jet's exit flow patern on mixing and combustion performance. *Progress in Energy and Combustion Science*, 32:496–538, 2006.

[9] G. Tashtoush, M. I. Al-Widyan, and A. O. Al-shyoukh. Combustion performance and emissions of ethyl ester of a waste vegetable oil in a water-cooled furnace. *Applied Thermal Engineering*, 23:285–293, 2003.

[10] K. R. Mcmanus, U. Vandsburger, and C. T. Bowman. Combustor performance enhancement through direct shear layer excitement. *Combustion and Flame*, 82:75–92, 1990.

[11] S. A. Basha, K. RajaGopal, and S. Jebaraj. A review on biodiesal production, combustion, emissions and performance. *Renewable and Sustainable Energy Review*, 13:1628–1634, 2009.

[12] C.O. Paschereit and E. Gutmark. The effectiveness of passive combustion control methods. *Power for land, sea and air*, 1:361–374, 2004.

[13] A.R. Masri. Partial premixing and stratification in turbulent flames. *Proceedings of the Combustion Institute*, 35:1115–1136, 2015.

[14] E. Mastorakos, A.M.K.P. Taylor, and J.H. Whitelaw. Extinction and temper-

ature characteristics of turbulent counterflow diffusion flames with partial premixing. *Combustion and flame*, 91:40–54, 1992.

[15] S.R. Turns, F.H. Myhr, R.V. Bandaru, and E.R. Maund. Oxides of nitrogen emissions from turbulent jet flames: Part ii - fuel dilution and partial premixing effects. *Combustion and flame*, 93:255–269, 1993.

[16] B. Bennett, C.S. Mcenally, L.D. Pfefferle, and M.D. Smooke. Computational and experimental study of axisymmetric coflow partially premixed methane/air flames. *Combustion and flames*, 123:522–546, 2000.

[17] D. G. Lilley. Swirl flows in combustion: A review. *AIAA Journal*, 15(8):1063–1078, 1977.

[18] J. W. Daily. laser induced fluorescence spectroscopy in flames. *Progress in Energy and Combustion Science*, 23:133–199, 1997.

[19] E. J. Gutmark, T. P. Parr, K. J. Wilson, and K. C. Schadow. Active control in combustion systems with vortices. *Proceedings of the 4th IEEE Conference on Control Applications*, pages 679–684, 1995.

[20] R. S. Barlow. laser diagnostics and their interplay with computations to understand turbulent combustion. *Proceedings of the Combustion Institute*, 31:49–75, 2007.

[21] J. J. parham, G. J. Nathan, S. J. Hill, and P. J. Mullinger. A modified thring-newby scaling criterion for confined, rapidly spreading and unsteady jets. *Combustion Science and Technology*, 177:1421–1447, 2005.

[22] G. Li and E. J. Gutmark. Effect of exhaust nozzle geometry on combustor flow field and combustion characteristics. *Proceedings of the Combustion Institute*, 30:2893–2901, 2005.

[23] G. J. Nathan, P. A. M. Kalt, Z. T. Alwahabi, B. B. Dally, P. R. Medwell, and Q. N. Chan. Recent advances in the measurement of strongly radiating, turbulent reacting flow. *Progress in Energy and Combustion Science*, 38:41–61, 2012.

[24] A. Cavaliere and M. de Joannon. Mild combustion. *Progress in Energy and Combustion Science*, 30:329–366, 2004.

[25] Y. Cao, J. Wu, J. Mi, and Y. Zhou. flame structure of a jet flame with penetration of side micro-jets. *Chinese journal of chemical engineering*, 16(6):861–866, 2008.

[26] E. F. Hasselbrink, M. G. Mungal, and R. K. Hanson. Simultaneous planar velocimty measurements and oh imaging in a transverse jet flame. *Journal of Visualization*, 1(1):65–77, 1998.

[27] P. H. Renard, D. thevenin, J. C. Rolon, and S. Candel. Dynamics of flame/vortex interactions. *Progress in Energy and Combustion Science*, 26:225–282, 2000.

[28] A. Linan, M. Vera, and A. L. Sanchez. Ignition, lift off, and extinction of gaseous diffusion flames. *Annual Review of Fluid Mechanics*, 47:293–314, 2015.

[29] S. H. Chung. Stabilization, propagation and instability of tribrachail triple flame. *Proceedings of the Combustion Institute*, 31:877–892, 2007.

[30] S. Meares and A. R. Masri. A modified piloted burner for stabilizing turbulent flames of inhomogeneous mixtures. *Combustion and Flame*, 161:485–495, 2014.

[31] S. B. Pope. Turbulent premixed flames. *Annual Review for Fluid Mechanics*, 19: 237–270, 1987.

[32] K. M. Lyons. Toward an understanding of the stabilization mechanisms of

lifted turbulent jet flames: Experiments. *Progress in Energy and Combustion Science*, 33:211–231, 2007.

[33] P. Calvin and G. Joulin. Premixed flames in large scale and high intensity turbulent flow. *Le Journal de Physique-Letters*, 44, 1983.

[34] M. S. Mansour. A study of turbulent partially premixed flames based on simultaneous imaging of velocity field and oh radical. *Combustion Science and Technology*, 174:47–78, 2002.

[35] S. K. Aggarwal. Extinction of laminar partially premixed flames. *Progress in Energy and Combustion Science*, 35:528–570, 2009.

[36] F. El-Mahallawy, A Abdelhafez, and M. S. Mansour. Mixing and nozzle geometry effects on flame structures and stability. *Combustion Science and Technology*, 61:805–822, 2007.

[37] M. S. Mansour, A. M. Elbaz, and M. Samy. The stabilization mechanism of highly stabilized partially premixed flames in a concentric flow conical nozzle burner. *Experimental Thermal and Fluid Science*, 43:55–62, 2012.

[38] P. Domingo and L. Vervisch. Triple flames and partially premixed combustion in auto-ignition of non-premixed turbulent mixtures. *International Symposium on Combustion*, 26(1):233–240, 1996.

[39] R. F. Huang and M. J. Yang. Thermal and concentration fields of burner attached jet flames in cross flow. *Combustion and Flame*, 105:211–224, 1996.

[40] D. S. Liscinsky, B. True, and J. D. Holdeman. Crossflow mixing of noncircular jets. *Journal of Propulsion and Power*, 12(2):225–230, 1996.

[41] M. Ihme and H. Pitsch. Prediction of extinction and reignition in non-premixed

turbulent flames using flamelet/progress variable model 1. a priori study and presumed pdf closure. *Combustion and Flame*, 155:70–89, 2008.

[42] C. N. Markides and E. Mastorakos. Measurements of scalar dissipation in a turbulent plume with planar laser-induced fluorescence of acetone. *Chemical Engineering Science*, 61:2835–2842, 2006.

[43] W. R. Hawthorne, D. S. Weddell, and H. C. Hottel. Mixing and combustion in turbulent gas jets. *Proceedings of the Symposium on Combustion and Flame, and Explosion Phenomena*, 1948.

[44] M. S. Mansour. A concentric flow conical nozzle burner for highly stabilized partially premixed flames. *Combustion Science and Technology*, 152:115–145, 2000.

[45] E. Mastorakos. Ignition of turbulent non premixed flames. *Progress in Energy and Combustion Science*, 35(1):57–97, 2009.

[46] T. Lieuwen, V. McDonell, D. Santavicca, and T. Sattelmayer. Burner development and operability issues associated with steady flowing syngas fired combustors. *Combustion Science and Technology*, 180:1167–1190, 2008.

[47] K. R. McManus, T. Poinsot, and S. M. Candel. A review of active control of combustion instabilities. *Progress in Energy Combustion and Science*, 19:1–29, 1993.

[48] K. Schadow, E. W. Hendricks, and R. J. Hansen. Recent progress in the implementation of active combustor control. *Unsteady Combustion*, 306: 139–160, 1996.

[49] N. Peters. Local quenching due to flame stretch and non-premixed turbulent combustion. *Combustion Science and Technology*, 30:1–7, 1983.

[50] M. S. Cha and S. H. Chung. Characteristics of lifted flames in non-premixed turbulent confined jets. *Symposium (International) on Combustion*, 26(1): 121–128, 1996.

[51] K. A. Watson, K. M. Lyons, J. M. Donbar, and C. D. Carter. On scalar dissipation and partially premixed flame propagation. *Combustion Science and Technology*, 175:649–664, 2003.

[52] D. Shimokuri and S. Ishizuka. Flame stabilization with a tubular flame. *Proceedings of the Combustion Institute*, 30:399–406, 2005.

[53] Y. C. Chen, N. Peters, G. A. schneemann, N. Wruck, U. Renz, and M. S. Mansour. The detailed flame structure of highly stretched turbulent premixed methane-air flames. *Combustion and Flame*, 107:233–244, 1996.

[54] G. Yu, J. G. Li, X. Y. Chang, L. H. Chen, and S. J. Sung. Fuel injection and flame stabilization in a liquid kerosene fuelled supersonic combustor. *Journal of Propulsion and Power*, 19(5):885–8933, 2003.

[55] G. A. Agoston, A. W. Noon, and T. D. Witherly. Experimental study of a reversed jet flameholder. *Winter Meeting of the Western States Section of the Combustion Institute*, 1958.

[56] I. Esquiva-Dano and D. Escudie. Influence of a bluff body's shape on the stabilization regime of non-premixed flames. *Combustion and Flame*, 127: 2167–2180, 2001.

[57] B. Li, E. Baudoi, R. Yu, Z. W. Sun, Z. S. Li, X. S. Bai, M. ALden, and M. S. Mansour. Experimental and numerical study of a conical turbulent partially premixed flame. *Proceedings of the Combustion Institute*, 32:1811–1818, 2009.

[58] B. Yan, N. Li, E. Baudoin, C. Liu, Z. W. Sun, Z. S. Li, X. S. Bai, M. Alden, G. chen, and M. S. Mansour. Structures and stabilization of low calorific value gas

turbulent partially premixed flames in a conical burner. *Experimental Thermal and Fluid Science*, 34:412–419, 2010.

[59] E. J. Gutmark and F. F. Grinstein. Flow control of noncircular jets. *Annual Review of Fluid Mechanics*, 31:239–272, 1999.

[60] T. H. New and W. L. Tay. Effects of cross-stream radial injections on a round jet. *Journal of Turbulence*, 7(57):1–19, 2006.

[61] P. Behrouzi, T. Feng, and J. J. McGuirk. Active flow control of jet mixing using steady and pulsed fluid tabs. *Journal of Systems amd Control Engineering*, 22: 381–392, 2008.

[62] Y. Saiki, Y. Suzuki, and N. Kasagi. Active control of swirling coaxial jet mixing with manipulation of large-scale vortical structures. *Flow Turbulence Combustion*, 86:399–418, 2011.

[63] N. Syred. A review of oscillation mechanisms and role of the precessing vortex core in swirl combustion systems. *Progress in Energy and Combustion Science*, 32:93–161, 2006.

[64] H. Liang and T. Maxworthy. Experimental investigations of a swirling jet in both stationary and rotating surrounding. *Experiments in Fluids*, 45:283–293, 2008.

[65] G. Raman and A. B. Cain. Innovative actuators for active flow and noise control. *Proceedings of the Institution of Mechanical Engineers, Part G: Journal of Aerospace Engineering*, 216:303, 2002.

[66] M. Hassaballa and S. Ziada. Self excited oscillations of two opposing planar air jets. *Physics of Fluid*, 27, 2015.

[67] P. Luo, Y. Fang, B. Wu, and H. Wu. Turbulent characteristics and design of transverse jet mixers with multiple orifice. *Industrial and Engineering Chemistry Research*, 2016.

[68] D. B. Bain, C. E. Smith, and J. D. Holdeman. Mixing analysis of axially opposed rows of jets injected into confined crossflow. *Journal of Propulsion and Power*, 11(5):885–893, 1995.

[69] J. D. Holdeman, D. S. Liscinsky, V. L. Oechsle, G. S. Samuelsen, and C. E. Smith. Mixing of multiple jets with a confined subsonic crossflow: Part 1- cylindrical duct. *Journal of Engineering for Gas Turbines and Power*, 119:852–862, 1997.

[70] R. D. Moser and R. Moin. The effects of curvature in wall-bounded turbulent flows. *Journal of Fluid Mechanics*, 175:479–510, 1987.

[71] D. J. Forliti, D. V. Salazar, and A. J. Bishop. Physics-based scaling laws for confined and unconfined transverse jets. *Experiments in Fluids*, 56(36):1–16, 2015.

[72] J. F. Seidel, C. Pappert, T. H. New, and H. M. Tsai. Effects of multiple radial blowing around a circular jet. *43rd AIAA Aerospace Sciences Meeting and Exhibit*, 2005.

[73] C. H. Birzer, R. M. Kelso, and B. B. Dally. Flame structure of jets in confined cross-flows. In *Proceedings of the Australian Combustion Symposium*. The University of Newcastle, 2011.

[74] R.L.J. Fernandes, A. Sobiesiak, and A. Pollard. Opposed round jets issuing into a small aspect ratio channel cross flow. *Experimental Thermal and Fluid Science*, 13(4):374–394, 1996.

[75] A. D. Gosman and R. Simitovic. An experimental study of confined jet mixing. *Chemical Engineering Science*, 41(7):1853–1871, 1986.

[76] G. D. Catalano, K. S. Chang, and J. A. Mathias. Investigation of turbulent jet impingement in a confined crossflow. *AIAA Journal*, 27(11):1530–1535, 1989.

[77] A. D. Birch, D. R. Brown, M. Fairweather, and G. K. Hargrave. An experimental study of a turbulent natural gas jet in a cross flow. *Combustion Science and Technology*, 66:217–232, 1989.

[78] R. V. Bandaru and S. R. Turns. Turbulent jet flames in a crossflow: Effects of some jet, crossflow, and pilot flame parameters on emissions. *Combustion and Flame*, 121:137–151, 2000.

[79] T. F. Fric and A. Roshko. Vortical structure in the wake of a transverse jet. *Journal of Fluid Mechanics*, 279:1–47, 1994.

[80] R. M. Kelso, T. T. Lim, and A. E. Perry. An experimental study of round jets in cross-flow. *Journal of Fluid Mechanics*, 306:111–144, 1996.

[81] D. Han and M. G. Mungal. Direct measurement of entrainment in reacting/non-reacting turbulent jet. *Combustion and Flame*, 124(3):370–386, 2001.

[82] J. D. Holdeman, R. Srinivasan, and A. barenfeld. Experiments in dilution jet mixing. *AIAA Journal*, 22(10):1436–1443, 1984.

[83] R. Andreopoulos and W. Rodi. Experimental investigation of jets in a crosflow. *Journal of Fluid Mechanics*, 138:93–127, 1984.

[84] L. L. Yuan and R. L. Street. Trajectory and entrainment of a round jet in crossflow. *Physics of Fluids*, 10:2323, 1998.

[85] S. H. Smith and M. G. Mungal. Mixing, structure and scaling of the jet in crossflow. *Journal of Fluid Mechanics*, 357:83–122, 1998.

[86] T. Cambonie, N Gautier, and J. L. Aider. Experimental study of counter-rotating vortex paid trajectories induced by a round jet in cross-flow at low velocity ratios. *Experiments in Fluids*, 54:1–13, 2013.

[87] J. N. Blanchard, Y. Brunet, and A. Merlen. Influence of a counter rotating vortex pair on the stability of a jet in a cross flow: an experimental study by flow visualizations. *Experiments in Fluids*, 26:63–74, 1999.

[88] A. Krothapalli, L. Lourenco, and J. M. Buchlin. Separated flow upstream of a jet in a cross-flow. *AIAA Journal*, 28:414–420, 1990.

[89] A. Erogly and R. E. Breidentha. Structure, penetration and mixing of pulsed jets in crossflow. *AIAA Journal*, 39(3):417–423, 2001.

[90] S. Muppidi and K Mahesh. Study of trajectories of jets in crossflow using direct numerical simulations. *Journal of Fluid Mechanics*, 530:81–100, 2005.

[91] K. C. Marr, N. T. Clemens, and O. A. Ezekoye. Mixing characteristics and emissions of strongly-forced non-premixed partially premixed jet flames in crossflow. *Combustion and Flame*, 159:707–721, 2012.

[92] C. G. Ball, H. Fellouah, and A. Pollard. The flow field in turbulent round free jets. *Progress in Aerospace Sciences*, 50:1–26, 2012.

[93] W. J. A. Dahm and P. E. Dimotakis. Measurements of entrainment and mixing in turbulent jet. *AIAA Journal*, 25(9):1216–1223, 1987.

[94] T. L. Labus and E. P. Symons. Experimental investigation of an axisymmetric free jet with an initially uniform velocity profile. *National Aeronautics and Space Administration*, 1972. Technical Note.

[95] J. Mi, D. S. Nobes, and G. J. Nathan. Influence of jet exit conditions on the

passive scalar field of an axisymmetric free jet. *Journal of Fluid Mechanics*, 432: 91–125, 2001.

[96] W. M. Pitts. Reynolds number effects on the mixing behavior of axisymmetric turbulent jets. *Experiments in Fluids*, 11:135–141, 1991.

[97] J. Mi, G. J. Nathan, and D. S. Nobes. Mixing characteristics of axisymmetric free jets from a contoured nozzle, an orifice plate and a pipe. *Journal of Fluids Engineering*, 123:878–883, 2001.

[98] P. Behrouzi and J. J. McGuirk. Flow control of jet mixing using a pulsed fluid tab nozzle. *Proceedigs of the 3rd AIAA Flow Control Conference*, pages 1–20, 2006.

[99] R. C. Deo and G. J. Nathan. The influence of nozzle exit geometric profile on statistical properties of a turbulent jet plane. *Experimental Thermal and Fluid Science*, 32:545–559, 2007.

[100] K. B. M. Q. Zaman. Axis switching and spreading of an asymmetric jet: the role of coherent structure dynamics. *Journal of Fluid Mechanics*, 316:1–27, 1996.

[101] F. Hussain and H. S. Husain. Elliptic jets. part 1. characteristics of unexcited and excited jets. *Journal of Fluid Mechanics*, 208:257–320, 1989.

[102] S. Bernero and H. E. Fiedler. Application of particle image velocimetry and proper orthogonal decomposition to the study of a jet in a counter flow. *Experiments in Fluids*, pages 2274–2281, 2000.

[103] M. H. Gazzah, N. Boughattas, H. Belmabrouk, and R. Said. The dynamic field in a turbulent round jet discharging into a co-flowing stream. *Natural Science*, 2(6):635–640, 2010.

[104] R. A. Antonia and R. W. Bilger. An experimental investigation of an axisymmetric jet in a co-flowing air stream. *Journal of Fluid Mechanics*, 61(4):805–822, 1973.

[105] V. Raman and R. O. Fox. Modelling of fine particle formation in turbulent flames. *Annual Review for Fluid Mechanics*, 48:159–190, 2016.

[106] K. R. Sreenivasan and R. A. Antonia. The phenomenology of small-scale turbulence. *Annual Review of Fluid Mechanics*, 29:435–472, 1997.

[107] A. Lozano, B. Yip, and R. K. Hanson. Acetone: a tracker for concentration measurements in gaseous flows by planar laser-induced fluorescence. *Experiments in Fluids*, 13:369–376, 1992.

[108] P. Sarathi, R. Gurka, G. A. Kopp, and P. J. Sullivan. A calibration scheme for quantitative concentratin measurements using simultaneous piv and plif. *Experiments in Fluids*, 52:247–259, 2012.

[109] P. A. M. Kalt and G. J. Nathan. Corrections to fcilitate planar imaging of particle concentration in particle laden flows using mie scattering, part 2: Diverging laser sheets. *Applied Optics*, 46:7227–7236, 2007.

[110] C. Venderwel and S. Tavoularis. On the accuracy of plif measurements in slender plumes. *Experiments in Fluids*, 55:1–16, 2014.

[111] D. S. Dandy and S. R. Vosen. Numerical and experimental studies of hydroxyl radical chemiluminescence in methane-air flame. *Combustion Science and Technology*, 82(1-6):131–150, 1992.

[112] J. M. Donbar, J. F. Driscoll, and C. D. Carter. Reaction zone structure in turbulent nonpremixed jet flames - from ch-oh plif images. *Combustion and Flame*, 122: 1–19, 2000.

[113] A. R. Choudhuri and S. R. Gollahalli. Laser induced fluorescence measurements of radical concentrations in hydrogen-hydrocarbon hybrid gas fuel flames. *International journal of Hydrogen Energy*, 25:1119–1127, 2000.

[114] D. J. Forliti and P. J. Strykowski. Controlling turbulence in a rearward-facing step combustor using counter current shear. *Fluids Engineering*, 127:438–448, 2005.

[115] C. L. Douay and T. M. Faure. Stereoscopic piv using optical flow: application to a cavity recirculation. *Experiments in Fluids*, 54:1–15, 2013.

[116] O. Uzol and C. Camci. The effect of sample size, turbulence intensity and the velocity field on the experimental accuracy of ensemble averaged piv measurements. *4th International Symposium on Particle Image Velocimetry*, 2001.

[117] D. J. Forliti and P. J. Strykowski K. Debatin. Bias and precision errors of digital particle image velocimetry. *Experiments in Fluids*, 28:436–447, 2000.

[118] M. Y. Leong and G. S. Samuelsen. Optimization of jet mixing into a rich, reacting crossflow. *Journal of Propulsion and Power*, 2000.

[119] K. Knowles and M. Myszko. Turbulence measurements in radial wall jets. *Experimental Thermal and Fluid Science*, 17(1-2):71–78, 1998.

Appendices

Appendix A

Australasian Fluid Mechanics Conference 2014

19th Australasian Fluid Mechanics Conference
Melbourne, Australia
8-11 December 2014

Mixing Field Characteristics of Multi-lateral Jets Injected into a Round Pipe Flow

C.X. Thong[1], P.A.M. Kalt[1], B.B. Dally[1], C.H. Birzer[1]

[1]School of Mechanical Engineering
The University of Adelaide, South Australia 5005, Australia

Abstract

Jet in cross-flow is a well-studied and characterised fluid-mixing phenomenon. In several combustion applications, the use of laterally placed side-jets can be used to produce jets into a confined cross-flow (JICCF). These flows can be expected to have similar mixing as the traditional jet in cross-flow cases and therefore provide a potentially cost-effective means of optimising a combusting jet flow. However, there are limits to the data currently available on the fundamentals of JICCF. Hence, the current study investigates the flow structures formed in a round pipe flow modified by four equi-spaced side jets. Non-reacting, isothermal experiments are conducted in water on a central nozzle with four smaller jets located one central diameter upstream of the nozzle exit plane. The induced flow structures are visualised using Planar Laser Induced Fluorescence (PLIF). The operating conditions are varied to explore the role of jet injection to primary flow ratio, whilst the bulk flow rate is maintained at a constant level. The analysed data identify the formation of various flow regimes as the relative momentum-flux ratio induced via side jet injection is increased. The behaviour of the side jets within the main jet is substantially different from similar side-jet injection into an unconfined flow. The results show that several flow regimes can be discerned, namely: a non-impinging flow; impinging flow with no backflow; and impinging flow with backflow. It is found that the mixing trends and resulting regimes have consequences for the emerging near-field mixedness.

Introduction

Combustion is a widely used method to convert the chemical energy that lies dormant within fuels into other forms of energy such as heat, light and kinetic energy. Fuel mixing in combustion is important as combustion can only be achieved when both fuel and air are mixed at the molecular level. To enhance mixing for turbulent jet flames, the method of jets in a confined cross-flow is investigated.

Jets in a confined cross-flow (JICCF) have been studied primarily for the applications in jet-fume dilution and Rich Burn/Quick Quench/Lean Burn (RQL) combustors [5]. The similarity between these applications includes the need for a rapid quenching process, that is, either to reduce a high temperature fume to an acceptable temperature level that is less damaging for turbine materials, or quick quenching from a rich combustion to a lean combustion zone to reduce oxides of nitrogen (NOx) emission [11]. These processes are generally conducted by injecting fluid (air/water) at relatively lower temperature into the rich fume/combustion-product region. The question of applying similar concepts for active turbulent jet flame mixing control and possibility of stabilizing the flame has been raised in light of increased interest in reducing combustion pollutant emission and enhancing flame stability under a wide range of operating conditions.

In many JICCF applications, mixing is reliant on the induced shear vortices, in particularly the Counter-rotating Vortex Pairs (CVP). The CVP phenomenon has been investigated extensively in the Jet in Cross–flow (unconfined flow) studies [9,12]. It is insufficient to rely only on the induced CVPs for turbulent mixing as they do not contribute much to the large scale turbulent structures in the flow, but this can be overcome by impinging the jets upon the confinement wall or on opposing jets [4]. However, most studies on JICCF found that jets impingement may not be favourable for the mixing applications mentioned earlier [3]. This prompted many studies to not probe further into the impinging cases thus contributing to the paucity of data available in this flow mode.

No “rule of thumb” law for good mixing has been established through JICCF studies [5]. The jet penetration into the cross-flow is an important parameter, and on a case by case basis depending on the confinement geometry, it can be characterised by means of the relative jet injection to primary flow momentum-flux ratio, as shown in the equation

$$J = \frac{(\rho V^2)_{inj}}{(\rho V^2)_p} \quad (1)$$

Where J is the momentum-flux ratio, ρ is the respective fluid densities, and V is the respective fluid velocity [5,11].

Most studies conducted on JICCF involve injecting streams of flow into a cross–flow of varying temperature, thus very little information is available on isothermal flow cases. Most studies involve injecting cooler air into air streams of relatively higher temperature, thus profiling the temperature variances at a certain point downstream to quantify for flow mixing [10,11]. The mixing mechanisms are influenced by the fluid density gradient, and thermal and molecular diffusion is not unity for all flows. Through viscosity, temperature also plays a part in mixing intensity [2]. While temperature measurements were conducted at the exit plane and for selective cases, no quantitative data are available on the impact of side injection on the mixing fields inside and outside the primary jet flow.

The current study explores the flow field and development of multiple jets impingement with increasing relative momentum-flux ratio, inside a round pipe in an isothermal flow environment. The aim of the current work is to assess the progression of the flow modes and their corresponding flow structures. This is achieved through an experimental investigation.

Methodology

Experiments were conducted in a water tunnel with a working section measuring 500 × 500 × 1800 mm^3. The experimental arrangement is shown in figure 1. A Perspex pipe with 56mm primary internal diameter (D) is fitted with four radially aligned equi-spaced 6mm Perspex jets located at one primary diameter upstream of the pipe (primary) exit. Perspex pipes are used for

the nozzle construction to allow optical access into the pipe. The region of interest in the nozzle is aligned with the centre of the tunnel's working section.

Flow for both the primary nozzle and side-injectors are sourced from different reservoirs respectively. Primary reservoir is seeded with Rhodamine 6G of concentration 0.1g/400L while the jet–injectors' reservoir comprises of clean water.

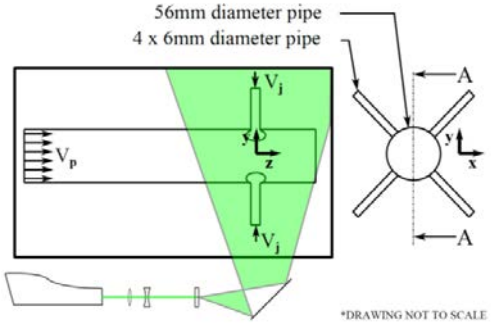

Figure 1. Schematic diagram of the experimental arrangement.

Planar Laser Induced Fluorescence (PLIF) is conducted using a Quantel Brilliant B Nd:YAG twin laser, frequency doubled to 532nm and double-pulsed at 10Hz. An optics train consisting of a combination of cylindrical and spherical optics lenses are used to produce a 2mm thickness laser sheet to illuminate the region of interest.

Images are captured on a Princeton Megaplus II Charged Coupled Devices (CCD) camera with a 2048 × 2048 pixels array. Image collection is done through the software EPIX XCAP 3.8. The camera is fitted with Tamron f1/4D telephoto lens and an addition of orange glass filter to capture PLIF images. The physical imaged spaced is approximated to be 200 × 200 mm^2. The spatial resolution ranges from 10.3 to 10.6 px/mm depending on camera readjustments. The timing for the laser beam discharge and CCD shuttle control is done using a Berkeley Nucleonics Corp (BNC) 565 delay generator.

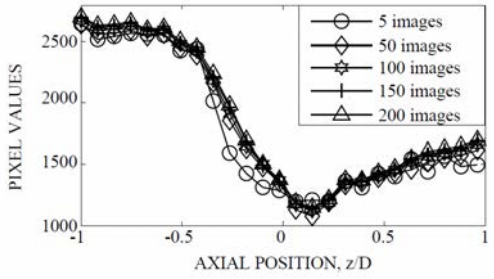

Figure 2. Mean flow centreline pixel values for different numbers of averaged images.

Figure 2 shows the statistics independence test carried out on different number of images in the ensemble of the J = 132 case. As the numbers of averaged images increases from 5 through 200 images, the mean centreline pixel values start converging on a single profile. The profile for 200 images overlaps with that of 150 images. This goes to show that the ensemble of 213 images is sufficient to present the current results.

The ensemble of 213 PLIF images is processed using OMA–X [7] following [6] and [8]. The PLIF images are predominantly calibrated with the unmixed dye solution (100% dye mixture concentration). Each PLIF image is calibrated with the upstream primary flow which remains unmixed with the injections stream.

Momentum-flux ratio, J	**18**	**35**	**58**	**90**	**132**	**186**
Primary Flow rate, $\dot{m}_p$ [L/h]	440.1	425.5	410.8	396.1	381.5	366.8
Injection Flow Rate, $\dot{m}_{inj}$ [L/h]	43.1	57.52	71.9	86.3	100.7	115.0
Massflow ratio, $\dot{m}_{inj}/\dot{m}_p$	0.098	0.135	0.175	0.218	0.264	0.313

Table 1. Experimental flow parameters.

The experimental matrix for the current study is as presented in table 1. The primary flow rate is reduced gradually through the datasets and correspondingly, the injection flow rate is increased to compensate for the loss of primary flow whilst maintaining a constant total flow rate.

Results and Discussion

The x, y and z-axis in the following figures denote the direction into the page, upwards, and stream-wise, respectively. The axial stream-wise distance is normalized to the primary nozzle diameter (D) and z/D = 0 indicates the jet-injectors' location whilst z/D = 1 indicates the nozzle exit.

The typical instantaneous PLIF images in figure 3 show the flow condition for increasing jet-to-primary flow momentum-flux ratio. The large scale mixing structures induced in the flow can be observed qualitatively from the figure. The dye-mixture fraction is obtained by normalizing the local signal values with the unmixed dye signal far upstream of the mixing region. Thus, the dye-mixture fraction value of 1.0 (the brightest region) corresponds to unmixed dye-mixture (purely primary flow fluid) whilst dye mixture fraction of value 0.0 signifies pure jet injection fluid. The increase in relative momentum-flux ratio (J) in figure 3 corresponds to a gradual change in the flow modes.

The streaming flow mode, where separate individual streams are formed, can be seen from figure 3(a). The increase in J leads to jets over-penetration and impinges at a location downstream of the jet–injectors' location in figure 3(b). A further increment in the J (figure 3(c)) shows the jet injections impinging at a shorter distance downstream in comparison to that in figure 3(b). The formation of backflow in the cases with relatively higher J cases can be observed in figures 3(d) through 3(f).

The mean PLIF dye mixture fraction images corresponding to cases shown in figure 3 is compiled from the ensemble average and is presented in figure 4. The different trends corresponding to the increase in J can be better observed through the dye mixture fraction images.

Figure 4(a) shows that little signal is captured of the jet-injection stream (darker region). The J value in this case is relatively lower than the other cases that the injection fluids are convected downstream without much penetration into the flow. The "residual" signal captured in this figure suggests that the flow mixing is reliant on the formation and development of the Counter–rotating Vortex Pairs (CVP).

A triangular jet-injection fluid region can be observed in figure 4(b) and (c). This is akin to a potential core of a simple jet and indicates the impinging of the lateral jets. A transition from impinging to a backflow mode can be observed in figure 4(d). This is characterized by the gradual changes to the downstream

injection fluid profile, that is, the transition from a triangular profile to a thicker stream-like profile.

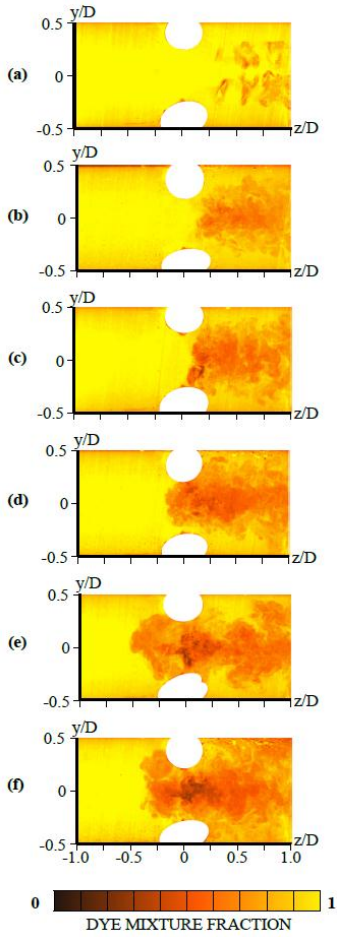

Figure 3. Typical instantaneous image for test cases (a) J = 18, (b) J = 35, (c) J=58, (d) J = 90, (e) J = 132, and (f) J = 186.

Figure 5 shows the centreline dye-mixture fraction profile for all of the investigated cases as indicated by the legends. Observing the profile for case J = 18 shows a gradual decrease in dye mixture fraction from approximately z/D = 0.25 onwards. This gradual depreciation from an unmixed dye-mixture plateau of 1.0 is consistent with the gradual penetration of CVPs into the imaged region. Cases from J = 18 to J = 186 feature a similar plateau region upstream, which corresponds to the unmixed dye region. The axial location when the dye-mixture fraction value begins to decrease shifts upstream with the increase in J. Cases with the impinging flow mode, J = 35 and J = 58 show a sharp drop from the unmixed plateau. Cases with backflow, J = 132 and J = 186, shows a consistent arch-like profile which is initiated upstream of z/D = 0 as a result of the induced backflow. From the plotted profiles, it is clear that the separate trends can be discerned into separate regimes. A streaming flow mode (such as that in figures 3(a) and 4(a)) is represented by J = 18; impinging flow mode is represented by groups of J = 35 and J = 58; and backflow mode represented by groups of J = 132 and J = 186.

The mixedness of a flow is an indication to how well the flow mixes in comparison to a homogenously mixed flow. The local mixedness, θ_i for the current study is defined by:

$$\theta_i = \begin{cases} \frac{|(f_i - f_{max})|}{(f_{max} - f_{hom})}, & f_i \geq f_{hom} \\ \frac{f_i}{f_{hom}}, & f_i < f_{hom} \end{cases} \quad (2)$$

Where f_i is the local dye mixture fraction at a local axial location, f_{max} defines the local maximum dye mixture fraction at the unmixed section of the flow, and f_{hom}, the homogenous dye mixture fraction value, defined by

$$f_{hom} = \frac{\dot{m}_p}{\dot{m}_p + \dot{m}_{inj}} \quad (3)$$

Where $\dot{m}_p$ defines the primary flow rate whilst $\dot{m}_{inj}$ defines the injectors flow rate. Mixedness of 1.0 indicates a homogenous mixture whilst mixedness of 0.0 indicates an unmixed flow.

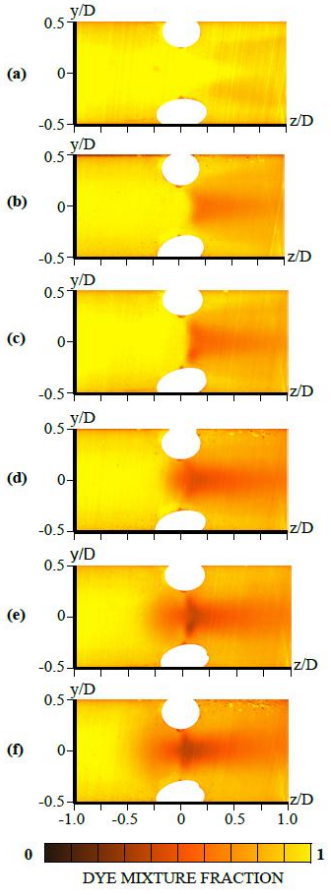

Figure 4. Mean dye mixture fraction images at the centre plane for cases (a) J = 18, (b) J = 35, (c) J=58, (d) J = 90, (e) J = 132, and (f) J = 186.

Figure 6 shows the profile of centreline mixedness for the cases investigated. Differences in mixing trends between case J = 18; J = 35, 58; and J = 132, 186 are noticeable. For J = 18, the flow remain unmixed until z/D = 0.25 where it starts to increase to a homogenous mixedness at z/D = 0.8. Despite the homogenous mixing, flames in such mode exits the nozzle in separate individual streams [1].

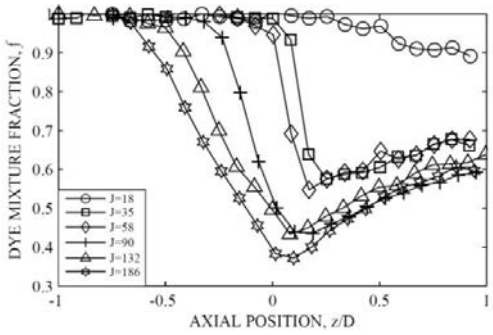

Figure 5. Centreline dye mixture fraction for increasing momentum-flux ratio $18 \leq J \leq 186$.

Similar trends can be observed for cases $J = 35$ and $J = 58$ where the mixedness increases from z/D = 0 and peaks at 1.0 close to z/D = 0.05 before decreasing and increases gradually to 0.8 at the nozzle exit. The spike region correlates well with the jet injections' impingement and over-penetration as discussed before. For cases of $J = 132$ and $J = 186$, the mixedness increases upstream of the jet injectors' location at z/D = 0 by the backflow. A steep increase in mixedness is followed by a recess to a local minimum which anchors onto the jet injections' impingement point. It can also be observed that the mixedness values for $J = 35$, $J = 58$, $J = 132$ and $J = 186$ collapses onto each other at locations $0.5 < z/D < 1.0$. A slight deviation in trend however can be detected for case $J = 90$ which has been identified as the transitioning point from an impingement flow mode to backflow mode.

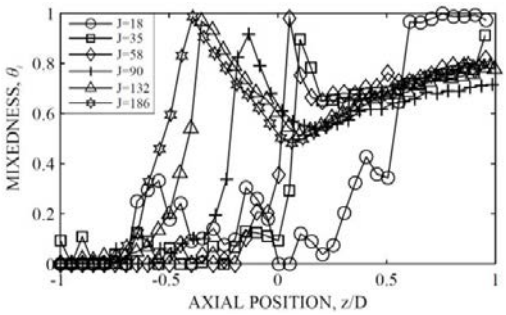

Figure 6. Centreline mixedness for increasing momentum-flux ratio, $18 \leq J \leq 186$.

Most of the other cases ($J = 35$ through 186) show a similar mixedness trend with the exception of case $J = 90$. The characteristic differences between the cases are the initiation point for the dye-mixture fraction in figure 5, which moves progressively upstream with increase J. Correspondingly, the point when the peaks in the mixedness plot also progresses upstream.

The highest mixedness achieved in the current study at the pipe outlet, z/D = 1, stems from case $J = 18$. However, a well-mixed centreline at the outlet should not be taken as a "good" mixing system and due considerations must also be given to the flow exit profiles highlighted in [1]. By comparing the instantaneous and the mean dye mixture fraction image in figures 3(a) and 4(a), it is intuitive to expect separate injection streams to emanate from the nozzle exit into the environment. The "potential core" seen in cases $J = 35$ through $J = 186$ may have a positive influence on the flame stability relative to the flow mode in case $J = 18$.

Conclusions

The current study investigates planar dye-mixture fraction profile in a pipe flow modified by four equally spaced side-jets with water as the working fluid. The primary mass-flow is decreased gradually whilst the injection-flow is increased to keep the total mass-flow in the pipe constant. The scalar field is visualized using PLIF technique.

The instantaneous results of the investigated cases serve as a good initial indication of the mixing intensity inside the pipe. It can be observed that the mixing intensity between the different streams (primary and injection streams) increases with respect to the relative momentum-flux ratio, J. Mean dye mixture fraction images presented show averaged dye distribution for the respective cases from a streaming flow mode to the backflow mode. By studying the centreline flow data, several flow trends can be discerned from the grouping of the centreline flow plots which corresponds to the flow mode: streaming mode; impingement mode; and backflow mode. The transition region from the impingement to the backflow mode is also captured in case $J = 90$.

References

[1] Birzer, C.H., Kelso, R.M. & Dally, B.B., Flame Structure of Jets in Confined Cross-flows, in *Proceedings of the Australian Combustion Symposium*, 2011.

[2] Brown, G.L. & Roshko, A., On Density Effects and Large Structure in Turbulent Mixing Layers, *Journal of Fluid Mechanics*, **64**, 1974, 775-816.

[3] Doerr, T., Blomeyer, M. & Hennecke, D.K., Optimization of Multiple Jets Mixing with a Confined Flow, *Journal of Engineering for Gas Turbines and Power*, **119**, 1997, 315-321.

[4] Gosman, A.D. & Simitovic, R., An Experimental Study of Confined Jet Mixing, *Chemical Engineering Science*, **41**, 1986, 1853-1871.

[5] Holdeman, J.D., Liscinsky, D.S., Oechsle, V.L., Samuelsen, G.S. & Smith, C.E., Mixing of Multiple Jets with a Confined Subsonic Crossflow: Part I-Cylindrical Duct, *Journal of Engineering for Gas Turbines and Power*, **119**, 1997, 852-862.

[6] Kalt, P.A.M., Birzer, C.H. & Nathan, G.J., Corrections to Facilitate Planar Imaging of Particle Concentration of Particle-laden Flows using Mie Scattering, Part 1: Collimated Laser Sheets, *Applied Optics*, 2007, **46**, 5823-5834.

[7] Kalt, P.A.M. & Long, M., OMA for MAC OS X, www.oma-x.org, 2014.

[8] Kalt, P.A.M. & Nathan, G.J., Corrections to Facilitate Planar Imaging of Particle Concentration in Particle-laden Flows using Mie Scattering. Part 2: Diverging Laser Sheets, *Applied Optics*, **46**, 2007, 7227-7236.

[9] Kelso, R.M., Lim, T.T. & Perry, A.E., An Experimental Study of Round Jets in Cross-flow, *Journal of Fluid Mechanics*, **306**, 1996, 111-144.

[10] Kroll, J.T., Sowa, W.A. & Samuelsen, G.S., Optimization of Orifice Geometry for Crossflow Mixing in a Cylindrical Duct, *Journal of Propulsion and Power*, **16**, 2000, 929-938.

[11] Leong, M.Y. & Samuelsen, G.S., Mixing of Jet Air with a Fuel-Rich, Reacting Crossflow, *Journal of Propulsion and Power*, **15**, 1999, 617-622.

Appendix B

Australian Combustion Symposium 2015

Proceedings of the Australian Combustion Symposium
December 7-9, 2015, The University of Melbourne

Effect of multi-lateral fuel jet injection on the flow field of Methane-Air turbulent flame

C.X. Thong[1, *], B.B. Dally[1], C.H. Birzer[1], P.A.M. Kalt[1]
[1]Centre for Energy Technology
School of Mechanical Engineering
The University of Adelaide SA 5005 Australia

Abstract
Multi-lateral jet injection concepts have a long history in industry and for various purposes, be it for hot combustion product quenching or for general mixing applications. The current study involves injecting fuel (CNG) through lateral side jets, a short distance upstream of a round jet air nozzle exit, with a flame stabilizing at the jet exit. Flame photography and Particle Imaging Velocimetry measurements were conducted as part of a preliminary study to investigate the effect of lateral injection on flame flow field, stability and appearance. For this study, the bulk flow velocity is kept constant whilst mass-flows of air and fuel are varied, which effectively changes the jet-to-cross-flow momentum ratio and equivalence ratio, ϕ. The resulting velocity maps are processed to acquire the flow field and the resulting turbulence intensity. It is found that the change in flow conditions upstream in the nozzle affects the nearfield in both the lifted and attached flames up to two diameters downstream. The correlation between the sidejet-to-primary-flow momentum ratio, flow turbulence intensity, and their corresponding flames are presented and discussed.

Keywords: Partially Premixed Flame, Particle Imaging Velocimetry, Jet in Cross Flow, PIV.

Nomenclature

V_b	Bulk velocity (m/s)
JICF	Jet in Cross Flow
G_{inj}/G_P	Fuel to cross-flow momentum ratio
G_{inj}	Fuel injection momentum(kg.ms^{-2})
G_P	Primary flow momentum ratio
U	Mean velocity (ms^{-1})
u'	Velocity root mean square (ms^{-1})
u'/U	Turbulence intensity
ϕ	Equivalence ratio
NOx	Nitrous oxide
CNG	Compressed Natural Gas
Re_{Db}	Bulk flow Reynolds Number based on primary jet diameter

1. Introduction

Jet in cross-flow (JICF) is a classical fluid mechanics case that has been studied extensively over the decades. Although the most common cases involve flow out of chimneys that results in counter rotating vortices, JICF arrangements can be found mostly in chemical mixing, fuel and combustion quenching, and for fume dispersion. In most JICF applications in the industry, the main flow is often confined with multiple lateral jets involved [1,3]. Confinements can significantly influence the JICF behavior, in particularly the jet spread, jet trajectory and etc, but little studies on the effect of confinement on jets interaction can be found.

Studies have been conducted to investigate the effectiveness of multiple JICF to quench hot combustion products [1,7]. These studies have contributed much to the foundation of the Rich Burn Quick Quench Lean Burn (RQL) combustors, which have been proven to reduce NOx in combustion. The quick quenching and mixing effect of JICF is attributed to its complex induced structures and vortices such as counter rotating vortex pairs (CVP) and horse-shoe vortices. However, the effects of the JICF induced fuel-air mixing have not been investigated for turbulent jet flames.

Previous work by the authors [2] has classified the resulting flow of JICF in terms of momentum ratio of the side-jet to the primary flow:

$$\frac{G_{inj}}{G_P} = \frac{(\rho V^2 A)_{inj}}{(\rho V^2 A)_P} \quad (1)$$

where ρ is fluid density [kg/m^3], V is the velocity [m/s], and A is the hydraulic area for both the jet (*inj*) and primary confinement (*P*) [m^2]. Equation (1) will be used throughout this study to classify the various flows and mixing regimes by varying the G_{inj}/G_P of the flow. This ratio has consequences on the flow downstream, in particularly towards the potential core of the jet outflow [2,3].

The potential of JICF in partial premixing fuel and air for combustion is untapped. Partial premixing of the fuel and air offers advantages in terms of pollutants control and flame stability. Other example of premixing method includes recessing a fuel tube

* Corresponding author:
Phone: (+61) 8 8313 1120
Email: chia.thong@adelaide.edu.au

concentric to a central jet of air (effectively an air co-flow) [4]. Partial premixing of fuel with air prior to combustion helps to increase flame stability and delay flame lift-off.

In this paper, the flow field of a multilateral jet burner is investigated by varying both fuel (sidejet) and air (central flow) velocities whilst keeping the bulk flow a constant. This effectively varies the G_{inj}/G_P and equivalence ratio (ϕ) of the fuel mixture. Particle Imaging Velocimetry is conducted to study the planar flow field along the centerline of the flow within the flame. Flame photography is used to compare different flames in relations to the varying fuel momentum ratio and ϕ.

2. Experimental set up

2.1 Multi-lateral jet burner

Figure 1 shows the experimental set up, the top view and the cross section of the symmetrical 4-jets configuration burner used in the experiments. The primary diameter (D_P) measures 25.4mm whilst the side jets are each 3mm in bore diameter (D_{inj}) and are attached laterally to the primary pipe nozzle and placed 90 degrees relative to the adjacent jets. The jets are located at approximately 1 D_P upstream of the nozzle exit.

The flames investigated here comprise of compressed natural gas (CNG) – jets issuing into a primary cross-flow of air. The cases tested have conserved bulk velocity (V_b) of approximately ~3.1 m/s which translates to Re_{Db} ≈5000. The air and fuel mass flow rate are varied, which effectively manipulates the jet injection to cross-flow momentum ratio (G_{inj}/G_P), and the fuel-air equivalence ratio (ϕ). The experimental parameters are presented in Table 1. Both air and fuel flow rates are controlled using ABB rotameters with pressure regulators.

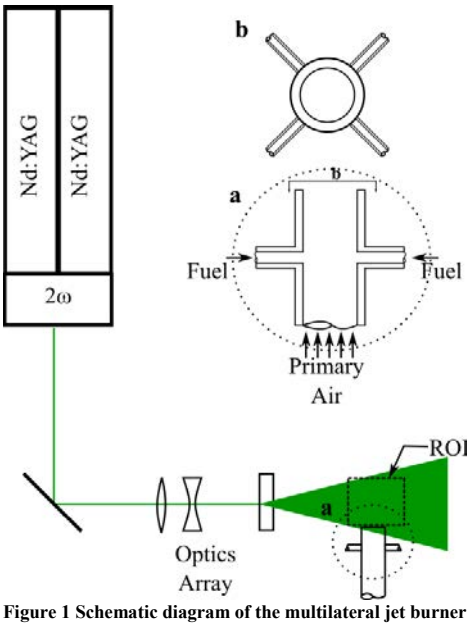

Figure 1 Schematic diagram of the multilateral jet burner experimental set up.

2.2 Optical set up

Velocity field was measured using cross correlation Particle Imaging Velocimetry technique, conducted in the TEC Laboratory at the University of Adelaide. The region of interest (ROI) is illuminated by a Quantel Brilliant B, double-pulsed Nd:YAG laser using the second harmonics at 532nm. Laser power was set to approximately 800mW. The time delay between successive laser pulses was 70μs. Both fuel and air flow streams are seeded with Sigma-Aldrich Titanium(IV) dioxide, rutile powder (<5µm) via external cyclone seeders.

The imaging system comprised of a Princeton Instruments Megaplus II ES4020 camera running in triggered double exposure mode at a 2.5Hz duty cycle. Collection optics were a Tamron 90-200 compound lens fitted with a 532nm band-pass interference filter imaging a region of approximately 86mm by 86mm onto a CCD detector of 2048 pixels by 2048 pixels. The spatial resolution is therefore ~24px/mm. The imaging was repeated for both the 45º and 90º plane (angle of imaging plane relative to the adjacent jets). The resulting Mie-scattering of titanium dioxide particles (<5μm) introduced into the flow were processed using PIVView software [5]. Cross-correlation was performed on an interrogation window of 32 pixels by 32 pixels with 50% overlap. Gaussian peak fitting was selected to avoid peak locking effect and give sub-pixel on the displacements. The PIV ensemble consisted of 500 image pairs. The PIVView output data are imported into freeware OMA-X[6] for compiling and further processing.

The flame photographs are taken with a standard NIKON Digital Single Lens Reflex (DSLR) camera. Different exposure time, ISO, and aperture were tested, and a suitable setting is used for all the presented photographs. The photographs are taken at constant height throughout the flame sets.

3. Results and Discussion

The flame photographs in Fig. 2 are arranged in decreasing order of jet-to-cross-flow momentum ratio with Fig. 2(a) corresponding to the G_{inj}/G_P=0.8 case and Fig. 2(e) corresponding to the G_{inj}/G_P=0.2

Table 1 Experimental parameters for the tested flame conditions

Cases	Jet to cross flow momentum ratio, G_{inj}/G_P	Fuel to air equivalence ratio, ϕ
i63p40	0.8	5.3
i57p42	0.6	4.6
i50p44	0.4	3.8
i44p46	0.3	3.2
i37p48	0.2	2.6

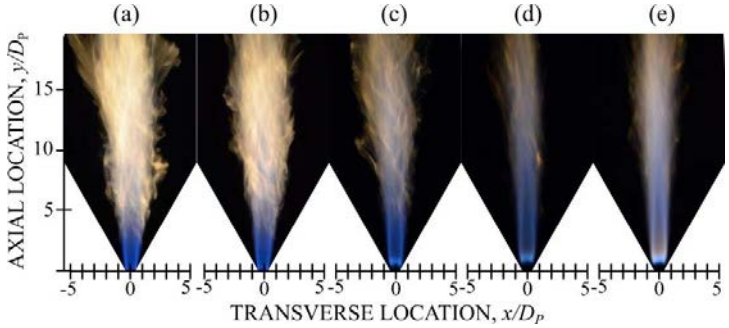

Figure 2 Photographs of flames taken by a standard DSLR exposed for 1.0s at ISO 400 and f#32 under different mixing conditions: a)G_{inj}/G_P=0.8; b)G_{inj}/G_P=0.6; c)G_{inj}/G_P=0.4; d)G_{inj}/G_P=0.3; and e)G_{inj}/G_P=0.2.

case. Decreasing the G_{inj}/G_P also decreases equivalence ratio, ϕ of the mixture. The ϕ value is reduced from 5.3 for the case in Fig. 2(a) to 2.6 in Fig. 2(e), transiting from richer to leaner flame. The decreasing ϕ in the tested cases are reflected by the flames' luminosity in Fig. 2. The flame in Fig. 2(a) shows a brighter and sootier flame as compared with the leaner flames seen in Fig. 2(e). The photographs in Fig. 2 were taken at 1.0s exposure time, at ISO 400 and apperture (f#) 32.

From Fig. 2, it is clear that the different momentum ratios impact on the flames' appearances. The flame for both G_{inj}/G_P=0.8 and 0.6 are observed to be attached to the nozzle exit, and at G_{inj}/G_P=0.4, the flame transitions intermittently from attached to lifted; hence it is termed the "transitional flame". Flame lift-off can be seen more prominently for cases G_{inj}/G_P=0.3 and G_{inj}/G_P=0.2. From these figures, the lift-off height is estimated to be approximately 1D_P above the nozzle exit.

The G_{inj}/G_P values that denote the tested cases also reflect the different mixing regimes within the primary jet that are achieved before being expelled out to be burnt, which include [2]:

a) Backflow mode
b) Impinging mode
c) Streaming mode

Cases G_{inj}/G_P=0.8 and G_{inj}/G_P=0.6 corresponds to the backflow mode, as shown in the isothermal studies, whilst G_{inj}/G_P=0.4 to G_{inj}/G_P=0.2 correspond to that of an impinging flow mode.

For backflow mode, the fuel injected into the air cross-flow propagates upstream into the nozzle before being expelled. This partial premixing does not lead to flame propagation into the burner due to the flow conditions and rich mixtures.

Figure 3 shows the mean velocity field images with no smoothing and filter applied, for the different flames. Figure 3(a) to 3(e) show the axial velocity magnitude for the cases G_{inj}/G_P=0.8 to G_{inj}/G_P=0.2. The images to the left of each plot show the velocity field captured at the 45° plane (relative to the adjacent jets as indicated by the accompanying schematic drawings) whilst the right side of the plots show the velocity field captured at the 90° plane. The measurements cover the flow from centerline to 1D_P in the transverse location, and from the nozzle exit to approximately 2.5D_P downstream.

Figure 3(a) and 3(b) shows a flow-field that is similar to a round jet flow exit. Comparing the 45° plane to the 90° plane shows that both planes are symmetrical despite the location of the jets. Figure 3(c), 3(d) and (e) shows a "necking" in the flow field. The necking of the flow happens further downstream with reducing G_{inj}/G_P. This necking also coincides with the lift-off distance of the respective cases, which is observed to increase with reducing G_{inj}/G_P.

Figure 4 shows the centreline velocity decay plots for all tested cases. The outflow centerline velocity, U_C for each of the cases are normalized to their

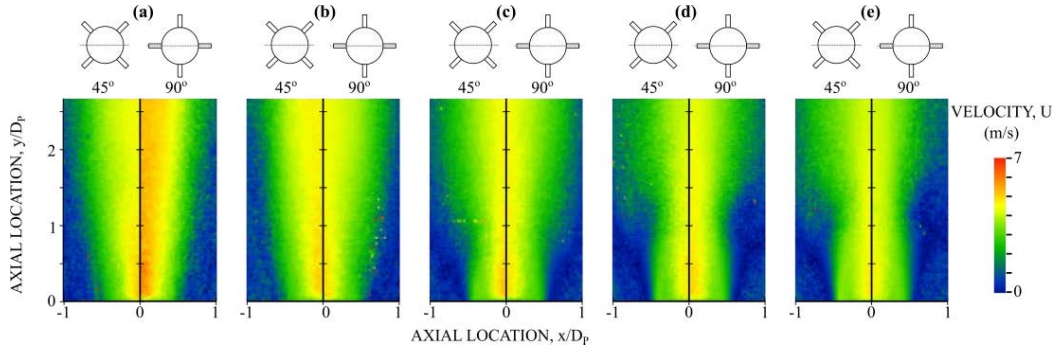

Figure 3 Mean velocity magnitude images at the 45° and 90° relative planes for cases: a)G_{inj}/G_P=0.8; b)G_{inj}/G_P=0.6; c)G_{inj}/G_P=0.4; d)G_{inj}/G_P=0.3; and e)G_{inj}/G_P=0.2. The schematic diagram above each sub-figure shows the orientation of the side jet nozzles relative to the laser plane (dashed line).

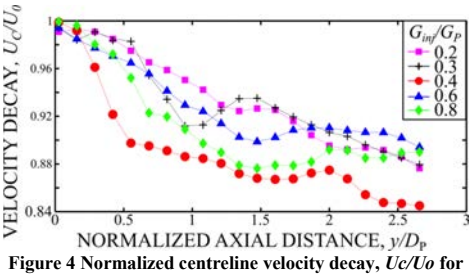

Figure 4 Normalized centreline velocity decay, *Uc/Uo* for the studied cases, measured at the centreline from the burner nozzle exit to approximately 2.5D_P downstream.

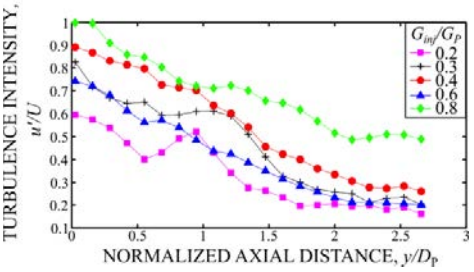

Figure 5 Turbulence intensity, *u'/U* for the studied cases, measured at the flow centreline from the nozzle exit to approximately 2.5D_P downstream.

respective centerline nozzle exit velocity, U_0 and is measured to approximately 2.5D_P downstream.

It is clear from Fig. 4 that the centerline velocity decay for these flames is different from a standard decay of a simple jet. The virtual origin seems to have shifted and the velocity decay is accelerated close to the jet exit, recovers slightly at y/D_P=1.5~2.0, before decaying again. The increase in decay rate close to the exit increases with the momentum ratio. Also noticeable is that the axial location of the velocity recovery for the G_{inj}/G_P=0.2 and 0.3 cases coincident with the lift-off height of these flames. The transitional case (G_{inj}/G_P=0.4) exhibits the largest drop in mean centerline velocity, i.e. 12% from the exit to around 0.5D_P before it plateaus and decays further past 2D_P. Modelling of similar cases in isothermal condition using commercially available Computational Fluid Dynamics package, ANSYS CFX reveals similar trend where the decay pattern further downstream (>2.5D_P) is similar to round jets with no side injection. This observation corroborates the fact that the side jets effect is limited to the flow in the near field region.

Figure 5 shows the turbulence intensity, u'/U at the flow centerline plotted from the nozzle exit to approximately 2.5D_P downstream. The turbulence intensity is obtained by normalizing fluctuating component of (u') to their respective local mean velocity (U). Similar to the trends observed in Fig. 4, the turbulence intensity is affected up to the measured axial location in this study and becomes quite similar further downstream. While there is a clear trend of an increase in turbulence intensity at the jet exit corresponding to the increase in the momentum ratio, the case G_{inj}/G_P=0.6 does not follow this trend. The increase in turbulence intensity around y/D_P=1 seems to be associated with flame ignition and coincides with lift-off height location. Most of the tested cases reduces to a consistent u'/U = 0.2~0.3 except for G_{inj}/G_P=0.8 case which remains much higher at around u'/U≈0.6.

Generally, despite the increase in ϕ, the lift off distance is decreased. This particular trait of this fuel-air mixing method shows the increasing flame stability with increasing G_{inj}/G_P. By increasing the momentum ratio, the side jets interact with the adjacent jets, which promotes more mixing and hence producing a delayed flame lift off.

4. Conclusion

The flow field and stability of a multi-lateral jet burner of methane-air mixture are presented in this paper. It is found that changes in the jet to cross-flow momentum ratio has significant effect on the resulting flows up to 2 primary diameter downstream, and this is reflected in both the velocity decay plot and the turbulence intensity. However, the short downstream distance that is affected by the change in jet to primary flow momentum-ratio is sufficient to affect the flame stability drastically. Further work is underway to investigate the flame structures generated by the multilateral jet mixing technique and correlated to the velocity field, and flame stability.

4. Acknowledgments

This work was made possible using the equipment at the Centre for Energy Technology at the University of Adelaide and the financial support of ARC Discovery.

5. References

[1] J.D. Holdeman, D.S. Liscinsky, V.L. Oechsle, G.S. Samuelsen and C.E. Smith, Journal of Engineering for Gas Turbines and Power. **119** (1997), pp. 852–862

[2] C.X. Thong, P.A.M. Kalt, B.B. Dally and C.H. Birzer, Exp Fluids. **56** (15) (2015), pp. 1–16

[3] T. New and W. Tay, Journal of Turbulence **7** (57) (2006), pp. 1–20

[4] S. Meares and A.R. Masri, Combustion and Flame **161** (2014), pp. 484–495

[5] PIVTEV GmbH [www.pivtec.com]

[6] P.A.M. Kalt and M.B. Long, [www.oma-x.org]

[7] M.Y Leong and G.S. Samuelsen, Journal of Propulsion and Power, **16** (5)(2000), pp. 729-735.

Appendix C

Australian Conference on Laser Diagnostics in Fluid Mechanics and Combustion 2015

Proceedings of the Australian Combustion Symposium
December 7-9, 2015, The University of Melbourne

Effect of multi-lateral fuel jet injection on the flow field of Methane-Air turbulent flame

C.X. Thong[1, *], B.B. Dally[1], C.H. Birzer[1], P.A.M. Kalt[1]
[1]Centre for Energy Technology
School of Mechanical Engineering
The University of Adelaide SA 5005 Australia

Abstract
Multi-lateral jet injection concepts have a long history in industry and for various purposes, be it for hot combustion product quenching or for general mixing applications. The current study involves injecting fuel (CNG) through lateral side jets, a short distance upstream of a round jet air nozzle exit, with a flame stabilizing at the jet exit. Flame photography and Particle Imaging Velocimetry measurements were conducted as part of a preliminary study to investigate the effect of lateral injection on flame flow field, stability and appearance. For this study, the bulk flow velocity is kept constant whilst mass-flows of air and fuel are varied, which effectively changes the jet-to-cross-flow momentum ratio and equivalence ratio, ϕ. The resulting velocity maps are processed to acquire the flow field and the resulting turbulence intensity. It is found that the change in flow conditions upstream in the nozzle affects the nearfield in both the lifted and attached flames up to two diameters downstream. The correlation between the sidejet-to-primary-flow momentum ratio, flow turbulence intensity, and their corresponding flames are presented and discussed.

Keywords: Partially Premixed Flame, Particle Imaging Velocimetry, Jet in Cross Flow, PIV.

Nomenclature

V_b	Bulk velocity (m/s)
JICF	Jet in Cross Flow
G_{inj}/G_P	Fuel to cross-flow momentum ratio
G_{inj}	Fuel injection momentum(kg.ms^{-2})
G_P	Primary flow momentum ratio
U	Mean velocity (ms^{-1})
u'	Velocity root mean square (ms^{-1})
u'/U	Turbulence intensity
ϕ	Equivalence ratio
NOx	Nitrous oxide
CNG	Compressed Natural Gas
Re_{Db}	Bulk flow Reynolds Number based on primary jet diameter

1. Introduction

Jet in cross-flow (JICF) is a classical fluid mechanics case that has been studied extensively over the decades. Although the most common cases involve flow out of chimneys that results in counter rotating vortices, JICF arrangements can be found mostly in chemical mixing, fuel and combustion quenching, and for fume dispersion. In most JICF applications in the industry, the main flow is often confined with multiple lateral jets involved [1,3]. Confinements can significantly influence the JICF behavior, in particularly the jet spread, jet trajectory and etc, but little studies on the effect of confinement on jets interaction can be found.

Studies have been conducted to investigate the effectiveness of multiple JICF to quench hot combustion products [1,7]. These studies have contributed much to the foundation of the Rich Burn Quick Quench Lean Burn (RQL) combustors, which have been proven to reduce NOx in combustion. The quick quenching and mixing effect of JICF is attributed to its complex induced structures and vortices such as counter rotating vortex pairs (CVP) and horse-shoe vortices. However, the effects of the JICF induced fuel-air mixing have not been investigated for turbulent jet flames.

Previous work by the authors [2] has classified the resulting flow of JICF in terms of momentum ratio of the side-jet to the primary flow:

$$\frac{G_{inj}}{G_P} = \frac{(\rho V^2 A)_{inj}}{(\rho V^2 A)_P} \quad (1)$$

where ρ is fluid density [kg/m^3], V is the velocity [m/s], and A is the hydraulic area for both the jet (*inj*) and primary confinement (*P*) [m^2]. Equation (1) will be used throughout this study to classify the various flows and mixing regimes by varying the G_{inj}/G_P of the flow. This ratio has consequences on the flow downstream, in particularly towards the potential core of the jet outflow [2,3].

The potential of JICF in partial premixing fuel and air for combustion is untapped. Partial premixing of the fuel and air offers advantages in terms of pollutants control and flame stability. Other example of premixing method includes recessing a fuel tube

* Corresponding author:
Phone: (+61) 8 8313 1120
Email: chia.thong@adelaide.edu.au

concentric to a central jet of air (effectively an air co-flow) [4]. Partial premixing of fuel with air prior to combustion helps to increase flame stability and delay flame lift-off.

In this paper, the flow field of a multilateral jet burner is investigated by varying both fuel (sidejet) and air (central flow) velocities whilst keeping the bulk flow a constant. This effectively varies the G_{inj}/G_P and equivalence ratio (ϕ) of the fuel mixture. Particle Imaging Velocimetry is conducted to study the planar flow field along the centerline of the flow within the flame. Flame photography is used to compare different flames in relations to the varying fuel momentum ratio and ϕ.

2. Experimental set up

2.1 Multi-lateral jet burner

Figure 1 shows the experimental set up, the top view and the cross section of the symmetrical 4-jets configuration burner used in the experiments. The primary diameter (D_P) measures 25.4mm whilst the side jets are each 3mm in bore diameter (D_{inj}) and are attached laterally to the primary pipe nozzle and placed 90 degrees relative to the adjacent jets. The jets are located at approximately 1 D_P upstream of the nozzle exit.

The flames investigated here comprise of compressed natural gas (CNG) – jets issuing into a primary cross-flow of air. The cases tested have conserved bulk velocity (V_b) of approximately ~3.1 m/s which translates to Re_{Db} ≈5000. The air and fuel mass flow rate are varied, which effectively manipulates the jet injection to cross-flow momentum ratio (G_{inj}/G_P), and the fuel-air equivalence ratio (ϕ). The experimental parameters are presented in Table 1. Both air and fuel flow rates are controlled using ABB rotameters with pressure regulators.

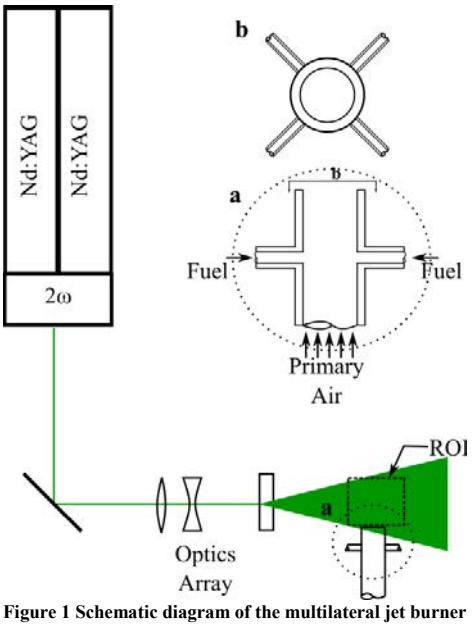

Figure 1 Schematic diagram of the multilateral jet burner experimental set up.

2.2 Optical set up

Velocity field was measured using cross correlation Particle Imaging Velocimetry technique, conducted in the TEC Laboratory at the University of Adelaide. The region of interest (ROI) is illuminated by a Quantel Brilliant B, double-pulsed Nd:YAG laser using the second harmonics at 532nm. Laser power was set to approximately 800mW. The time delay between successive laser pulses was 70μs. Both fuel and air flow streams are seeded with Sigma-Aldrich Titanium(IV) dioxide, rutile powder (<5µm) via external cyclone seeders.

The imaging system comprised of a Princeton Instruments Megaplus II ES4020 camera running in triggered double exposure mode at a 2.5Hz duty cycle. Collection optics were a Tamron 90-200 compound lens fitted with a 532nm band-pass interference filter imaging a region of approximately 86mm by 86mm onto a CCD detector of 2048 pixels by 2048 pixels. The spatial resolution is therefore ~24px/mm. The imaging was repeated for both the 45º and 90º plane (angle of imaging plane relative to the adjacent jets). The resulting Mie-scattering of titanium dioxide particles (<5μm) introduced into the flow were processed using PIVView software [5]. Cross-correlation was performed on an interrogation window of 32 pixels by 32 pixels with 50% overlap. Gaussian peak fitting was selected to avoid peak locking effect and give sub-pixel on the displacements. The PIV ensemble consisted of 500 image pairs. The PIVView output data are imported into freeware OMA-X[6] for compiling and further processing.

The flame photographs are taken with a standard NIKON Digital Single Lens Reflex (DSLR) camera. Different exposure time, ISO, and aperture were tested, and a suitable setting is used for all the presented photographs. The photographs are taken at constant height throughout the flame sets.

3. Results and Discussion

The flame photographs in Fig. 2 are arranged in decreasing order of jet-to-cross-flow momentum ratio with Fig. 2(a) corresponding to the G_{inj}/G_P=0.8 case and Fig. 2(e) corresponding to the G_{inj}/G_P=0.2

Table 1 Experimental parameters for the tested flame conditions

Cases	Jet to cross flow momentum ratio, G_{inj}/G_P	Fuel to air equivalence ratio, ϕ
i63p40	0.8	5.3
i57p42	0.6	4.6
i50p44	0.4	3.8
i44p46	0.3	3.2
i37p48	0.2	2.6

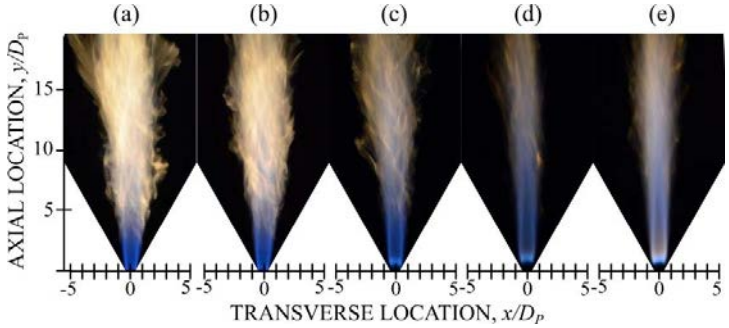

Figure 2 Photographs of flames taken by a standard DSLR exposed for 1.0s at ISO 400 and f#32 under different mixing conditions: a)G_{inj}/G_P=0.8; b)G_{inj}/G_P=0.6; c)G_{inj}/G_P=0.4; d)G_{inj}/G_P=0.3; and e)G_{inj}/G_P=0.2.

case. Decreasing the G_{inj}/G_P also decreases equivalence ratio, ϕ of the mixture. The ϕ value is reduced from 5.3 for the case in Fig. 2(a) to 2.6 in Fig. 2(e), transiting from richer to leaner flame. The decreasing ϕ in the tested cases are reflected by the flames' luminosity in Fig. 2. The flame in Fig. 2(a) shows a brighter and sootier flame as compared with the leaner flames seen in Fig. 2(e). The photographs in Fig. 2 were taken at 1.0s exposure time, at ISO 400 and apperture (f#) 32.

From Fig. 2, it is clear that the different momentum ratios impact on the flames' appearances. The flame for both G_{inj}/G_P=0.8 and 0.6 are observed to be attached to the nozzle exit, and at G_{inj}/G_P=0.4, the flame transitions intermittently from attached to lifted; hence it is termed the "transitional flame". Flame lift-off can be seen more prominently for cases G_{inj}/G_P=0.3 and G_{inj}/G_P=0.2. From these figures, the lift-off height is estimated to be approximately 1D_P above the nozzle exit.

The G_{inj}/G_P values that denote the tested cases also reflect the different mixing regimes within the primary jet that are achieved before being expelled out to be burnt, which include [2]:

a) Backflow mode
b) Impinging mode
c) Streaming mode

Cases G_{inj}/G_P=0.8 and G_{inj}/G_P=0.6 corresponds to the backflow mode, as shown in the isothermal studies, whilst G_{inj}/G_P=0.4 to G_{inj}/G_P=0.2 correspond to that of an impinging flow mode.

For backflow mode, the fuel injected into the air cross-flow propagates upstream into the nozzle before being expelled. This partial premixing does not lead to flame propagation into the burner due to the flow conditions and rich mixtures.

Figure 3 shows the mean velocity field images with no smoothing and filter applied, for the different flames. Figure 3(a) to 3(e) show the axial velocity magnitude for the cases G_{inj}/G_P=0.8 to G_{inj}/G_P=0.2. The images to the left of each plot show the velocity field captured at the 45° plane (relative to the adjacent jets as indicated by the accompanying schematic drawings) whilst the right side of the plots show the velocity field captured at the 90° plane. The measurements cover the flow from centerline to 1D_P in the transverse location, and from the nozzle exit to approximately 2.5D_P downstream.

Figure 3(a) and 3(b) shows a flow-field that is similar to a round jet flow exit. Comparing the 45° plane to the 90° plane shows that both planes are symmetrical despite the location of the jets. Figure 3(c), 3(d) and (e) shows a "necking" in the flow field. The necking of the flow happens further downstream with reducing G_{inj}/G_P. This necking also coincides with the lift-off distance of the respective cases, which is observed to increase with reducing G_{inj}/G_P.

Figure 4 shows the centreline velocity decay plots for all tested cases. The outflow centerline velocity, U_C for each of the cases are normalized to their

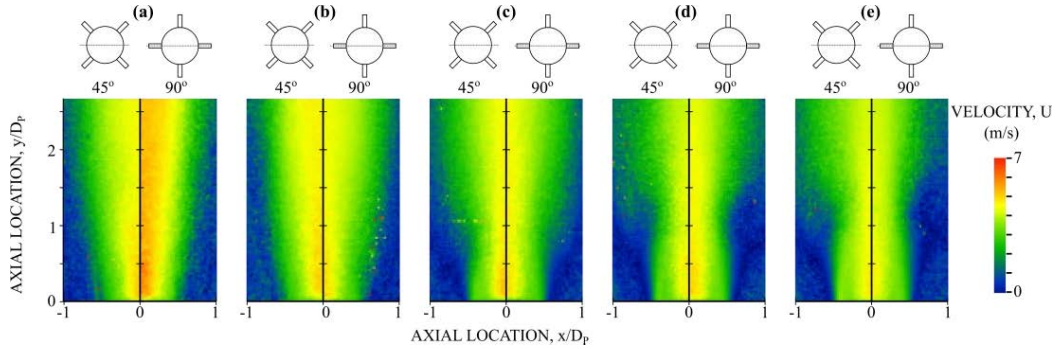

Figure 3 Mean velocity magnitude images at the 45° and 90° relative planes for cases: a)G_{inj}/G_P=0.8; b)G_{inj}/G_P=0.6; c)G_{inj}/G_P=0.4; d)G_{inj}/G_P=0.3; and e)G_{inj}/G_P=0.2. The schematic diagram above each sub-figure shows the orientation of the side jet nozzles relative to the laser plane (dashed line).

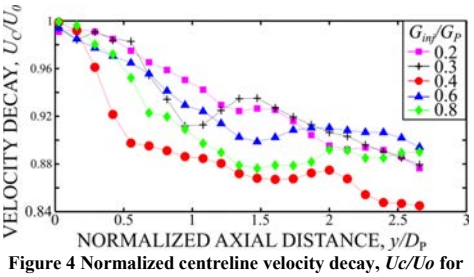

Figure 4 Normalized centreline velocity decay, *Uc/Uo* for the studied cases, measured at the centreline from the burner nozzle exit to approximately 2.5D_P downstream.

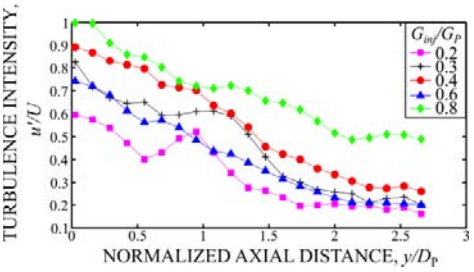

Figure 5 Turbulence intensity, *u'/U* for the studied cases, measured at the flow centreline from the nozzle exit to approximately 2.5D_P downstream.

respective centerline nozzle exit velocity, U_0 and is measured to approximately 2.5D_P downstream.

It is clear from Fig. 4 that the centerline velocity decay for these flames is different from a standard decay of a simple jet. The virtual origin seems to have shifted and the velocity decay is accelerated close to the jet exit, recovers slightly at y/D_P=1.5~2.0, before decaying again. The increase in decay rate close to the exit increases with the momentum ratio. Also noticeable is that the axial location of the velocity recovery for the G_{inj}/G_P=0.2 and 0.3 cases coincident with the lift-off height of these flames. The transitional case (G_{inj}/G_P=0.4) exhibits the largest drop in mean centerline velocity, i.e. 12% from the exit to around 0.5D_P before it plateaus and decays further past 2D_P. Modelling of similar cases in isothermal condition using commercially available Computational Fluid Dynamics package, ANSYS CFX reveals similar trend where the decay pattern further downstream (>2.5D_P) is similar to round jets with no side injection. This observation corroborates the fact that the side jets effect is limited to the flow in the near field region.

Figure 5 shows the turbulence intensity, u'/U at the flow centerline plotted from the nozzle exit to approximately 2.5D_P downstream. The turbulence intensity is obtained by normalizing fluctuating component of (u') to their respective local mean velocity (U). Similar to the trends observed in Fig. 4, the turbulence intensity is affected up to the measured axial location in this study and becomes quite similar further downstream. While there is a clear trend of an increase in turbulence intensity at the jet exit corresponding to the increase in the momentum ratio, the case G_{inj}/G_P=0.6 does not follow this trend. The increase in turbulence intensity around y/D_P=1 seems to be associated with flame ignition and coincides with lift-off height location. Most of the tested cases reduces to a consistent u'/U = 0.2~0.3 except for G_{inj}/G_P=0.8 case which remains much higher at around u'/U≈0.6.

Generally, despite the increase in ϕ, the lift off distance is decreased. This particular trait of this fuel-air mixing method shows the increasing flame stability with increasing G_{inj}/G_P. By increasing the momentum ratio, the side jets interact with the adjacent jets, which promotes more mixing and hence producing a delayed flame lift off.

4. Conclusion

The flow field and stability of a multi-lateral jet burner of methane-air mixture are presented in this paper. It is found that changes in the jet to cross-flow momentum ratio has significant effect on the resulting flows up to 2 primary diameter downstream, and this is reflected in both the velocity decay plot and the turbulence intensity. However, the short downstream distance that is affected by the change in jet to primary flow momentum-ratio is sufficient to affect the flame stability drastically. Further work is underway to investigate the flame structures generated by the multilateral jet mixing technique and correlated to the velocity field, and flame stability.

4. Acknowledgments

This work was made possible using the equipment at the Centre for Energy Technology at the University of Adelaide and the financial support of ARC Discovery.

5. References

[1] J.D. Holdeman, D.S. Liscinsky, V.L. Oechsle, G.S. Samuelsen and C.E. Smith, Journal of Engineering for Gas Turbines and Power. **119** (1997), pp. 852–862

[2] C.X. Thong, P.A.M. Kalt, B.B. Dally and C.H. Birzer, Exp Fluids. **56** (15) (2015), pp. 1–16

[3] T. New and W. Tay, Journal of Turbulence **7** (57) (2006), pp. 1–20

[4] S. Meares and A.R. Masri, Combustion and Flame **161** (2014), pp. 484–495

[5] PIVTEV GmbH [www.pivtec.com]

[6] P.A.M. Kalt and M.B. Long, [www.oma-x.org]

[7] M.Y Leong and G.S. Samuelsen, Journal of Propulsion and Power, **16** (5)(2000), pp. 729-735.